Title

Using MiniCLEAN and measurements of microphysical material properties in the vacuum ultraviolet regime to inform next-generation dark matter and neutrino detectors

Author

Benson, Christopher Pete

Publication Date

2018

Peer reviewed|Thesis/dissertation

Using MiniCLEAN and measurements of microphysical material properties in the vacuum ultraviolet regime to inform next-generation dark matter and neutrino detectors

by

Christopher Pete Benson

A dissertation submitted in partial satisfaction of the

requirements for the degree of

Doctor of Philosophy

in

Physics

in the

Graduate Division

of the

University of California, Berkeley

Committee in charge:

Professor Gabriel D. Orebi Gann, Chair
Professor Daniel McKinsey
Professor Karl A. van Bibber

Summer 2018

Using MiniCLEAN and measurements of microphysical material properties in the vacuum ultraviolet regime to inform next-generation dark matter and neutrino detectors

Abstract

Using MiniCLEAN and measurements of microphysical material properties in the vacuum ultraviolet regime to inform next-generation dark matter and neutrino detectors

by

Christopher Pete Benson

Doctor of Philosophy in Physics

University of California, Berkeley

Professor Gabriel D. Orebi Gann, Chair

Many compelling pieces of indirect evidence pointing to the existence of dark matter. While a confirmed and direct signature of dark matter has yet to be observed, many theoretical models have been developed in an attempt to explain the indirect evidence, and to provide phenomenological models that can be tested with targeted experiments. The WIMP is a well-motivated dark matter candidate currently being sought for by several experiments. A variety of detector technologies are utilized, including liquid noble detectors, to look for WIMP scattering as a direct signature of dark matter.

The CLEAN experiment is a proposed single-phase, monolithic, large-scale liquid argon experiment designed to look for high-mass WIMPs. A liquid neon target could be exchanged with the argon target to study solar neutrinos and to test the A^2 dependence of a possible dark matter signal. Before scaling up to the multi-tonne scale of the full CLEAN detector, the design philosophy and background rejection capabilities required for the next-generation project are being tested using the MiniCLEAN prototype. As of mid-2018, MiniCLEAN has been constructed at SNOLAB and is currently being filled with natural liquid argon for a dark matter run. Following a short dark matter run, MiniCLEAN will be spiked with elevated levels of ^{39}Ar to test the scaling limits of pulse shape discrimination, the primary method for electronic background rejection. These results will inform existing experiments and the next-generation of large-scale liquid argon detectors.

A good understanding of light propagation is critical for optical experiments such as CLEAN, whose event reconstruction and background rejection relies primarily on scintillation light collection. This work presents two classes of complementary results which are expected to improve the modeling of scintillation light collection in current and future neutrino and dark matter detectors. These are, first, the dependence of the scintillation light time structure (triplet lifetime) and relative light yield of gaseous argon as a function of impurity level and, second, the measurement of several parameters critical to constructing a microphysically-motivated model of tetraphenyl butadiene (TPB) wavelength shifting thin

films - a technology which is commonly used in many existing and proposed liquid noble gas experiments.

To Chelsey

Contents

List of Figures

List of Tables

Acknowledgments

First of all, I would like to thank Prof. Gabriel Orebi Gann for her guidance, insight and steadfast support as my adviser. I have learned much during my time in her research group and I am very thankful for the opportunity to work along side such wonderful, kind, and knowledgeable people. I am especially thankful for Gabriel's resolve during times of uncertainty and for her emphasis of a well-balanced hardware, software, and analysis education.

I would also like to thank my friends in MiniCLEAN collaboration for all they have taught me and for persisting through numerous challenges. In particular, I'd like to thank Chris Jackson for his guidance and for taking over project management of MiniCLEAN, Tom Caldwell for being an invaluable source of knowledge and his essential role in detector construction and modeling, Steve Linden for his commitment and continuous on-site presence, Ryan Wang for his contributions to analysis and continued support, others who have spent many hours shifting and/or on-site (Kimberly Palladino, Antonio Ledesma, Gabriel Ortega, Kolahal Bhattacharya, Brianna Grado-White, Amanda Bacon), and the SNOLAB staff for their support of the experiment. I'd also like to thank Josh Klein for stepping in as the experiment spokesperson during a time of great need and for his valuable insight. Also, thank you to Victor Gehman for his support during and knowledge during the early stages of the VUV work.

In addition, I would like to thank my family and friends for their continuous love and support. Their compassion and encouragement helped Chelsey and I through the long hours, uncertainty, and stress of graduate school. We have many fond memories of this time, and will continue to cherish them for years to come.

Lastly, I thank my wonderful wife, Chelsey, for her love and endless support during this journey. I couldn't have done it without you. We made it!

Chapter 1

Introduction

1.1 Evidence for Dark Matter

The first evidence that the matter composition of universe was not well understood was F. Zwicky's 1933 discovery of gravitational anomalies in the Coma Clusters [1]. Using the Virial Theorem and measurements of the motion of galaxies within the cluster, Zwicky determined the gravitational potential and speed of the galaxies to be larger than what could be accounted for by estimations of the visible mass. Zwicky wrote in his seminal paper that these galaxies must be bound together by "*dunkle Materie*", or dark matter.

Galactic Rotation Curves: Approximately fifty years later, Rubin *et al.* put Zwicky's claim to the test by measuring the rotation speed of several individual galaxies [2]. Presented in Fig. 1.1, Rubin determined that the measured rotational velocity, $v(r)$, of luminous matter away from the central luminous region of several spiral galaxies was approximately constant as a function of radius, r, and much greater than expected when only considering the visible luminous matter (stars, luminous gas, etc.). This observation conflicted with the expectation, using Newtonian mechanics, that the rotational velocity of luminous matter of a galaxy for objects outside of r (assuming the bulk of the galaxy's matter is inside r) should fall off as $v(r) \propto 1/\sqrt{r}$. The observation of constant rotational speed value at large radius implies that the mass density distribution beyond the luminous region of the galaxy scales as $1/r^2$, which is most easily explained by the presence of a uniform halo of gravitating and non-luminescent matter. Further, they determined that the relative abundance of the non-luminescent matter must be approximately 6 times more than the visible matter to account for the large rotational speeds.

Bullet Cluster: As astronomical observation techniques improved in the decades following Rubin's result, the indirect evidence of dark matter continued to mount. In particular, the development of gravitational lensing techniques provided the ability to map matter distributions in galactic clusters. Because large accumulations of matter induce curvature in

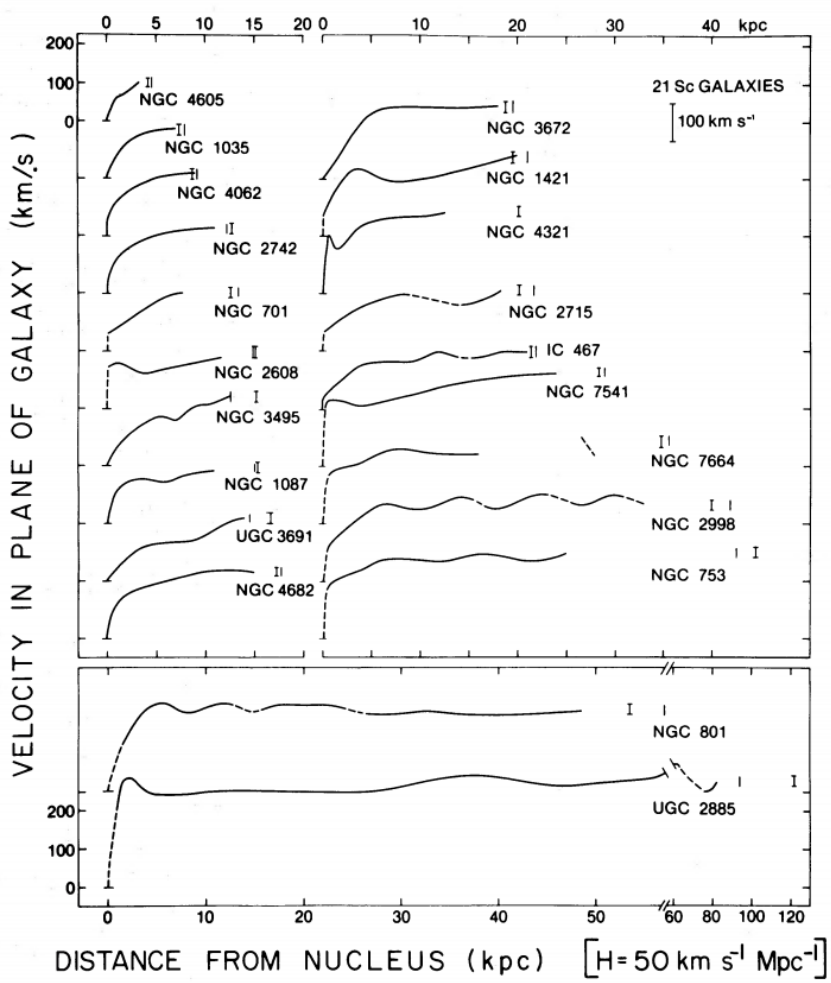

Figure 1.1: The measured rotational velocity for 21 spiral galaxies. The mean velocity in the plane of the galaxy is shown as a function of the linear distance from the nucleus [2].

local regions of space, the trajectory of light passing though these regions may be bent when compared to a flat metric of empty space. This creates a convex lensing effect, known as weak lensing, where the observed distortion of several separate objects allows for the reconstruction of the matter distribution in the region.

The bullet cluster (1E0657-558), discovered in 2005, is one such observation that provides compelling evidence for the existence of dark matter [3]. The false-colored image shown in Fig. 1.2 shows the aftermath of a recent (on cosmological timescales) collision of two clusters of galaxies 3.7 billion light-years away. The red regions indicate hot gas (emitted X-rays) due to collisions with baryonic matter when the galactic clusters passed through each other. The blue regions represent the concentration of matter determined by gravitational lensing. This image clearly shows that the bulk of the mass of the galaxy clusters passed through each

other with little interaction while the baryonic matter, such as gas and dust, was shocked, heated and slowed due to collisions. The spatial separation in the baryonic (red) and the mass peaks (blue) was found to be significant to 8σ, which strongly suggests that the overwhelming majority of matter is these galaxy clusters is weakly interacting and non-luminous.

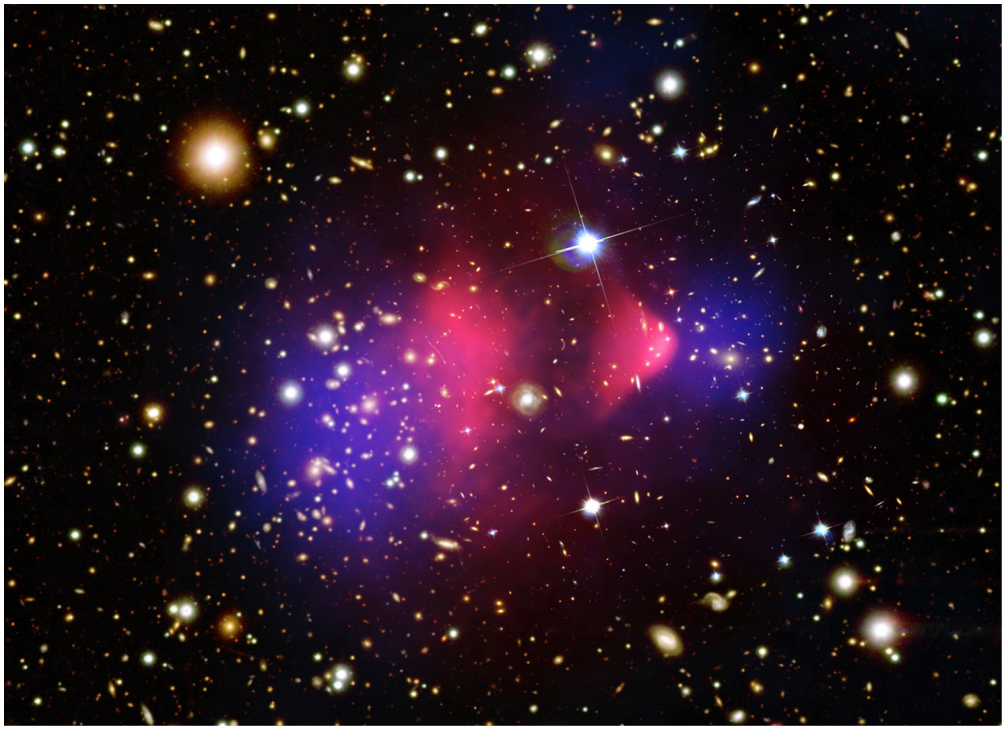

Figure 1.2: A false-colored image of a collision of two clusters of galaxies 3.7 billion light-years away. The red regions indicate gas heated by collisions with baryonic matter when the galactic clusters passed through each other. The blue regions represent the concentration of matter determined by gravitational lensing. The spatial separation in the baryonic (red) and the mass peaks (blue) was found to be significant to 8σ, which suggests that the overwhelming majority of matter is these galaxy clusters is weakly interacting and non-luminous [3].

Additional gravatational lensing studies have provided insight on the mass distribution present in other galactic clusters. In particular, the studies described in [4, 5] mapped the matter distribution of the galactic cluster 0024+1654. While the individual galaxies were each shown to contain large amounts of non-luminous matter, the intergalactic space between the galaxies in the dense cluster also contained a significant concentration of non-luminous matter.

The underlying structure observed in weak lensing of a single galactic cluster is consistent with other very large-scale structures identified by the Sloan Digital Sky Survey which extends to distances of 600 Mpc [6]. In order for structure to be visible over these large scales, density fluctuations are required to have been present very early in the universe. As

discussed in greater detail in Sec. 1.2, it is hypothesized that dark matter froze out long before the recombination, which laid the seeds for the required density fluctuations in the early universe.

Cosmic microwave background: The final piece of indirect evidence to be discussed is related to measurements of anisotropies in the cosmic microwave background (CMB), the oldest light in the universe orginating from the recombination epoch. The WMAP experiment collected nine years of data, with which it precisely mapped the CMB [7]. The famous CMB mapping illustrates the observed temperature fluctuations (left-side image of Fig. 1.3). The structure of the temperature profile anisotropies in the CMB contains a remarkable amount of information relating to the expansion and evolution of the early universe toward the matter densities observed today.

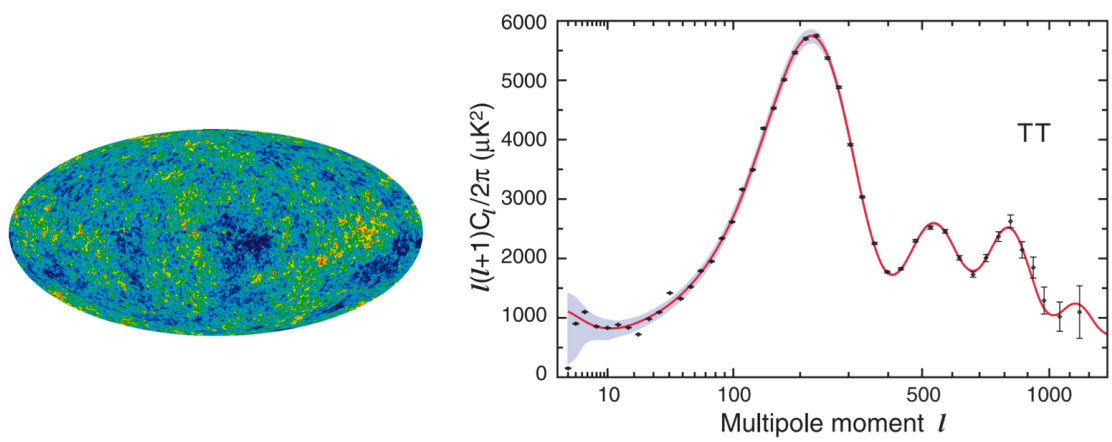

Figure 1.3: Left: Temperature flucations mapping of the CMB as measured by the WMAP collaboration [8]. Right: The WMAP temperature angular power spectrum from the WMAP data set. The red line is the best fit to the data. [7]

Considering the cosmology Friedmann equations in the lambda cold dark matter model (ΛCDM) in Eq. 1.1 and Eq. 1.2:

$$\left(\frac{H}{H_0^2}\right)^2 \equiv \frac{1}{H_0}\left(\frac{\dot{a}}{a}\right)^2 = \Omega_m\left(\frac{a_0}{a}\right)^3 + \Omega_k\left(\frac{a_0}{a}\right)^2 + \Omega_\Lambda \tag{1.1}$$

$$\frac{1}{H_0^2}\frac{\ddot{a}}{a} = -\frac{1}{2}\Omega_m\left(\frac{a_0}{a}\right)^3 + \Omega_\Lambda \tag{1.2}$$

where Ω_m is the matter density, Ω_Λ is the cosmological constant, Ω_k is the curvature of the universe relative to the critical density today such that $\Omega_m + \Omega_\Lambda + \Omega_k = 1$, H is the Hubble constant, a is the scale factor at time t and the subscript 0 denotes the value

today. The mass term can further be separated into the sum of baryonic matter, Ω_b, and non-baryonic dark matter, Ω_χ, using the relationship $\Omega_m = \Omega_b + \Omega_\chi$.

Using the 9-year data set from the WMAP CMB survey, combined with other CMB measurements, baryon acoustic oscillation measurements, and independent measurements of the Hubble constant, the WMAP collaboration performed a six parameter fit to the parameters in the ΛCDM model to precisely measure the matter content of the universe [7]. The fitted parameters were the dark energy density ($\Omega_\Lambda h^2$), the dark matter density ($\Omega_\chi h^2$), the baryonic matter density (Ω_m), the amplitude of the curvature perturbations, the scalar spectral index of inflation, and the optical depth of reionization. The previously mentioned h is defined by $H = 100h$ km/s/Mpc. The fit in [7] found the best fit values for $\Omega_b = 0.04628 \pm 0.00093$, $\Omega_\chi = 0.2402^{+0.0088}_{-0.0087}$, and $\Omega_\Lambda = 0.7135^{+0.0095}_{-0.0096}$. The temperature angular power spectrum collected and used in the fitting of these parameters is shown in the right-side plot of Fig. 1.3 taken from [7].

Given the consistency in the various data sets with the ΛCDM model, and the expectation that the universe contains a substantial amount of dark matter from the previously discussed evidence, the CMB measurements provide strong indirect evidence for the existence of dark matter.

1.2 The WIMP Model

Given the strong indirect evidence of dark matter discussed in Sec. 1.1, many particle-based models of dark matter have been developed for experimental testing. The weakly interacting massive particle (WIMP) is one such model which is well motivated, widely studied, and the subject of this section. Alternative dark matter candidate models are discussed in Sec. 1.3.

The WIMP dark matter candidate is a long-lived particle thought to have a mass roughly between 10 GeV and a few TeV and to interact with standard model particles via the weak interaction. Interestingly, a long-lived particle of this mass scale with interactions on the order of the weak scale can be calculated to reproduce the observed dark matter relic density if it were in thermal and chemical equilibrium with the "hot soup" of standard model particles after inflation, but before recombination [9].

For instance, following the formalism laid out in [9], if the number density of χ particles is in thermal equilibrium with the soup, the annihilation rate of χ particles into lighter particles can be expressed as $\langle\sigma_a v\rangle n_\chi$, where σ_a is the annihilation cross section and $\langle\sigma_a v\rangle$ is the velocity averaged total annihilation cross section into lighter particles. Using the Boltzmann equation, the time evolution of the χ number density, n_χ, is expressed in Eq. 1.3 as:

$$\frac{dn_\chi}{dt} + 3Hn_\chi = -\langle\sigma_a v\rangle \left[(n_\chi)^2 - \left(n_\chi^{eq}\right)^2\right]. \tag{1.3}$$

For a rapidly accelerating universe which cools and leaves thermal equilibrium, a long-lived χ particle would freeze out with the relic density of approximately $H = \langle\sigma_a v\rangle n_\chi$.

Numerical solutions to Eq. 1.3 for increasing values of the velocity averaged total cross section are shown in Fig. 1.4. For increasing cross section, the χ particles would remain in thermal equilibrium longer, which would yield a lower relic density.

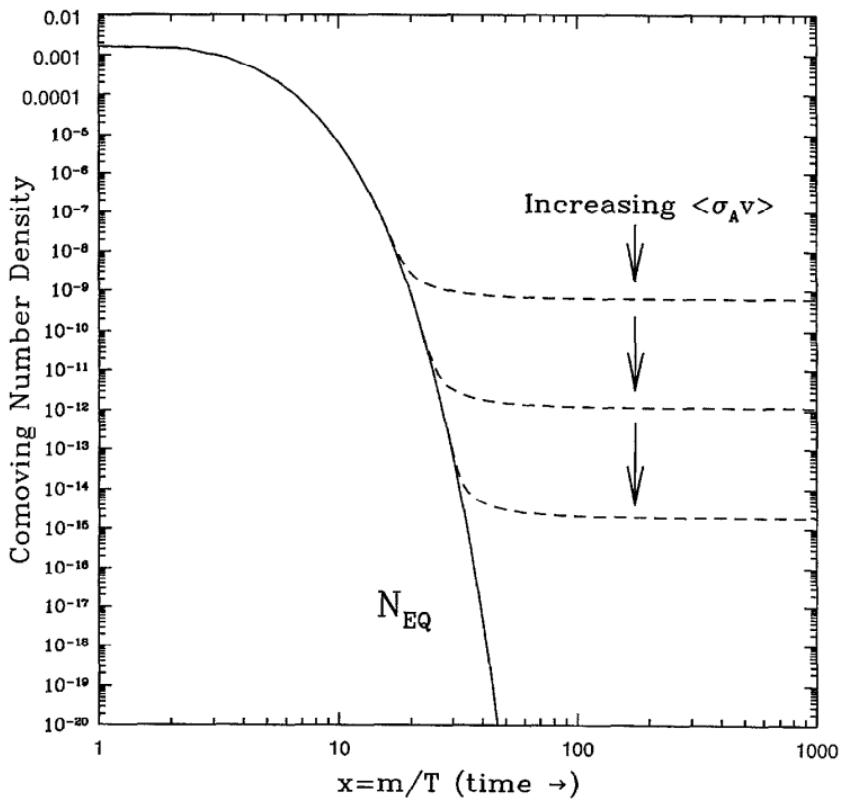

Figure 1.4: Numerical solutions to the number density presented in Eq. 1.3. The solid line indiciates the thermal equilibrium abundance while the dashed lines represent the freeze-out relic abundance for increasing values of the velocity averaged total annihilation cross section. As the annihilation cross section increases, the relic density decreases. Figure from [9], which is originally from [10].

An approximate numerical solution of Eq. 1.3 by [9] yields a present χ density in units of the critical density as Eq. 1.4:

$$\Omega_\chi h^2 = \frac{m_\chi^2}{\rho_c} \approx 3 \times 10^{-27} \mathrm{cm}^3/\mathrm{s}/\langle \sigma_a v \rangle. \tag{1.4}$$

Recalling the fitted values of $\Omega_\chi h^2$ from the WMAP experiment discussed in Sec. 1.1, if one considers a velocity averaged total cross section on the order of the weak scale, i.e. $\langle \sigma_a v \rangle \approx 10^{-25}$ cm^3/s, the relic abundance that results is within an order of magnitude of the WMAP observations. This coincidence between the weak scale interaction and the

relic density is often referred to as the "WIMP miracle" and provides a strong theoretical motivation to search for WIMPs.

Additionally, WIMP-like particles naturally occur in various theoretical frameworks. Such a particle fits nicely within supersymmetric models as it is hypothesized to be the lightest supersymmetric particle (LSP) [9]. The LSP is a particularly attractive WIMP candidate as it provides the correct R-parity, which is important in guaranteeing its long term stability on cosmological time-scales. As discussed in [11], searches for exotic isotopes imply that a LSP has to be neutral, which leaves two supersymmetric candidates: the sneutrino, and a neutralino. As recent WIMP searches have ruled out the sneutrino as the primary component of dark matter in our galaxy's halo, most current WIMP searches look for the neutralino.

It should be noted that many non-supersymmetric extensions of the Standard Model also contain viable WIMP candidates. These could include the lightest T-odd particle in the "Little Higgs" models or "techni-baryons".

Many experiments are aimed at observing WIMP particle interactions directly using particle physics detectors. The most direct method of observing WIMPs is to study scattering off of baryonic matter via the weak interaction. One such detector is the focus of this work and the methodology of "direct detection" is covered in Chapter 2. Other, though more indirect methods to detect dark matter would be to observe the signature from WIMP-WIMP annihilation from astronomical sources where WIMP densities are expected to be high (such as at the center of the Milk Way) [12], or as missing energy from WIMP production at collider experiments (such as at the LHC) [13].

1.3 Alternatives to the WIMP Model

While the WIMP model, discussed in Sec. 1.2, is a popular and well-motivated dark matter candidate, competing alternative models also exist. A summary of several alternative dark matter candidates are presented in this section.

1.3.1 Axions

The axion is a dark matter candidate, which was introduced by Peccei and Quinn to solve the strong CP problem [14]. The existence of axions would help resolve a naturalness problem related to the very small scale of CP-violation observed in QCD interactions. While, in principle, the CP-violation term in the Standard Model may exist anywhere between 0 and 2π, limits on neutron electric dipole measurements suggest that this term is very close to zero. It seems "unnatural" for this value to be so small without some other explanation.

As shown by Peccei and Quinn [14], a new symmetry may be introduced by promoting the CP-violating scalar to a field. The resulting spontaneous symmetry breaking of this new symmetry would lead to the creation of a new particle - a Nambu-Goldstone Boson called

the axion. As a consequence, this would naturally relax the scale of the CP-violating term to zero thus providing a solution to the naturalness problem.

Axions are expected to have a very small mass, to couple to standard model particles very weakly, and be stable on cosmological time scales. The weak coupling suggests that axions would not have been in thermal equilibrium in the early universe, so the resulting relic density will depend on the production mechanisms.

The two most popular axion models are the DFSZ [15] and KSVZ [16] models. The models predict that axions could be detectable via a decay to photons with a width given by Eq. 1.5:

$$\Gamma_{a\to\gamma\gamma} = \frac{g_{a\gamma\gamma}^2 m_a^3}{64\pi} = 1.1 \times 10^{24}\ \mathrm{s}^{-1} \left(\frac{m_a}{\mathrm{eV}}\right)^5 \tag{1.5}$$

Several experiments are searching for this signature using tuneable resonant cavities with high magnetic fields. A leading experiment is the **A**xion **D**ark **M**atter e**X**periment (ADMX), which attempts to detect RF photons by resonant conversion of axions to photons in a magnetic field [17, 18]. The resonance of the cavity is adjustable allowing for a sweeping search of the vast possible phase space. Fig. 1.5 shows the progress that ADMX has made in sweeping out the mass/coupling phase space in searching for axions. While several constraints have been made by other measurements, the ADMX has been able to start directly probing the axion phase space predicted by the DFSZ and KSVZ models (shown as yellow bands).

The HAYSTAC experiment is a new Haloscope experiment at Yale which has introduced several significant innovations pioneered by the ADMX experiment. [19] The first results were released in late 2017.

1.3.2 Sterile Neutrinos

While standard model neutrinos are generally not considered to be a viable candidate able to completely explain dark matter, a heavier (keV mass scale) sterile neutrino could be a potential dark matter candidate. In the Neutrino Minimal Standard Model (νMSM), it is hypothesized that a sterile neutrino would be a neutral lepton without coupling to standard model particles, except through mixing with the other known neutrino flavors. Sterile neutrinos would only be produced through oscillations with standard model neutrinos where the coupling can be set low enough that it can be made a viable dark matter candidate. Further, because the sterile neutrino must be sufficiently long-lived (on cosmological time scales) to be a viable dark matter candidate, strict bounds are placed on the Yukawa couplings and other plausible beyond-the-standard-model interactions, as well as the mass mixing angle parameter (black line in Fig. 1.6). The upper limit on the sterile neutrino mass in Fig. 1.6 is set by searches for a dark matter decay line from X-ray surveys while the lower mass limit is set by detailed analysis of the Milky Way's dwarf spheroidal galaxies [22]. Considering each of these constraints, the lightest sterile neutrino mass (as predicted by the νMSM) is between 1 and 50 keV.

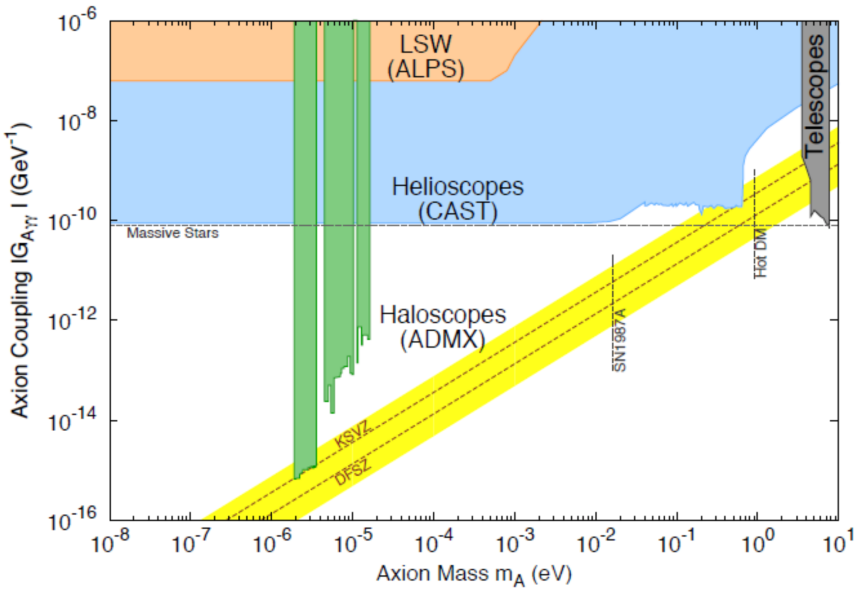

Figure 1.5: Axion coupling as a function of axion mass parameter space. The generic DFSZ [15] and KSVZ [16] models are shown as a yellow band. The remaining shaded regions are exclusion regions from various axion searches. Results from ADMX are also shown and labeled. Figure taken from [20], which is originally from [21].

1.3.3 MACHOs

An alternative theory for dark matter is that cosmological studies are under-counting the amount of cold baryonic matter which is not easily visible. This could be objects, commonly referred to as massive compact halo objects (MACHOs), that emit little or no light (such as cold gas, brown dwarfs, stellar black hole remnants, neutron stars, etc.) To study this hypothesis, the MACHO collaboration performed a search of the Large Magellanic Cloud (LMC) using gravitational microlensing techniques and set a limit of MACHO content of $20^{+30}_{-12}\%$ of the total dark matter composition. The OGLE collaboration conducted another study, this time focusing on limits of MACHO content in the galactic halo, with significantly more data and set a limit of $3 \pm 2\%$ [23]. Given this evidence, it is generally accepted that MACHOs may compose a small amount of the dark matter content, but their observed contribution is far too small to account for the expected abundance of dark matter in the universe.

1.3.4 Modified Gravity

Lastly, attempts have been made to modify existing gravity theories to expalin the observed indirect evidence of dark matter rather than relying on a particle-based explanation. As explained in [24], while Modified Newtonian Dynamics (MOND) reproduces many observations

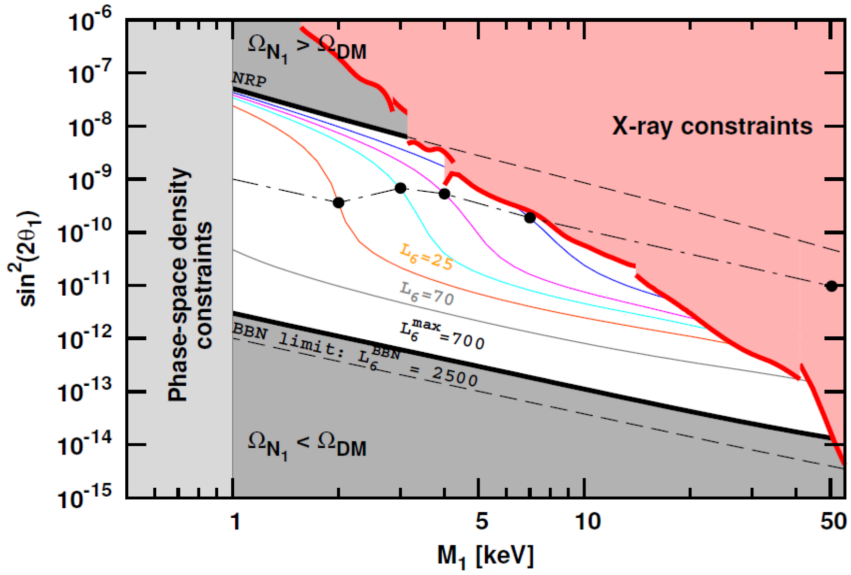

Figure 1.6: Bounds of the sterile neutrino mass and mixing angle as predicted by the νMSM model. Several other measurements have constrained the possible phase space to 1 to 50 keV mass. [22].

on galactic scales (in particular galactic rotation curves) without introducing particle dark matter, these theories are purely non-relativistic which run into trouble when attempting to embed them into relativistic field theory. In particular, attempting to embed MOND into relativistic field theory requires the introduction of additional fields which leads to "considerable arbitrariness" [25]. Additionally, the structure of the universe at the largest of scales still requires some form of particle dark matter, even with the use of modified gravity, to be consistent with observations [26].

Recent measurements from the LIGO experiment [27] have placed significant constraints existing relativistic MOND theories that provide predictions on the speed of gravitational waves differing from that of light. The approximately 1 second time difference between a gravitational wave signal and a short gamma ray burst from a distant binary neutron merger (BNS) event (GW170817) provides strong evidence that gravitational wave velocities are close to the speed of light, as predicted by General Relativity. This evidence places strong constraints on many existing relativistic MOND theories, providing further evidence that dark matter should exist in a particle form [28].

Given these constraints, the fact that the previously discussed dark matter models are consistent with well established framework of quantum field theories, and the extraordinary historical success of General Relativity under experimental tests [24], it is generally accepted that dark matter is likely of the particle form as opposed to being solely explained by modified gravity theories.

Chapter 2

Direct Detection of WIMPs

Chapter 1 introduced several dark matter candidates. The focus of this work narrows to consider the direct detection of WIMP candidates.

In principle, there are several ways WIMPs could be detected. As mentioned in Sec. 1.2, ongoing experiments are searching for WIMP-WIMP annihilation in regions where the WIMP density is expected to be large (center of the Milky Way) by looking for X-ray signatures [12]. Experimental searches at large colliders, such as the LHC, are looking for evidence of WIMP production in the form of missing energy. An overview of these collider searches can be found in [13].

The most direct method for detecting WIMPs, however, would be observations of WIMP scattering off of standard model particles using very low background detectors. The methodology and experimental approaches used in WIMP scattering searches are the topic of this chapter and, more broadly, this work.

Sec. 2.1 discusses the kinematics of WIMP scattering. Sec. 2.2 covers the nucleon scattering parameter space probed by various experiments. Sec 2.3 provides an overview of the various detector technologies used in WIMP searches. Lastly, Sec. 2.4 provides additional information on scintillation in liquid noble targets - a topic central to the work presented in later chapters.

2.1 Standard WIMP Scattering

As discussed in Sec. 1.2, a non-zero coupling to standard model particles is required in order for WIMPs to achieve the correct relic abundance. This implies that WIMPs could be directly observed via nucleon scattering interactions with a target composed of standard model particles. In supersymmetric models, this process is complex and mediated by several interactions. However, to ensure a WIMP theory is consistent with observations of large-scale cosmological structures, the WIMPs must also be non-relativisitic. This additional non-relativistic constraint allows for significant theoretical simplifications in the derivation of interaction cross-sections. Following [30], the non-relativistic limit of the WIMP interactions

with standard model particles (quarks and gluons) reduces to two interactions which can be considered separately: spin-dependent interactions, and spin-independent interactions. The spin-dependent interactions consider the coupling of the WIMP spin to the nuclear spin, while the spin-independent interactions consider the coupling of the WIMP mass to the mass of the nucleus.

The derivation of the spin-dependent and spin-independent cross-sections was performed by Jungman, Kamionkowski, and Griest in [9] and is summarized below. It is worth noting that the results of this derivation are general enough to cover a wide range of WIMP models, which allows for comparisons between targets and experimental techniques. However, the predicted cross-section on nucleons for supersymmetric WIMPs are highly model-dependent.

Following [9, 29], the standard cross-section at zero momentum transfer is defined in Eq. 2.1 as:

$$\sigma_{0,s} = \int_0^{4m_r^2 v^2} \frac{d\sigma\,(q=0)}{d|\mathbf{q}|^2} d|\mathbf{q}|^2, \tag{2.1}$$

where $\mathbf{q}$ is the momentum transfer, v is the speed of an incident WIMP, m_r is the reduced mass of the nucleus with mass m_n and a WIMP with mass m_χ ($m_r = m_n m_\chi/(m_r + m_\chi)$).

Spin-independent interaction: The spin-independent interaction, typically dominated by Higgs and squark exchange, can be written as [9]:

$$\sigma_{0,s}^{SI} = \frac{4m_r^2}{\pi}\left[f_p Z + f_n\,(A-Z)\right]^2, \tag{2.2}$$

where A is the atomic number, Z is the number of protons in the nucleus, and f_p and f_n are the (model-dependent) effective couplings to the proton and neutron respectively. In most models, f_p and f_n are comparable, which leads to a simplification where the cross-section depends on a single parameter with an "enhancement" that scales with the square of the target atomic number (A^2). This is explicitly shown in Eq. 2.3 as:

$$\sigma_{0,s}^{SI} \approx \frac{4m_r^2 f_p^2 A^2}{\pi}. \tag{2.3}$$

Since this relationship depends on the properties of the WIMP as well as the target material, it is helpful to derive a target-independent cross-section to allow for direct comparisons between various experiments. Such a relationship is defined in Eq. 2.4 as:

$$\sigma_0^{SI} = \frac{\sigma_{0,s}^{SI}}{A^2}\frac{m_p^2}{m_r^2}, \tag{2.4}$$

where m_p is the reduced mass of the proton and WIMP.

Spin-dependent interaction: Now considering the spin-dependent scattering, the differential cross-section for spin-dependent interactions from [9] is shown in Eq. 2.5 as:

$$\frac{d\sigma^{SD}}{d|\mathbf{q}|^2} = \frac{8G_F^2}{\pi v^2}\frac{J+1}{J}\left[a_p\langle S_p\rangle + a_n\langle S_n\rangle\right]\frac{S\left(\mathbf{q}\right)}{S\left(0\right)}, \tag{2.5}$$

where G_F is the Fermi constant, v is the speed of an incident WIMP, J is the spin of the nucleus, $\langle S_p\rangle$ and $\langle S_n\rangle$ are the expectation values of the spin content of the protons and neutron groups respectively, a_p and a_n are the model-dependent matrix coefficients for the proton and neutron couplings to the WIMP respectively, and $S\left(\mathbf{q}\right)$ is the nuclear form factor for the spin-dependent interactions. The values for $\langle S_p\rangle$ and $\langle S_n\rangle$ are computed from detailed nuclear physics calculations for a specific nucleus type. Using the differential cross-section for spin-dependent interactions (Eq. 2.5) in the integral of Eq. 2.1, the total cross-section for zero momentum transfer spin-dependent interactions is evaluated to be [9]:

$$\sigma_0^{SD} = \frac{32G_F^2 m_r^2}{\pi}\frac{J+1}{J}\left[a_p\langle S_p\rangle + a_n\langle S_n\rangle\right]^2 \tag{2.6}$$

Ratio of interaction strengths: For a general target, the total cross-section is the sum of the spin-independent and spin-dependent components. It is useful to evaluate the relative magnitudes of spin-dependent to the spin-independent cross-section. This ratio is defined in Eq. 2.7 as:

$$\frac{\sigma_0^{SD}}{\sigma_0^{SI}} = \frac{4\left(\langle S_p\rangle + \langle S_n\rangle\right)^2 J\left(J+1\right)}{A^2}\left[\frac{a_p\langle S_p\rangle + a_n\langle S_n\rangle}{\langle S_p\rangle + \langle S_n\rangle}\right]^2\frac{2G_f^2}{f_p^2}, \tag{2.7}$$

and uses the simplifying assumption of $f_p = f_n$. Eq. 2.7 is split into terms such that the first one is intended to emphasize the nuclear dependence. The exact value of the ratio is model-dependent but if one considers the case of a B-ino in the large quark mass limit (example taken from [9]), the ratio becomes:

$$\frac{\sigma_0^{SD}}{\sigma_0^{SI}} = 250\frac{4\left(\langle S_p\rangle + \langle S_n\rangle\right)^2 J\left(J+1\right)}{A^2}. \tag{2.8}$$

This suggests that the spin-independent interaction would dominate for approximately $A > 20$. As shown in [31] and [32] (referenced in [9]), when considering a wider view of the possible parameter space of supersymmetric models, the atomic number limit of $A > 30$ can be used as a general "rule-of-thumb" when estimating the threshold where the spin-independent interaction becomes dominant.

In practice, there are many nuclei which do not have a net nuclear spin (i.e. $J = 0$) which makes them only sensitive to spin-independent interactions. This is the case for ^{40}Ar, which is the target of primary relevance to this work.

Spin-independent interaction differential scattering rate: Narrowing the discussion to only considering the spin-independent interaction, using the derived definitions of the WIMP total cross-section (Eq. 2.3 and Eq. 2.4) and following the process laid out in [9] and [33], the WIMP differential scattering rate can be written as:

$$\frac{dR}{dE} = \frac{\rho_0}{m_\chi} \frac{\sigma_0^{SI} A^2}{2m_p^2} F^2(E) S(E), \tag{2.9}$$

where R is the WIMP scattering rate, E is the recoiling energy of the nucleus, ρ_0 is the local dark matter density, m_χ is the WIMP mass, $F(E)$ is the nuclear form factor, and $S(E)$ is a kinematic term accounting for the expected velocity distribution of local WIMPs and Earth's motion in the Milky Way.

The differential scattering rate (Eq. 2.9) is split into four terms, where each has a physical explanation. The first term depends on the local dark matter density (ρ_0). Using the well-motivated spherical halo model, the local dark matter density is estimated to be in the range of 0.2-0.4 GeVc^{-2}cm^{-3}. The second term reflects the cross-sectional and atomic number dependence for spin-independent scattering (previously discussed).

The third term represents the effect of the nuclear form-factor, which depends on the target atom. Fig. 2.1 shows the calculated form factor for various targets. The form-factor captures the loss of coherence as the de Broglie wavelength of the WIMP approaches the scale of the target nucleus. Additional material on the form factors can be found in [33, 34].

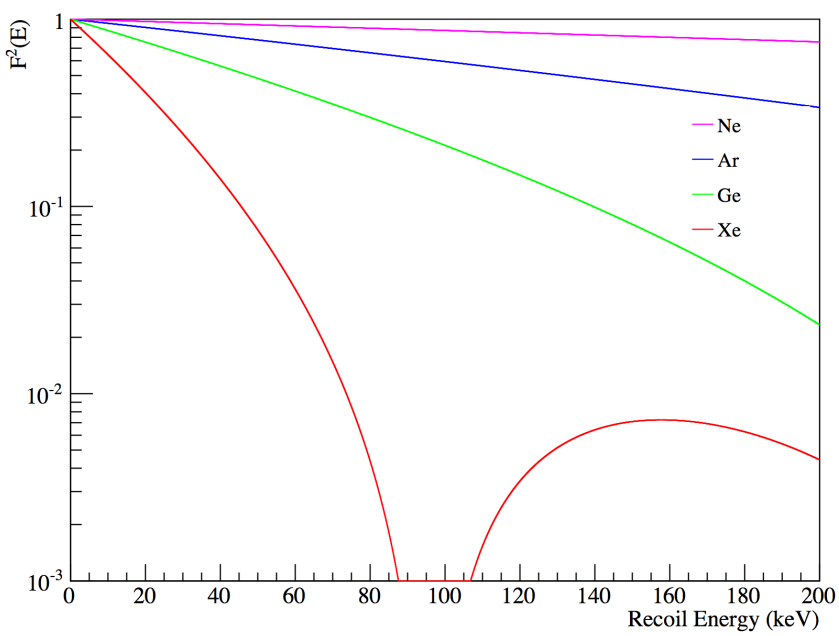

Figure 2.1: Nuclear form factor for Ne, Ar, Ge, and Xe using the Helm factor [34]. Figure taken from [29].

Lastly, the fourth term captures the kinematics of WIMPs scattering off of terrestrial targets. This includes the consideration of the velocity distribution of local WIMPs and the motion of the Earth relative to the center of the Milky Way and the Sun. The WIMP velocity distribution is typically assumed to follow a Maxwell-Boltzmann distribution [35, 36].

Combining each of the factors in Eq. 2.9 provides an estimate of the differential scattering rate for WIMPs in terrestrial detectors for various targets. Fig. 2.2 shows the scattering rate of WIMPs of select masses (30 GeV and 300 GeV) on various targets. Clearly, the target choice is important and depends on the WIMP mass/energy range of interest for a specific search.

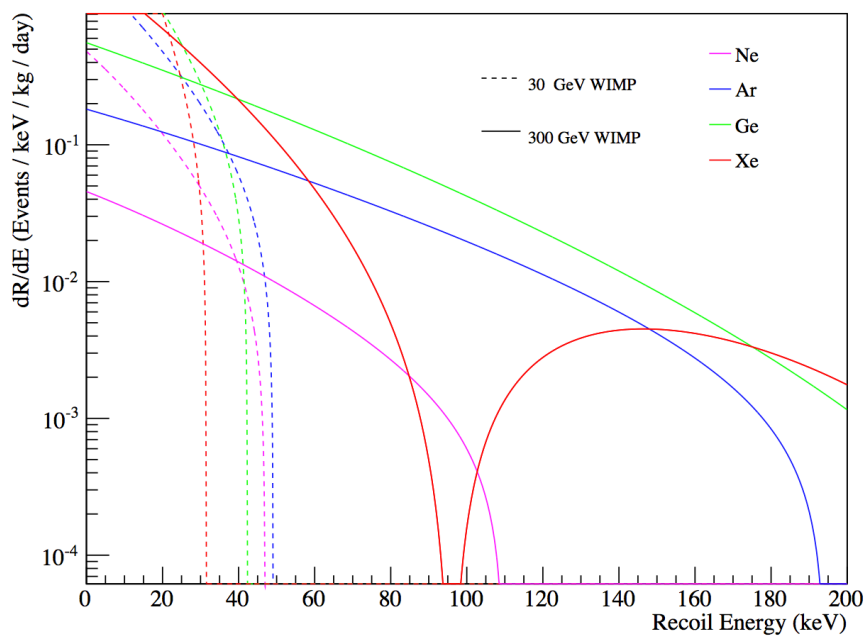

Figure 2.2: The differential rate for 30 and 300 GeV WIMPs on Ne, Ar, Ge, and Xe. For a given target and WIMP mass, the rate decays approximately exponentially with energy until the cutoff defined by the maximum energy which can be transferred to the nucleus given the galactic escape velocity. Figure and caption taken from [29].

2.2 Nucleon Scattering Parameter Space

Recalling the differential scattering rate per kg (Eq. 2.9), the total scattering rate in a detector with fiducial mass M_t can be evaluated by integrating over the energy range of interest. This is shown in Eq. 2.10 as [29]:

$$S = M_t \int_{E_1}^{E_2} \epsilon\left(E\right) \frac{dR}{dE} dE, \tag{2.10}$$

where $\epsilon(E)$ is the recoil energy-dependent, detector-specific efficiency for observing a nuclear recoil signal, and E_1 and E_2 are the lower and upper energy bounds of the nuclear recoil energy region of interest (ROI).

Following [29], the probability mass function for the observed number of events, N, including an expected total background rate, B, and signal, S, in the energy ROI for a WIMP search with time exposure, T, is a Poisson distribution defined in Eq. 2.11 as:

$$P(N) = \frac{(T(S+B))^N}{N!} e^{-T(S+B)} \tag{2.11}$$

Because WIMP searches look for rare events, a null signal is anticipated. Therefore, most reported results to date are limits on the WIMP cross-section for a given WIMP mass. Several approaches can be used for limit setting. The most commonly applied are frequentist, Feldman-Cousins [37], maximum gap [38], and Bayesian techniques. A summary of Bayesian and frequentist limit setting approaches in the context of rare event searches can be found in [39, 40].

As an example of a process to evaluate a dark matter cross-section limit, a Bayesian approach is considered and closely follows the process outlined in [29]. For a given dark matter mass, m_χ, a Bayesian upper limit on the WIMP-nucleon cross-section, σ_l, is defined by Eq. 2.12 as:

$$1 - CL = P(\sigma \geq \sigma_l | N = N_{obs}) = \frac{\int_{\sigma_l}^{\infty} \mathcal{L}(N|S,B) P(\sigma_0) d\sigma_0}{\int_0^{\infty} \mathcal{L}(N|S,B) P(\sigma_0) d\sigma_0} \tag{2.12}$$

where N_{obs}, the number of observed events, is held fixed, CL is the the confidence level (usually 90%), S and B are the expected signal and background rates respectively, $\mathcal{L}(N|S,B)$ is the Likelihood function for the number of events observed, and $P(\sigma_0)$ is the prior probability density for the cross-section. With a flat prior, Eq. 2.12 becomes Eq. 2.13:

$$P(\sigma \geq \sigma_l | N = N_{obs}) = \frac{\int_{\sigma_l}^{\sigma_{max}} \mathcal{L}(N|S,B) d\sigma_0}{\int_{\sigma_{min}}^{\sigma_{max}} \mathcal{L}(N|S,B) d\sigma_0} \tag{2.13}$$

where the prior is defined by Eq. 2.14 as:

$$P(\sigma_0) = \begin{cases} \frac{1}{\sigma_{max} - \sigma_{min}}, & \sigma_{min} \leq \sigma_0 < \sigma_{max} \\ 0, & \text{otherwise.} \end{cases} \tag{2.14}$$

σ_{min} and σ_{max} are cross-sections well beyond the cross-sections of interest. Now considering the number of events in time exposure T, the Likelihood function can be expressed as:

$$\mathcal{L}\left(N|S,B\right) = \int dE \int dB \int dL_{eff} \int dv_{esc} \int dv_e \int dv_0 \int d\rho_0$$
$$\times\, p(E)p(B)p(L_{eff})p(v_{esc})p(dv_{esc})p(dv_e)p(dv_0)p(\rho_0)\frac{T^{N_{obs}}\left(S+B\right)^{N_{obs}}}{N_{obs}!}e^{-T(S+B)} \quad (2.15)$$

where $p(x)$ represents a Gaussian PDF truncated at zero with a central value equal to x and an uncertainty σ_x. The $p(E)$ term handles the finite energy resolution of the detector under consideration, $p(B)$ is related to the background rates in the detector, and L_{eff} quantifies the uncertainty in the scintillation physics (more details provided in Sec. 2.4). The remaining factors ($p(v_{esc})$, $p(dv_{esc})$, $p(dv_e)$, $p(dv_0)$, $p(\rho_0)$) are nuisance parameters, which account for the uncertainty in the astrophysical parameters used in evaluating the previously discussed scattering rates (Sec. 2.1 and Eq. 2.9). In practice, the nuisance parameters are usually held constant for the purpose of limit setting so that the comparison of different experiments can be performed on equal footing.

By using Eq. 2.15 in Eq. 2.13, a limit, σ_l can be placed on the zero momentum transfer WIMP-nucleon cross-section for a given WIMP mass from a given experiment.

Using limit setting methodologies, such as the previously discussed Bayesian approach, several experiments have set WIMP-nucleon cross-section limits as a function of WIMP mass. Fig. 2.3 shows several spin-independent limits set by various experiments.

Several of these experiments will be summarized in Sec. 2.3. Various detector technologies have been used to push limits to remarkably small cross-sections. As of late 2017, the current best limits for the spin-independent cross-section are from XENON1T with a minimum cross-section limit of 7.7×10^{-47} cm^{-2} at a WIMP mass of 35 GeV c^{-2} at a 90% confidence interval [41]. The orange shaded region at small cross-section values labeled "neutrino coherent scattering" represents a region in phase space where the standard direct detection techniques will run into an irreducible background dominated by solar neutrinos in the low mass region (< 10 GeV c^{-2}) and atmospheric/diffuse supernova neutrinos at larger WIMP masses (> 100 GeV c^{-2}). The yellow shaded region represents limits set by ATLAS in the high mass regime following mSUSY studies at the LHC.

Fig. 2.4 shows spin-dependent cross-section limits set by various experiments. The top plot is for spin-dependent coupling to the neutron while the bottom plot is for couplings to the proton. Competitive direct detection, spin-dependent limits have been set by PICO and LUX.

2.3 Methods of Direct Detection

Various classes of detectors are used for WIMP detection. In general, the detectors can be categorized (non-exclusively) into four categories related to signal class: Scintillation, Ionization, Phonon, and superheated liquid bubble chambers. These detector categories are

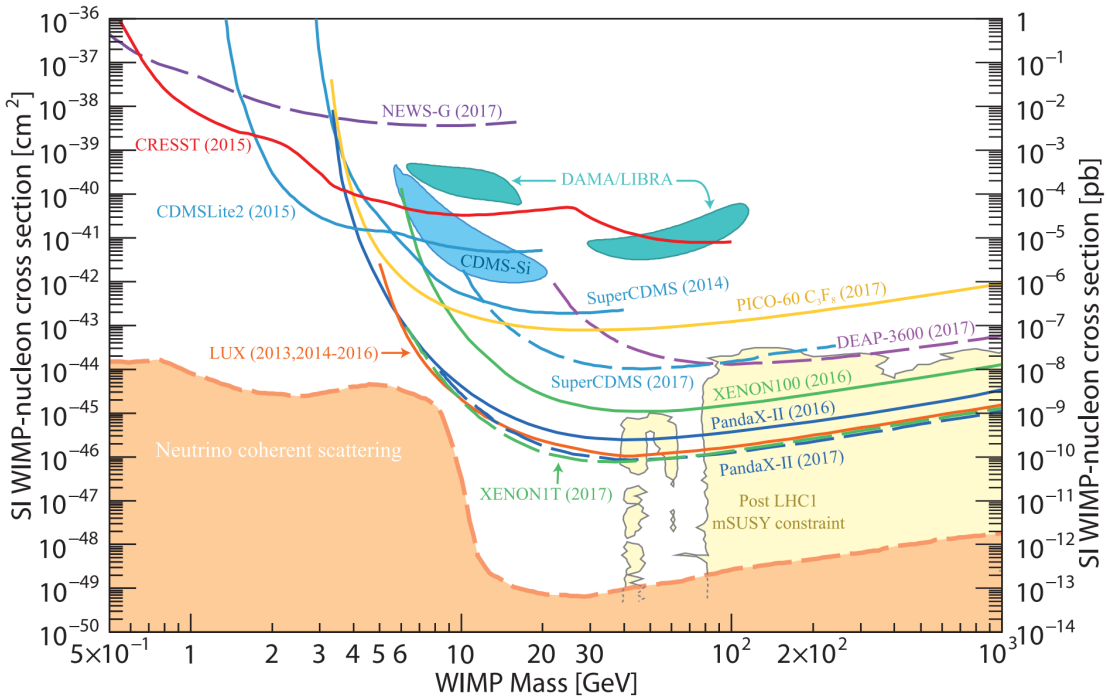

Figure 2.3: WIMP cross-sections (normalized to a single nucleon) for spin-independent coupling versus mass. The DAMA/LIBRA, and CDMS-Si enclosed areas are regions of interest from possible signal events (discussed more in Sec. 2.3). The yellow region shows a scan of the parameter space of 4 typical SUSY models (CMSSM, NUHM1, NUHM2, pMSSM10), which integrates constraints set by ATLAS Run 1. Figure from [24].

shown in Fig. 2.5 along with examples of experiments that fall into each category. Note that several experiments, such as LUX, can detect more than one signal type.

2.3.1 Solid State Detectors

Ionization Collection: This class of detectors typically use Ge and Si to detect the ionization charge induced by WIMP recoils. The advantage of these detectors is the ability to create high purity detectors with low thresholds and good energy resolution. The disadvantages are difficulty of scaling to large detectors and the inability to differentiate between electronic and nuclear recoils for background discrimination.

An example of this type of experiment is CoGeNT [62]. CoGeNT is a sub-keV threshold, 443 g P-type point contact Ge detector used to search for WIMPs at the Soudan Underground Laboratory. It searches for a modulated signal in the energy range of 0.5 to 2.0 keV. A modulated signal from an unknown source was reported and found to be consistent with expectations using the standard galactic WIMP halo assumptions [63]. This phase space has since been ruled out by other experiments and is not considered to be a detection of WIMPs.

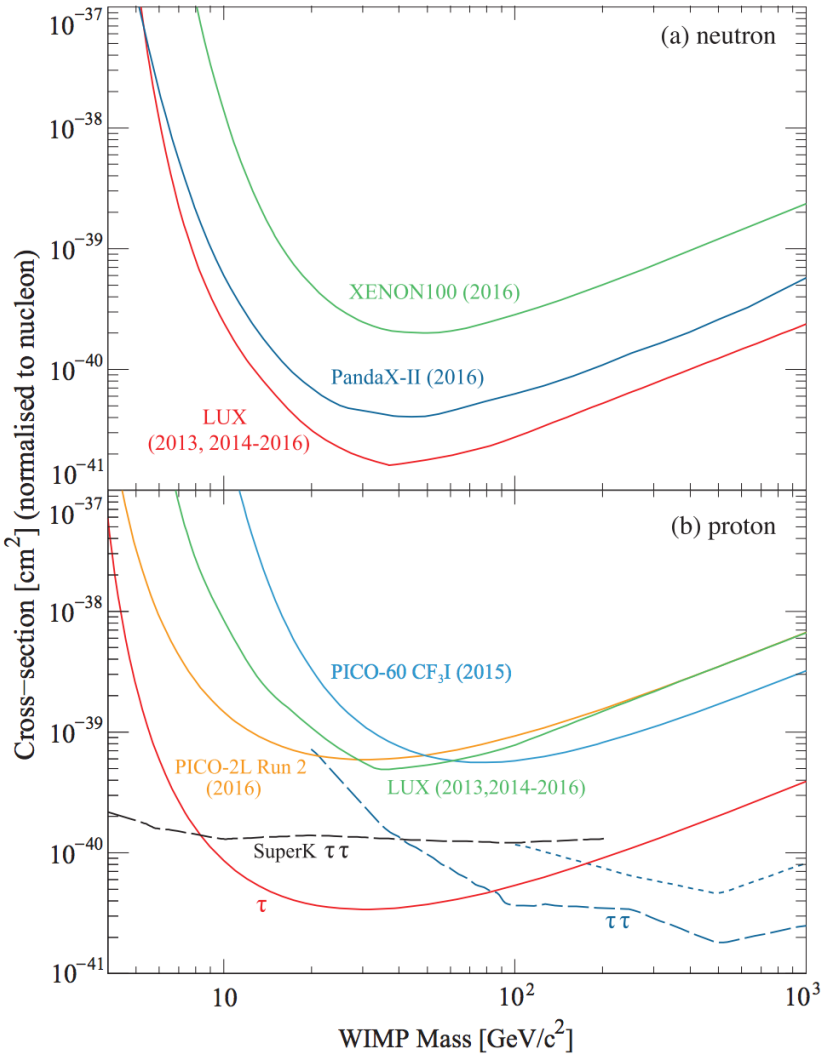

Figure 2.4: WIMP cross-sections for spin-dependent coupling versus mass. The top plot is for couplings to protons while the bottom is for neutrons. Other indirect results from SuperKamiokande and IceCube are also presented. Figure from [24].

It should be noted that next-generation neutrinoless double beta decay experiments, such as MAJORANA DEMONSTRATOR [64] and GERDA [65], use similar detectors with larger masses (made of Ge), reduced backgrounds, and small energy thresholds. It is expected that these experiments will be sensitive to low mass WIMPs with spin-independent cross-sections on the order of 10^{-44} cm^2 [66, 67].

Phonon Collection: Solid state detectors are also used to look for phonons created by recoils in the target. Typically these detectors operate as cryogenic bolometers at mK

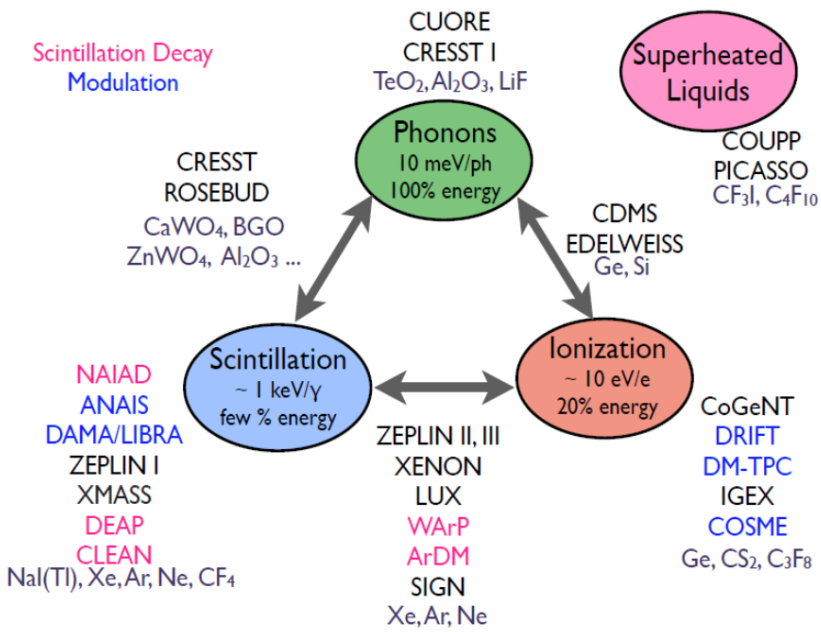

Figure 2.5: A summary of existing experimental direct detection techniques from [42]. Experiments at the corners of the triangle search for signatures in either the phonon, scintillation, or ionization signal channels. Experiments along the edges have sensitivity to a combination of two channels.

temperatures. The advantages of this approach are that the entire recoil energy can be determined by the thermal and athermal phonon populations, and the ability to leverage low-temperature phenomena, such as superconducting states, for novel readout techniques [42]. For example, the use of transition edge sensors allows for very low threshold searches with excellent energy resolution.

An example of an experiment which only detects a phonon signal is CUORE [69]. CUORE is a neutrinoless double beta decay experiment that consists of several towers of TeO_2 crystals (955 crystals in total) operated as a cryogenic bolometer at <10 mK in the Gran Sasso Laboratory. Each crystal is instrumented with a thermistor which measures the increase in the temperature when a particle interacts with the crystal. While the primary focus of the experiment is searching for neutrinoless double beta decay, it could be leveraged for dark matter searches (i.e. a 2013 solar axion search [70]).

Ionization + Phonon Collection: As seen in Fig. 2.5, there are some experiments which look for both ionization and phonon signatures from recoils. This is possible because charge carriers may be collected in detectors made of Ge and Si with electric fields on the order of V/cm without overwhelming the signal in the phonon channel.

A leading experiment using this approach is SuperCDMS [71]. SuperCDMS is being constructed at SNOLAB in Canada and will primarily search for dark matter with mass $<$ 10 GeV. It consists of several towers of cylindrical Ge and Si detectors (1.39 kg/detector) instrumented in two configurations: a phonon only detector and a phonon+ionization channel detector. The phonon only detector is expected to have better energy resolution and to be sensitive to lower energy recoils when compared to the phonon+ionization style detector [71]. The advantage of the phonon+ionization style detector is to allow for electronic and nuclear recoil discrimination. Using these techniques, SuperCDMS is expected to place strong limits in the light-WIMP mass region.

2.3.2 Superheated Liquid Detectors

Another class of detectors takes the form of bubble chambers. Labeled as "Superheated Liquids" in Fig. 2.5, the mature bubble chamber technology has recently undergone a revival and is being used for direct detection experiments. These experiments work under the principle that a particle depositing energy within a certain distance in a superheated liquid above a threshold will induce a phase change, which creates bubbles. Experiments typically detect the bubbles optically and/or acoustically. Because these bubble chambers operate strictly as threshold detectors, where the threshold is set by thermodynamic properties (pressure and temperature), the deposited energy can not be directly extracted. However, due to smaller dE/dx of electronic recoils compared to nuclear recoils, the threshold can be tuned such that most γ and β backgrounds do not cross the threshold which makes the detector effectively "blind" to many backgrounds. α and neutron backgrounds remain a challenge due to their high dE/dx, so tight background controls and estimations remain a priority. Progress has been made in discriminating αs from nuclear recoils using acoustic signatures, which shows promise [29, 72, 73]. Several examples of various event types are shown in Fig. 2.6.

The relatively small scale of these experiments suggests that they have limited sensitivity to spin-independent interactions. However, by choosing targets which are compatible with the superheated liquid approach and have relatively large expected proton spin-dependent couplings to WIMPs, such as fluorine based compounds, they have produced competitive proton spin-dependent interaction limits (Fig. 2.4).

Examples of bubble chamber experiments are PICASSO [74], COUPP [75], and PICO [76]. The PICO experiment, currently operating at SNOLAB, is a result of the joint effort of the PICASSO and COUPP collaborations. It contains 52$\pm$0.5 kg of C_3F_8 and is instrumented with visual and acoustic sensors. In 2017, PICO reported the best spin-dependent cross-section limit at 3.4×10^{-41} cm^2 for a WIMP mass of 30 GeV c^{-2} with 1167 kg-day exposure using a 3.3 keV threshold [76].

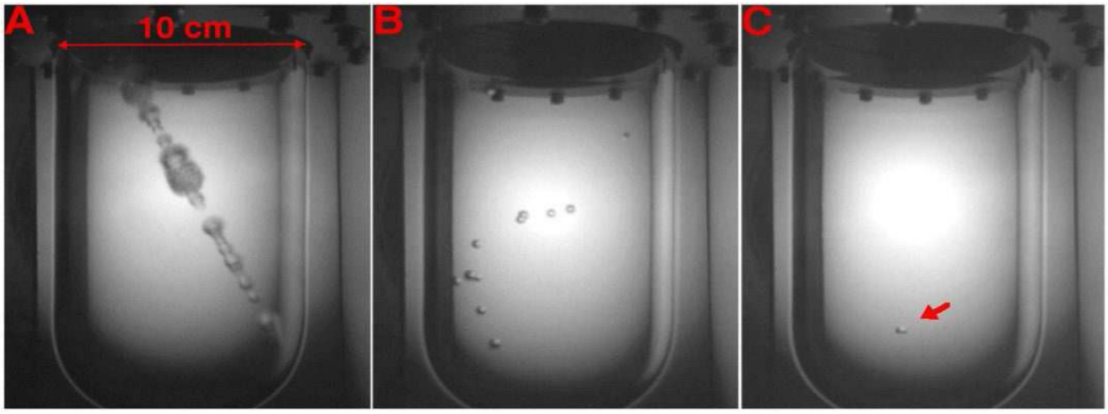

Figure 2.6: Various events from the COUPP 1.5 kg CF3I chamber. Left: A through-going cosmic ray muon. Center: A candidate neutron event producing several bubbles separated by a few cm. Right: A WIMP-like nuclear recoil producing a single bubble in the chamber. Figure and caption from [29].

2.3.3 Scintillator Detectors

Detectors that collect scintillation light are used extensively in dark matter experiments due to their ability to detect single photon levels of light using mature light collection technologies, such as photomultiplier tubes (PMTs). The scintillation light produced is proportional to the energy deposited in the target. Low energy thresholds for scintillation enables searches for low-energy physics interactions on the order of keV (depending on the scintillator).

Generally, scintillator experiments belong to one of the two classes: solid or liquid. These are discussed in Sec. 2.3.3.1 and Sec. 2.3.3.2 respectively.

2.3.3.1 Solid Phase Scintillators

Solid scintillator experiments typically use crystals, such as NaI and CsI, as targets instrumented by PMTs. For nuclear recoils, the amount of scintillation light produced is suppressed (when compared to electronic recoils) by an energy-dependent quenching factor of 0.3 for Na and 0.09 for Iodine recoils [42]. Scintillation light produced by nuclear recoils is generally produced more promptly after the interaction than light from electronic recoils, leading to observable differences in pulse shape. This discrimination technique, referred to as pulse shape discrimination (PSD), allows for a degree of particle identification. PSD is also used in liquid scintillators and is discussed in detail in Sec. 2.4.2.

Examples of experiments that use solid scintillators are DAMA/LIBRA [43], ANAIS [45], NAIAD18 [46], and ELEGANT V [47]. DAMA/LIBRA consists of a 5x5 grid of high radiopurity NaI crystals (9.7 kg/detector) encapsulated inside a high-purity copper housing with quartz light guides to couple to external PMTs. The PSD utilized in DAMA/LIBRA was too

weak to be used on an event-by-event basis, so it was instead used to look for an expected modulated WIMP signal correlated with the Earth's motion around the sun.

DAMA/LIBRA published results indicating an observed signal consistent with the expected WIMP modulation (teal regions in Fig. 2.3). However, limits set by other detectors with much higher sensitivity are in tension with this result. Many believe the observed modulated signal is due to other backgrounds whose intensity may vary on a similar annual scale. One example could be a varying background of neutron production in surrounding materials from a modulated flux of ^{8}B solar and atmospheric neutrinos [44].

2.3.3.2 Liquid Noble Gas Detectors

Direct detection dark matter experiments that extract a signal via scintillation in liquid generally use liquid noble targets instrumented by PMTs. In addition to the widespread use of liquid noble targets in dark matter experiments, they have many characteristics which make them favorable for low-energy physics searches and are becoming important to numerous experimental efforts including neutrino and other particle detectors, searches for the neutron's electric dipole moment and measurements of the neutron lifetime [48, 49, 51, 77, 78, 79, 60, 80, 81, 82, 83, 56, 59, 52, 84].

The properties of these elements, particularly in the liquid phase, are very attractive. They have exceptionally high scintillation yield (20,000–40,000 photons/MeV), which results in good energy resolution and low threshold. Table 2.1 provides a summary of other relevant properties of several liquid noble target species. Their high density makes them more self-shielding than water or organic liquid scintillators. Due to commercial availability of the target and ease of transportation/purification [42], liquid noble targets can be scaled to very large sizes relatively easily. Tracking detectors can be constructed by applying an electric field across the bulk and collecting the ionization signal. The specifics of the scintillation process in noble gases, covered in Sec. 2.4.1, means they are almost transparent to their own scintillation light. Additionally, the time structure of that light is dependent on the incident particle type, allowing for pulse shape analysis to distinguish nuclear from electron recoils (PSD, discussed in more in Sec. 2.4.2).

Detection of the vacuum ultraviolet (VUV) scintillation light produced by noble gas targets is a critical challenge common to this class of detectors. As shown in Fig. 2.7, the scintillation wavelengths can range from 175 nm for Xenon down to near 80 nm for Helium and Neon. Light of these wavelengths is strongly absorbed by most materials, including those commonly used for optical windows. Many experiments sidestep the issue of directly detecting VUV light though the use of wavelength shifting (WLS) films which absorb the VUV light and reemit photons, typically in the visible spectrum. The visible photons can then easily be detected using PMTs.

Liquid noble gas detectors generally come in two classes: single-phase and dual-phase detectors. Each of these are discussed below.

Element	Helium	Neon	Argon	Xenon
Atomic Number	2	10	18	54
Atomic Mass	4.0	20.2	40.0	151.3
Boiling Point (K)	4.2	27.1	87.3	165.0
Liquid Density at 1 atm (g/cm^3)	0.125	1.21	1.40	2.94
Scintillation Yield (photons/keV)	19	30	40	42
Peak Scintillation λ (nm)	80	78	128	175
Triplet Time Constant (μs)	13×10^6	15	1.6	0.03

Table 2.1: A tabulation of approximate relevant scintillation properties for several liquid noble species. Values from [29].

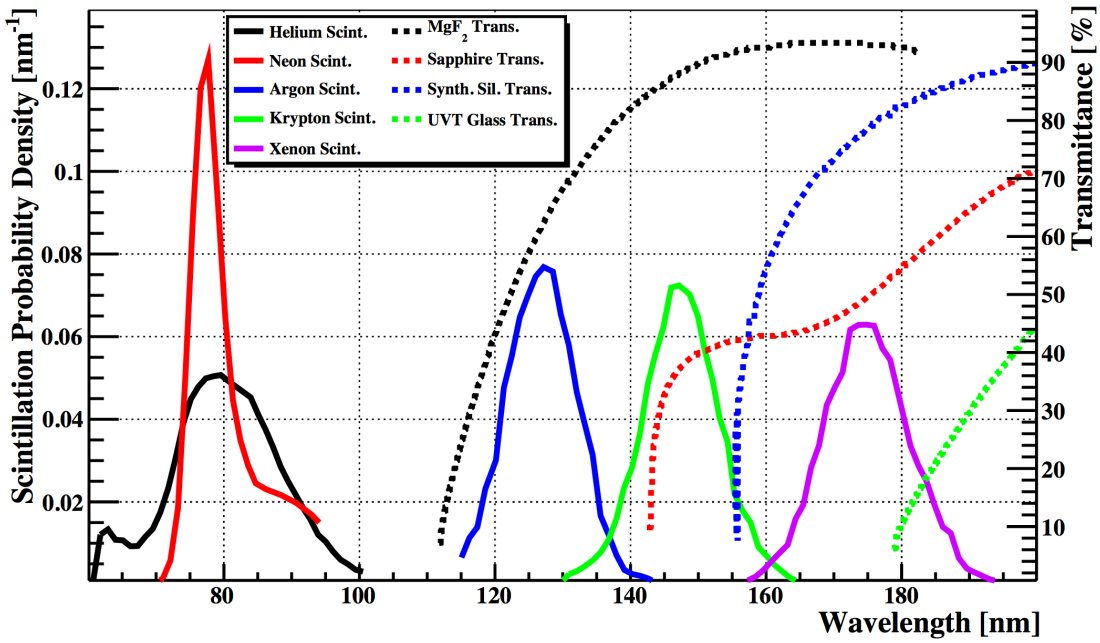

Figure 2.7: Scintillation wavelengths for various noble gases, along with the transmission of some commonly used optical windows. [93]

Single-phase: As suggested by the name, single-phase detectors only contain a one phase which is usually liquid in a zero-field configuration. Examples of single-phase liquid noble gas experiments are MiniCLEAN [50], DEAP-3600 [51], and XMASS [52]. MiniCLEAN is the subject of this work and will be discussed in detail in Chapters 3 and 4. DEAP-3600, shown on the left-side of Fig. 2.8, is a liquid argon experiment located at SNOLAB. The experiment contains 3600 kgs of liquid argon in a spherical acrylic vessel with 255 inward-looking PMTs coupled using 45 cm acrylic light guides. A wavelength shifting thin film of tetraphenyl butadiene was deposited in situ on the inner surface of the acrylic sphere to convert the

scintillation light to the visible spectrum for detection (more on this in Sec. 2.4.3). As of 2018, the DEAP-3600 experiment is taking data to improve upon their dark matter limit set in 2017 [53].

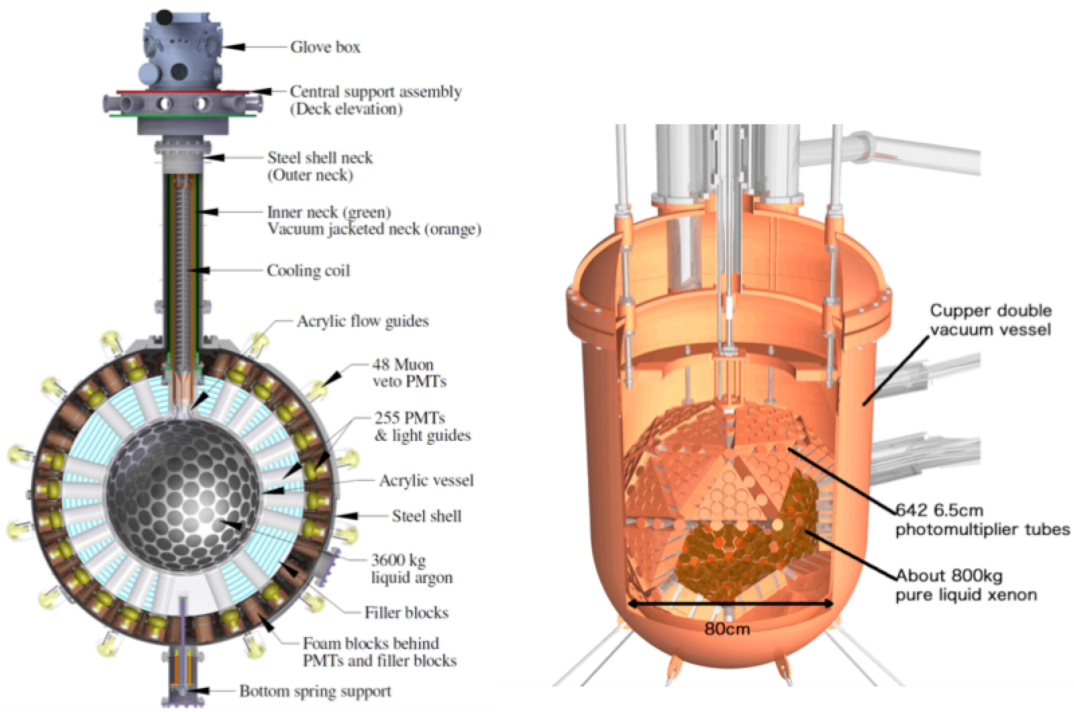

Figure 2.8: Left: An annotated model of the DEAP-3600 experiment at SNOLAB. Image from [51]. Right: An annotated image of the XMASS experiment. Image from [54].

Similarly, the XMASS experiment, shown in the right-side image of Fig. 2.8, is a spherical detector with approximately 850 kg of liquid Xenon (LXe) surrounded by 642 6.5 cm PMTs. XMASS relies on eliminating backgrounds using the outer layer of approximately 750 kg of LXe and an active veto to suppress external backgrounds.

Dual-phase: Dual-phase liquid noble gas detectors are a powerful class of detector technology that has been central to recent dark matter searches. These detectors typically operate as a time projection chamber (TPC), with both a liquid and gas phase. As shown in the right-side image of Fig. 2.9, when a particle interacts in the bulk liquid target, a prompt scintillation light signal is generated (S1). Ionization electrons, created during the primary interaction, drift in the electric field toward the gas region and create an electro-luminescence pulse (S2) when they pass across the liquid-gas phase boundary. PMTs at the top of the detector collect the S2 signal, where the X-Y position of the interaction can be determined from the hit distribution on the PMTs. The Z position is determined by evaluating the

time difference between the S1 and S2 signals with knowledge of the mean drift velocity of electrons in the field. This technique allows for very good 3D position reconstruction of events and tracks [56]. Additionally, the time structure of the S1 signal and the ratio of the primary to secondary signals offers discrimination between nuclear and electronic recoils with the efficiency determined by the noble element, strength of the electric field applied, and purity of the target.

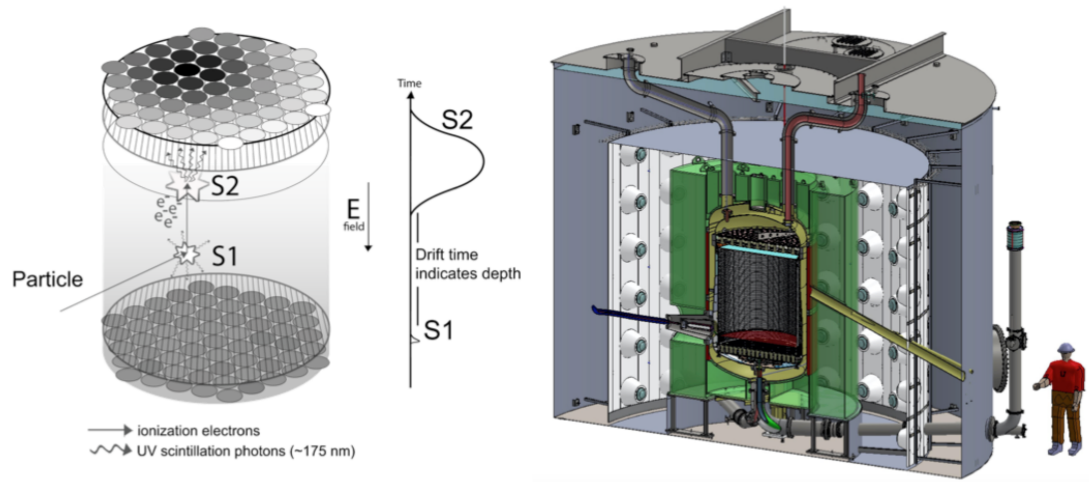

Figure 2.9: Left: Schematic of a dark matter interaction in a two-phase xenon detector. The primary interaction produces scintillation light (S1). The ionization electrons, created during the primary interaction, create an electroluminescence pulse (S2) after entering the gas region above the liquid. Image and caption from [56]. Right: Cutaway drawing of the LZ detector system. The LXe-TPC is surrounded by the outer detector (OD) tanks (green) and light collection system (white), all housed in a large water tank (blue-grey). Conduits penetrate the various regions and boundaries to deliver services to the LXe-TPC: PMT and instrumentation cables (top and bottom, red); cathode high voltage (lower left with cone); purified LXe (bottom center, green); neutron beam conduit (right, yellow and pitched). Image and caption from [59].

Xenon is a commonly used target for dark matter searches with TPCs due to its high atomic mass, particle identification abilities, and lack of naturally occurring long-lived isotopes. Examples of LXe TPC detectors are XENON1T [41], PandaX-II [55], LUX [56, 57], ZEPLIN-III [58], and LZ [59]. As mentioned in Sec. 2.2, as of late 2017 XENON1T currently holds the best limit on the WIMP spin-independent cross-section at 7.7×10^{-47} cm^{-2} for a mass of 35 GeV c^{-2}. The LUX and ZEPLIN collaborations have combined their efforts to construct a 7 tonne dual-phase detector, LZ, which is expected to probe cross-sections at the scale of 10^{-48} cm^{-2}. A diagram of the LZ detector is shown on the right-side of Fig. 2.9.

Liquid argon has also been used in dual-phase experiments, as in the case of the DarkSide [60] and ArDM [61] experiments. The DarkSide collaboration has utilized underground

sources of argon which contains 1000 times less cosmogenically activated ^{39}Ar than than natural argon.

2.4 Scintillation in Noble Targets

This section discusses scintillation in liquid noble targets. Sec. 2.4.1 provides an overview of the scintillation physics. Sec. 2.4.2 expands upon the powerful PSD capabilities in noble targets. Lastly, Sec. 2.4.3 provides an introduction to a wavelength shifter, tetraphenyl butadiene, commonly used with argon experiments.

2.4.1 Scintillation production

Fig. 2.10 shows the mechanism of scintillation light production in a noble liquid target of species X. This process is generally the same for the most commonly used liquid noble targets (He, Ne, Ar, and Xe).

When an incident particle impinges on a target atom, atom X is either excited or ionized. The ratio of the number of ions (N_i) to the number of excitons (N_{ex}) depends on the relative cross-sections for atomic excitation versus ionization of the incident particle and the characteristic average energy required to produce either an ion or exciton (W). Stated explicitly, an energy deposition of E_0 will produce N_{ex} and N_i according to the relationship defined in Eq. 2.16 as:

$$E_0 = \frac{W}{L}\left(N_{ex} + N_i\right) \tag{2.16}$$

where L is an empirical characterization value which takes into account losses due to atomic motion rather than the production of ions or excitons by Lindhard, et al [85, 86]. Following the excitation path in Fig. 2.10, the excitons (X^*) combine with ground state atoms to produce excited dimer molecules ($X^* + X \rightarrow X_2^*$) in the lowest excited state which are either in the singlet ($^1\Sigma_u^+$) or triplet ($^3\Sigma_u^+$) molecular states [126]. The singlet and triplet states then decay radiatively to VUV scintillation photons according to their respective time constants, τ_1 and τ_3.

Nuclear recoils (large dE/dx) can produce regions containing a high density of excitons. Excitons can combine to form an ion via biexcitonic quenching: $X^* + X^* \rightarrow X_2^{**} \rightarrow X^+ + e^-$. The electron and ion pairs can then undergo recombination though a Penning process [87] which results in the formation of an exciton ($X^+ + e^- + X \rightarrow X_2^+ + e^- \rightarrow X^{**} + X + \text{heat} \rightarrow X^* + X$).

For a TPC detector, the presence of an electric field reduces the recombination probability, leading to scintillation quenching [88, 89]. Fig. 2.11 shows evidence from the SCENE experiment (using a liquid argon target) of decreasing scintillation light yield of the S1 signal from nuclear recoils for increasing field strength. It should be noted that nuclear recoils in LXe TPCs show much less dependence on field strength.

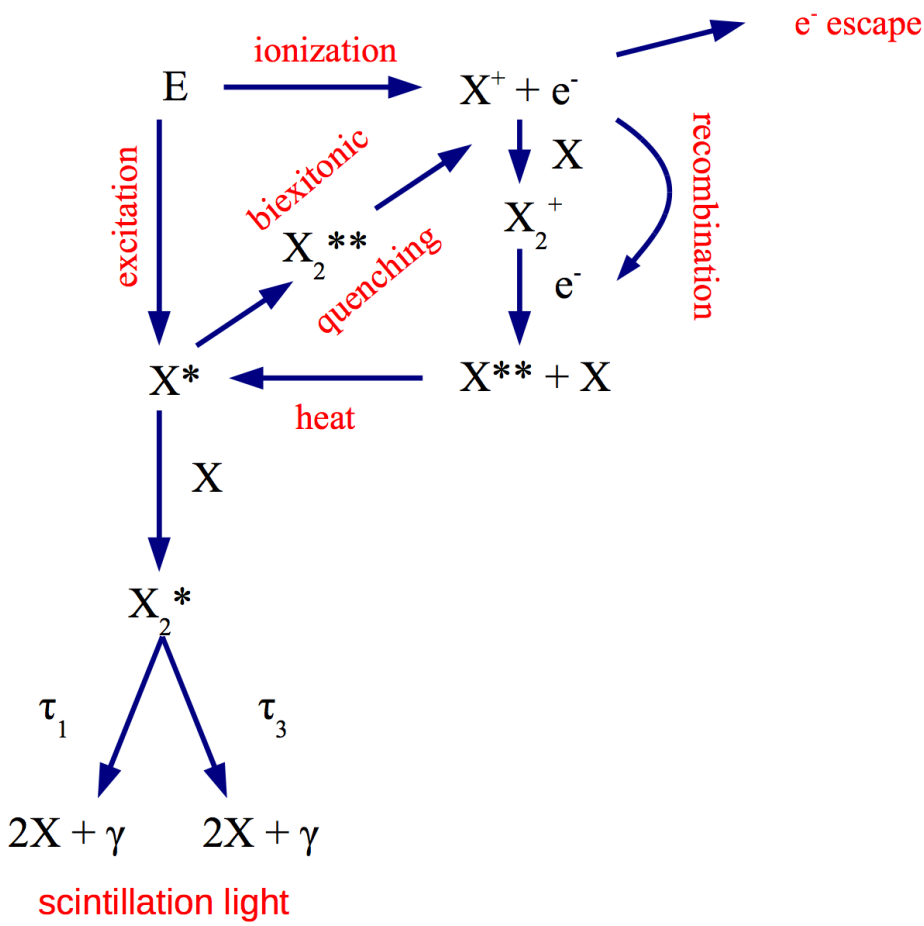

Figure 2.10: A schematic of the various processes contributing to LAr scintillation and ionization. Figure and caption from [29].

It is observed that nuclear recoils produce less light than electronic recoils for an equivalent amount of deposited energy. The nuclear recoil efficiency (L_{eff}) is commonly used to convert the observed energy (usually in photoelectrons) of a nuclear recoil into an electronic recoil equivalent measurement. Some of the nuclear recoil quenching is predicted by Lindhard [85], but an additional factor is required to account for the previously discussed biexcitonic quenching (Birks saturation) [90]. In general, L_{eff} depends on recoil energy but is approximately 0.27 for nuclear recoils with deposited energies on the order of tens of keVs for a liquid argon target.

In the presence of impurities (e.g. O_2, N_2, H_2O), there is a probability that a dimer molecule will undergo a non-radiative collisional reaction with an impurity molecule. This non-radiative quenching process is in competition with the de-excitation process that leads to light emission. The singlet state is not strongly affected by this process, due to its very fast

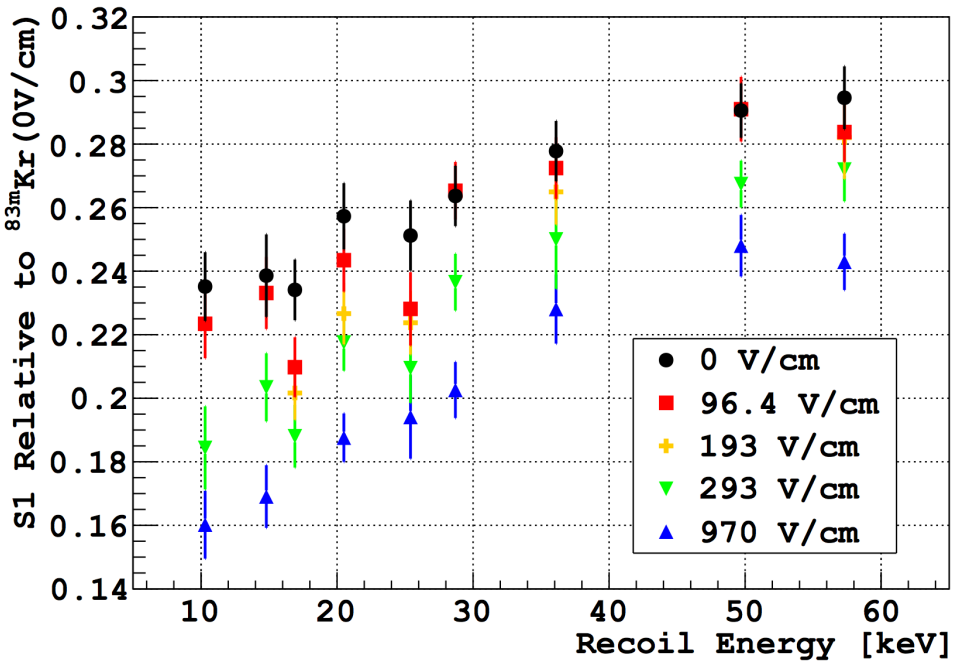

Figure 2.11: S1 yield as a function of nuclear recoil energy measured at five drift fields (0, 96.4, 193, 293 and 970 V/cm) relative to the light yield of ^{83m}Kr at zero field. Figure and caption from [89].

decay time, but with sufficiently high impurity concentrations (> 100 ppm) the singlet state can begin to be quenched as well [91]. However, even impurity concentrations < 100 ppm can significantly reduce the triplet lifetime and total light yield. As such, the measurement of triplet lifetime can lead to an understanding of impurity level in a target like argon. The measurement of this impurity dependence in gaseous argon is the subject of Chap. 5.

2.4.2 Pulse Shape Discrimination

Recalling the discussion in Sec. 2.4.1, each excimer which produces scintillation light upon disassociation is either in the singlet or triplet state. The decay time of the singlet state is very fast and on the order of several nanoseconds. The triplet state must undergo a spin flip transition to decay which makes its time constant usually much longer. As seen in Tab. 2.1, liquid argon has a triplet time constant of 1.6 μs - much longer than the singlet time constant. The two decay time scales can be clearly seen in left-side figure in Fig. 2.12, which shows an average trace from scintillation light in liquid argon [92].

On average, the ratio of triplet to singlet states produced depends on interaction type. Electronic recoils (i.e. β and γ) produce relatively more triplet states than nuclear recoils because ionization allows the freed electron's spin to be randomized prior to recombination,

making the triplet state more probable than states produced via the excitation path in Fig. 2.10. As a consequence, electronic recoil events contain more late scintillation light than nuclear recoil events, allowing for powerful event type classification from the temporal pulse shape of scintillation in an event window. This technique is commonly referred to as pulse shape discrimination (PSD).

An example of a simple discriminant one could use to classify electronic and nuclear recoils is the prompt fraction [92]. For a voltage waveform $V(t)$, for example, the prompt fraction is defined as the fraction of charge in a prompt window. This is defined in Eq. 2.17 as:

$$f_p = \frac{\int_{T_i}^{\epsilon} V(t)\, dt}{\int_{T_i}^{T_f} V(t)\, dt} \tag{2.17}$$

where T_i is the start of the event window and typically before the prompt peak, T_f is the time defined by the end of the event window, and ϵ is the upper bound on the prompt integration window which depends on the timing characteristics of the target.

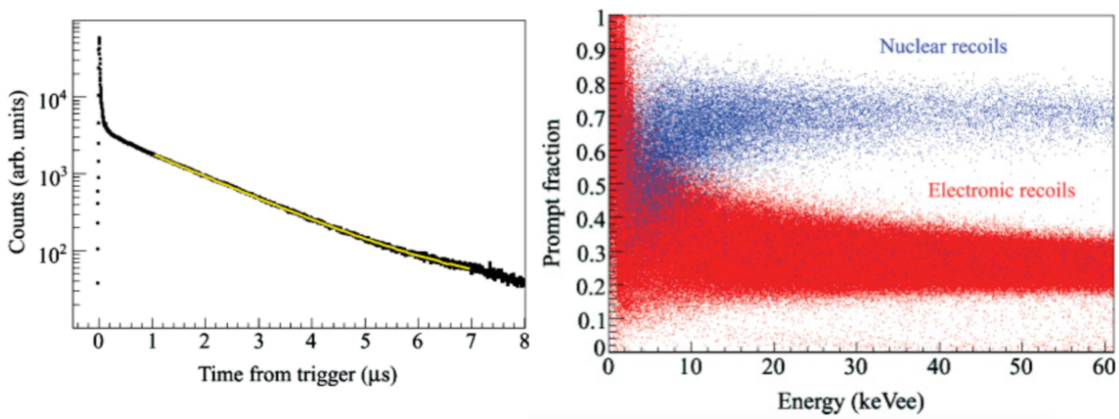

Figure 2.12: Left: Example fit of a single exponential to an average trace to measure the long time constant in liquid argon. Figure and caption from [92]. Right: Scatter plot of f_p vs energy for tagged electronic and nuclear recoils. Figure and caption from [92].

The right-side figure in Fig. 2.12 demonstrates the ability for f_p to discriminate between electronic and nuclear recoils as a function of energy. Using this technique, electron recoils can be discriminated from nuclear recoil signals (i.e. WIMPs) with a high degree of certainty allowing for powerful background rejection. The following chapters will discuss the Mini-CLEAN detector, whose primary goal is to test PSD to the levels required for a monolithic, large-scale, next-generation dark matter detector.

2.4.3 Wavelength Shifting Thin Films

As discussed in Sec. 2.4 and shown in Fig. 2.7, the wavelength of scintillation light produced by liquid noble targets is in the vacuum ultraviolet (VUV) spectral regime. For targets other than Xe, the scintillation light can not be easily directly detected using PMTs. Therefore, a wavelength shifter is often used as an intermediate step in the optics chain to down convert the energetic VUV photons to visible photons so they can be easily detected using PMTs.

One commonly used WLS is tetraphenyl butadiene (TPB). TPB thin films have been widely studied [93, 150, 151, 152, 153, 122, 154, 155, 156, 157, 158] and are regularly used for many experimental programs [77, 78, 79, 60, 51, 49, 80, 81] due to their relatively high efficiency. TPB may also be easily applied to surfaces using standard techniques, such as vacuum deposition in a thermal evaporator. The reemission spectrum of TPB has been measured and its shape is well understood at cryogenic temperatures [154] and room temperature [93].

Chapters 6 and 7 discuss work led by the author to measure the quantum efficiency and other microphysical properties of TPB thin films. These results are expected to improve the modeling and understanding of TPB films.

Chapter 3

The MiniCLEAN Experiment

This chapter provides an overview of the MiniCLEAN experiment.

3.1 Detector Overview

Many past, current, and future neutrino experiments have adopted the approach of using simple, monolithic detector designs with high PMT coverage to view an active target [96, 97, 98, 99]. Examples of these detectors are the SNO+ experiment and the KamLAND experiment, which are shown in Fig. 3.1. The success of these monolithic detectors demonstrates the scalability of a relatively simple detector geometry instrumented with PMTs for low-background searches.

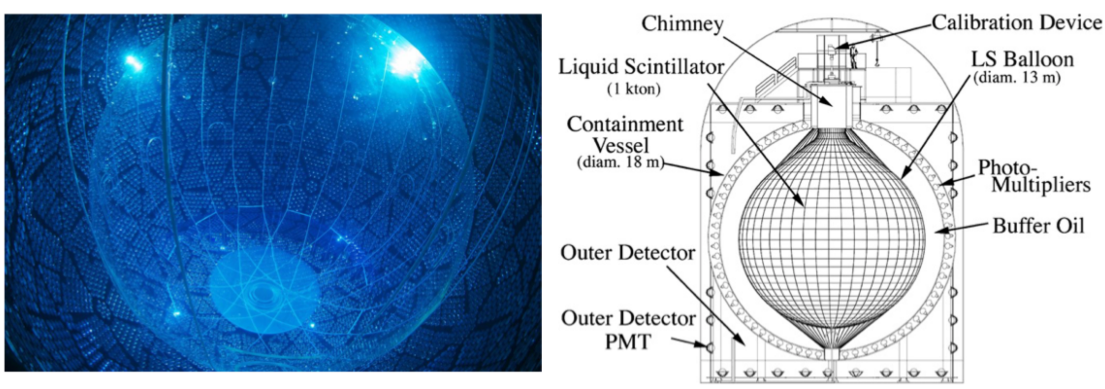

Figure 3.1: Left: A photo of the SNO+ detector late in 2016 submerged in ultrapure water. Right: A schematic of the KamLAND experiment. [100]

The **C**ryogenic **L**ow **E**nergy **A**strophysics with **N**oble Liquids (CLEAN) program seeks to replicate this simple and scalable detector design philosophy for WIMP dark matter searches

and low energy solar neutrino experiments. Two different targets could be used in a staged approach in a CLEAN experiment: Liquid argon and liquid neon.

As discussed in Sec. 2.4, liquid argon is a particularly favorable target for a monolithic CLEAN detector concept due to its scintillation properties (high scintillation yield and ability to perform PSD), affordable commercially available supply, and relatively high atomic number. Using a liquid neon phase at large detector scales allows for a low energy solar neutrino program in addition to independently testing the expected A^2 dependence of a WIMP cross section if a signal were to be observed in the argon phase.

The DEAP and CLEAN programs have adopted a staged approach where the efficacy of key technologies is demonstrated before the scale-up to the ultimate goal of a single-phase, monolithic, mutli-tonne scale detector. The three staged experiments for the CLEAN program are the MicroCLEAN, MiniCLEAN and CLEAN. The MicroCLEAN [101] and DEAP-1 [102] experiments served as single-phase prototypes for the "intermediate scale" MiniCLEAN [49] and DEAP-3600 [51] experiments that exist at SNOLAB in 2018. The results from the MiniCLEAN and DEAP-3600 experiments will inform the design and performance for the monolithic scale single phase experiments.

Fig. 3.2 shows a cartoon diagram of single-phase CLEAN style detector. Analogous to large scale neutrino experiments like SNO, a CLEAN detector takes a spherical geometry with inward looking PMTs placed on the outer perimeter of the inner vessel allowing for a 4π PMT coverage. The inner and outer vessels are constructed using a high strength metal alloy, likely stainless steel, to allow for scaling to very large sizes. The PMTs are immersed in the cryogen target and operate cold. The inward facing PMTs are coupled to light guides which contain an acrylic substrate at the end of the light guide at small radii. A wavelength shifting thin film, likely made of TPB, is deposited on the inner most face of the acrylic substrates to form a wavelength shifting boundary on the outer edge of the target volume.

The inner vessel (IV) is contained inside of an outer vessel (OV). The OV operates as a cryostat where high-vacuum is maintained in the space between the IV and OV for thermal insulation. The OV exists inside of a water tank to shield from externally produced backgrounds. The water shield volume can be instrumented with PMTs to be used as an active veto to suppress external backgrounds.

When a particle interacts in the liquid argon target volume, scintillation light (peaked at 128 nm) is produced isotropically. These VUV photons propagate through the target volume until they are absorbed by the wavelength shifter (WLS) boundary. The WLS boundary consists of a tetraphenyl butadiene (TPB) thin film and is required to down-convert the energetic VUV scintillation photons to a visible spectrum wavelength that can be detected by the PMTs. Visible photons reemitted by the wavelength shifting thin film propagate down the light guides and are detected by the inward facing PMTs (optical cassette assemblies are shown in the right image in Fig. 3.3).

The efficiency of the wavelength shifting process by TPB is an important parameter as it is an intermediate step in the optics chain. This efficiency, as well as other microphysical properties of TPB, was studied in detail by the author and are the subject of Chapters 6 and 7.

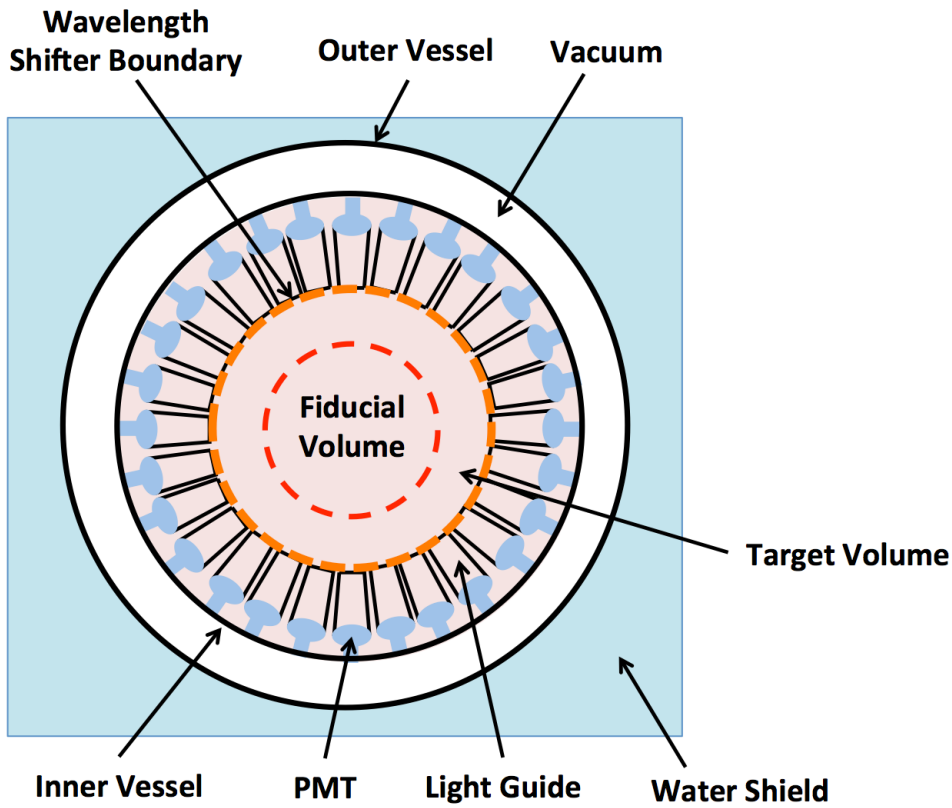

Figure 3.2: An annotated cartoon representation of a CLEAN style detector.

A key benefit of a large detector with a high mass target is the resulting self-shielding of outer regions of the target volume to create a clean, inner fiducial volume. In principle, the larger the scale of the detector, the greater the ability to shield the fiducial region from external backgrounds. Because the PMTs and light guides are submerged in cryogen, the LAr extends outside of the target volume and provides a high-density shield against external backgrounds, such as gammas and neutrons from the PMTs. It is also important to note that scintillation light produced in the liquid argon outside of the target volume is not detected by the PMTs because it is outside the inner TPB boundary and is not wavelength shifted (i.e. the PMTs are not directly sensitive to the VUV scintillation light). This design ensures that argon scintillation light is only detected from events inside of the target volume while allowing argon outside of the target volume to still be used as a passive shield.

A primary objective of the MiniCLEAN detector is to test the design principles outlined for a CLEAN-style detector before scaling up to very large sizes. This includes demonstrating the efficacy of the design but proving the background rejection techniques required for a very large detector using natural argon. A detailed overview of the MiniCLEAN detector and its supporting systems are the subject of this chapter and will be described in detail in the coming sections.

Fig. 3.3 shows an annotated CAD rendering of the MiniCLEAN detector and a single optical cassette assembly. Fig. 3.3 provides a more accurate visualization of the MiniCLEAN detector than its conceptual CLEAN cartoon counterpart in Fig. 3.2.

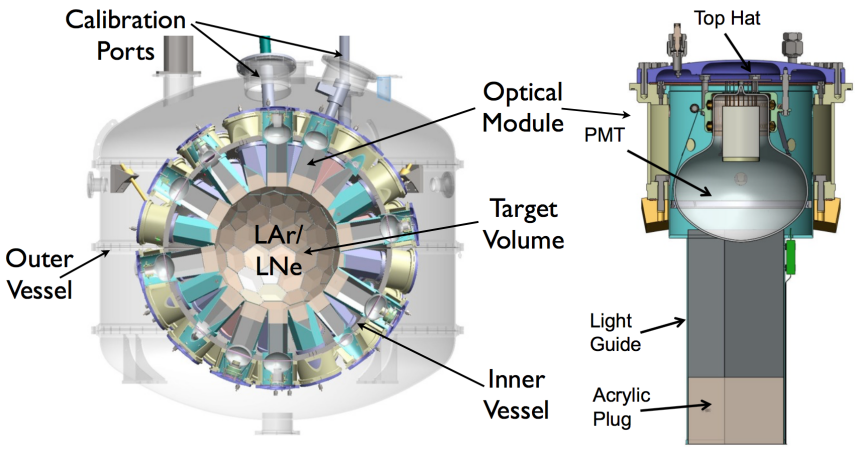

Figure 3.3: Left: An annotated and rendered image of MiniCLEAN. The inner vessel is installed in the outer vessel. Right: Rendering of a single PMT and light guide assembly. Images from [29].

Fig. 3.4 shows images of the assembled IV (left) and OV (right). The IV is approximately 2 meters in diameter when fully assembled. The construction and commissioning of the IV and OV are described in detail in Sec. 4.2.

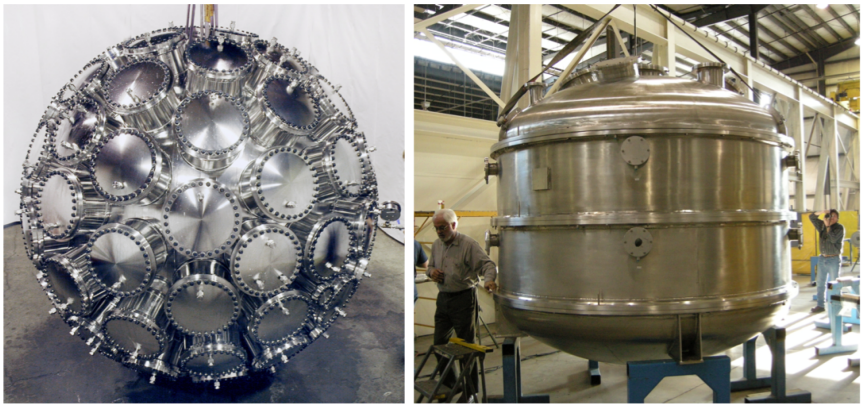

Figure 3.4: Left: A photo of the assembled IV. Right: A photo of the assembled outer vessel during inspection at the manufacturer (PHPK) shortly after its construction. Image from [29].

3.1.1 Cryogenic System

MiniCLEAN is cooled using a Gifford-McMahon cryocooler which is mounted on the OV (OV-D flange). The cold head is coupled to two oxygen-free, high thermal conductivity (OFHC) copper "cold fingers" on the IV using 24 flexible OFHC copper braids. A CAD drawing of the entire cooling assembly is shown in the top-left image of Fig. 3.5, while the bottom-left photo in Fig. 3.5 shows the copper braid coupled to an external portion of one of the cold fingers. The top portion of the cryocooler assembly is in an air-filled flange mounted on the outside of the OV. An air-filled hose runs the helium lines and power cable to the overhead deck through the water shield tank. A photo of the cryocooler's helium compressor, located at the bottom of the SNOLAB's Cubehall, is shown in the right-side annotated photo in Fig. 3.5.

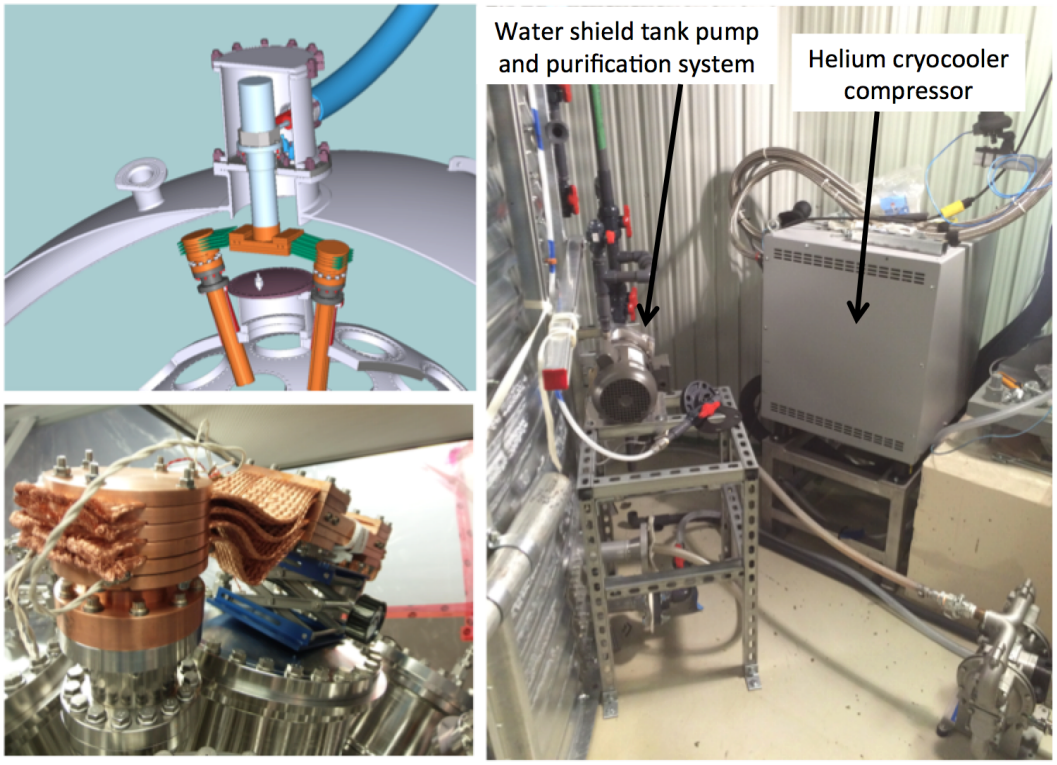

Figure 3.5: Left: A CAD drawing of the cryocooler mounted on the MiniCLEAN vessel. Copper cold fingers extending into the IV volume are coupled to the cold head using copper braids [29]. Right: An annotated image of the helium cryocooler compressor used to supply helium to the cryocooler installed on the OV (left image). Also shown is the water shield tank circulation pump and purification system.

The helium supplied to the OV-mounted cryocooler from the compressor operates in a closed-loop. The compressor is water cooled and shares a chilled water loop with the DEAP-3600 experiment. The cooling power of the cryocooler as a function of helium temperature

is shown in the left image of Fig. 3.6. This cooling is sufficient to liquefy and maintain a LAr target but will require an upgrade for a LNe phase. Cooling and liquefying progressed slower than expected during the commissioning of MiniCLEAN so a LAr condenser (Sec. 4.3.1) was installed to improve cooling and liquefaction efficiency.

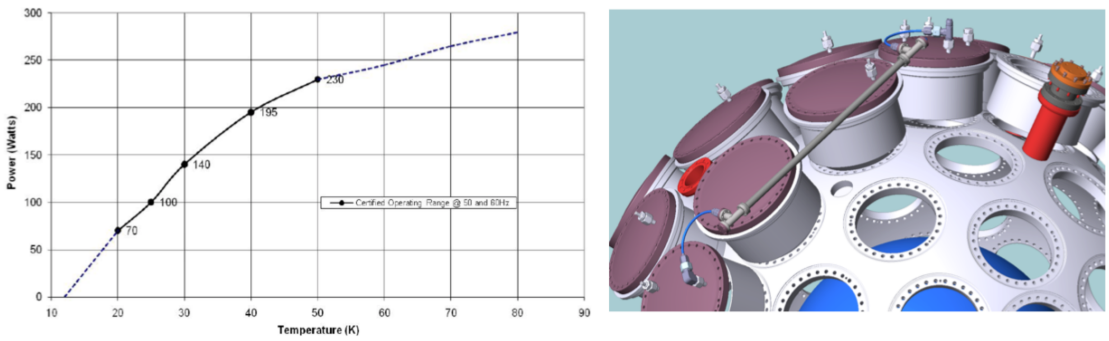

Figure 3.6: Left: The cooling capacity of the AL325 cryocooler as a function of helium temperature. Right: A CAD drawing of the IV level meter installed on the outside of the IV.

Temperature sensors and cartridge heaters are located near the cryocooler cold head and on the thermal copper coupling elements shown in the left-side images of Fig. 3.5. A PID temperature controller is used to control the temperature of the thermal coupling elements using the heaters to throttle cooling power. Additional temperature sensors are also located at several locations on the IV to monitor temperatures.

The total heat load on the IV is estimated to be approximately 65 W, where the dominant heat loads are from thermal radiation, PMT bases, and OV-IV supports at 22.3 W, 12.1 W, and 11.0 W respectively. Multiple layers of multilayer insulation (MLI) were installed on the inner surface of the OV to reduce the heat load from thermal radiation and can be seen in Fig. 4.3.

The LAr level in the IV is monitored using two capacitive level meters. The first is installed on the side of the upper third of the IV (thin tube seen in the right-side image in Fig. 3.6), which provides level sensitivity for LAr levels approximately 2/3 to completely full. The second level meter exists in the liquid buffer volume above the detector (left-side image in Fig. 4.5).

3.1.2 Purification System

As discussed in Sec. 2.4.1, the scintillation properties (yield and time profile) of gaseous and liquid argon are very sensitive to impurities. Therefore, MiniCLEAN has strict purity requirements for its argon target which is achieved using a gas purification system. The argon target is purified in gaseous phase and reliquefied inside of the IV during liquid phase

filling. The purification system contains two primary components: a SAES PS4-MT3-R-1 getter and an activated charcoal trap.

A heated zirconium cartridge inside the getter is used to reduce most impurities (H_2, CH_4, H_2O, CO, N_2, O_2 and CO_2) in gaseous argon to < 1 ppb levels. The getter requires the inputted gas to be 99.999% pure. This is achieved by using argon boil-off from a liquid argon dewar supplied by Air Liquide Canada rated to 1 ppm impurity levels. Boil-off from liquid argon dewars is preferred over cylinders because the boil-off contains much less radon due to radon's 202 K boiling point. Additionally, given the large amount of argon that requires purification for the complete filling of MiniCLEAN, it is logistically easier to transport 240 L dewars of LAr than many pressurized cylinders of gaseous argon.

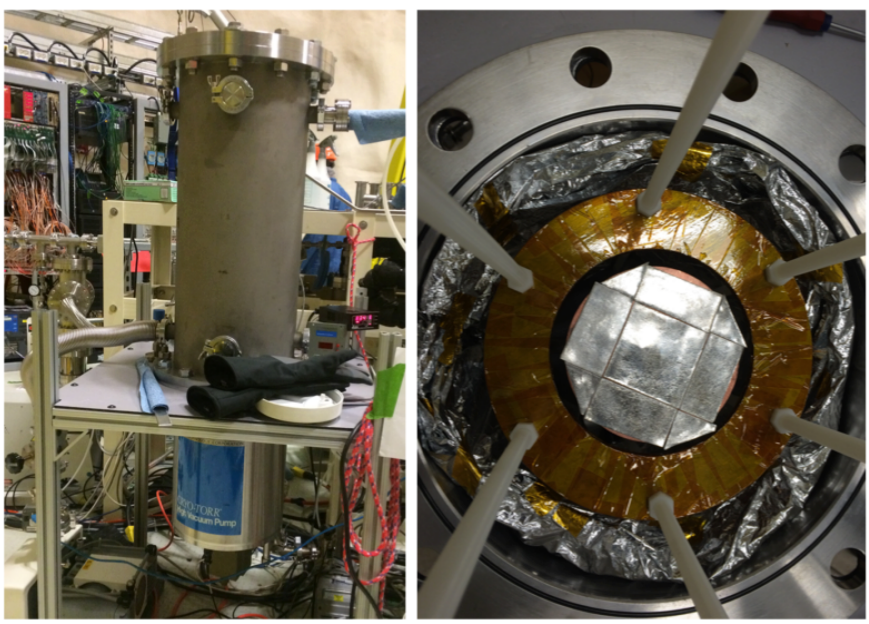

Figure 3.7: Left: A photo of the installed charcoal trap assembly. The outer cylinder housing acts as a cryostat with the a smaller inner cylinder containing the activated charcoal. Right: A view of the cold head assembly inside of the charcoal trap (charcoal trap inner vessel not visible). Indium sheets are used to improve thermal conductivity between the cold head and the inner charcoal trap vessel.

Radon is not readily removed from the argon gas by the getter, so an activated charcoal trap is used to cryoabsorb radon to reduce its concentration before flowing into the IV [103, 104]. The trap contains approximately 1.2 kg of Calgon Type PCB-LS 4x8 mesh activated charcoal, and is isolated from the rest of the purification system with 2 μm filters. The charcoal trap is cooled using a helium cryocooler (shown in Fig 3.7).

Additional details of the purification system and its commissioning are provided in Sec. 4.3.

3.2 Data Acquisition System

This section provides an overview of MiniCLEAN's data acquisition, active veto system, and magnetic field compensation system.

Fig. 3.8 provides a cartoon schematic of the data acquisition system (DAQ). The DAQ description provided in this section relies heavily on the description provided in [29].

MiniCLEAN's IV contains 92 inward looking PMTs. High voltage is supplied to the PMTs using a VISyN high voltage mainframe. Voltages and programmable trip current values can be set on a channel by channel basis. The PMT signal and voltage are carried using the same cable (RG-68 in air, Gore 30 AWG in the OV vacuum) for each PMT. Custom HV blocking cards are used to filter out the DC component, and send the resulting signal to a set of 12 CAEN V1720 250 MHz digitizers (one sample every 4 ns) which are configured to store 16 μs waveforms. Each digitizer card contains 8 inputs with a 12-bit ADC and a dynamic range of 2 Volts.

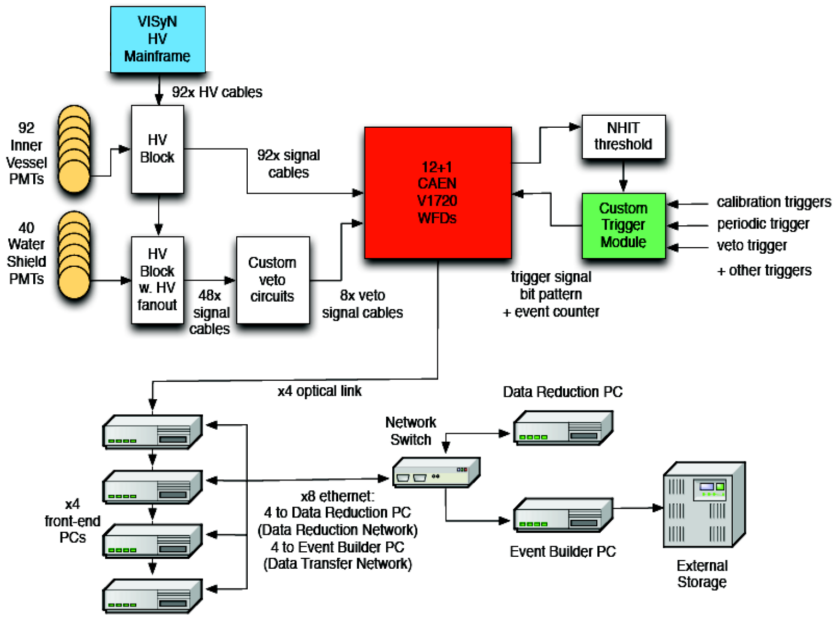

Figure 3.8: An overview of MiniCLEAN's data acquisition system. [29]

Each digitizer outputs a signal which is proportional to the number of channels on each card which are over a programmable threshold. These outputted signals are summed across the 12 digitizers to determine the total number of channels over threshold. This is compared to an adjustable "channel over threshold" value within a 16 ns coincidence window to determine if the detector should trigger. Typically five or more channels are required for this "Nhit" trigger. The "Nhit" trigger is also referred to as the "physics" trigger. Additional trigger inputs all triggering of the DAQ for calibration purposes.

Due to the high data rate from 92 channels of 16 μs waveforms acquired at 500 Hz or higher, full waveforms cannot be written to disk for all events. The CAEN V1720 digitizers can be operated in a zero-length encoding (ZLE) mode where regions of time in which the signal has not crossed threshold (with 16 ns granularity) are not sent over the optical link to be written to disk. In addition to the 16 ns regions where a sample has crossed threshold, programmable length pre- and post-sample regions are also included with each block of ZLE data for post-processing baseline evaluation. Once triggered, the DAQ system sends event summary data to a PC which, in real time, evaluates whether the event could be of interest based on any or all of the amount of charge observed, the estimated prompt fraction, and the charge centroid. Depending on the event summary information, the DAQ system records either the full ZLE waveforms, summary information (charge, time, etc) for each block of ZLE data, or channel level summary data. This process of information reduction based on the on-line classification of events is referred to as the software trigger. The software trigger was developed and tested in the Monte Carlo simulations of the DAQ for ^{39}Ar decay events prior to being implemented.

The DAQ system as described with the software trigger is rate limited at 1.8 kHz by readout of the CAEN V1720 digitizers. With fairly minimal hardware upgrades, the system could be configured to handle up to 4.3 kHz. Although this is more than sufficient for an atmospheric LAr run with MiniCLEAN, this is still well below the event rate required for an ^{39}Ar spike run (discussed in Sec. 3.6). However, the system does not apply any cuts in hardware before triggering the digitizers. A simple addition to the DAQ in which a discriminator cuts high energy events in hardware (with some prescaling) will be necessary for the spike run.

3.2.1 Water Shield and Veto System

As mentioned in Sec. 3.1, the OV is installed in a water tank to provide shielding against external backgrounds. The water tank can be instrumented with an active veto system to allow for rejection of through-going muons, which may be correlated with detector triggers. The veto system was not installed for initial data run in the interest of schedule, but can be installed later as all of the hardware needed is underground. This section provides a brief overview of the veto system. For a more detailed discussion see [94].

As seen in Fig. 3.8, MiniCLEAN's DAQ is designed to accept signals from veto PMT cables. The veto PMTs are to be installed on the inner wall of MiniCLEAN's 18 ft. diameter and 26 ft. tall cylindrical water tank. Through-going muons produce Cherenkov radiation as they pass through the water which can be detected by the veto PMTs in the tank. This allows for the construction of a veto tag to reject coincident physics triggers inside of MiniCLEAN, which could be a result of neutron cascades and other spallation products that could mimic a WIMP signal. 48 8" SNO era PMTs are arranged into 12 vertical strings (containing 4 PMTs each), which provides approximately 1% of photocathode coverage inside of the water tank. The inner layer of the water tank is white which allows from some reflections of Cherenkov radiation to assist with light collection.

Fig. 3.9 provides information on the expected rates of muons and the expected efficiency of veto system operating in the MiniCLEAN water tank. The left plot in Fig. 3.9 shows the muon flux measured at SNO as a function of azimuth angle plotted along with the MiniCLEAN shield tank cross-section with a total muon flux of 3.31 ± 0.1 (stat) ±0.09 (syst) muons/s/cm^2 as measured by SNO [107]. According to Jaditz [94], this provides an estimate of the total muon flux of 9.8 ± 0.3 μ/day incident on the MiniCLEAN water shield tank.

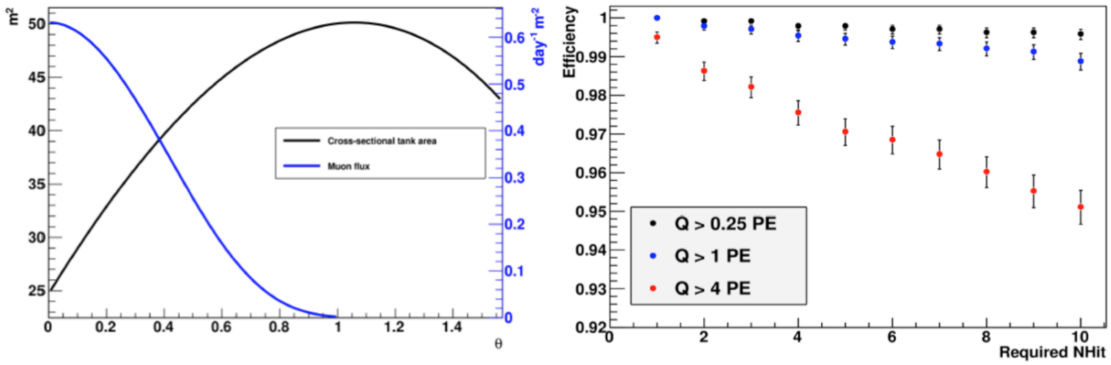

Figure 3.9: Left: The modeled muon flux at SNOLAB from [106] and cross sectional area for MiniCLEAN as a function of angle incident muon angle. This gives an expected muon rate of 9.8 ± 0.3 μ/day incident on the shield tank. Figure taken from [94]. Right: Efficiency of muon tag as a function of the required number of hit PMTs for a veto tag. Taken from [94].

The right-side image shows the results of a study done by Steve Jaditz in [94] to evaluate the tagging efficiency of a veto system as a function of the number of required coincident hits on veto PMTs and photoelectron threshold. For a 0.25 PE PMT threshold and for a coincident hit requirement of 2 PMTs, simulations show that 99% tagging efficiency can be achieved. Using a more strict veto tag requirement, such as 5 or more hits and 4 PE per PMT, is expected to still perform at about 97%.

3.2.2 Magnetic Field Compensation System

It is known that the presence of a magnetic field can negatively affect the efficiency of a PMT. The relative orientation of the PMT in the field also affects the PMT's performance. The left figure in Fig. 3.10 shows the PMT efficiency as a function of magnetic field strength and direction for a PMT whose dynode stack is oriented parallel (red) and perpendicular (blue, solid) to the magnetic field as measured by Hamamatsu Photonics.

For a spherical detector geometry like MiniCLEAN, the optimal choice of the magnitude of the magnetic field at the location of the PMTs is zero. MiniCLEAN uses a magnetic compensation system to zero-out the Earth's magnetic field, which is discussed in detail in [105]. In summary, six coils are arranged in a Helmholtz coil configuration and installed

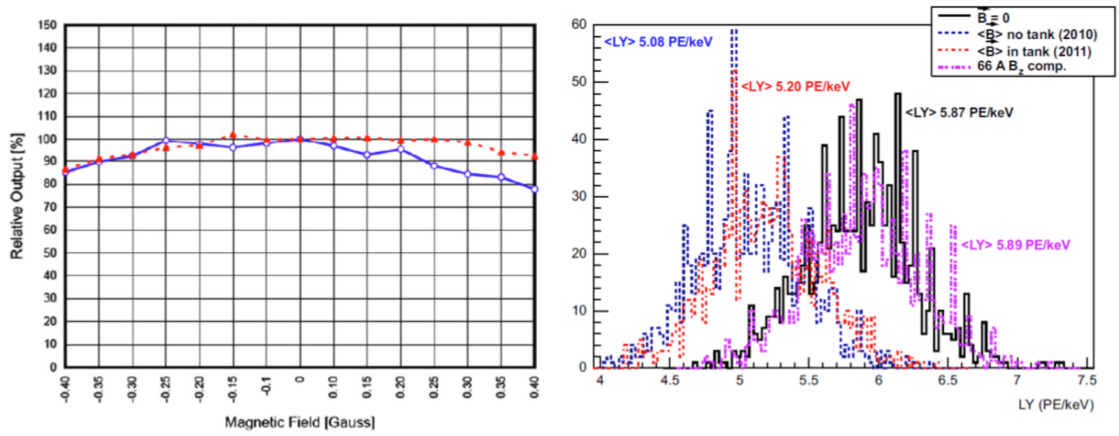

Figure 3.10: Left: The relative efficiency of an R5912PMT as a function of magnetic field strength as measured by Hamamatsu Photonics. The red dashed line is for a magnetic field parallel to the dynode stack while the blue solid line is for a field perpendicular to the axis of the dynode stack. Right: Results for a Monte Carlo simulation of detector light yield from electronic recoils in MiniCLEAN. Zeroing the field in the water tank is expected to improve the efficiency of the PMTs, thus increasing the light yield. Figures taken from [29].

on the exterior wall of the water shield tank. These coils are used to produce an offsetting magnetic field to zero out the total field in the region near the PMTs. Five magnetic field sensors are installed at various locations on the outside of the OV which can measure the direction and magnitude of the field at their location. Field readings from the sensors inform manual adjustments of the currents in the coils to zero out the field.

The left figure in Fig. 3.10 shows simulation predictions of detector light yield from electronic recoils from ^{39}Ar decays with and without the zeroing of the Earth's magnetic field in the water tank. The simulation predicts that the light yield may be increased by approximately 0.67 PE/keV using the magnetic compensation system.

3.3 Simulation and Analysis Framework

This section provides an overview of the simulation and analysis framework used by MiniCLEAN. Sec. 3.3.1 provides descriptions of the software framework, RAT, and the detailed Monte Carlo model of MiniCLEAN used in RAT. Sec. 3.3.2 describes the general analysis approach using RAT and a subset of important discriminators used in most analyses.

3.3.1 RAT

The Reactor Analysis Tool (RAT) is a detailed GEANT4 based, microphysical simulation and analysis framework first written for the Braidwood experiment [108]. Versions of RAT

are currently being used by several experiments, including SNO+ [97], DEAP-3600 [51] and MiniCLEAN [49].

RAT combines useful features from several software packages. In particular, RAT incorporates the electromagentic and hadronic physics simulations provided by GEANT4 [109, 110], the data storage and processing tools provided by ROOT [111], parts of the scintillation and PMT simulation from GLG4sim (an open source package released by the KamLAND collaboration), and much of the design philosophy of SNOMAN from the SNO collaboration [29]. The RAT design philosophy can be described by the following points: [112]

- Provide a simple interface to analyze Monte Carlo generated events, as well as real data, from disk with the same software and minimal command changes. Using the same framework to analyze simulation and data ensures processing consistency when comparing simulation and data.
- Allow for modular, user-controlled analysis of events. It should be straightforward for users to introduce and test their own code into the analysis process.
- Separate analyses into small tasks which can be developed asynchronously by different people, yet integrated with minimal difficulty.
- Wrap GEANT4 in a flexible application that allows users to accomplish a variety of analyses without having to recompile RAT when making small changes, such as PMT calibration constants or material properties.

Detector simulations in RAT seek to accurately simulate each step in the detection process - from primary/secondary particle propagation to simulation of DAQ electronics and data storage. The typical sequential steps which are involved in a full simulation of the detector are described in the list below.

1. Use GEANT4 to propagate primary and secondary particles, such as electrons, gammas, nuclear recoils (WIMPs), and neutrons through detector materials.
2. Production of the extreme ultraviolet (EUV) scintillation light by charged particles in the argon/neon target.
3. Propagation of the individual photons (EUV and wavelength-shifted photons) through the detector using GEANT4. Both bulk and surface optical properties of the materials (argon, TPB, glass, metal surfaces) are included.
4. Detection of photons at the PMTs. Realistic pulses, based on measurements described in [29], are produced. Realistic modeling of the timing, charge, and shape/timing variations are considered.
5. Detector triggering, electronics noise modeling, waveform digitization, ZLE encoding, and data packing for readout are also included in simulations.

A detailed model of the MiniCLEAN detector is constructed in RAT for simulations. Fig. 3.11 provides renderings of this model. The left-side image in Fig. 3.11 shows the full model of the IV installed in the OV, which is installed in the water shield tank. The right-side image shows a rendering of one-quarter of the MiniCLEAN IV where the PMT top hat assemblies (red), light guides, acrylic plug with a TPB coating, and the light guide tessellation are visible. Material properties, such as characteristic wavelength-dependent absorption lengths, indexes of refraction, surface roughness properties, etc., are all included and modeled.

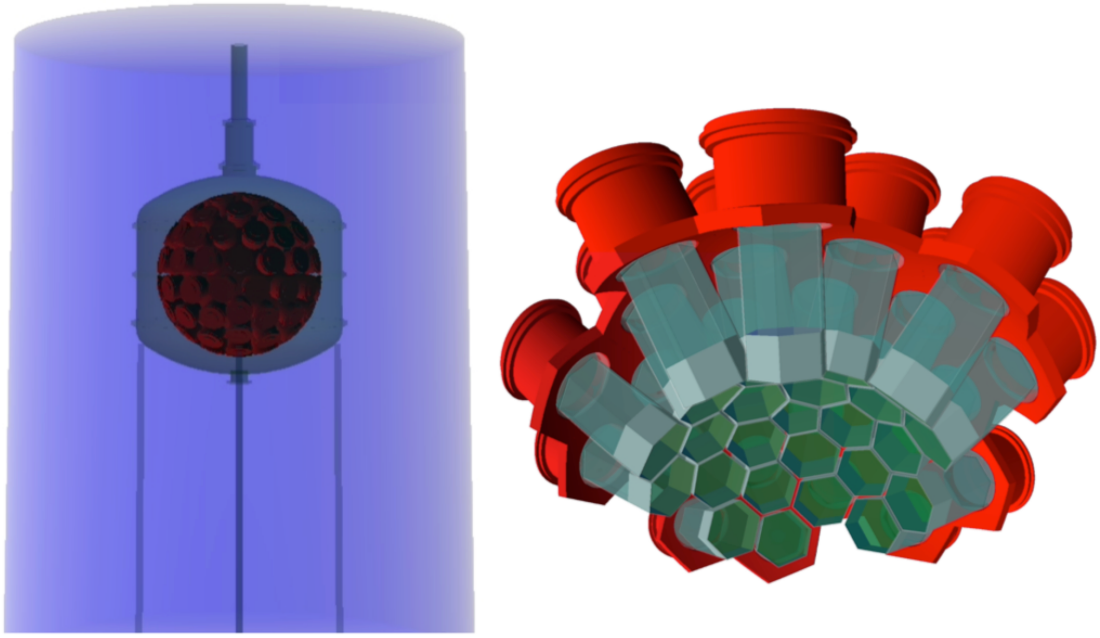

Figure 3.11: Renderings of the MiniCLEAN model in RAT. The left image shows the entire detector (IV, OV, water shield) while the right-side image shows a cut-away of the IV. Figures taken from [29].

As previously mentioned, data files which have been written to disk can be read into RAT and analyzed using custom processors. Because the last step of the Monte Carlo is packing digitized data using the same method that is done in the actual DAQ, simulation and data may be read into RAT from disk and analyzed by processors in identical manners so that data and simulation can be compared on equal footing. When performing simulations, truth information is often stored (in a parallel branch in the ROOT data structure) along with the raw PMT signal information for debugging and processor development. A general description of the data processing chain and an introduction to commonly used discriminators are discussed in greater detail in Sec. 3.3.2.

3.3.2 Analysis Overview

This section provides an overview of the analysis chain used in MiniCLEAN. A description of the general processing order and an introduction to several commonly used discriminators is provided.

3.3.2.1 Analysis Chain

When data from disk (simulated or real data) is loaded into RAT for processing, the events are processed in the order in which they were saved and, in general, independent of other events. The set and order of processors to be run on loaded data are specified by user defined macros. Some processors have prerequisites for the order in which processors must be run so the execution order of processors is important. Parameterized variables used as inputs to processors, such as PMT calibration constants, are loaded in from human-readable database files. This allows for easy adjustment without the need for recompiling.

Common classes of processors used by RAT in analysis are: DAQ, calibrated waveform, pulse finder, PMT calibration, simple discriminator processors, advanced reconstruction processors. Each of these processor classes are described below.

DAQ: The DAQ processor is responsible for constructing many of the fundamental data objects used further in the analysis chain. For example, C++ objects representing the digitizers are created for the intuitive representation of data being read from disk or simulated. This processor is also responsible for extracting the digitized data and properly interpreting its compression format.

Calibrated Waveform: Once the fundamental objects required for analysis are initialized by the DAQ processor, the calibrated waveform processor is usually run. The processor converts the raw waveform blocks outputted by the digitizer to calibrated waveform blocks by subtracting the baseline, flipping the signal, and converting ADC counts to a voltage in volts. The baseline for each channel is assumed to be flat over the 16 μs event window. The processor also detects saturation of the digitizers and sets the appropriate cut bits accordingly. In addition, the processor calculates the summed calibrated waveform for all PMTs, and sets the calibrated trigger time. The calibrated trigger time is defined as the time of the peak of the summed calibrated waveform in nanoseconds since the first sample of the event within a specified range of the end of the presample buffer.

Pulse Finder: Following the execution of the calibrated waveform processor, the individual pulses within the waveforms are now ready to be identified. This is done using the "Pulse Integration Window Processor". This processor scans calibrated waveforms, looking for regions where the integral of a small region of the waveform crosses a specified threshold. To determine the left and right edges of a pulse, the processor walks forward and backward from the peak until the integral in that window no longer exceeds a less stringent threshold.

A look-ahead region can be used to extend a pulse's boundaries for pulses closely spaced in time. The processor also includes options for improved baseline subtraction over the default methods used in the calibrated waveform processor.

Once the boundaries of the pulse are identified and the baseline subtraction has been performed, each iteration the processor calculates the gain corrected charge integral and locates the peak of the pulse. These values are stored in the ROOT data structure as a "Pulse" object with several attributes containing relevant information for each pulse.

PMT Calibration: Several processors are used for PMT calibration. These processors allow for in-situ calibration of the PMTs for each data run.

The "Dark Hit Calibration Processor" extracts dark rates and dark hit charge distributions (which are generally lower in mean charge than single PE charge distributions) for each PMT using random trigger events.

The "SPE Calibration Processor" determines the charge distribution of single photoelectrons (SPE) for each PMT. This calibration is performed using scintillation light at late times in the event window. At late times, pulses found in scintillation events are likely to be due to only single photoelectrons or dark hits. Using the dark hit charge distribution and dark hit rates extracted by the previously mentioned dark hit calibration processor, the true SPE distribution can be fit by correcting for the dark hit contamination. This process is discussed in greater detail in Sec. 3.5.3.

Lastly, the "Board Alignment Processor" uses periodically injected pulses on each of the digitizer boards to allow for monitoring and correction of the relative time offset between the boards.

The three previously mentioned PMT calibration processors belong to a special processor class that extract the PMT calibration constants by integrating over all the events in a data run to populate histograms for fitting. The resulting calibration constants are then used as inputs to the calibrated waveform and pulse finding processors during a second pass of data reconstruction.

Discriminator Processors: Following the calibration of waveforms and identification of pulses, several useful discriminators can be evaluated. The modular design philosophy of RAT makes it easy for various processors to be inserted or removed at will, based on the needs of an analysis. Several of these discriminators are described in Sec. 3.3.2.2. Examples of discriminators evaluated by processors of this class are the prompt fraction (f_p), f_α, and the charge centroid position reconstruction.

Single PE Arrival Time: At this stage in the analysis chain, the waveforms have been calibrated, pulses have been identified, and simple discriminators have been evaluated. However, using methods developed by Caldwell which are described in detail in [29, 113], the likely timing of single photoelectrons can be estimated from pulse times, even in regions where pulses contain multiple photoelectrons. This processor accomplishes this by estimating the

Name	Description
f_p	Fraction of charge in prompt region of event window
f_α	Fraction of charge in an intermediate window used to classify α events on TPB
ℓ_r	Likelihood ratio of a nuclear recoil from PE arrival times
ℓ_α	Likelihood ratio of α scintillation on TPB from PE arrival times
Q_{tot}	Total charge in units of photoelectrons (PE)
Q_{ratio}	Maximum fraction of total charge on one PMT
R/R_{TPB}	Radius ratio - Reconstructed radius divided by TPB radius

Table 3.1: A summary of commonly used cut variables in MiniCLEAN analyses.

number of photoelectrons (PE) in each pulse of a waveform using a Bayesian calculation based on the time distribution of the scintillation light in the detector's target material and the SPE charge distribution of the PMT under consideration. The result is a more accurate estimate of the total number of PE and their arrival times.

Advanced Reconstruction Processors: Using the results from the single PE arrival time processor, more sophisticated discriminators may be evaluated to help improve event classification. In particular, the "Likelihood recoil processor", referred to as ℓ_r, evaluates a normalized log-likelihood ratio for observing photoelectrons (PE) at the times from the single PE counter under seperate evaluation of the nuclear and electronic recoil hypotheses. Another example of an advanced reconstruction processor is the ShellFit position and energy reconstruction fitter. More sophisticated than a simple charge weighted position centriod calculation previously discussed, ShellFit performs a maximum likelihood estimation of the electron-equivalent kinetic energy and position of an event through a more careful handling of the optics in the fitter based on the reconstructed position of the event. More details of these advanced discriminators and their development may be found in [29].

3.3.2.2 Common Discriminators

As previously mentioned, several discriminators are evaluated in the analysis chain and used to classify events for the construction of data cuts. Several common cuts are summarized in Tab. 3.1.

From Tab. 3.1, the prompt-fraction, f_p, is a simple discriminant which is the ratio of charge observed in the prompt window to the total charge in the event window and is explicitly defined in Eq. 2.17. Because the time separation between the singlet and triplet states is significant in argon, f_p can be used as a particle discriminator. The bounds of the prompt window are set by the characteristic time scales of the scintillation light (discussed in Sec. 2.4). For use with a liquid argon target in MiniCLEAN, the prompt window integration bounds for f_p are set -28 ns to 80 ns.

f_α is similar in nature to f_p, except for its use of an intermediate scale integration window instead of a prompt window to discriminate between TPB scintillation from α interactions

and other events. This is discussed more in Sec. 3.4.2. The integration window used for f_α is 13 ns to 775 ns.

ℓ_r is a normalized likelihood ratio test statistic used to improve classification of nuclear and electronic recoils. ℓ_r evaluates the likelihood that the set of observed single photoelectron arrival times using the time PDFs for a nuclear recoils hypothesis. Details on the specifics of ℓ_r and its development can be found in [29].

ℓ_α is very similar to ℓ_r except constructed to evaluate the likelihood of α induced scintillation in the TPB boundary. Additional discussion of ℓ_α can be found in [94].

Q_{tot} quantifies the total amount of charge (in units of PE) which is proportional to the deposited energy. This is used for energy cuts in defining the energy region of interest.

Q_{ratio} is defined as the maximum observed charge on a single PMT to the total charge in an event. This is a measure of how isotropic an event is which can be used to cut events where the majority of charge is collected by one PMT, as would be the case for high-voltage breakdown.

The ratio of the reconstructed event radius to the radius of the TPB boundary is considered for making radial cuts.

Using these discriminators, cuts have been defined and optimized in various studies by collaboration members using Monte Carlo and gas data. For a high-mass WIMP search where the energy region of interest is between 12.5–25 keV_{ee}.

Units of keV_{ee}, where the "ee" subscript stands for electron-equivalent, is defined as the observed energy deposition of an event assuming the scintillation light was produced from an electronic recoil. This is necessary, recalling the discussion in Sec. 2.4.1, because nuclear recoils are known to produce less scintillation light (by a factor of approximately 0.3 in liquid argon) per keV of deposited energy due to quenching from the high dE/dx nature of the interaction. This merits the use of keV_{ee} as a standardized unit when reporting observed energy from an event. Therefore, the recoil energy (in units of keV) of an event thought to be a nuclear recoil can then be determined by dividing the observed energy in units of keV_{ee} by the (energy-dependent) nuclear recoil quenching factor.

The following energy, radial and PSD cuts are expected to be used for a simple box analysis:

- Energy Cut - 75 PE $< Q_{tot} <$ 150 PE (assuming a light yield of 6 PE/keV_{ee})
- Radial Cut - $R/R_{TPB} < 0.65$ (i.e. fiducial radius = 295 mm)
- PSD Cuts - $f_p > 0.681$, $\ell_r > 0.373$

The use of these cuts will be further discussed in Sec. 3.4 in relation to their effectiveness at removing various backgrounds.

Background	Raw Rate	12.5–25 keVee	Fiducial Volume	PSD Cut
Intrinsic ^{39}Ar	1×10^{10}/yr	4.2×10^8	1.2×10^8	< 1
αs in acrylic	24×10^3/yr	284 ± 4	0.02 ± 0.01	$< 10^{-4}$
αs on acrylic	10×10^3/yr	1.0 ± 0.5	$\ll 1$	$< 10^{-4}$
αs in TPB	1×10^3/yr	75 ± 3	$(7 \pm 3) \times 10^{-3}$	$< 10^{-4}$
αs on TPB	10×10^3/yr	3000	0.82 ± 0.09	0.14 ± 0.05
PMT (α,n)	42×10^3/yr	352	91.6 ± 1.1	3.8 ± 0.02
Steel (α,n)	1840/yr			< 0.2
External n	3650/yr			0.08 ± 0.01
PMT γs	20×10^9/yr	6×10^6	3×10^5	< 0.08
Steel γs	9×10^9/yr	2×10^6	1×10^5	< 0.02
γ-e Cherenkov	3×10^8/yr	3500	< 0.1	< 0.1

Table 3.2: A summary of various classes of MiniCLEAN backgrounds. Each row is a different background class. Each successive column from left to right shows the impact of adding additional cuts.

3.4 Backgrounds

MiniCLEAN has several classes of backgrounds that require characterization. This section provides an overview of each background class.

A summary of the different backgrounds, raw rates, expected number of events in the energy region of interest, expected number in the fiducal volume, and the number surviving after PSD cuts (defined in Sec. 3.3.2.2) are provided in Tab. 3.2. These values were taken from background estimation studies performed by members, including the author, of the MiniCLEAN collaboration [29].

Each of these background classes are discussed in detail in Sec. 3.4.1 to Sec. 3.4.4.

3.4.1 ^{39}Ar β Decay

As seen in Tab. 3.2, the primary source of electronic recoils in MiniCLEAN are β decays from the ^{39}Ar isotope. ^{39}Ar in the Earth's atmosphere is created from cosmic rays, primarily from neutron capture on ^{40}Ar followed by the release of 2 neutrons [114]. For argon harvested from the Earth's atmosphere, the trace amounts of ^{39}Ar leads to a background rate of 1 Bq/kg of natural argon. This amounts to 500 Hz of ^{39}Ar decays in MiniCLEAN's 500 kg natural argon target, or approximately 10^{10} decays per year. Applying energy and fiducial volume cuts reduces the raw rate of 10^{10} decays per year to 4.2×10^8/year and 1.2×10^8/year respectively. Applying PSD cuts following the energy and fiducial volume cuts is then expected to reduce the expected number of events in the ROI to less than 1.

A measurement of the specific activity of ^{39}Ar in natural argon is presented in [116]. The beta decay energy spectrum, shown in Fig. 3.12, has an endpoint of 565 keV.

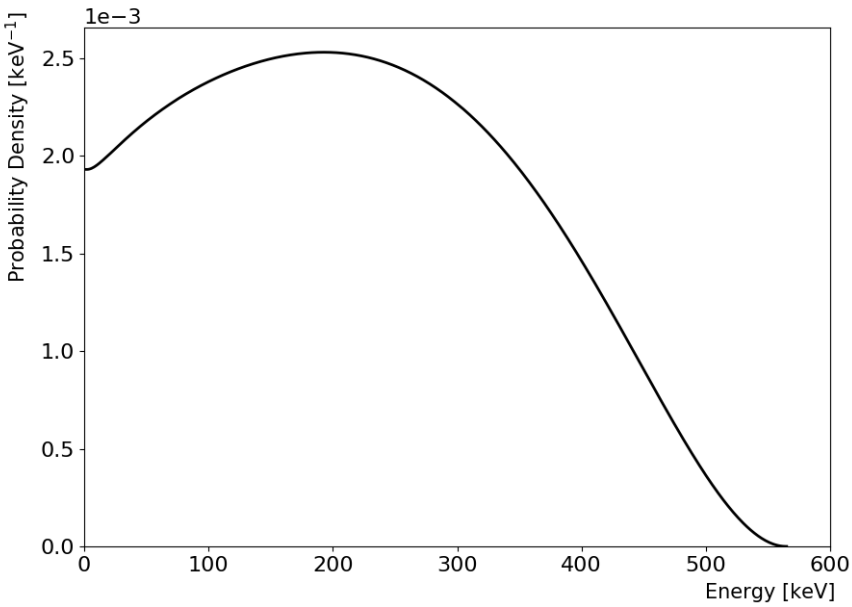

Figure 3.12: Simulated energy spectrum of ^{39}Ar beta decays. Spectrum from [116].

Quantifying the ability to identify and reject the intrinsic ^{39}Ar background is a key technical objective of MinCLEAN. Efforts to demonstrate the background rejection capabilities of PSD in LAr to the scale required in next-generation detectors is discussed in greater detail in Sec. 3.6.

3.4.2 α Decay Backgrounds

Rows 2 through 5 in Tab. 3.2 summarize the expected contribution from α decays to the overall background budget. α backgrounds observed in the active target volume come from ^{238}U and ^{232}Th decays in bulk acrylic or TPB, and daughter elements from radon decays which have been deposited on the TPB surface.

When α decays occur on the edge of the target volume, the decay products can deposit energy in the acrylic, TPB, or argon. Energy deposited in the acrylic is not observed, while the TPB and LAr scintillate at approximately 900 photons/MeV and 40,000 photons/MeV respectively. The energy scale of these α depositions is of order MeV so most events should be cut by the energy and fiducial volume cuts (as shown in Tab 3.2). However, due to the lower scintillation yield of TPB, the class of α events most likely to leak into the energy ROI are α scintillation in the TPB. Therefore this event class must be carefully considered.

It is known that the scintillation light time profile for α induced scintillation in TPB is different from argon, as shown in Fig. 3.13. The difference between the scintillation light profiles of TPB and argon motivates the development parameter, f_α, to help discriminate between nuclear recoils in argon (i.e. a WIMP signal) and α induced scintillation in TPB. f_α,

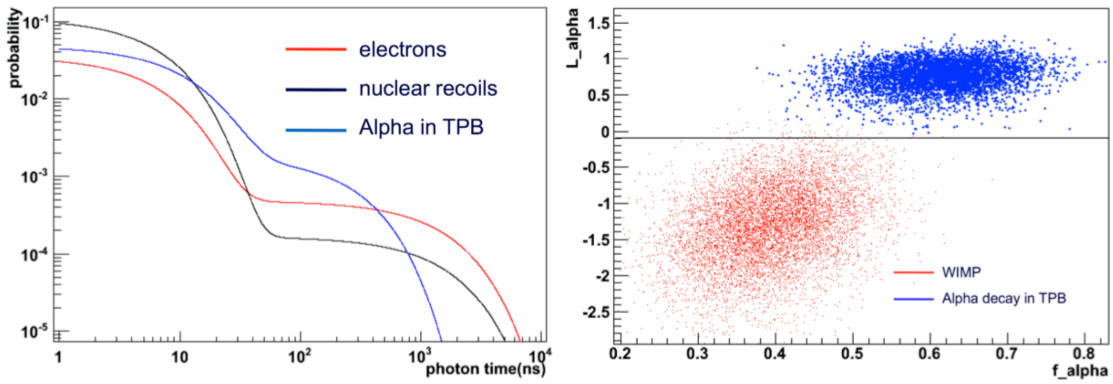

Figure 3.13: Left: Time profile for scintillation light for electronic and nuclear recoils in liquid argon and energy deposition from alphas in the TPB. Right: A 2D histogram of L_α and f_α for simulated WIMP recoils and α decays in TPB. Figures from [117].

very similar to f_p, is defined as the fraction of the total charge detected in the 13 ns to 775 ns window after an event trigger. As seen in Fig. 3.13, the time profile for α scintillation in TPB is significantly different in the intermediate region from those of electronic and nuclear recoils. This provides a powerful handle to classify these events for rejection. Enforcing a cut of $f_\alpha < 0.55$ and a requirement that no single PMT observes more than 10.5 % of the charge in an event has been shown to reduce the surface background event to 0.14 events/year in the WIMP energy ROI and fiducial volume for a rate of 1 α/m^2/day [29, 94].

A likelihood ratio, ℓ_α, which is similar in nature to the previously discussed ℓ_r, has also been developed to further enable event discrimination. A 2-d histogram of f_α and ℓ_α for simulated α events and WIMP is shown in the right-side of Fig. 3.13. Clearly, these discriminators provide a powerful method to reject α backgrounds.

3.4.3 Neutron Backgrounds

Neutrons are the most worrisome background class that MiniCLEAN must contend with. Elastically scattered neutrons in the target volume results in nuclear recoils which can mimic a WIMP signal. This background is mitigated by careful material selection and utilizing shielding (fiducialization and the acrylic light guides).

Due to the large water tank surrounding MiniCLEAN, the dominant source of neutrons in the IV is due to (α, n) reactions in the borosilicate PMT glass. Assays of the R5912-02 MOD borosilicate glass in [118] indicate ^{238}U and ^{232}Th are present in the glass at concentrations of 103 ppb and 170 ppb respectively. Using calculations from [119], MiniCLEAN expects a total yield of of 42,000 (α, n) neutrons per year from the PMT glass, as seen by the raw rate in Tab. 3.2. The energy spectrum of these neutrons is given by the orange line in Fig. 3.14. Even after energy, fiducial volume, and PSD cuts, neutrons from the (α, n) reactions in the

PMT glass are expected to be the dominant background in the region of interest at 3.8 ± 0.02 per year.

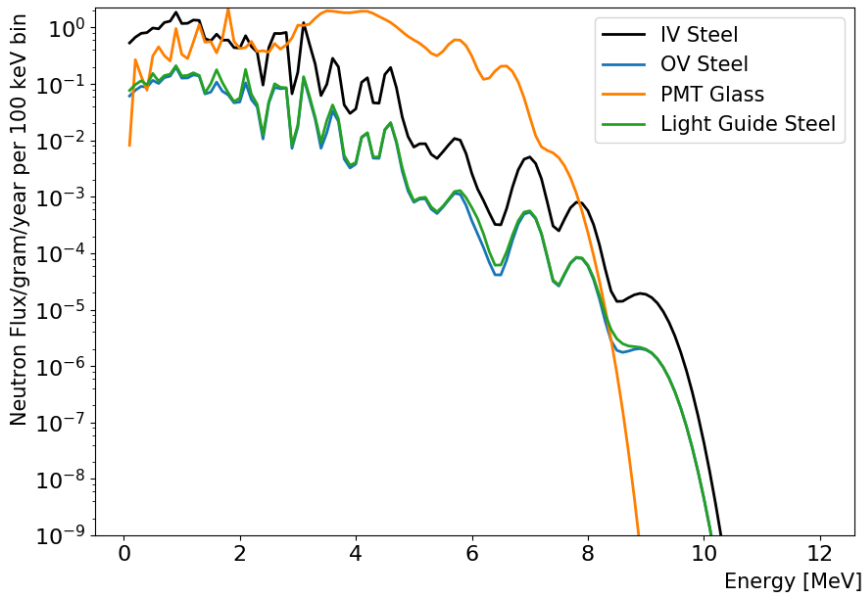

Figure 3.14: Energy spectrum of neutron background emitted from various elements in the IV. Energy spectra determined from calculations in [119].

For comparison, neutrons from residual ^{238}U and ^{232}Th decays in the IV and OV steel are expected to yield approximately 1840 (α, n) neutrons - significantly less than the PMT neutrons. The light guides also contain a small amount of steel which is considered to be negligible by mass compared to the IV and OV steel contributions. The energy spectra of the IV, OV, and light guide steel are also shown in Fig. 3.14.

External neutrons from sources outside of the water tank, including muons and lab rock, are expected to yield 3650 neutrons per year with 0.08 ± 0.01 events in the WIMP ROI. Additional information on the shield tank and active veto system has been provided in Sec. 3.2.1.

The neutrons from the PMTs shown in Tab. 3.2 are a dominant and irreducible background in the WIMP region of interest. The author has explored approaches to resolve multiple scatters inside of the target volume in order to reject a fraction of this background. At the time of this writing, no methods have been integrated into the analysis chain to improve neutron background rejection due to prioritization of other tasks. Rejecting neutrons by resolving multiple scatter is an area for improvement which could be addressed in the future and may become easier in a larger detector.

3.4.4 γ Ray Backgrounds

Similar to the neutron backgrounds previously discussed (Sec. 3.4.3), the dominant γ backgrounds are from the borosilicate PMT glass and stainless steel from the IV and OV. Assay results from [118] allow for the estimation of 29×10^9 γs per year with 70% coming from the PMTs (Tab. 3.2). The γs produce electronic recoils via Compton scattering in the LAr target volume. This gamma flux is attenuated by the external argon volume and acrylic plugs. The number of γs from these internal sources which pass the energy and fiducial cuts is much less than ^{39}Ar background component at 4×10^5. This remaining background can be easily cut using the previously discussed PSD techniques to levels on the order of 0.1 events/year.

The external γ flux has been measured at SNOLAB in [120] to be 10^{10} $\gamma/\mathrm{m}^2/\mathrm{yr}$ from ^{40}K, ^{238}U, and ^{232}Th, and (α, n) reactions in the rock. The water shield tank, with an attenuation length of roughly 10 cm for MeV scale γs, is an effective shield which drops this 10^{10} estimate to levels on the order of 10^3 before additional shielding of the IV and OV, LAr, and acrylic. The resulting survival rate for externally sourced gammas in the ROI is well below the previously discussed internal gammas and is thus considered negligible.

The γ-e component listed in Tab. 3.2 arises from the possibility that gammas may scatter an electron in the acrylic plugs or PMT glass. This may produce Cherenkov radiation which may be observed by the PMTs. However, the total yield of the Cherenkov radiation is often well below the analysis threshold and/or will likely reconstruct well outside of the fiducial volume, leading to rejection. It is estimated this will contribute < 0.1 counts per year to the region of interest.

3.5 Detector Calibration

This section provides an overview of detector calibration in MiniCLEAN. Sec. 3.5.1 and Sec. 3.5.2 covers the energy scale calibration of electronic and nuclear recoils using radioactive sources. Sec. 3.5.3 discusses methods used for PMT in situ calibration.

3.5.1 Electronic Recoils

As discussed in Sec. 3.3.2 and Sec. 3.4, understanding the response of electronic recoils is critical to MiniCLEAN's ability to reject the dominant backgrounds from ^{39}Ar and gammas.

Because ^{39}Ar is β background intrinsic to the argon target and is uniformly distributed, it can be used as an in situ calibration source. ^{39}Ar has a well defined energy spectrum, shown in Fig. 3.12, which allows MiniCLEAN to closely monitor the energy scale and position reconstruction of electronic recoils over time.

3.5.2 Nuclear Recoils

Calibration of detector response to nuclear recoils is performed using a tagged 74 MBq AmBe source manufactured by Eckert & Ziegler. The source produces approximately 5000 neutrons per second and is coupled to a pair of NaI scintillating crystals and ETL 9102 PMTs for tagging. The AmBe energy spectrum and a technical drawing of the source are shown in left and right images of Fig. 3.15 respectively.

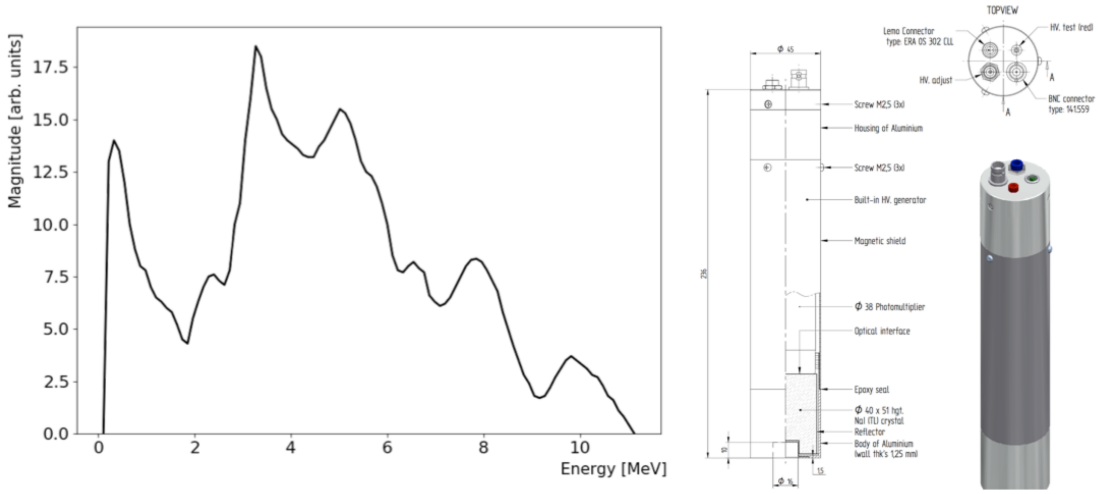

Figure 3.15: Left: Energy spectrum of neutrons emitted by the AmBe source. Right: A technical drawing of the AmBe neutron source. The pair of tagging PMTs and NaI scintillating crystal are visible. Drawing from [121].

The neutron source is deployed to a location near port OV-B in the water tank shield tank using a PVC pipe attached to the deck. This position allows the source to be located as close to the IV as possible with minimal water shielding between the IV and the source. The source is shared between MiniCLEAN and DEAP-3600 and may be used for periodic nuclear recoil response calibration.

3.5.3 PMT Calibration

Understanding the response of individual PMTs over time is crucial to event reconstruction. As discussed in Sec. 3.3.1, PMT calibration constants are also used in simulations for a full simulation of the data acquisition chain for detailed Monte Carlo and data comparison. PMT calibration constants are important inputs for event reconstruction in the analysis chain (Sec. 3.3.2.1). This section provides an overview of PMT calibration, which includes extraction of dark charge distribution and rates (Sec. 3.5.3.1), and SPE response of each PMT (Sec. 3.5.3.2). A complete description of the characterization of MiniCLEAN's R5912-02 MOD PMTs can be found in [29].

3.5.3.1 Dark Hit Charge Distribution

It is known that thermionic emission of individual electrons inside of the PMT photocathode and dynode structure produces pulses known as "dark hits" [29]. To study the dark hit rate and dark charge distribution, an external pulser is used to manually trigger the DAQ at a rate of several Hz in order to sample periods when the detector has not been triggered by a physics event.

The "DarkHitCal" processor in the analysis chain (described in Sec. 3.3.2.1) selects events which were triggered by the pulser. The observed PMT pulses are assumed to be dominantly dark hits distributed throughout the event window and are used to evaluate the dark charge response and rate. MiniCLEAN observes a dark rate of approximately 500 Hz and a characteristic dark charge distribution shown in left image in Fig. 3.16.

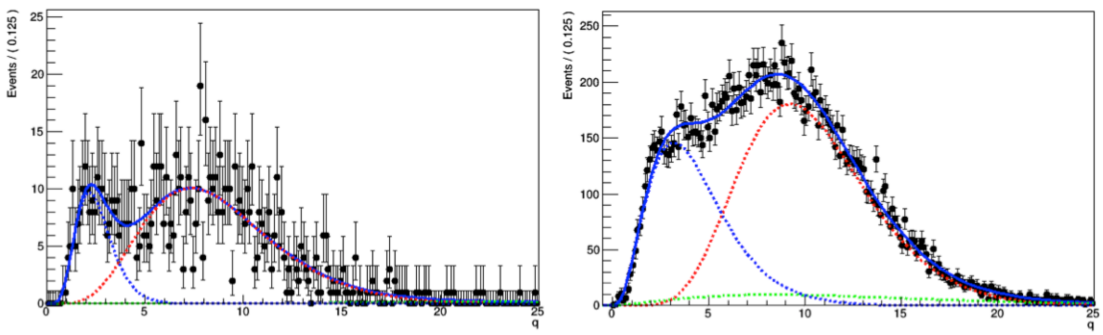

Figure 3.16: Left: Example of extracted dark hit distribution for PMT 25, but characteristic for most PMTs. Right: Example of an uncorrected SPE distribution for PMT 25. Both distributions are fit to a weighted sum of 3 gamma distributions (discussed in Sec. 3.5.3.2) where the solid line is the total fit and the dashed lines are the components contributions.

3.5.3.2 SPE Charge Distribution

The single photoelectron (SPE) response of PMTs is determined using the "SPECalib" processor. This processor utilizes late light in an event window from electronic recoil events (such as ^{39}Ar) to populate histograms for fitting. Late light is used to ensure the that the probability of photon pileup is low (photon pileup is likely early in the event window due to the fast singlet state).

The dark hit and SPE histograms populated by their respective processors are fit to a functional form which is the weighted sum of the three gamma distributions. While a sum of two gamma distributions was emperically established by Caldwell [29] to be the best fit for the R5912-02 MOD SPE distribution, a three gamma function was adopted and implemented by the author as it produced a better fit when considering the entire population of PMT responses for all of MiniCLEAN's data run configurations. An example of the fitted SPE distribution is shown in the right-side plot in Fig. 3.16 for a single PMT (PMT 25).

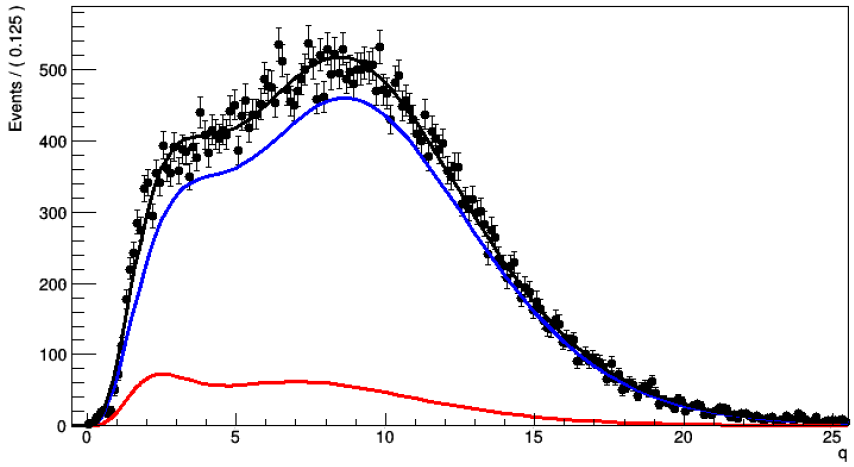

Figure 3.17: An example of the dark-hit corrected SPE distribution (blue) for PMT 25. Knowing the dark-hit rate and charge distribution (left plot in Fig. 3.16) allows for the extraction of the dark-hit corrected SPE distribution.

Because the SPE distribution shown on the right-side in Fig. 3.16 are populated from late light in a physics event, they contain real photons, but also some contamination from dark hits. Knowing the dark hit rate and dark charge distribution (discussed in Sec. 3.5.3.1), a simultaneous fit of the dark-hit corrected SPE distribution can be performed to disentangle the dark hit distribution contribution from the true SPE distribution. An example of this is shown in Fig. 3.17 where the red line is the dark hit contribution and the blue is the true, dark-hit corrected SPE distribution. The PMT calibration can be performed for each data run to track and appropriately model the SPE and dark hit distributions over time.

The shape parameters for the dark-hit and corrected SPE distributions fits are written to a file and used in a second pass reconstruction of the data to allow for accurate energy and position reconstruction. The shape parameters from the fits are also used in simulations of individual runs for detailed data to simulation comparison.

3.6 ^{39}Ar Spike

As described in detail in [29], a primary technical objective of MiniCLEAN is to evaluate at what target mass a single-phase LAr experiment becomes ^{39}Ar background limited for an energy threshold required for a sensitive WIMP search. As the scale of a next-generation, monolithic scale detector becomes larger, potential signal leakage into the region of interest and event pileup would become a significant issue.

The pileup effect is shown in Fig. 3.18 where the blue line shows a lower limit for the effective mass as a function of the true mass for a target which uses natural argon. As the actual mass of the LAr target is increased, event pile-up (and resulting dead-time) from the 1

Bq/kg ^{39}Ar decays in the natural argon would limit the attainable effective mass available for a WIMP search. The red line shows the impact of mass scaling for a factor of 100 reduction of ^{39}Ar in the natural argon, while the black dashed line shows the expected linear scaling if one assumes no loss from ^{39}Ar pile-up.

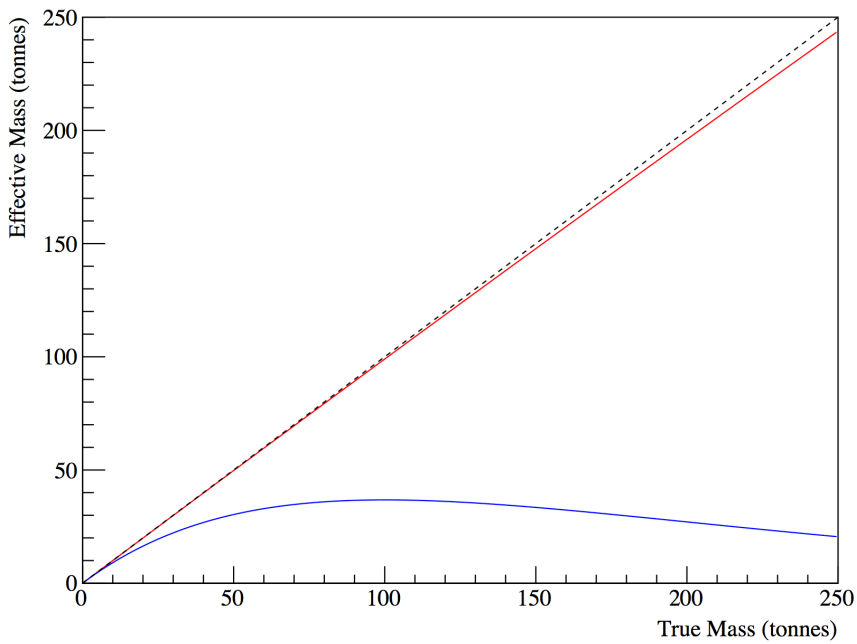

Figure 3.18: Projections of mass scaling to monolithic scale LAr detectors for natural argon (blue), argon where the ^{39}Ar content has been reduced by a factor of 100 (red), and the upper limit where pileup probability is zero (black dashed). As the scale of a detector increases, the high event rate from ^{39}Ar decays would reduce the effective mass for WIMP searches due to event pileup and increased detector deadtime. Reducing the concentration of ^{39}Ar can help alleviate this issue. Plot from [29].

The MiniCLEAN collaboration plans to spike the detector with levels of ^{39}Ar expected to be present in a multi-tonne scale, natural-argon detector in order to test the limits of PSD at the level required for next-generation experiments. This can be done with a filled detector by mixing a concentrated sample of ^{39}Ar with the target volume. The ^{39}Ar sample has been produced at Los Alamos National Laboratory (LANL) by irradiating a potassium target with neutrons above 2 MeV which leads to the creation of ^{39}Ar through the ^{39}K(n,p)^{39}Ar reaction.

With MiniCLEAN having a 500 kg active mass (0.5 tonnes), to achieve the level of a 100 tonne detector, MiniCLEAN would need to spike the ^{39}Ar by at least a factor of 200. A larger spike would actually need to be high to achieve the background in the fiducuial volume because a larger detector would sacrifice a small fraction of its volume due to efficient self-shielding in a large detector. With a modest upgrade to the DAQ electronics to allow for

higher trigger rates, the ^{39}Ar spike will attempt to demonstrate the PSD achievable in a detector which is of several-tens of tonnes of natural argon.

Chapter 4

Construction and Commissioning of MiniCLEAN

4.1 Overview

This section covers the construction and commissioning of the MiniCLEAN detector that was described in Chap. 3.

With the exception of the IV assembly (Sec. 4.2.1), the author played a major or leading role in each of the topics discussed in this chapter.

Sec. 4.2 covers the construction of the IV and OV, the installation of the IV into the OV, and the buildup of hardware to the deck. Sec. 4.3 covers the details of the purification system. Sec. 4.4 and Sec. 4.5 cover the data acquisition racks and the monitoring and control systems respectively. Lastly, Sec. 4.6 discusses the relevant procedures and documentation developed during the detector commissioning.

4.2 Construction and Installation

This section covers the construction and installation of the MiniCLEAN detector. Detector construction spanned from Oct. 2012 to June 2015. Sec. 4.2.1 and Sec. 4.2.2 cover the construction of the IV and OV respectively. Sec. 4.2.3 discusses the installation of the IV into the OV. Lastly, Sec. 4.2.4 covers the remaining buildup of various support systems and hardware upto and on the deck.

4.2.1 IV Construction

MiniCLEAN's IV was assembled and tested in SNOLAB's cryopit prior to installation in the OV. The assembly took place in a 12 ft^3 temporary soft-walled clean room, shown in the top-left of Fig. 4.1. The clean room was outfitted with sensors to monitor radon levels and particulate counts, and filters to reduce particle counts. The clean room was kept over-

pressured relative to lab pressure with compressed air from surface which contained a factor of 4 to 5 less radon than ambient lab air. Radon levels were monitored continuously during IV light-guide installation. [29]

Although the IV sphere was electropolished after initial machining, the 2760 threaded holes on the IV sphere (seen in top right of Fig 4.1) had to be thoroughly cleaned. This was because these bolt holes were in the clean volume due to the design choice to use inverted Conflat (CF) seals between the spools and the IV sphere to meet space requirements. The spools, tophat assemblies, and bolts were ultrasonically cleaned prior to installation. The top-right image in Fig. 4.1 shows a small number of spools installed on the IV sphere.

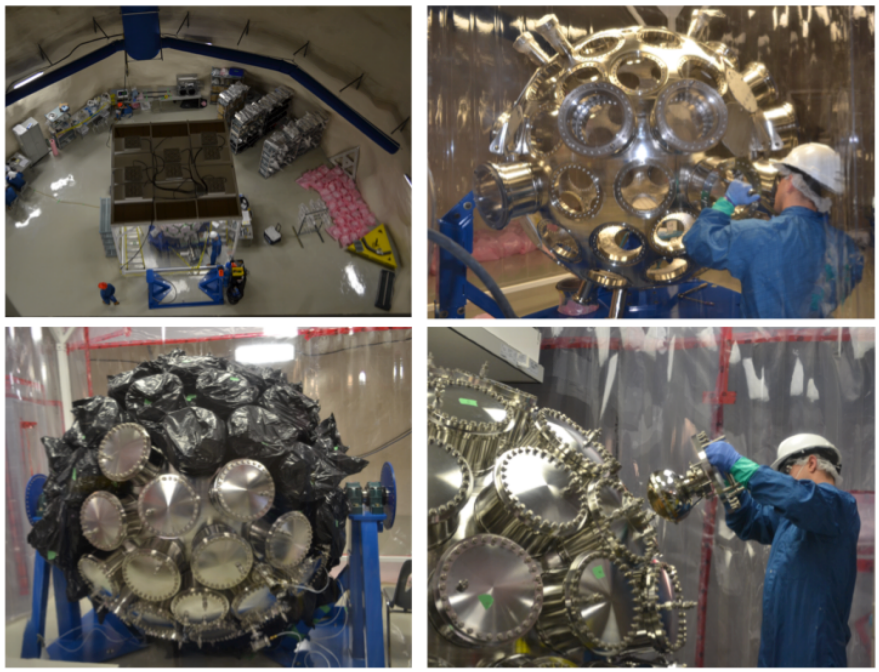

Figure 4.1: Several stages of the IV construction. Top-left: A top view of the Cryopit at SNOLAB. IV Assembly took place in a over-pressure, radon-monitored, tent. Top-right: Installation of several spools onto IV sphere. Bottom-left: Partially constructed IV. Incomplete tophat assemblies were covered with plastic bags to minimize radon exposure. Bottom-right: Installation of a PMT and tophat assembly. All images taken from [29].

As seen in the bottom-left image in Fig. 4.1, tophat ports which had not yet been completed were bagged and the IV was kept 1 psi over pressure with boil-off from a liquid nitrogen dewar. Dark plastic covered ports without tophats to protect the TPB inside from performance degradation from ambient UV light [122]. As an additional precaution, UV filters were placed on the lights inside of the clean room. The bottom-right photo in Fig. 4.1 shows the installation of a PMT and tophat assembly.

The left image in Fig. 4.2 shows a partial tessellation of the light guide assemblies inside of the IV. Acrylic blocks with a TPB coated surface (not shown) face inward create the outer

boundary of the cryogenic scintillator target volume.

Figure 4.2: Left: Partially complete tessellation of light guides inside of the IV. Right: A fully constructed IV prior to the connection of PMT signal cables. Images from [29].

The right image in Fig. 4.2 shows the fully constructed IV before connecting signal and instrumentation cables, the IV LAr level meter, and fill line tubing.

After the construction of the inner vessel was complete, PMT and sensor cables were connected to the IV and data runs were taken test the data acquisition, PMTs, and LED calibration system. All data sets were taken at room temperature in argon gas or vacuum.

4.2.2 OV Construction

Following the transportation of the OV into SNOLAB, the bottom portion of the OV was installed on the OV stand inside of the MiniCLEAN water tank. MLI super-insulation was installed onto the inner surface of the OV volume to reduce radiative heat transfer when under vacuum. The MLI super-insulation on the inner surface of the bottom portion of the OV is shown in the left image in Fig. 4.3. Also visible are the five cable horns which contain vacuum feedthroughs for PMT and instrumentation cables and a water-tight hose connection for cable routeing through the water tank to deck. The center photo in Fig. 4.3 looks up at the bottom of the OV from the floor of the water shield tank. The OV, OV stand, seismic isolation mounts, and air filled cable routing hoses are visible.

The right image in Fig. 4.3 shows an external view of the completed water shield tank. The black electrical cables used to produce the magnetic field for the magnetic compensation system (Sec. 3.2.2).

4.2.3 IV Installation

Once the construction and testing of IV was completed and the lower half of the OV was installed in the water tank, the IV was installed inside of the OV. The moving, lifting and

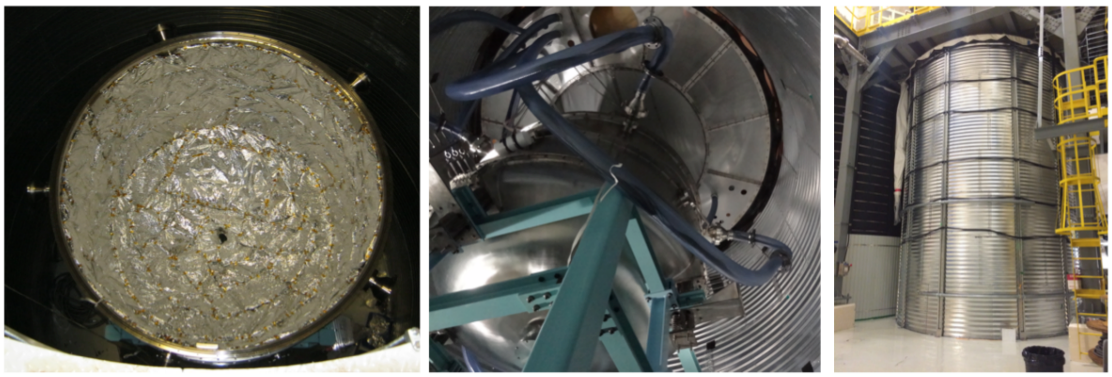

Figure 4.3: Left: Looking down on the empty lower hemisphere of the OV installed in the water tank. MLI insulation was installed on the inner surface of the OV for thermal insulation. Center: Looking up at the OV from the bottom of the water tank. The OV sits on seismic isolation springs attached to a stand (blue painted structure). Air filled hoses used to run PMT and sensor cables to deck are also visible. Right: An exterior photo of the completed water shield tank below the deck housing the OV. The black electrical cables on the side of the water tank are for the magnetic compensation system.

installation of the IV into the OV occurred on November 14, 2014. The left image in Fig. 4.4 shows the moving of the IV from the Cryopit into the Cubehall. The center image in Fig. 4.4 shows the lifting of the IV by a crane in the Cubehall for placement into the OV. The right image in Fig. 4.4 shows the IV installed inside the lower half of the OV.

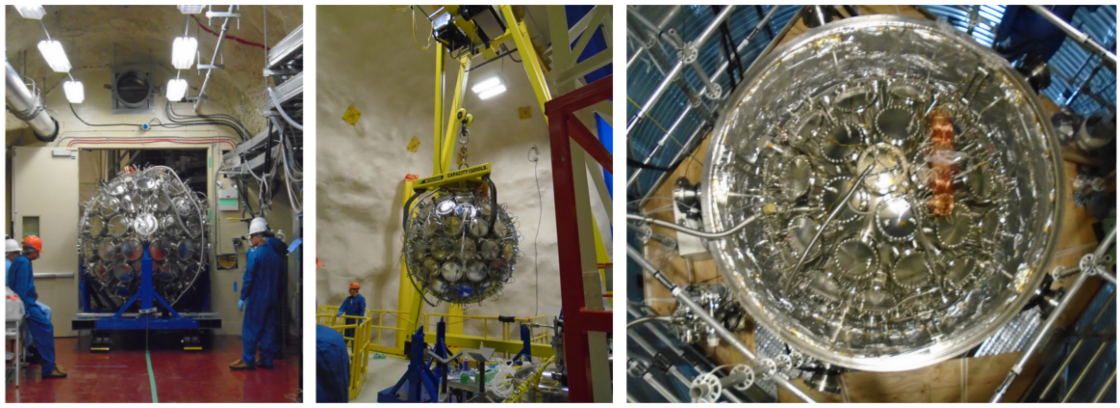

Figure 4.4: Left: Moving IV from the Cryopit to the Cubehall for final installation into OV. Center: Installing the IV into the OV using a crane. Right: IV installed in OV after crane lift. Images from [29].

Following the installation, vacuum and LED data confirmed that all of the PMTs were in working condition.

4.2.4 Deck Layout and Buildup

After the installation of the IV, the top hemisphere of the OV was installed and the buildup of the vertical piping and fill line connections to the overhead deck began. The vertical piping and fill lines are shown in all images of Fig. 4.5.

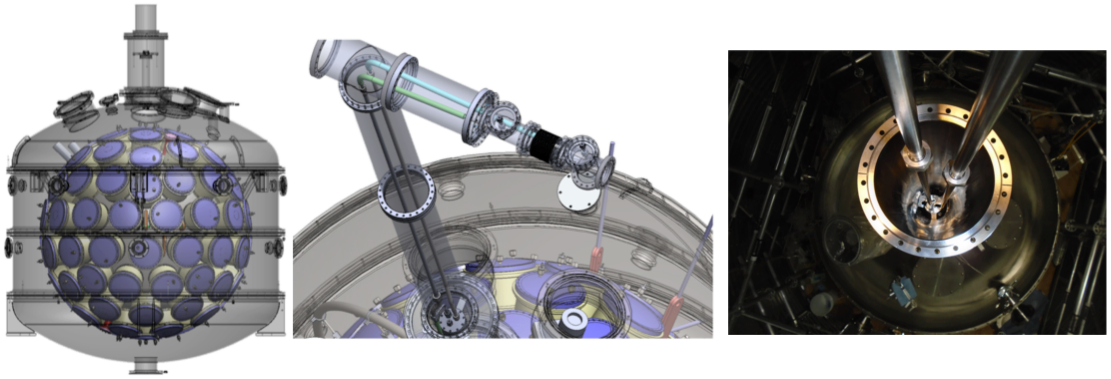

Figure 4.5: Left: A CAD model showing the IV installed in the OV. Also visible is a portion of the vertical piping assembly leading to the deck. Center: An angled top down view of the top of the OV showing the vertical OV piping with IV fill lines running up to the deck. Right: Looking down vertical piping connecting the OV to the deck during buildup. Two IV fill lines are visible. Images from [29].

The IV was kept over-pressure relative to the the lab with high-purity argon gas during piping buildup. All stainless steel tubing used for the fill lines were ultrasonically cleaned and baked prior to installation. The vertical fill lines and OV piping were incrementally constructed upward, starting at the top OV up to the deck. High-sensitivity helium leak checking was performed to verify seal integrity.

As seen in Fig. 4.5 and Fig. 4.6, the vertical piping was built up to the deck level. At the deck level, a "T" connection was coupled to horizontal bellows. The bellows, visible in left and center images of Fig. 4.6, decouple the motion of the detector from the deck and allow for vertical and horizontal displacements during a seismic event and various buoyancy conditions. Rollers on the deck piping support structure provide a rotational degree of freedom (center image in Fig. 4.6). The right side of the "T" connection (left image in Fig. 4.6) leads to an OV rupture disk and emergency vent line in the event that the OV vacuum becomes compromised from uncontrolled argon boil-off from the IV. The piping which extends to the emergency vent line connection is shown in the right image of Fig. 4.6. The left side of the "T" connection leads to the OV pumping station and IV fill line vacuum feed through.

The design layout of items on the MiniCLEAN deck are shown in Fig. 4.7. The gas processing, OV pumping station, calibration deployment systems, compressors, and other support/control hardware are located around the OV piping. The data acquisition, remote

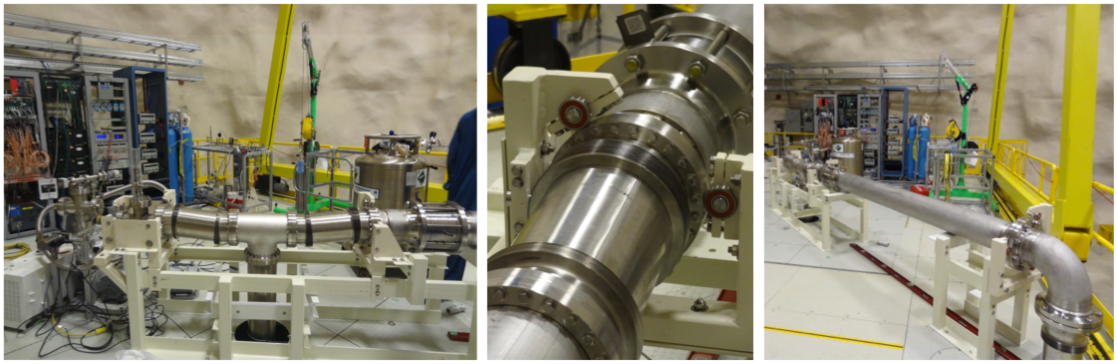

Figure 4.6: Left: Vertical piping coming up through the deck connecting to "T" flange and bellows at the deck. OV piping leading to the right connects to OV rupture disk and emergency vent line. OV piping leading to the left connects to OV pumping station and IV fill line feed through. Center: OV piping assembly sits on rollers to allow for rotation relative to deck. OV piping bellows decouple vertical and perpendicular OV displacement from deck. Right: OV piping connecting OV rupture disk to emergency vent line.

control hardware and other various other power supplies are located on the DAQ racks. An operator workstation and storage space is also present on the deck.

Fig. 4.8 shows a picture of the finished MiniCLEAN deck. The only major differences between the original layout design (Fig. 4.7) are both LAr dewars are located on the purification system side of the OV piping, the addition of the LAr condenser, and the steel protection structure encasing the OV piping.

4.3 Purification System

An annotated side-view photo of the gas purification system in its completed state is shown in Fig. 4.9. Major elements, such as the SAES Getter and charcoal trap (discussed in Sec. 3.1.2), are shown.

The purification system was assembled separately from the buildup of the OV piping discussed in Sec. 4.2.4. All valves and tubing are stainless steel and supplied from Swagelok. The purification system was assembled in sections and repeatedly helium leak checked as sections were tied together. Once the purification system was fully assembled, it was baked and purged. A residual gas analyzer (RGA) was used to check the purity of argon gas purified using the fully assembled system at the level of several ppm resolution of the RGA. The purification system was then coupled to the IV at the inlet and outlet, completing its installation.

A cartoon representation of the top-view of the purification system is shown in Fig. 4.10. Sets of manual and remotely controllable pneumatic valves are used throughout the system to control gas flow paths. Passive rupture disks and pressure control valves are in various

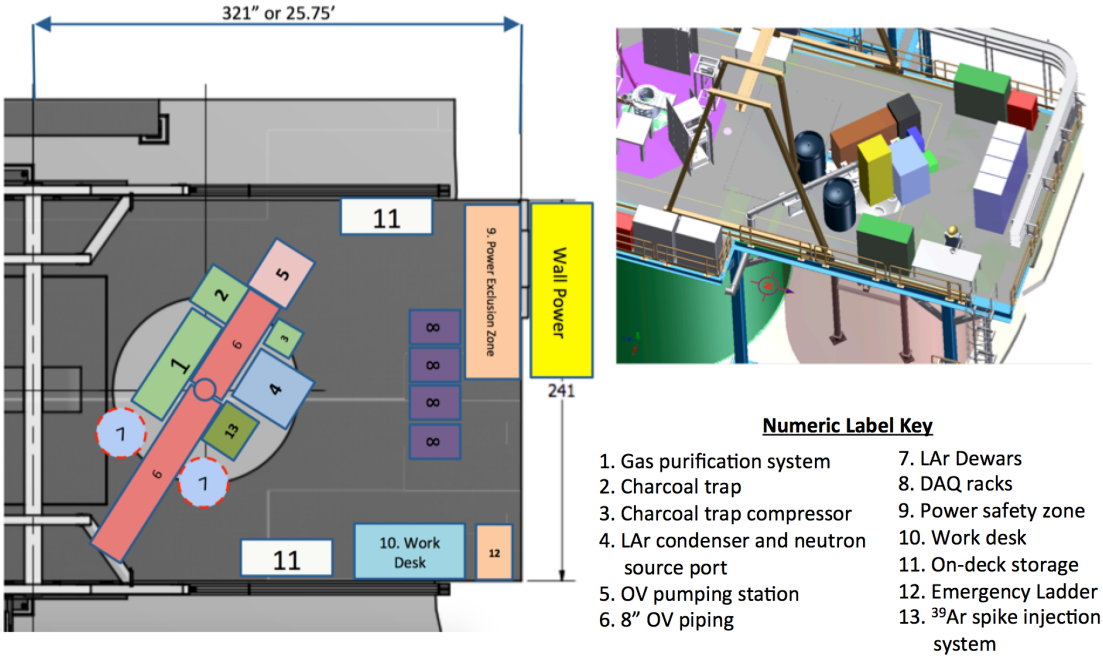

Figure 4.7: Left: An annotated cartoon of the MiniCLEAN deck layout in the Cubehall. Bottom-right: Labeling key for annotated cartoon on the left. Top-right: CAD representation of MiniCLEAN deck.

locations to provide emergency pressure relief. Also shown are a mass flow controller, pressure controller, and the location of several pressure transducers. The mass flow controller controls the flow rate of argon gas from boil-off of 99.999% pure commercial grade argon (supplied by Air Liquide) from a LAr dewar in to the getter/charcoal trap purification subsystems. The pressure controller monitors and controls the pressure in the IV on the outlet IV fill line. The downstream side of the pressure controller is held close to vacuum with the purification system outlet pump shown in Fig. 4.9.

Fig. 4.11 shows an example flow path of gas through the purification system for the common state of flowing into the IV from LAr dewar 1. Open valves are shown with a dashed border (green) while closed valves are shown with a solid border (red). The arrows (blue) indicate the direction of flowing argon gas.

The argon gas starts at the inlet from a dewar (dewar 1 in this example) and flows through the mass flow controller to the getter. The flow rate of the mass flow controller may be controlled remotely. The getter (Sec. 3.1.2) reduces impurity levels in the argon gas to approximately 1 ppb [123]. Because the getter does not also remove residual radon, the gas then flows to a cooled activated charcoal trap (Sec. 3.1.2) which reduces radon to accepable levels [103, 104]. The gas then flows through the LAr condenser (further discussed in Sec. 4.3.1), which is downstream of the outlet labeled "IV in".

If the pressure in the IV is higher than the remotely controllable pressure set point on

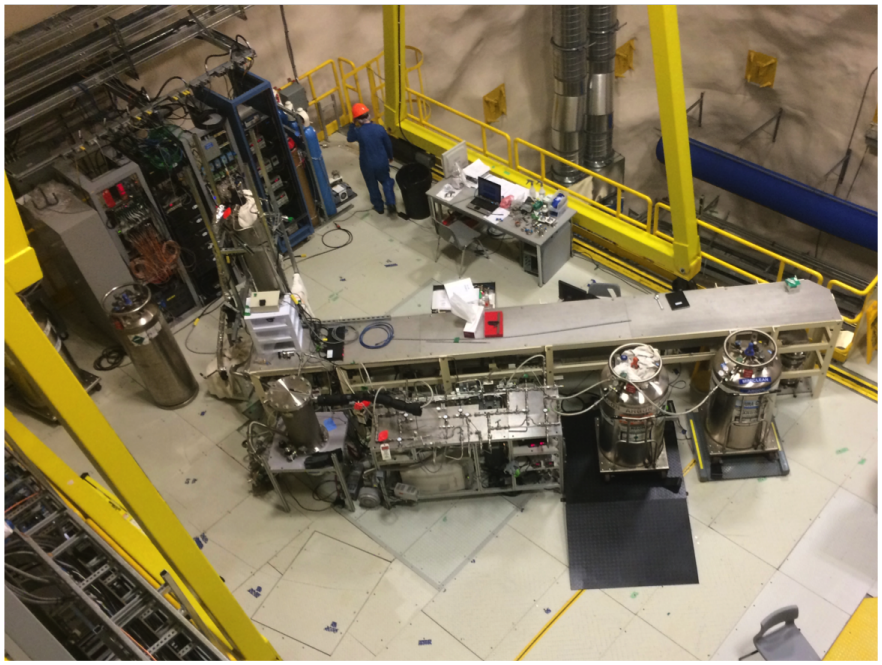

Figure 4.8: A photo of the completed MiniCLEAN deck from the top of the Cubehall.

the pressure controller, an internal valve in the pressure controller throttles the flow to the downstream vacuum pump. If the IV pressure is at or below the pressure controller set point, the pressure controller will be closed and there will be no flow through the pressure controller to the pump.

4.3.1 Liquid Argon Condenser

A liquid argon condenser assembly was re-purposed from the DEAP-1 experiment for use on MiniCLEAN to improve cooling power and liquid argon filling efficiency. The condenser was added between the "IV In" node, labeled in Fig. 4.10, and the IV fill line vacuum feed-through located on the OV piping (left image in Fig. 4.6).

Fig. 4.12 shows a photo and technical drawing of the liquid argon condenser. The condenser is a cylindrical assembly which contains an outer vessel and an inner vessel. The condenser outer vessel (COV) is used as a cryostat to thermally insulate the condenser inner vessel (CIV). The vacuum jacket between the CIV and the COV is maintained at pressures less than 10^{-5} Torr using a turbomolecular pump.

The CIV contains a pressurized volume of liquid nitrogen (LN_2). The pressure is set using a gas back-pressure regulator located on the flanges at the top. The back-pressure regulator is a passive device which controls the upstream pressure at the regulator and vents to atmosphere. The level of the liquid nitrogen in the CIV is measured using a capacitive cryogenic liquid level sensor. The level meter readout box also contains a LN_2 level controller

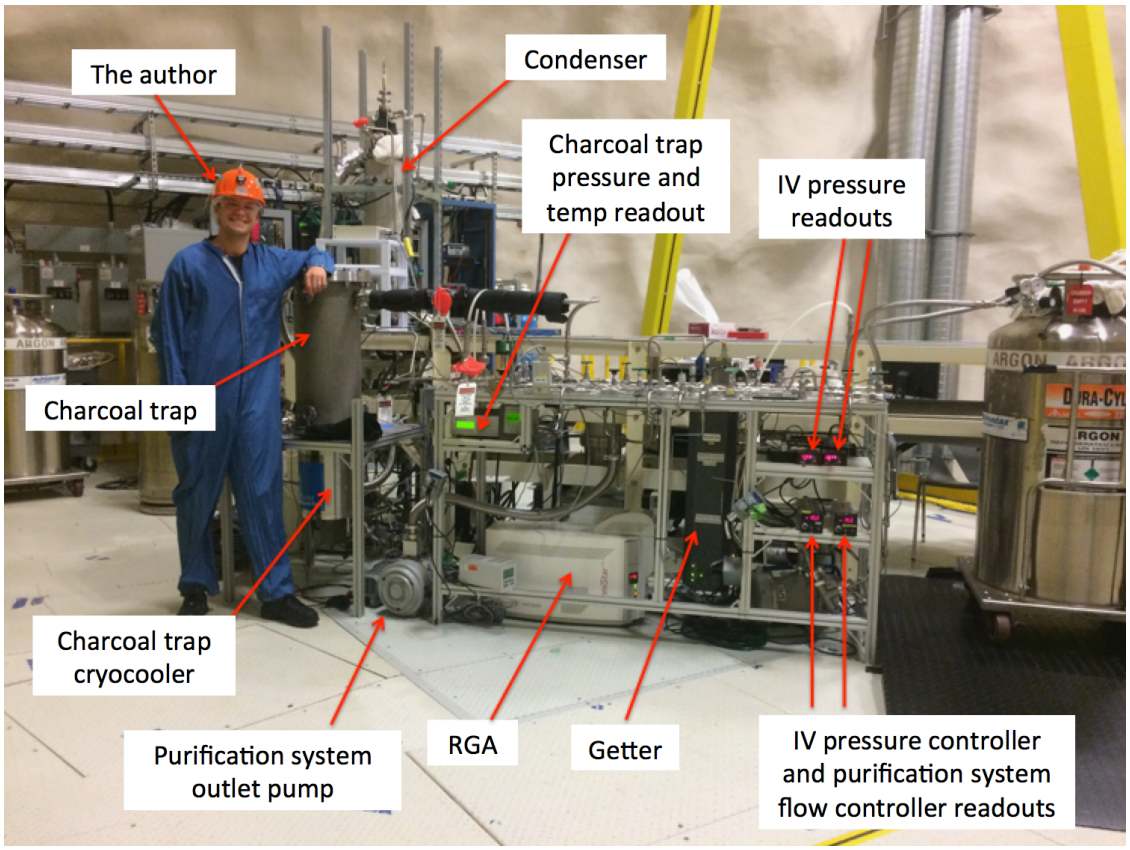

Figure 4.9: An annotated side-view photo of the completed purification system.

configured to toggle a solenoid valve connected to a LN_2 dewar to open/close when low/high LN_2 level controller setpoints are crossed to allow a near-constant LN_2 level to be maintained.

An IV fill line feed-through located at the top of the condenser allows high-purity gaseous argon from the purification system to be connected to a tube running through the pressurized LN_2 space in the CIV. The tube containing the flowing high-purity argon gas is coupled to a copper coil which runs through the liquid nitrogen volume. The gaseous argon is then liquified as it passes through the submerged copper tube. The LAr then flows out of the bottom of the CIV (via a vacuum feed-through), and out of the COV (via a vacuum feed-through), and into the IV fill lines leading to the detector.

The liquid nitrogen volume is pressurized relative to atmosphere to adjust the boiling point of the LN_2 to a pressure optimal for liquefying argon at the usual operating pressures of MiniCLEAN. Fig. 4.13 shows the boiling point temperature of liquid argon and nitrogen as a function of pressure. The data for these plots was taken from the National Institute of Standards and Technology (NIST) Chemistry WebBook, SRD 69 [124].

The intersection of the two purple dashed lines shows the 91 K liquefaction temperature of argon at typical 1500 mbar operating pressure of MiniCLEAN. It should also be noted that

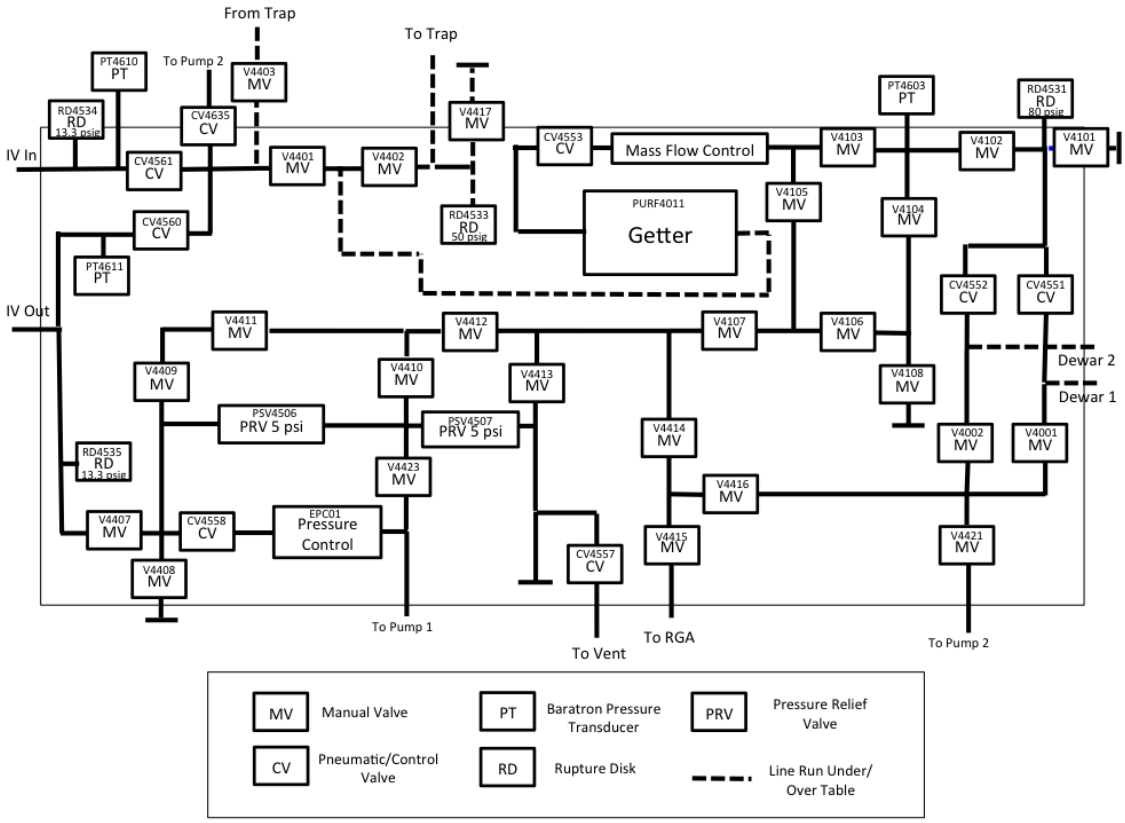

Figure 4.10: A cartoon representation of the top-view of the purification system. A key for the abbreviated labeling of common elements is provided at the bottom.

no liquid state for argon exists for temperatures less than approximately 84 K or pressures less than approximately 700 mbar. Therefore, in order to use LN_2 to liquefy argon in this manner, the boiling point of the LN_2 must be greater than the 84 K lower limit (preferably with some safety margin) and less than the 91 K argon liquefaction temperature for an IV pressure of 1500 mbar. This is achieved by pressurizing the LN_2 to pressures greater than approximately 2100 mbar. A CIV operating pressure of 2350 to 3000 mbar, indicated by the green shaded region, was chosen to provide a margin of safety above the 2100 mbar limit and be less than 3100 mbar for regulatory reasons.

4.4 DAQ Racks

As seen in Fig. 4.8, the DAQ racks are near the edge of the MiniCLEAN deck. Fig. 4.14 provides an annotated photo of the DAQ racks. The DAQ racks contain the detector data acquisition system, the local network switch, remote monitoring and control computer, instrumentation readout and control hardware, and various power supplies for systems such

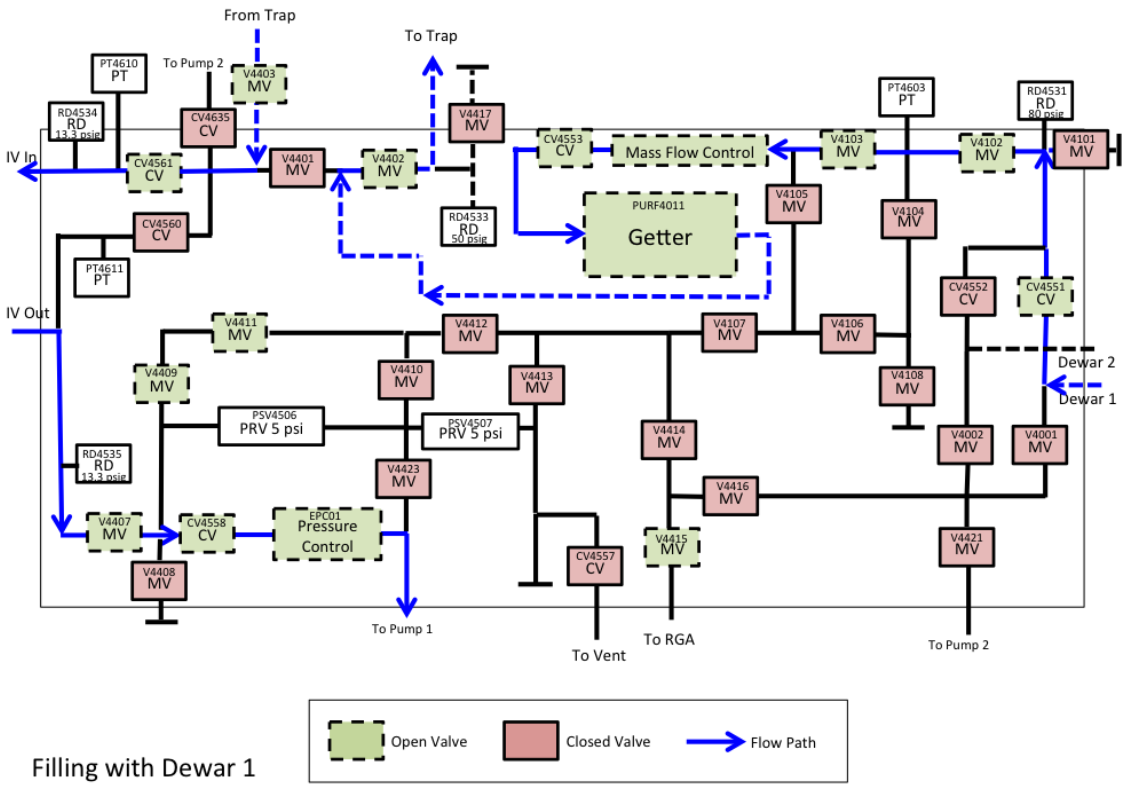

Figure 4.11: A cartoon representation of the flow path in the gas purification system for a common state of flowing into the IV from a LAr dewar 1.

as the magnetic compensation coils.

A description of the detector data acquisition system and magnetic compensation coils is provided in Sec. 3.2 and Sec. 3.2.2 respectively. Additional details of remote monitoring and control subsystems are provided in Sec. 4.5.

4.5 Control and Monitoring Systems

4.5.1 Overview

States and time series data from nearly all of MiniCLEAN's remotely readable and writable instruments are tracked and stored in a central monitoring and control system. Examples of remotely readable/writable instruments include, but are not limited to: purification system pressures and flow rates, SAES getter state and health status, OV vacuum pressure, turbo pump status, IV temperatures, IV cryocooler compressor state, and cooling water temperatures.

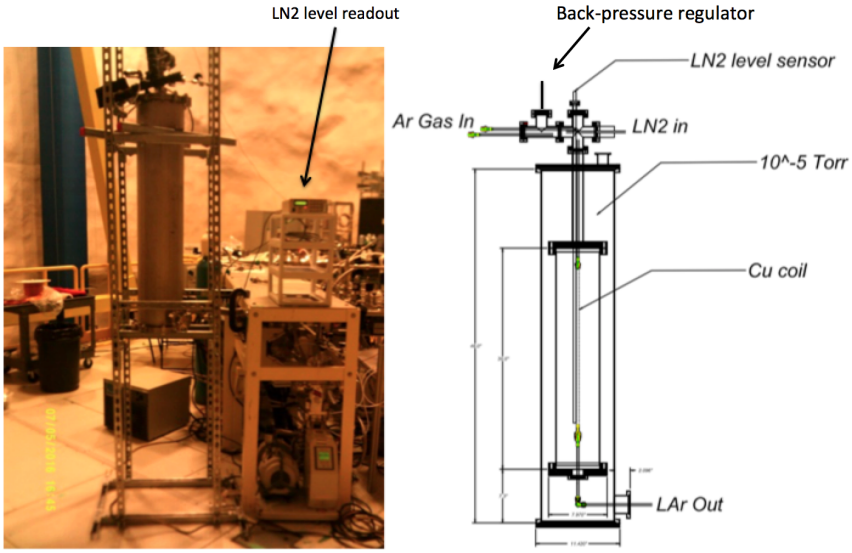

Figure 4.12: Left: A photo of the LAr condenser and LN_2 level meter readout on deck. Right: An annotated technical drawing of the condenser.

A diagrammatic representation of MiniCLEAN's remote monitoring and control system is shown in Fig. 4.15. A single computer, cleanpc06, acts as the command and control center for remote monitoring and control.

The central component of the system is a MySQL database hosted on cleanpc06. The database stores state information and time series command and read values from detector instruments. A PHP code base creates web pages, referred to as the Slow Controls, which are relayed to users over the Internet using an Apache web server hosted on cleanpc06. Additional details of the Slow Controls are covered in Sec. 4.5.3.

Each instrument being read out/commanded has an independent C or python process running on cleanpc06. This is represented by the green box with the dashed border inside of cleanpc06 in Fig. 4.15. Each process independently communicates with the MySQL database to write/read values. Likewise, the independent processes also communicate with their respective instruments over the local network, indicated by the thick single black arrow between the local network switch and cleanpc06 in Fig. 4.15 (only one arrow is used because cleanpc06 is connected to the local network switch by one Ethernet cable). Each independent process knows the IP address and port of its respective instrument and communicates via the various protocols defined by its back end code over the local network.

Instruments with Ethernet I/O communication ports, indicated by the purple box, are connected directly to the local network switch. Instruments with only serial I/O communication ports, represented by the red box, are connected to serial to Ethernet converters to allow for an Ethernet connection to the local network switch. The serial to Ethernet converters are located on the back of the DAQ racks and are highlighted in the right-side

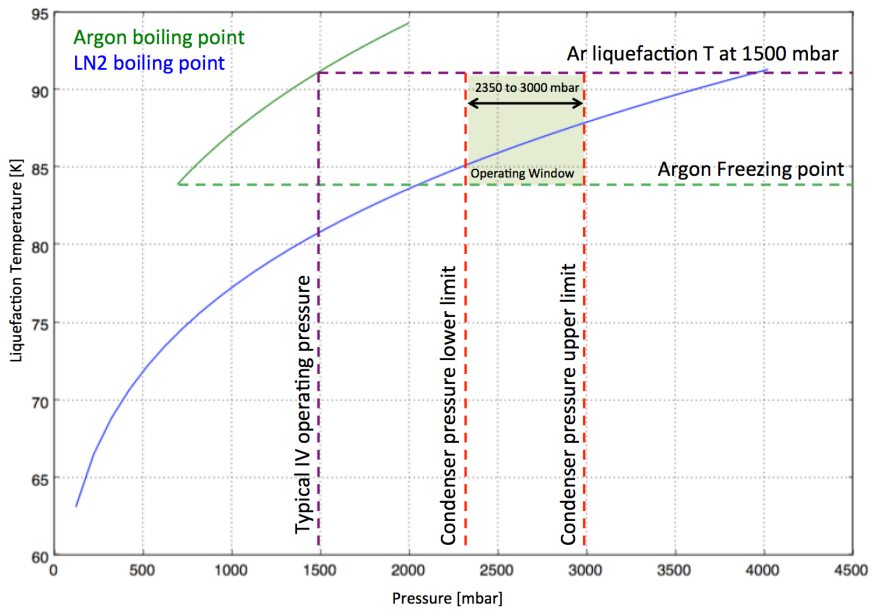

Figure 4.13: A plot liquid argon and liquid nitrogen boiling points as a function of pressure. Dashed lines highlight indicate important operating points. The green shaded region indicates the operating LN_2 pressure range for the condenser. Data used in plots taken from [124].

image of Fig. 4.16.

The "Slow Controls watchdog" is a persistent program that knows which of the independent back end processes should be running (via the MySQL database) and monitors their states. If a C or python process crashes, it is automatically restarted by the watchdog. The watchdog also provides a convenient way to start and stop back end processes by changing states in the MySQL database using the Slow Controls web interface.

An additional class of independent python processes also run on cleanpc06 and are indicated by the orange box in Fig. 4.15. These are the interlocks, alarms, and set controllers and are described in detail in Sec. 4.5.4. In summary, interlocks monitor critical systems and provide pre-programmed automatic responses to certain fault conditions, alarms alert users to potential issues (sensors out of recommended range), and set controllers enforce the standardization of interlocks and alarm sets.

4.5.2 Local Networking Hardware

As discussed in Sec. 4.5, Ethernet cables from instruments and cleanpc06 are connected to a local network switch to allow for communication. However, not all the of the hardware monitored or controlled have Ethernet I/O connections. Serial to Ethernet converters are used to convert several RS-232 serial connections to Ethernet. These are installed on the

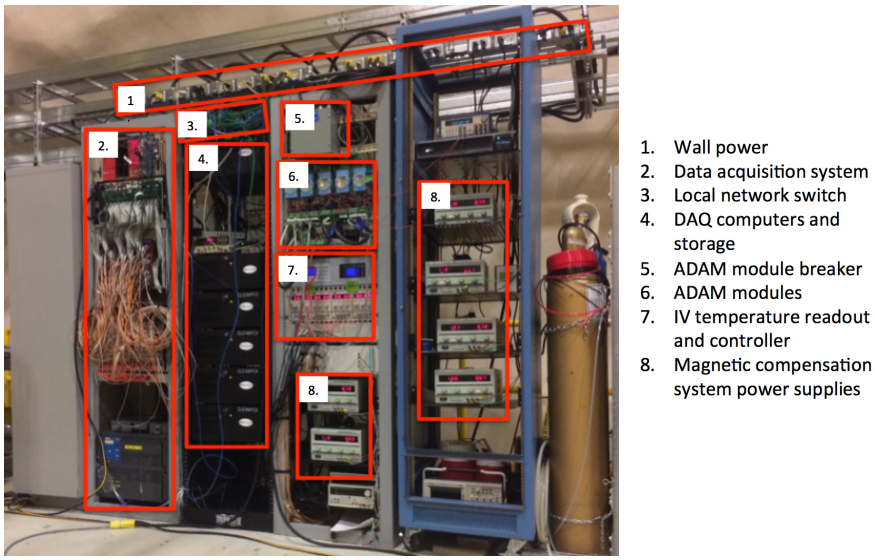

Figure 4.14: An annotated photo of the DAQ racks. Numeric label key is located on the right.

back side of the DAQ racks and are shown in the right-side image of Fig. 4.16.

Another class of instruments which require special hardware to be read out or commanded are instruments with digital or analog inputs or outputs. For example, the IV pressure controller (Fig. 4.10) produces an analog output signal (0 to 5 Volts and proportional to the pressure) but also accepts an analog input signal for remote control of the pressure set point. Similarly, a digital signal (0 or 5 Volts) is required to toggle a solenoid valve to open or close the pneumatic control valves on the purification system.

ADAM modules and signal cable breakout boxes, shown in the top-left photo of Fig. 4.16, are used to read and command digital and analog signals. Breakout boxes with screw terminals are used to easily select signals from individual pins of D-sub style connectors for connection to screw terminals on an ADAM module. ADAM modules contain various combinations of analog and digital sensing and commanding screw terminals which can be individually read or commanded. The ADAM modules contain an Ethernet I/O connection to allow for remote querying or commanding of any terminal. The ADAM modules Ethernet I/O ports are daisy chained together and connected to the local network switch.

As seen in Fig. 4.7, the purification system and other supporting subsystems are located near the center of the deck. The signal and power cables for instrumentation located at the center of the deck are run to/from the DAQ racks on cable trays located under the deck in the space between the water tank and the deck. The detector PMT and sensor cables from the air filled hoses also use these cable trays for routing to the DAQ racks. The bottom-left image in Fig. 4.16 shows an engineering drawing of the location of the cable trays used for cable routing.

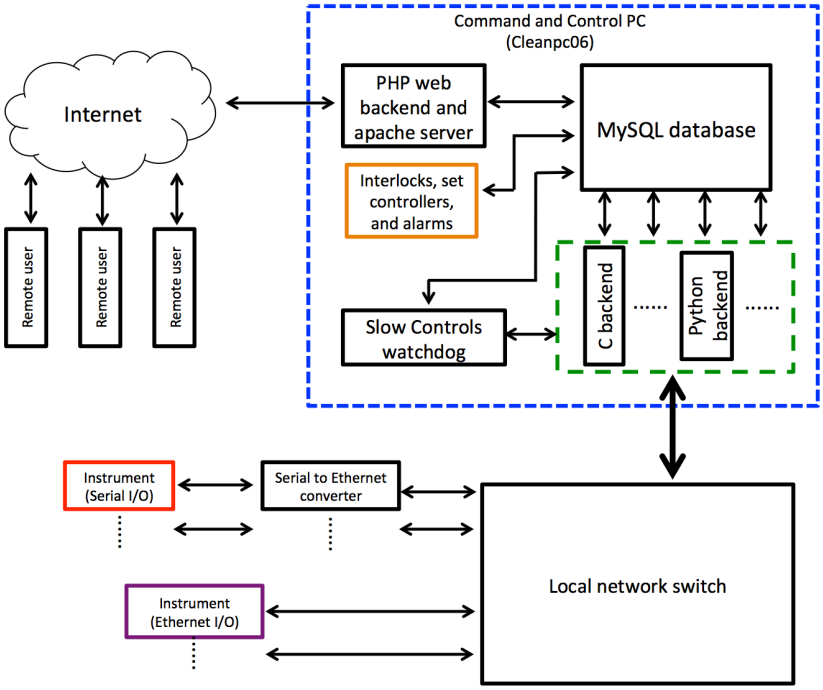

Figure 4.15: A cartoon representation of the instrumentation monitoring and control system. In summary, cleanpc06 houses a MySQL database, Apache web server, PHP website code, and instrumentation communication back-end code. Remote uses can monitor and control detector systems using the PHP web interface. State changes in the MySQL database are monitored and executed by C and python back-end parallel processes. The C and python back-end code communicate with instrumentation hardware (read and write) over a local network.

4.5.3 Online Monitoring and Control: Slow Controls

This section covers the Slow Controls web interface used for remote monitoring and control. As mentioned in Sec. 4.5.1 and shown in Fig. 4.15, cleanpc06 hosts a website where remote users can monitor and control MiniCLEAN subsystems over the Internet. Several screen shots of various Slow Controls pages are shown in Fig. 4.17.

While the website back-end architecture was written in PHP by James Nikkel, much of web-interface's configuration and some of the additional back-end code was written by the author. The back-end PHP code communicates with the MySQL database to populate web page fields when requested by remote users over the Internet.

The most commonly used page is the "Text" summary page, shown in the upper-left of Fig. 4.17. This page provides a summary of the most recently stored sensor values present in the MySQL database at the time of the web page query. Threshold alarms can be created, shown in the lower-right image of Fig. 4.17 and discussed in Sec. 4.5.4.1, for any sensor

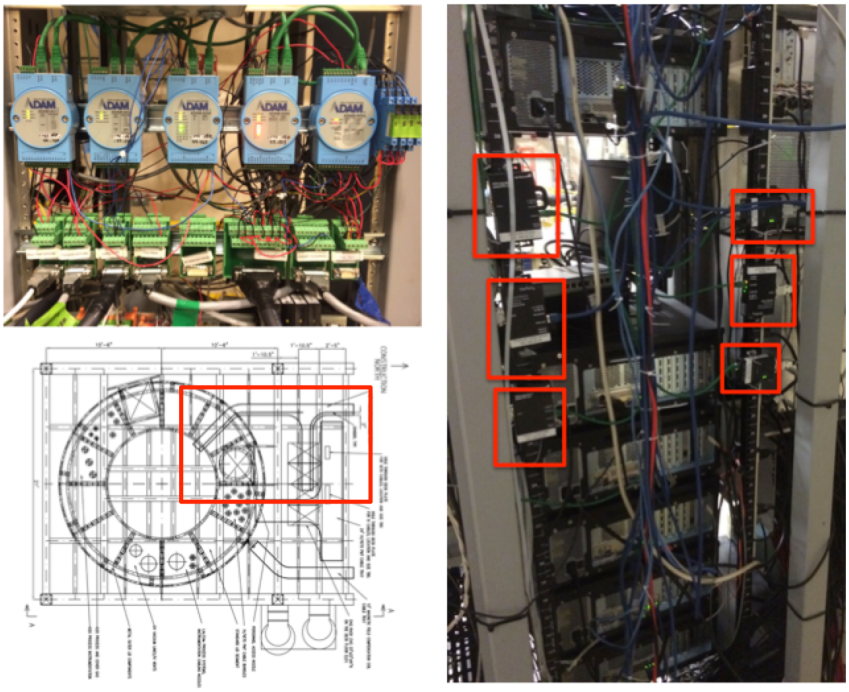

Figure 4.16: Top-left: ADAM control modules used to command/read instrumentation. Contains analog and digital ports. Bottom-left: An engineering drawing showing under-deck cable routing paths. PMT, instrumentation, and power cables run along these cable trays to connect the detector and center of deck to DAQ racks. Right: A photo of the back-side of one of the DAQ racks. Serial to Ethernet converters are highlighted and used to port several instrumentation serial connections onto the local network.

displayed on the text page. Sensor values which cross an alarm threshold are displayed in red (upper-left of Fig. 4.17). The subgroup to which an alarming sensor belongs is also changed to red to alert an operator to an issue if that subgroup is not being viewed. Sensor values which have not been updated in eight or more minutes are displayed in yellow (not shown) to alert a user to potentially stale sensor readings. The page is configured to automatically refresh after an adjustable amount of time (seen in upper left corner).

The bottom-left image in Fig. 4.17 shows the "Plot" functionality. Sensor values can be plotted over adjustable time ranges for more detail. This example shows the IV cryocooler compressor cooling water intlet temperature over 24 hours, but can be adjust to any time window for which there is data in the MySQL database.

The top-right image in Fig. 4.17 shows the "Control" page. Set points or various commands for instruments that can be remotely controlled may be adjusted on this page. Accessing this page requires the remote user to be logged into the page with a user name and password.

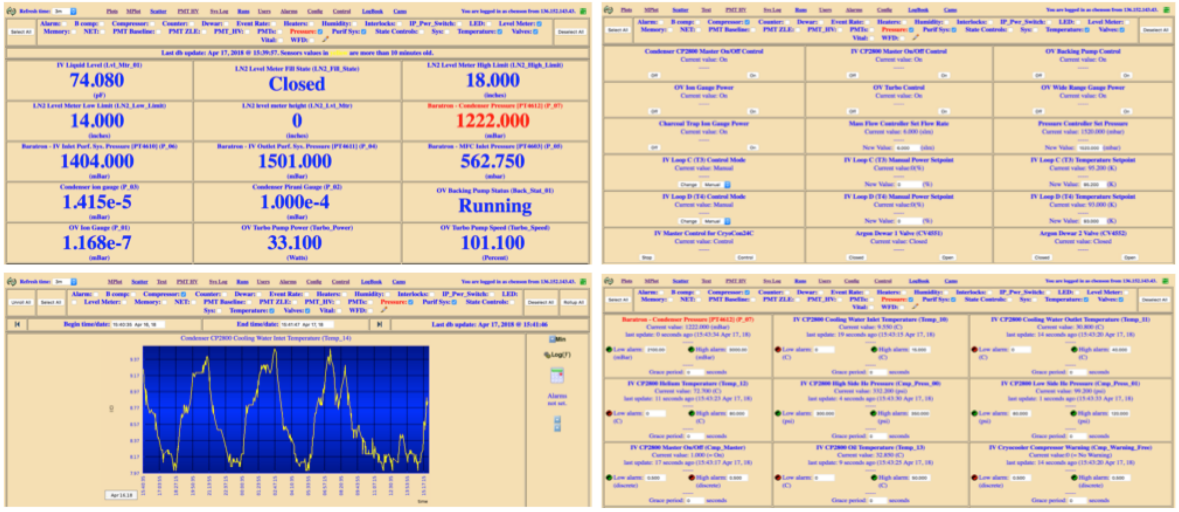

Figure 4.17: Screen shots of various Slow Controls pages. Top-left: A view of the the "Text" page which provides a summary of most recent values. The red value indicates a value with a triggered alarm. Bottom-left: A view of the "Plots" page used to plot values over time. Top-right: A view of the "Control" page used to remotely command various instruments. Bottom-right: A view of the alarm page used to set alarm thresholds on various sensors.

4.5.4 Alarms, Interlocks, and Set Controllers

As mentioned in Sec. 4.5.1, the MiniCLEAN monitoring and control system contains alarms, interlocks and set controllers whose purpose is to improve the robustness of the overall system. These are described in their individual subsections below.

4.5.4.1 Alarms

Threshold based alarms may be setup for any sensor whose state can be read out on the "Text" page of the Slow Controls. Both high low threshold alarms may be set where the region between the high and low threshold is interpreted as the acceptable operating range for the sensor. Alarm setting is performed using the "Alarms" page on the Slow Controls, shown on the bottom-right in Fig. 4.17.

When a sensor value crosses an active alarm threshold, an alarm is triggered on the Slow Controls. A user on the Slow Controls will be alerted to the alarm by text turning red (top-left of Fig. 4.17) and an audible alarm sound. Additionally, an automated email with a description of the alarm will be sent to personnel listed as "On-Call" in the users profile. A Slow Controls user must then acknowledge the alarm to stop the audible alarm. Automated emails will continue to be sent to on-call users every five minutes until the alarm is acknowledged on the Slow Controls.

4.5.4.2 Interlocks

Software interlocks allow for automated, pre-determined actions to be executed under certain well-defined fault conditions with the intent of putting a problematic subsystem into a safe and predictable state until it can be address by an operator. Interlocks are designed to handle anticipated fault conditions where the required response time to address an issue is of order seconds to minutes. These interlocks aid operators by responding to specific scenarios that require a response time faster than the average operator's ability to identify, understand and respond. Care was taken to design interlocks whose responses were targeted and independent/decoupled from other interlocks from a system point of view. This was to ensure that the triggering of one interlock would reliably put the system into a well-understood state and would not cause a chain reaction of additional interlocks to trigger.

Fig. 4.18 shows a top-level view of the typical decision flow for software interlocks. All of the interlocks are written in Python and are executed as independent parallel processes on cleanpc06.

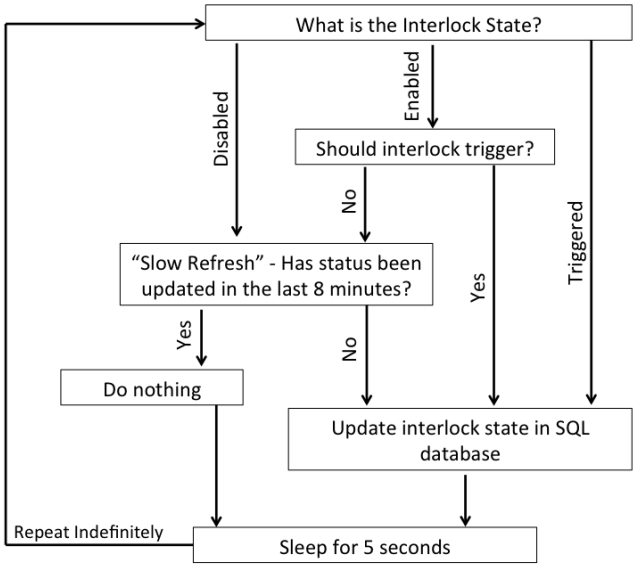

Figure 4.18: A typical top-level decision flow for software interlock processes.

Starting from the top of Fig. 4.18, the interlock determines if it should be active by checking its commanded state in the MySQL database. Interlocks may be set to enabled or disabled using the Slow Controls command page. If the interlock is "Disabled", it then checks the last time its readable state (i.e. the state displayed on the Slow Controls "Text" and "Plots" page) had been updated and refreshes it every 8 minutes. This process is referred

Name	Fault Condition	Action
Interlock01	IV cryocooler compressor cooling water loop overheating	Shutdown compressor
Interlock02	Low dewar weight when flowing	Divert flow to pump
Interlock03	High pressure at mass flow controller while flowing	Divert flow to pump
Interlock04	High pressure at IV inlet	Divert flow to pump
Interlock05	Incorrect vent valve state	Sync with commanded state
Interlock06	Vacuum at OV turbo pump compromised	Shutdown turbo pump and isolate
Interlock07	Trap/condenser vacuum compromised	Shutdown turbo pump
Interlock08	Irregular OV pump speed and power	Shutdown turbo pump and isolate
Interlock09	Auto purge air filled hoses	Purge air filled hoses with compressed air
Interlock10	High pressure in LAr condenser	Controlled vent condenser of LN_2 vapor space

Table 4.1: A table of deployed interlocks. A description of the scenario and action taken when the interlock is triggered.

to as the "Slow refresh" and is required to ensure interlock states are not displayed as stale (yellow) on the Slow Controls "Text" page.

If the interlock is "Enabled", custom logic to check for various trigger conditions is executed. A single interlock may have more than one type of trigger condition but the trigger response is designed to be the same, regardless of trigger condition, to ensure design simplicity. Typically, an interlock queries the latest values of various sensor readings or states from the MySQL database and compares them to other instruments or thresholds to determine if a trigger condition is met. If a trigger condition is met, the state of the interlock in the Slow Controls is set to "triggered" to allow an alarm to be triggered and the response logic is executed. Typical responses include opening/closing values on the purification system to divert flow, or powering off instruments. If a trigger condition is not met (this is true the vast majority of the time), the interlock state is updated using the previously mentioned "slow refresh" approach. This process flow is contained within an infinite loop with a wait time of around five seconds between each loop iteration.

Table 4.1 provides a tabulation of the deployed interlocks. The name, fault condition and automated action taken by the interlock are shown.

4.5.4.3 Set Controllers

The alarms and interlocks introduced in Sec. 4.5.4.1 and Sec. 4.5.4.2 are useful tools to increase the robustness of the detector subsystems. However, these tools are only effective if they are enabled with appropriate settings. To improve operational quality assurance, interlock and alarm set controllers were constructed to enforce the standardization of set of interlocks and alarms for various common operating conditions.

Fig. 4.19 presents table of standardized interlocks set for "Off", "Minimal", and "Flowing" operating states. This table shows which interlocks and interlock settings should be active for various conditions. This standard was coded into a Python script, structurally similar to the process shown in Fig. 4.18. Thirty minutes before the end of each eight hour shift, the interlock set controller scans the state of the interlock settings and compares it to the standards defined in Fig. 4.19. Any discrepancies with the standard are identified, summarized, and emailed to all operators listed as "On-shift" or "On-call". It is the responsibility of the operator on shift to investigate the dependencies and resolve when appropriate. The design choice was made to not allow the controller to automatically resolve observed discrepancies (instead of sending a summary in an email to operators) to minimize the risk of unintended consequences.

Name	Additional Setting	Off	Minimal	Filling
Interlock01		Off	On	On
	Interlock01Val	40 C	40 C	40 C
Interlock02		Off	Off	On
	Interlock02Val	300 lbs	300 lbs	300 lbs
Interlock03		Off	Off	On
	Interlock03Val	3000 mbar	3000 mbar	3000 mbar
Interlock04		Off	Off	On
	Interlock04Val	1600 mbar	1600 mbar	1600 mbar
Interlock05		Off	On	On
Interlock06		Off	On	On
Interlock07		Off	On	On
Interlock08		Off	On	On
Interlock09		Off	On	On
	Interlock09Val	90 mins	90 mins	90 mins
Interlock10		Off	On	On

Figure 4.19: Standardized interlock sets for off, minimal and flowing detector state. The red shading indicates a disabled state while the green indicates an enabled state.

An analogous set controller was constructed for alarms and operates identically to the previously discussed interlock set controller. The standardized alarm sets are not shown for the sake of brevity, but are defined in a way very similar to what is shown for the interlock sets in Fig. 4.19.

Standard Procedures	
Power Outage Restart Procedure	MCL-OPR-4017
Venting Outer Vessel Procedure	MCL-OPR-4021
Pumping Down Outer Vessel Procedure	MCL-OPR-4022
Changing Dewars Procedure	MCL-OPR-4023
Sampling Dewar with RGA Procedure	MCL-OPR-4024
Turning On High Voltage Procedure	MCL-OPR-4027
Turning Off High Voltage Procedure	MCL-OPR-4028
Starting and Stopping DAQ Runs Procedure	MCL-OPR-4029
Initializing DAQ PCs	MCL-OPR-4030
Controlled IV Boil-off Procedure	MCL-OPR-4031
Starting Gas Flow in Purification System Procedure	MCL-OPR-4037
Stopping Gas Flow in Purification System Procedure	MCL-OPR-4038
Turning on the IV Heaters	MCL-OPR-4039
LRC Emergency Shutdown	MCL-OPR-4040
Condenser Procedure	MCL-OPR-4041
Checklists	
Shift Checklist: Filling	MCL-OPR-4025
Shift Checklist: Running	MCL-OPR-4026
Emergency Procedures	
Emergency Shutdown Procedure	MCL-OPR-4011
Emergency IV Venting Procedure	MCL-OPR-4033
Emergency Purification System Venting Procedure	MCL-OPR-4034
Slow Controls Fault Condition Guide	MCL-OPR-4035
Supporting Material	
Introduction for MiniCLEAN Procedures	MCL-OPR-4036
Standard Detector States	MCL-OPR-4016
Slow Controls Interlocks	MCL-OPR-4020

Table 4.2: A tabulation of standard operating procedures and related documentation. Document identification numbers are shown on the right.

4.6 Operational Procedures and Documentation

The author was heavily involved in creating, documenting, and editing the operational procedures and supporting documentation required for final SNOLAB approvals to commence filling operations. Table 4.2 provides a listing of the procedures and supporting documentation used for steady state operations.

Chapter 5

Purity Dependence of Gaseous Argon Scintillation

This chapter provides an overview of measurements of scintillation properties of a cold gaseous argon target in MiniCLEAN as a function of total impurity level. The author played a leading role in this study. The material presented in this chapter is in the process of being published (summer 2018) [125].

Sec. 5.1 provides an overview of scintillation in gaseous argon and a summary of previous measurements. Sec. 5.2 provides an overview of measurement methods. Sec. 5.3 describes measurements of the triplet time constant and relative component light yield as a function of impurity level. Lastly, Sec. 5.4 discusses these results.

5.1 Scintillation in Gaseous Argon

This section provides an overview of scintillation processes in gaseous argon. While an overview of scintillation in liquid argon was provided in Sec. 2.4.1, the literature suggests there is additional complexity in the time profile and scintillation spectrum of gaseous argon when compared to liquid argon.

Structure of gaseous argon scintillation spectrum The spectrum of the scintillation light in gaseous argon, as defined by the literature, is produced in three continuous bands. The first continuum ranges from 104 nm to 110 nm, the second continuum peaks at 128 nm, and the third continuum ranges from 180 nm to 230 nm.

The mechanism of primary scintillation light from the second continuum results from the disassociation of argon dimer pairs in their lowest molecular energy state and is the same for liquid and gaseous argon, as described in Sec. 2.4.1.

The first spectral continuum (104 nm to 110 nm) shares the same origin as the second continuum but from higher vibrational states [129, 130]. The origin of the third continuum is still under debate, with several authors postulating different chemical processes [131, 132,

133, 134]. According to the most recent study [135], at least four different states are involved in the process.

In general, the relative contributions from each of the three continua depends on the pressure of the gaseous argon. The intensity of the first continuum decreases with increasing pressure, due to radiation trapping [129], and becomes negligible for pressures approaching 1 bar. The second continuum's contribution is small at low pressure but becomes dominant for pressures larger than approximately 0.8 bar. Contributions from the third continuum are observable for pressures greater than 230 mbar, with the spectral structure depending on pressure [135].

The MiniCLEAN detector filled with gaseous argon operates at approximately 1.5 bar. This suggests scintillation light from the second and third continua are observable. For a liquid argon target, however, the first and third continuum are highly suppressed, leaving only the second continuum (128 nm light).

Time structure of scintillation light The literature also provides insight on the relative timing of the various scintillation continua, as previously discussed [135, 137, 138]. Because the first contiuum is highly supressed in MiniCLEAN for a liquid or gaseous target (discussed previously), the remaining discussion is narrowed to the scintillation timing profiles of the second and third continuua. Scintillation light from the third continuum is very fast and contributes mainly to detected prompt light [138], where prompt light in MiniCLEAN refers to the first 80 ns of the 16 μs event window. As previously discussed, light from the second continuum is produced on two well-separated time scales: a fast time constant from the singlet state, and a slow time constant from the triplet state. According to [138], the scintillation light from the singlet state should also be part of the prompt light (along with the third continuum) but slightly delayed (on the order 10 nanoseconds compared to the third continuum). Depending on the time resolution of the detector, the temporal separation between the third continuum light and the singlet light of the second continuum may or may not be observable.

Additional evidence of the temporal separation between the second and third continua is shown in Fig. 5.1 taken from. [135]. Fig. 5.1 shows time-binned integrated spectra of scintillation light from heavy ion beam excitation at 1500 mbar. The plots are arranged top to bottom in time and show measured spectra of scintillation light integrated over the specified time bin. For integration windows early in time, the third continuum spectrum (180–230 nm) dominates. However, at later times, such as the 16 to 32 ns window, the 128 nm peak from the singlet state of the second continuum increases and will eventually become dominant (especially at much later times when delayed light contributions from the triplet state become substantial). The peak at 155 nm, which is technically between the second and third continua as defined by the literature, is associated to the "left turning point" which was found and unambiguously assigned by synchrotron excitation experiments [136]. Therefore, Fig. 5.1 clearly shows some amount of temporal separation between the second and third continuum in the prompt window.

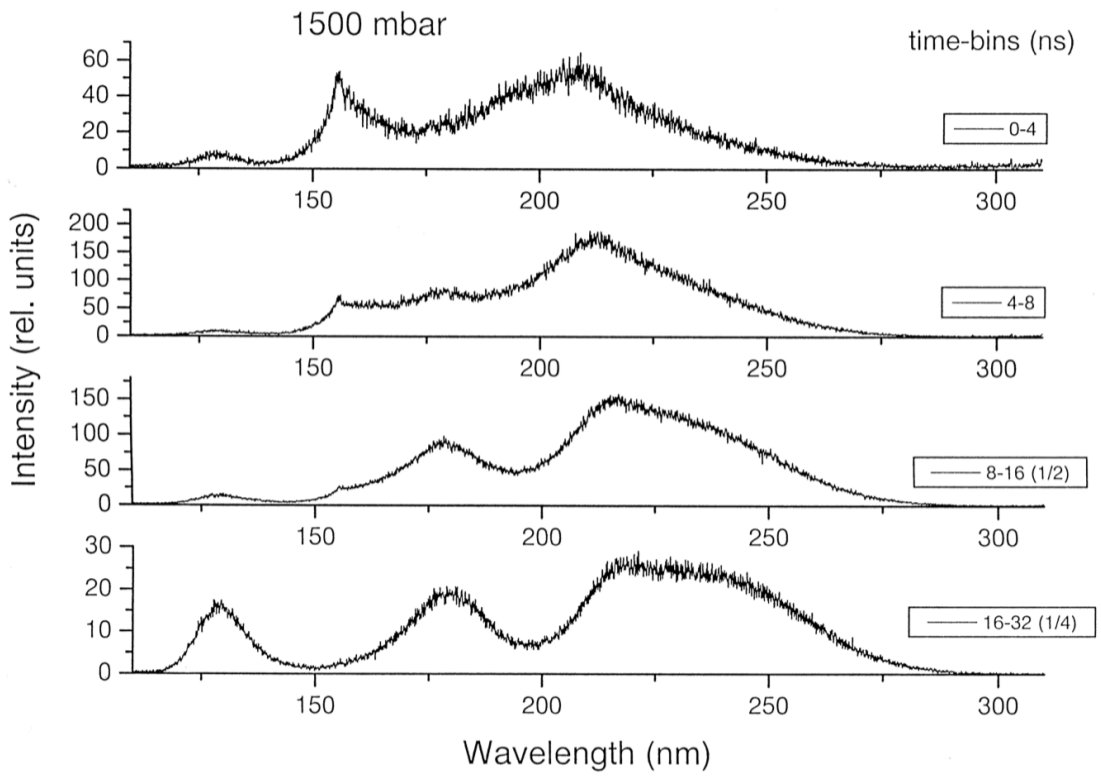

Figure 5.1: Time-binned integrated spectra of gaseous argon scintillation light from 100 MeV heavy ion beam excitation at 1500 mbar. At early times, the scintillation light is dominated by the third continuum. At later times, the second continuum peak centered around 128 nm starts to become significant and dominates at later times. Figure from [135].

While scintillation light from the singlet state of the second continuum and light from the third continuum contributes to the prompt peak ($t < 80$ ns), light from the triplet state of the second continuum dominantly populates the late light in an event window due to its long decay time constant. A summary of several measurements of the triplet state lifetime are provided in Tab. 5.1. Upper limits on the total impurity levels from these studies are also presented because, as discussed previously in at the end of Sec. 2.4.1, the presence of impurities may significantly reduce the triplet state lifetime and overall light yield.

Dependence on Gas Density As seen in Tab. 5.1 values for the triplet time constant vary from 2.8 to 3.24 μs. Besides impurity levels, another reason for the variation could be explained by differences in the number density which is also tabulated in Tab. 5.1. The decay time constant (inverse of lifetime) plotted as a function of number density is shown in Fig. 5.2 for the various measurements reported in Tab. 5.1. The dashed line in Fig. 5.2 is the expected functional form of the triplet decay rate as a function of density from [127]. It can

Table 5.1: Triplet lifetime in gaseous argon. The variation of lifetimes is due to both density and (presumably) impurity level. Only upper limits on impurity are reported. The results are ordered by lifetime.

τ (μs)	**Ref.**	**Density** ($10^{20} cm^{-3}$)	**Impurity level**	**Particle type**
2.8	Thonnard *et al.* [129]	0.19	$<$ 2 ppm	β
2.84±0.02	Gleason *et al.* [139]	4	$<$ 1 ppm	β
2.86	P. Millet *et al.* [140]	0.1- 0.26	$<$ 1 ppm	α
2.88±0.08	K. Mavrokoridis *et al.* [91]	0.24	$<$ 1ppb	α
2.9	Carvalho *et al.* [141]	3	not reported	β
3.0±0.05	Suemoto *et al.* [142]	2.2	$<$ 10 ppm	β
3.14 ±0.067	C. Amsler *et al.* [138]	0.32	$<$ 9 ppb	α
3.15±0.05	P. Moutard *et al.* [127]	0	$<$ 1 ppm	γ
3.2 ± 0.3	Keto *et al.* [143]	2.6	$<$ 2 ppm	β
3.22±0.042	Oka *et al.* [144]	0.32	$<$ 5 ppm	β
3.24±0.05	F. Marchal *et al.* [145]	0.2	$<$1 ppm	γ

be seen from Fig. 5.2 that the decay rate decreases (i.e. the lifetime increases) as the density decreases. At low number density, the probability for a dimer state to be formed decreases, which results in smaller decay rates (longer lifetimes) in pure argon. However, even with an impurity level of 1 ppm, the density effect alone can not explain the variation of triplet decay rates (or lifetime) measurements. A more complete explanation requires the inclusion of the effects of impurities, which have been investigated by several groups [91, 138].

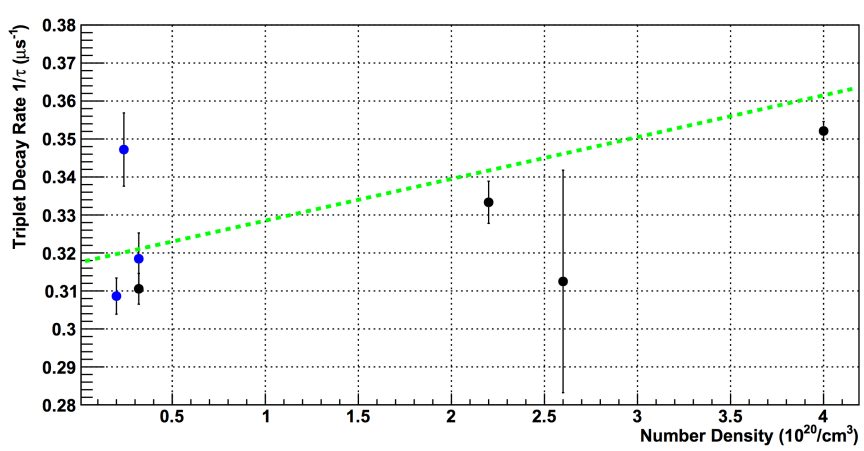

Figure 5.2: Triplet decay rate (inverse lifetime) versus density from Tab. 5.1. The dashed line is a fit of rate versus density from [127]. The blue dots are from relatively recent results (after 2000) while the black dots are older results.

5.2 Methodology

Given the spread in the measurements of the triplet time constant in gaseous argon provided by the literature for various impurity limits (Tab. 5.1) and the observation that impurities can strongly quench scintillation light and shorten the triplet time constant [91, 138], a characterization of the light yield and triplet time constant as a function of impurity level would be a useful and interesting quantity for experiments. Access to this result would enable experiments to use the measured triplet time constant as a proxy for impurity levels in a gaseous argon target.

The MiniCLEAN experiment, described in Chapter 3, is a detector well suited to make such a measurement. The digitization of full waveforms at 250 MHz, ability to determine the arrival time of single photons, large event window (16 μs), and uniform distribution of an ^{39}Ar β source throughout the target volume allows for a precise measurement of the triplet time constant. Additionally, MiniCLEAN's purification system is rated for purifying gaseous argon to a level of 1 ppb. This can provide a large dynamic range to measure impurity dependent properties if starting at a large known impurity level and purging to a lower impurity value.

The MiniCLEAN collaboration was able to measure triplet time constant and relative light yield (relative contributions from each component) as a function of total impurity level during a period in 2017 when the impurity levels in the detector were reduced from 40 ppm to the of order ppb. This section provides an overview of the methodology of this measurement.

Sec. 5.2.1 summarizes the extraction of the triplet time constant and event selection. Sec. 5.2.2 describes the purging process and Sec. 5.2.3 details the modeling of impurity levels over time.

5.2.1 Triplet Time Constant Extraction

To determine the triplet state lifetime and relative contributions from various scintillation light components, the distribution of single photoelectron arrival times integrated over many events classified as electronic recoils (dominantly ^{39}Ar - event selection covered in Sec. 5.2.1.1) was fit to a weighted sum of three exponential decays convolved with a time resolution Gaussian plus a flat background. This function is explicitly defined in Eq. 5.1 as:

$$f(t) = G(t, \mu, \sigma) \otimes [A \cdot e^{-\frac{t}{\tau_1}} + B \cdot e^{-\frac{t}{\tau_2}} + C \cdot e^{-\frac{t}{\tau_3}}] + D \tag{5.1}$$

where $G(t, \mu, \sigma)$ is the detector time resolution function with floating parameters for its mean (μ) and standard deviation (σ), the coefficients A, B, and C are the normalization weights for each of the exponential decay functions, D is the normalization constant for the flat background component, and τ_1, τ_2, and τ_3 and the floating decay coefficients for the prompt, intermediate and late decay constants respectively. The μ in the resolution Gaussian is interpreted as a global offset in time while the σ is interpreted as the time resolution. The function is fit to the vast majority of the event window (-32 ns to 15500 ns)

where zero is defined as the waveform peak set by calibration processors during reconstruction (Sec. 3.3.2.1).

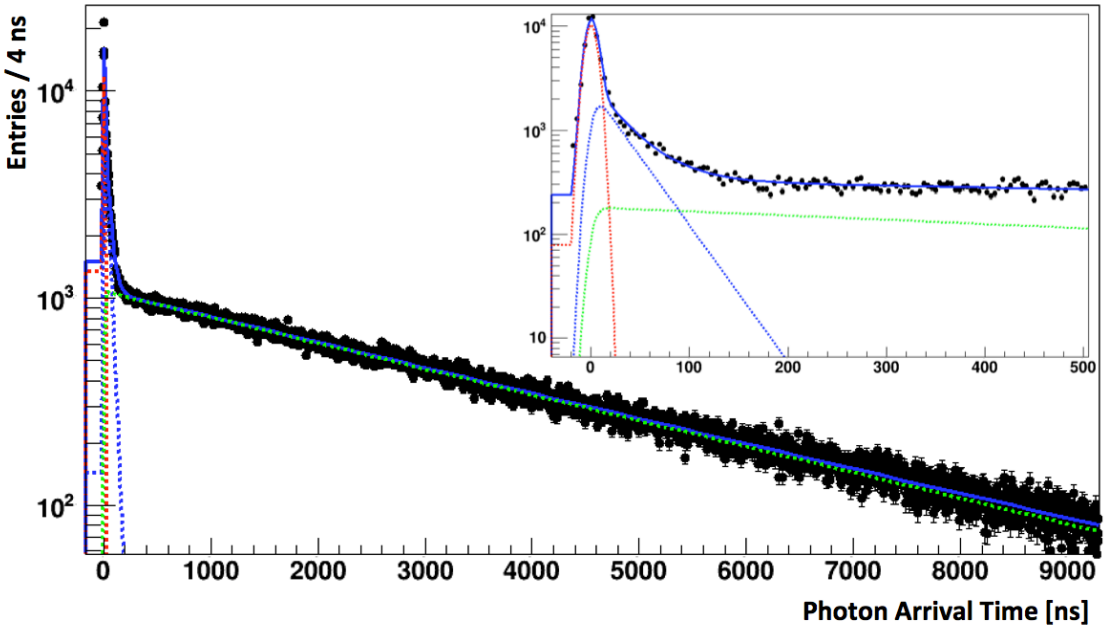

Figure 5.3: Distribution of single photoelectron arrival times integrated over one hour of events classified as electronic recoils. Also shown is a fit to the functional form described by Eq. 5.1 for events late in the pump/purge process shown in Fig. 5.10 (i.e. long triplet lifetime). The full fit is shown as a solid line along with the weight component contributions (dotted). A view of early times in the event window is shown in the upper-right.

Fig. 5.3 shows the result of fitting the single photoelectron arrival time for 1 hour of electronic recoil events to the functional form described by Eq. 5.1 for events late in the pump/purge process shown in Fig. 5.10 (i.e. long triplet lifetime). The solid blue line represents the total fit while the dotted red, blue and green lines represent the weighted contribution from each component. The smaller plot in the upper-right of Fig. 5.3 provides a "zoomed-in" view at small times for a better look at the prompt and intermediate components. The fitted flat background component is not visible on the y-scale due to its very small fitted contribution.

Not only does a three exponential decay plus a flat background model fit the data well, as seen in Fig. 5.3, it is well-motivated by the underlying physics. The prompt exponential is expected to be made up of contributions from the fast light from the third continuum as well as light from the single state of the second continuum. The intermediate component is thought to be composed of contributions from PMT late and double pulsing, studied extensively by Caldwell in [29], and possibly delayed emissions from TPB when excited by the scintillation light of the second continuum, as suggested by Segreto [146]. The late

component is motivated by the decay of the triplet state of the second continuum. Finally, a flat background is expected to contribute from PMT dark hits expected to be distributed uniformly in time at a rate of a several hundred Bq.

The fit was performed using RooFit [147] on one-hour blocks of data throughout the course of the data taken during the entire pump/purge process described in Sec. 5.2.2. The fitted time constant for the late component, τ_3, and its associated uncertainty quoted by the fit are the values plotted over time in Fig. 5.10.

5.2.1.1 Event Selection Cuts

As mentioned in Sec. 5.2.1, the events used to populate the single photoelectron arrival time distribution shown in Fig. 5.3 are from events classified as electronic recoil-like. Electronic recoil events are used to populate the distribution because they contain more scintillation light from the triplet state of the second continuum (i.e. late light) than nuclear recoils. Additionally, because the gaseous argon target contains an intrinsic ^{39}Ar background which is uniformly distributed and decaying at the rate of 1 Bq/kg, it provides a natural choice for an excitation source to select on.

Recalling MiniCLEAN's commonly used discriminators defined in Sec. 3.3.2.2, the prompt fraction (f_p), charge ratio (Q_{ratio}), and radius cubed ratio ($\mathrm{R}^3/\mathrm{R}^3_{TPB}$) are natural choices for selecting electronic recoil events.

Because the prompt fraction is the fraction of the total charge in the prompt region of the event window, smaller f_p valves correspond to events with more late light, i.e. electronic recoils.

Recalling the definition of Q_{ratio} as the ratio of the maximum amount of charge observed on a single PMT to the total charge observed on all of the PMTs, it may be used as a rough measure of the isotropy of the scintillation light. Because the scintillation light is emitted isotropically, events which are in the bulk of the target volume should hit several PMTs, yielding a small Q_{ratio}, while events very close to the edge (i.e. the TPB boundary) should disproportionately hit the closest PMT, producing a large Q_{ratio}.

Fig. 5.4 shows a 2D histogram of f_p and Q_{ratio} for NHit triggered events late in the pump/purge process (i.e. low impurity levels) with no cuts applied. The class of electronic recoil events are clearly visible as the at low f_p and low Q_{ratio}. This peak is dominated by ^{39}Ar decays (Sec. 3.4.1) in the gas target along with contributions from gammas from ^{238}U and ^{232}Th decays in the PMTs and steel (Sec. 3.4.4). Other events at high f_p and high Q_{ratio} are attributed to alpha decays on the edge of the detector and HV breakdown at the PMT bases in gaseous argon.

PMT base discharge is a problem when operating in gaseous argon, where the PMT bias voltage is sufficient to cause breakdown over distances less than a centimeter. The bases of most PMTs used in MiniCLEAN were coated in epoxy, so the breakdown rate in gas is relatively low and the bases which were not conformally coated remained off during the cold gas runs as an added precaution. However, during a breakdown event, once a base begins to discharge, the spark path provides a preferred route for continued discharge. This situation

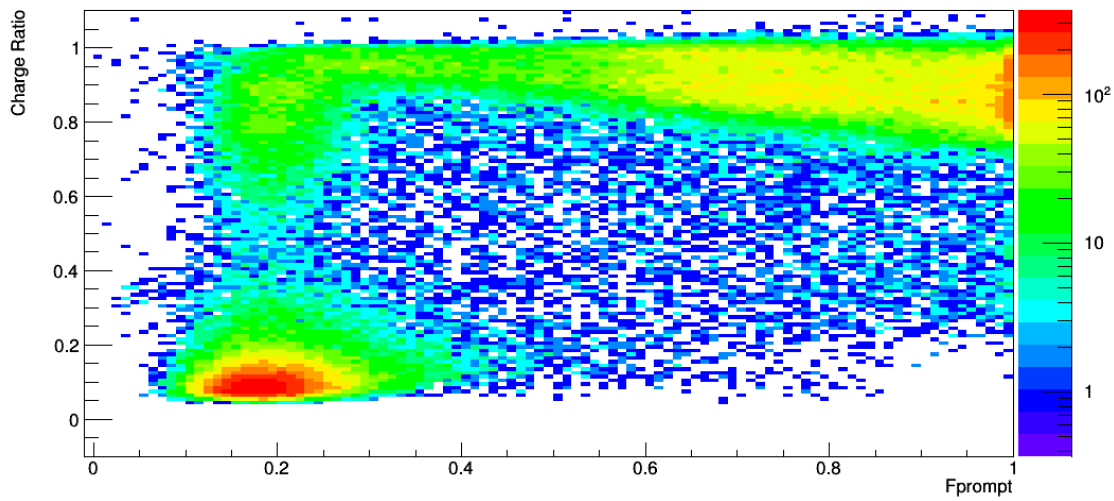

Figure 5.4: A 2D histogram of charge ratio (Q_{ratio}) and the prompt fraction (f_p) for NHit triggered events late in the pump/purge process. The peak at low f_p and low Q_{ratio} are the electronic recoil events selected for this study.

is often seen as in data as an event with a Q_{ratio} very close to one because the PMT which is undergoing discharge will see the vast majority of the charge in the event. However, it was determined that Q_{ratio} does not always cut the discharge events, especially when light from the breakdown is detected by other PMTs. As shown in Fig. 5.5, the distribution reconstructed radius after applying $Q_{ratio} < 0.6$ and $f_p < 0.5$ cuts still yields a peak at large radius where most of these events were found to be caused by breakdown in gas. This, along with the desire to make a fiducial cut to reduce edge backgrounds, motivates the use of a radial cut. Using Monte Carlo studies and comparison to data, a cut of $\mathrm{R}^3/\mathrm{R}^3_{TPB} < 0.7$ was chosen.

The right-side image in Fig. 5.5 shows the effect of applying the $\mathrm{R}^3/\mathrm{R}^3_{TPB} < 0.7$ cut on the distribution shown in Fig. 5.4.

As seen in Fig. 5.6, as the pump/purge process (to be discussed in Sec. 5.2.2) continues, the triplet time constant recovers to larger values due to reductions in impurity levels. A consequence of such a large change in the observed triplet time constant is a resulting change in the observed f_p, as shown in Fig. 5.7. As discussed earlier, because f_p is the fraction of total charge observed in prompt window, as the triplet time constant becomes larger, a smaller fraction of the overall charge will lie in the prompt window, leading to an expected reduction in the observed f_p value.

Referring back to the 2D histograms of Q_{ratio} and f_p presented in Fig. 5.4 and Fig. 5.5, the electronic recoil peak seen at low Q_{ratio} and low f_p will start at high f_p and low Q_{ratio} at the beginning of the pump/purge process (high impurity levels) and sweep to low Q_{ratio} and low f_p as impurity levels are reduced.

Given that the peak value of f_p changes significantly during the course of the pump/purge

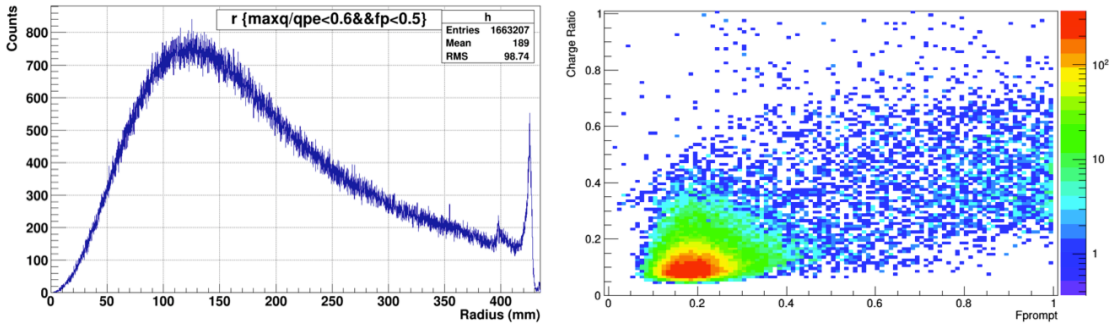

Figure 5.5: Left: Reconstructed event radius from charge centroid (Sec. 3.3.2) after $Q_{ratio} < 0.6$ and $f_p < 0.5$ cuts for the event distribution similar to that shown in Fig. 5.4. The peak at large radius is attributed to HV breakdown on a single PMT which pulls the reconstructed radius to the edge of the detector. This motivates the use of a $\mathrm{R}^3/\mathrm{R}^3_{TPB} < 0.7$ to cut breakdown events as well as to establish a fiducial volume. Figure from [95]. Right: The same 2D histogram as Fig. 5.4 after applying the radial cut $\mathrm{R}^3/\mathrm{R}^3_{TPB} < 0.7$ for a data set taken late in the pump/purge process.

process, a hard cut for event selection is not applied to f_p. For reasons provided throughout this section, $\mathrm{R}^3/\mathrm{R}^3_{TPB} < 0.7$ and $Q_{ratio} < 0.6$ cuts are applied to the data for event selection. These cuts allow for the inclusion of the large electronic recoil peak throughout the entirety of the pump/purge cycle while excluding the vast majority of edge events (αs and HV breakdown).

54 of the 92 PMTs on MiniCLEAN were used in this analysis. Of the 38 PMTs not used in this analysis, 19 were not working, 7 remained off as a precautionary measure due to their lack of conformal coating on the base, 4 were excluded due to excessive noise rates, and the remaining 8 were turned on part way though the pump/purge but were excluded so that the total number of PMTs contributing to the PE hit time distributions was constant and consistent.

5.2.2 Data Set Overview

The data set for this analysis was taken between March 31st and April 14th 2017. In the weeks prior to the March 31st start, it was determined that the cold gaseous argon target inside of the IV contained a total impurity level of 40 ppm of air from a one-time air leak. Because the scintillation properties of argon are very sensitive to impurity levels, the impurities needed to be purged prior to filling with liquid argon.

Using a residual gas analyzer (RGA) sensitive to impurity levels on the order of ten ppm, it was determined that the total impurity level in the IV was 40.9 ± 2.6 ppm which mostly consisted of nitrogen and oxygen. The relative concentrations of the nitrogen and oxygen contaminants were consistent with air.

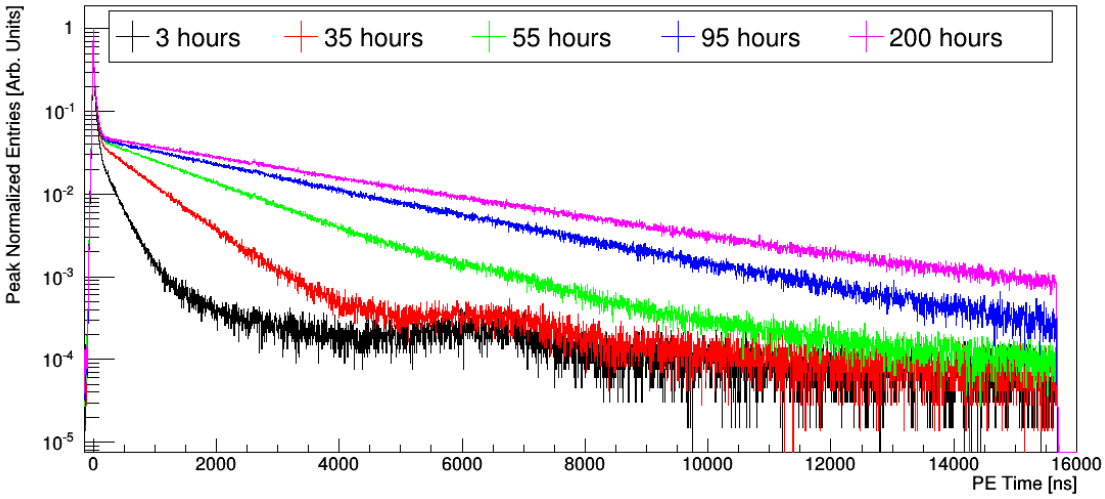

Figure 5.6: Several distributions of single PE arrival time for electronic recoil events integrated over several hours of data taking. The different colors represent the measured distributions for various points in elapsed time after the start of the pump/purge process. As the pump/purge process continues, the impurity levels are reduced and the triplet lifetime increases to longer times. The bump near 6500 ns is from after-pulsing in PMTs [29]. The peaks at 0 ns are normalized to unity for each distribution.

It was determined that a series of pumping and purging cycles were required to incrementally reduce the impurity levels to ppb levels required for liquid argon filling. This would be done by boosting the pressure in the IV using purified argon from the purification system (with 1 ppb levels of impurities) to approximately 1550 mbar followed by pumping down the IV to approximately 1450 mbar and repeating. Conceptually a pump/purge cycle reduces the impurity levels in the target gas by pumping out gaseous argon containing impurities (when dropping the pressure) and replacing the removed volume with high purity argon rated at 1 ppb from the purification system. Even though a small fraction of the total amount of the gas target, on the order of 5 to 10%, is being replaced each cycle, after many pressure cycles the purity of the target should return to acceptable ppb levels.

Physics data were taken during the vast majority of time the pump/purge cycles were ongoing in order to monitor the recovery of the triplet time constant. Fig. 5.8 shows the complete set of 240 pressure cycles, starting on March 31st and ending on April 14th where the IV Outlet pressure is the measured pressure from sensor PT4611 in Fig. 4.11.

Fig. 5.9 is a zoomed-in version of Fig. 5.8 and shows several pressure cycles near the beginning of the full pump/purge period. Each full cycle (i.e. peak to peak time) is on the order of 90 minutes and the pressure change is approximately linear in time during the pressure boosting and pump down periods.

Fig. 5.10 shows the measured triplet time constant throughout the full pump/purge period. The specifics of the extraction of the measured triplet time constant are covered in

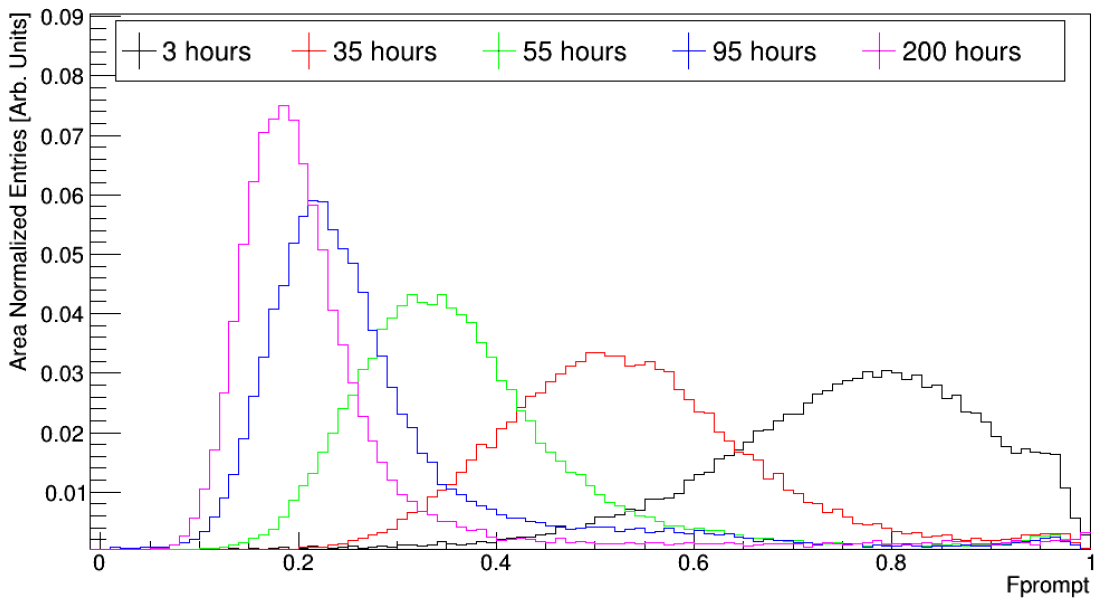

Figure 5.7: Several measured f_p distributions for electronic recoil events for various points in elapsed time since the start of the pump/purge process. The shift toward lower f_p values at later times is a consequence of the recovering late component during the pump/purge. Each distribution is area normalized.

Sec. 5.2.1.

5.2.3 Modeling Impurity Levels Over Time

With measurements of the IV pressure over time and a measurement of the initial impurity levels, a model of the impurity level as a function of time was developed. Because the RGA is only sensitive to impurity levels of the order of 10 ppm, it was only used to measure the initial impurity. Any estimations of impurity levels less than several ppm were derived from the recursive model described in this section.

The fraction of gas removed and replaced each pump/purge cycle is determined by evaluating the pressure change from the peak to the trough during the pump down phase of a cycle. An offline Python analysis evaluats the peak and trough times and values, indicated by the red and green dots respectively in Fig. 5.9. The difference in the peak and trough values are used to determine the fraction of gas removed (at constant impurity level) during a pump down cycle. When the gas is replaced by high purity gaseous argon during the pressure boosting phase, the total impurity level in the detector is reduced.

IV pressure readings are queried and stored by the Slow Controls monitoring and control system (Sec. 4.5) at a rate of 0.25 Hz - much faster than the time scale of a pump/purge cycle. The step in the pressure reading immediately after the peak/trough values is on average

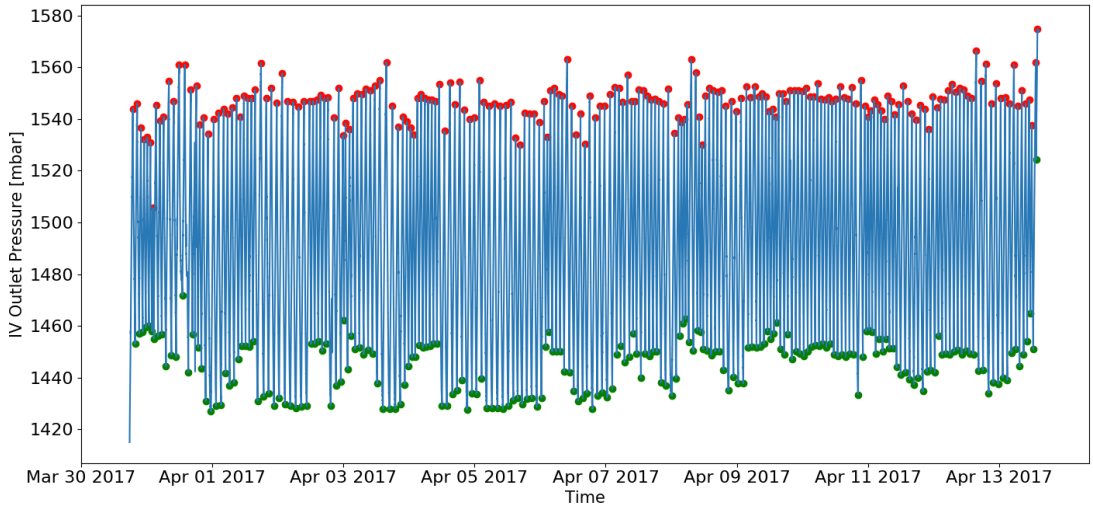

Figure 5.8: The IV pressure over the course of the entire pump/purge period. A total of 240 pressure cycles were performed to restore the gas purity in the IV. The green and red dots represent the minimum and maximum pressure in each cycle.

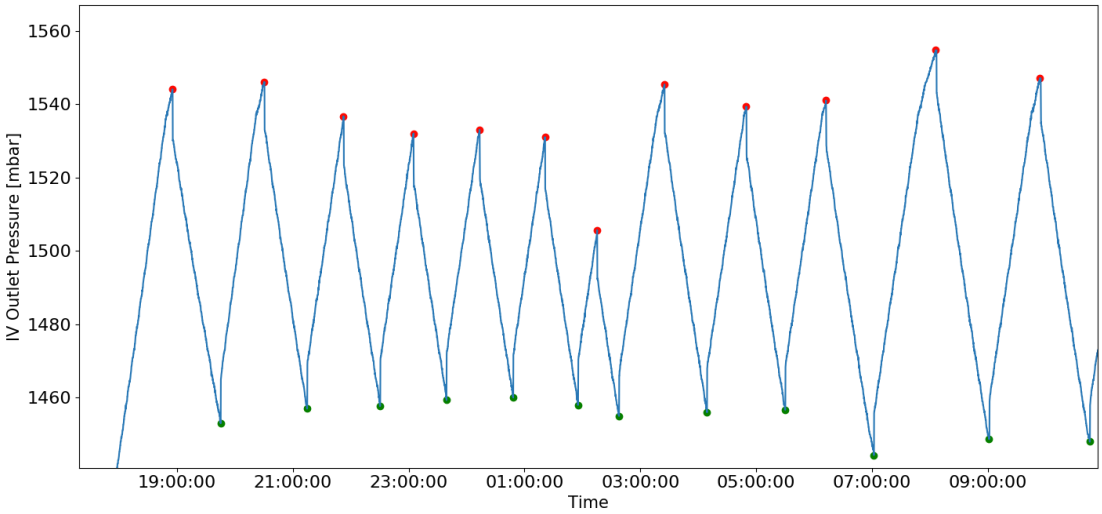

Figure 5.9: A zoomed-in plot of the first several pressure cycles shown in Fig. 5.8.

12 mbar and is explained by a pressure drop near the IV outlet pressure sensor (PT4611 in Fig. 4.11) when transitioning between pumping on the detector and boosting the pressure. When transitioning from boosting the IV pressure to pumping down (near the peak), the pressure controller (EPC01 in Fig. 4.11) setpoint pressure is reduced to a value less than the current pressure which prompts the pressure controller to throttle open to start pumping down the IV via "pump 1". This causes gas to flow from the IV outlet port to the pressure

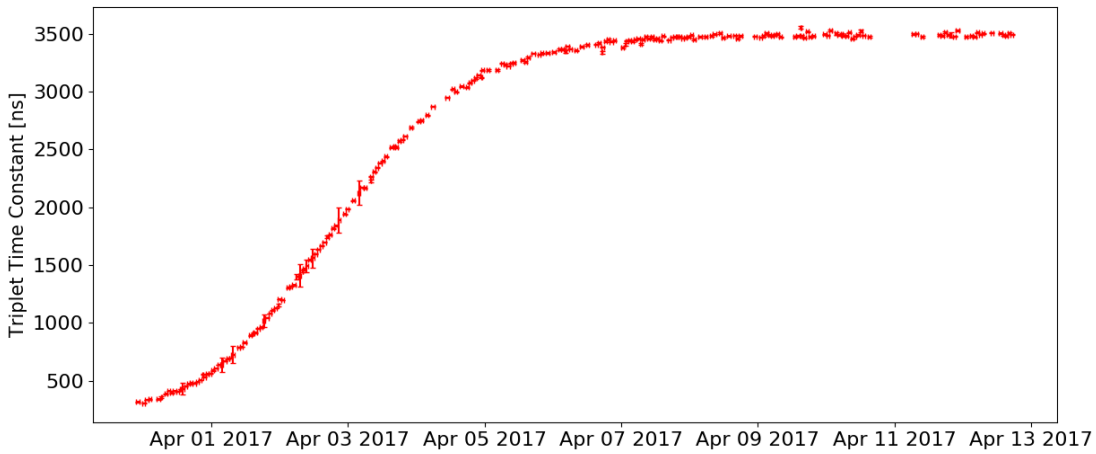

Figure 5.10: Measured triplet time constant as a function of time over the full period of pump/purge cycles. Each data point is the fitted triplet time constant one hour of integrated data from dominantly ^{39}Ar decays in gaseous argon the MiniCLEAN target volume.

controller, inducing a pressure drop at the node where the IV pressure measurements are being taken (PT4611). On the other hand, when transitioning from the pump-down phase to the pressure-boosting phase, the pressure controller setpoint is increased to a value greater than the current IV pressure. This prompts the pressure controller to close to allow pressure to build in the IV, causing the flow to the pressure controller to stop and allowing PT4611 to acquire a static pressure reading. The induced pressure offsets are consistent near the peak and the trough and are corrected for when evaluating the fraction of gas removed.

Fig. 5.11 shows the impurity model over time using the recursive model described above and measurements of the fraction of gas removed and replaced from pressure cycle measurements. The initial impurity level begins at 40 ppm. The lower limit of 1 ppb is enforced by the upper limit of impurity levels specified by the SAES getter used in the purification system.

5.3 Results

This section covers the major results of this study. Sec. 5.3.1 provides a measurement of the triplet time constant as a function of total impurity level. Sec. 5.3.2 discusses the measurement of the relative light yield on a component basis as a function of total impurity level.

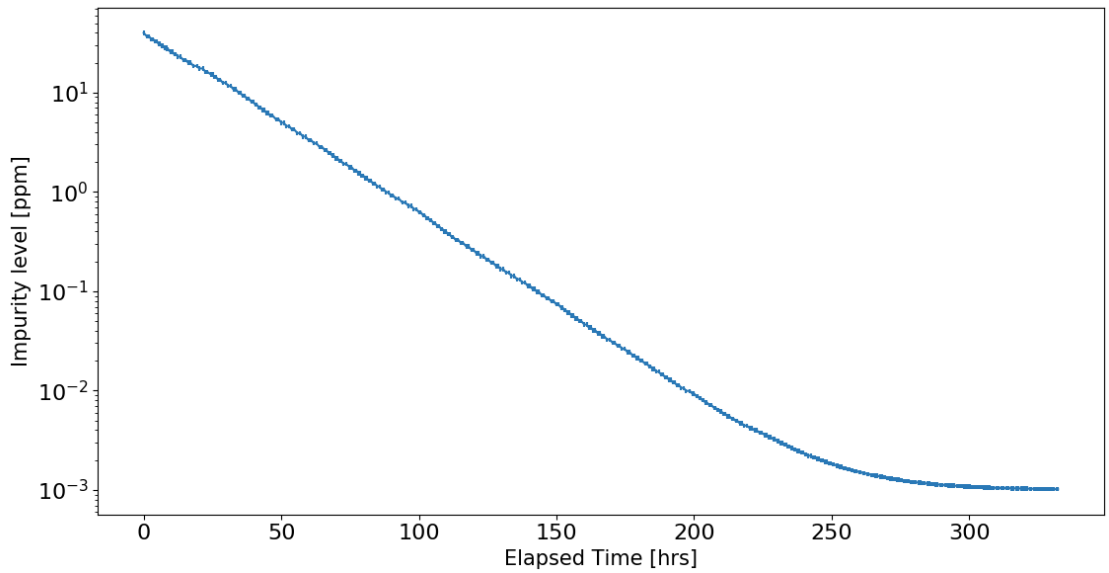

Figure 5.11: Estimated impurity level over time using recursive modeling of impurity levels.

5.3.1 Triplet Time Constant vs. Impurity Level

Time correlating the model of total impurity levels over time developed in Sec. 5.2.3 (Fig. 5.11) and the measurement of the triplet time constant over time in Sec. 5.2.1 (Fig. 5.10), yields a measurement of the triplet time constant as a function of total impurity level. Shown in Fig. 5.12, the triplet time constant improves with decreasing impurity level and plateaus in the 10s of ppb with a triplet time constant of approximately 3484 ns.

The data in Fig. 5.12 is fit to a functional form defined as:

$$\tau_m = \frac{\tau_N}{1 + k_1 \cdot \eta} \tag{5.2}$$

where τ_m is the measured triplet time constant, τ_N is the natural triplet lifetime with zero impurity present in the gaseous argon target, η is the total impurity level in ppm, and k is a fitting constant.

Alternatively, the triplet lifetime can be converted to a decay rate, shown in Fig. 5.13, and fit a linear function (the inverse of Eq. 5.2) defined in Eq. 5.4 as:

$$R_m = R_N \cdot (1 + k_2 \cdot \eta) \tag{5.3}$$

where R_m and R_N are the triplet decay rates (inverse of lifetime). The product of R_N and k is interpreted as the reaction rate of per ppm of impurities between the argon and an impurity molecule. The rate defined in this way has been measured by several groups in [131, 144, 148].

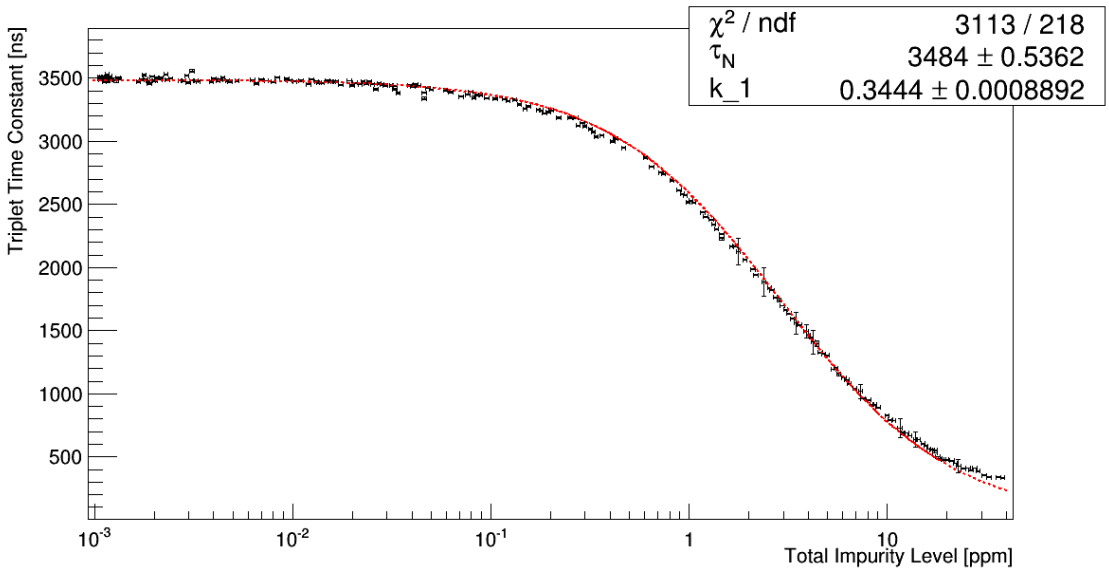

Figure 5.12: Measured triplet time constant as a function of impurity level. Also plotted is the fit result for a function of the form Eq. 5.2.

Based on RGA scans, it is known that the dominant impurity species in this data set were oxygen and nitrogen at operating temperatures less than 140 K. It has been shown in [91] that the quenching effects from nitrogen diminish for impurity levels less than 1 ppm, therefore it is assumed that the quenching is mostly due to oxygen when the total impurity level is below 1 ppm. Thus, the reaction rates from this fit are found to be 11.7×10^{-10} cm^3/s and are assumed to be the reaction rate between argon dimers in the triplet state with oxygen. This measurement agrees with values in the literature where [144] reports 2.6×10^{-10} cm^3/s and [91] reports 35×10^{-10} cm^3/s

It should be noted that the fitted χ^2 in Fig. 5.12 and Fig. 5.13 are both large. This is due to the disagreement in the high impurity region. This implies either this functional form does not describe the behavior well at high impurities (approximately > 1 ppm) or some additional systematic errors occur in this region. We are unaware of such additional systematic errors in our data so it is suspected that the functional form is altered at large impurity levels due to nitrogen, which is known to only significantly quench the triplet state for concentrations greater than 1 ppm [91].

5.3.1.1 Uncertainties

Several uncertainties were considered in the evaluation of the triplet time constant result. These are described below.

The statistical uncertainty on the triplet time measurements was extracted from the uncertainty on the fit value of the natural triplet time constant and found to equal $\pm$ 0.01%.

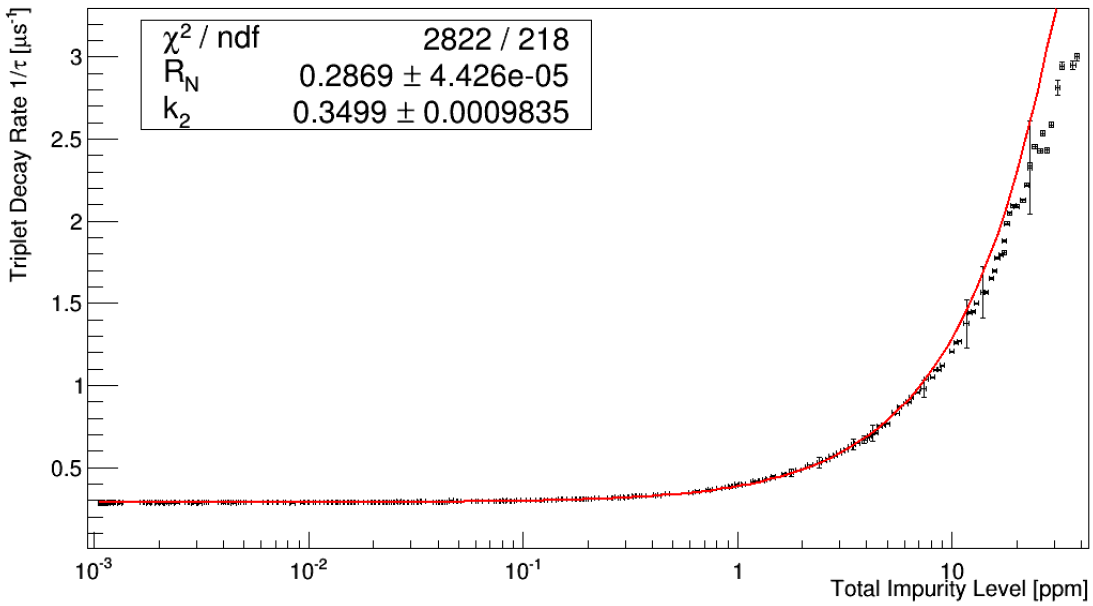

Figure 5.13: Triplet state decay rate as a function of total impurity level. Also plotted is the fit result for a function of the form Eq. 5.4.

The method for extracting the triplet time constant reported in Sec. 5.3.1 with the methodology described in Sec. 5.2 was developed and performed by the author. This was done as an independent cross-check of an analysis performed by J. Wang in [95] using a different analysis method. The two distinct analyses yielded consistent results and the difference between the two provides a systematic uncertainty of ± 0.40%.

J. Wang evaluated a collection of systematic uncertainties using his approach which yielded a total systematic uncertainty of ± 1.84 %. Described in further detail in [95], Wang considered systematic uncertainty sources from gaseous argon density variations (±0.07%), PMT gain variation (±0.26%), pulse finding algorithm uncertainty (±0.39%), uncertainties in the IV pressure while pumping on the IV (±0.73%), PMT event rate various (±0.96%), and an uncertainty on the radial cut (±1.31%).

Adopting the conservative approach of adding all of these uncertainties in quadrature yields a total uncertainty of ± 1.88% uncertainty.

5.3.2 Relative Light Yield vs. Impurity Level

The fitting procedure described in Sec. 5.2.1 is not only used to extract the triplet time constant, but also used to determine the relative light yield of each component. The weighting coefficient of each component (A, B, C, and D in Eq. 5.1) can be used to provide insight into how the overall amount of light produced by each component changes as a function of impurity level.

Fig. 5.14 shows the fitted weight parameter for each component as a function of measured triplet time constant. Each data point is a three component fit performed on the single PE arrival time distribution for electronic recoil events integrated over approximately one hour of data. However, because the integration time binning is not exactly one hour (due to the specifics related to time intervals on which data is parsed and written to disk), the components have been normalized such that their value should be equal to exactly one hour so that they can be compared on equal footing. The underlying assumption behind this method is that the event rate generating the electronic recoils is constant over the entirety of the pump/purge process, which is a reasonable assumption, since the impurities should not affect the rates of radioactive sources triggering the detector.

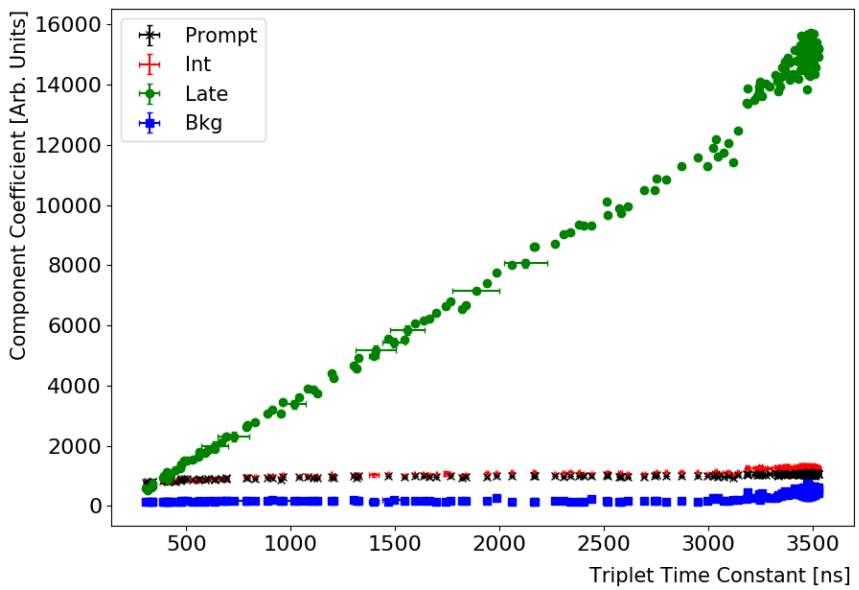

Figure 5.14: The fitted weighting coefficients for each component (A,B,C, and D) in Eq. 5.1 plotted as a function of measured triplet time constant (τ_3). The prompt, intermediate, and background components are approximately independent of the measured triplet time constant (i.e. impurity level), while the weighting of the late component depends strongly on the triplet time constant.

As seen in Fig. 5.14, the prompt and intermediate components remain approximately constant while the late component's weighting increases with measured triplet time constant. This is consistent with what is seen Fig. 5.6. As the triplet time constant becomes longer, the total area of the late component increases, so the overall weighting of its component will increase.

Given these component weighting coefficients, a ratio of the relative contribution from components can be evaluated. In particular, the ratio of the late component to the sum of

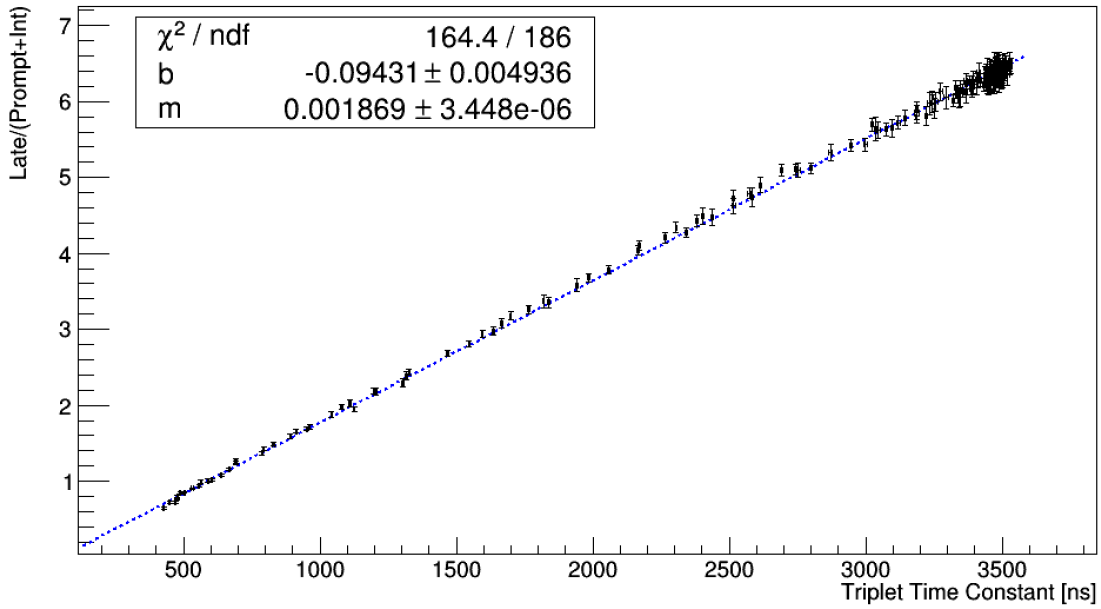

Figure 5.15: The component coefficient ratio Late/(Prompt + Intermediate) plotted as a function of measured triplet time constant. The data is fit to a linear relationship with good agreement. The relative contribution of the late component compared to the earlier components increases as the triplet time constant increases.

the prompt and intermediate components (i.e. Late/(Prompt + Intermediate) or C/(A+B)) is evaluated, plotted in Fig. 5.15, and fit to a line defined by :

$$f(\tau) = b + m \cdot \tau \tag{5.4}$$

where b is the intercept and m is the slope. This ratio is interesting because it quantifies the relative light yield of the late component (triplet state of the second continuum) compared to the prompt components (singlet state of the second continuum and contributions from the third continuum). This result shows that the late component's contribution increases linearly with measured triplet time constant while the prompt components remains unaffected.

The systematic bump in the absolute values of the component coefficient values seen around a measured triplet time constant of 3200 ns in Fig. 5.14 is correlated with turning on 8 additional PMTs part of the way through the pump/purge process. While single PE contributions from these PMTs were excluded from the analysis, the overall cross-talk background levels increased due to these PMTs being on. This systematic step is not present when taking the ratio (Fig. 5.15) as the overall amount of noise on each component increased proportionally.

5.3.2.1 Uncertainties

Several uncertainties were considered for the ratio presented in Sec. 5.3.2.

The statistical uncertainty is taken to be the uncertainty in the fitted values of the coefficients propagated through the evaluation of the Late/(Prompt + Intermediate) ratio for each point shown in Fig. 5.15. This yields an average statistical uncertainty of 1.23% when averaging over all of the points shown in Fig. 5.15.

Two systematic uncertainties are considered. The first is the spread in the Late/(Prompt + Intermediate) ratio at long triplet time constant values. Evaluating this number provides a handle on the spread in the ratio result once the measured triplet time constant has stabilized. Fig. 5.17 shows profile histograms of the triplet time constant (left) and Late/(Prompt + Intermediate) (right) ratio axes plotted in Fig. 5.15 for measured triplet time constant between 3400 ns and 3550 ns. Once the triplet time constant measurement stabilizes to 3480 ns, the distribution in the left-side histogram of Fig. 5.17 motivates placing a cut at 3425 ns to define the population of events from which to evaluate the spread in the ratio.

The right-side histogram in Fig. 5.17 is the distribution of measured Late/(Prompt + Intermediate) ratios after a cut of > 3425 ns on the measured triplet time constant is applied. This distribution is then fit to a Gaussian and the fitted standard deviation is taken to be the systematic spread in the evaluation of the Late/(Prompt + Intermediate). This yields an uncertainty of 1.29%. While this uncertainty was evaluated using the distribution of Late/(Prompt + Intermediate) at the stable end of the large measured triplet time constant values, it is assumed to be representative of the spread in the ratio at shorter triplet times and is applied as a flat uncertainty to all values. Given the good agreement with a linear fit to the ratio in Fig. 5.15, this is thought to be a reasonable and conservative assumption.

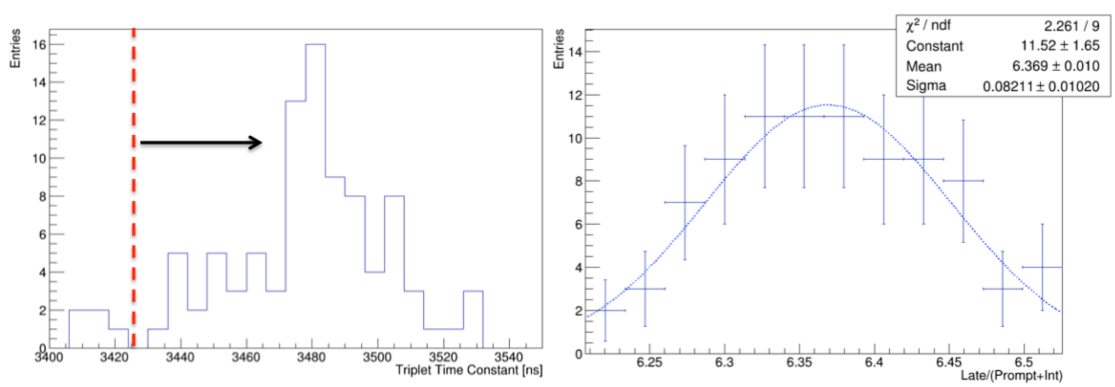

Figure 5.16: Profile histograms of the axes in Fig. 5.15 at late triplet time constant. Left: Distribution of measured triplet time constant for large values. Right: Distribution of Late/(Prompt + Intermediate) ratio values after applying a cut of $t_3 > 3425$ ns. The distribution is fit to a Guassian whose width is taken to be the systematic uncertainty in the spread in the ratio result.

The second systematic uncertainty considered is related to the fitted background contribution. As discussed in Sec. 5.2.1 and presented in Eq. 5.1, the single photoelectron arrival times are fit to the sum of three exponential plus a flat background. While the fitted background contribution is small, a systematic uncertainty on this background is evaluated by adding $\pm$ 1σ from the uncertainty in the fitted background coefficient to the late coefficient and determining the change in the Late/(Prompt + Intermediate) ratio. The uncertainty in background coefficient is added/subtracted to the late coefficient because the late component is the dominant component for the majority of the event window, so therefore a mis-characterization of the fitted flat background component would affect the late component more than prompt and intermediate components.

Fig. 5.17 shows the percent uncertainty as a function of measured triplet time constant in the evaluation of the Late/(Prompt + Intermediate) ratio when adding/subtracting the uncertainty in the fitted background coefficient from the late coefficient. The uncertainty is large at short triplet time constant because the background coefficient is larger (on a relative basis compared to the late coefficient) when compared to later times. For long measured triplet time constants, the systematic uncertainty from the background coefficient is found to be approximately 0.2%.

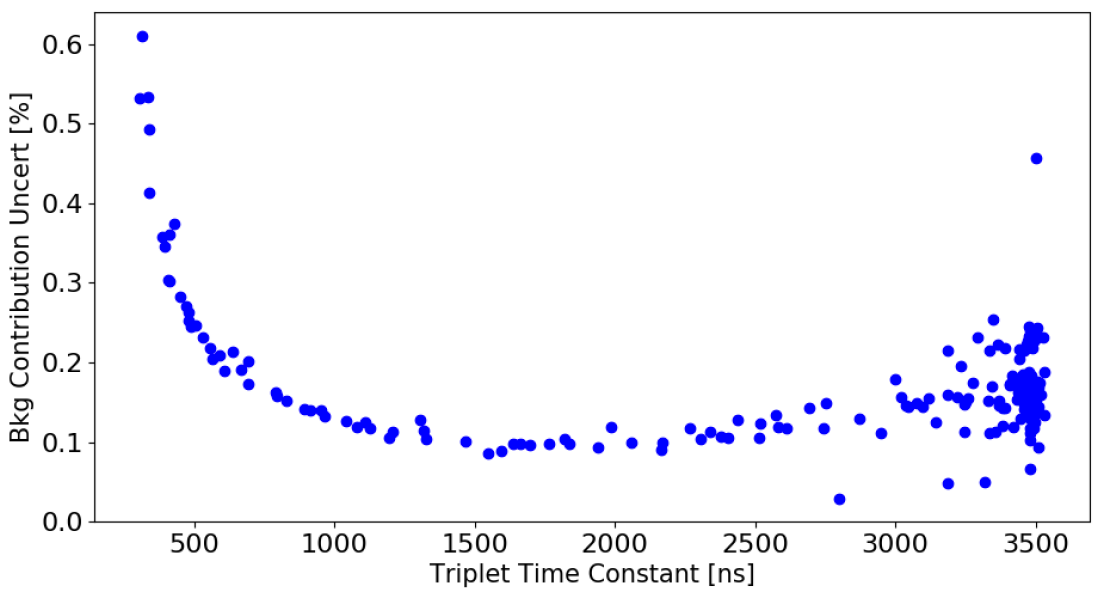

Figure 5.17: The percent uncertainty in the Late/(Prompt + Intermediate) ratio as a function of measured triplet time constant when adding and subtracting 1σ of the background coefficient to the late coefficient. At long triplet time constant, the systematic uncertainty from the background component is found to be approximately 0.2%.

The total uncertainty is evaluated by summing each of these uncertainties in quadrature. For Late/(Prompt + Intermediate) ratio values at long triplet time constant values, this

yields a total uncertainty of approximately ± 1.79%.

5.4 Discussion

To the best of the MiniCLEAN collaboration's knowledge, the fitted triplet time constant of 3484 ± 65 ns for gaseous argon at 1.5 bar and at a temperature of less than 140 K is the longest measurement of the triplet state lifetime. The dependence of the triplet lifetime on impurity level (assuming the impurity source is air) was also determined (Fig. 5.12) and fit to a functional form described by Eq. 5.2. A reaction rate between impurities and triplet state excimers (assumed to be dominated by O_2 for impurities less than 1 ppm) was found to be 11.7×10^{-10} cm^3/s and is consistent with previous measurements. The dependence of the measured triplet time constant on impurity level is an important indicator for the cleanliness of a detector when direct measurement of the impurity levels is not possible or impractical. This result is expected to be useful to experiments which contain high purity cold gaseous argon.

Also presented was the relative light yield contribution of the late component to the prompt components and its dependence on total impurity level (Fig. 5.14). A linear dependence on measured triplet time constant was found where the late component contributed 6.37 ± 0.11 times more light than the sum of the prompt and intermediate components for a measured triplet time constant of 3484 ns. This result is consistent with a comparable result of 5.5 ± 0.6 in [138] where the measured triplet time constant was 3140 ± 61 ns, while providing a more precise result across a larger range of impurity levels.

As previously discussed in Sec. 2.4.1 and shown in Figs. 5.6 and 5.15, the triplet state lifetime and relative contribution to the light yield increase for lower total impurity levels. This is because the presence of impurities quenches the triplet excimer state via non-radiative de-excitation reactions. When the impurity levels are large, the non-radiative de-excitation interaction probability is high for the long-lived triplet states which reduces the measured triplet time constant. As a consequence, the non-radiative de-excitation also quenches the light from this state. This naturally leads the the observed result where the total light yield contribution from the triplet component relative to the prompt components strongly depends on the impurity level. Therefore these results are consistent and expected under the explanation of non-radiative de-excitation of triplet states via interactions impurities.

If one considers the introductory discussion of the contribution and possible temporal separation of scintillation light from the singlet state of the second continuum and the light from the third continuum in Sec. 5.1, this would motivate the development of other coefficient ratios. For example, if the singlet state of the second continuum was observed to be sufficiently separated in time from the fast scintillation light of the third continuum, one could be able to fit the contributions from these separately and evaluate ratios such as the second continuum component to the third continuum component as a function of impurity level. Unfortunately, MiniCLEAN does not have the timing resolution to separate the singlet

state of the second continuum from the third continuum in the prompt peak so this is not possible.

Additionally, the author suspects the contents of the intermediate component to be a combination of instrumentation effects and delayed emission from the TPB (as suggested by [146]), in unknown proportions. Comparing the intermediate region with previous double and late pulsing measurements performed on a single cold PMT in [29] suggests that the intermeidate region may be composed of roughly 50% double/late pulsing and 50% delayed reemission light. However, the scale of the hypothesized delayed reemission is not consistent with the scale suggested by [146]. Without a separate pulsed light source to independently determine the double/late pusling rates for each of the PMTs, it is difficult to untangle this intermediate region from PMT effects and delayed light from the TPB.

Lastly, it should also be noted that this study did not attempt to measure or include potential effects of trace Xe and Kr on the scintillation light intensity. Elevated levels of Kr and Xe were not observed in the RGA scan and the author assumes that these elements are present in their natural trace abundance proportional to the initial air impurity. Any affects from Xe and Kr on the scintillation light are assumed to be high-order effects.

In conclusion, it is expected that this results will be useful for experiments using high-purity gaseous argon. This will provide an ability to indirectly track impurity levels using measurements of the triplet time constant in gas. The author also expects the relative light yield measurements to help improve the modeling of light yield in gas when the dependence on impurity levels needs to be taken into account.

Chapter 6

Wavelength Shifter R&D: Introduction and Setup

This chapter covers research and development wavelength shifting thin films and makes heavy use of material published by the author in [149].

As mentioned in Sec. 2.4.3, TPB is a commonly used wavelength shifter which has been widely studied [93, 150, 151, 152, 153, 122, 154, 155, 156, 157, 158] and is commonly used in the form of vacuum-deposited thin films in many experimental programs [77, 78, 79, 60, 51, 49, 80, 81] due to their relatively high wavelength shifting efficiency. There is a need to understand the underlying microphysical optical properties of TPB films across the full wavelength spectrum of liquid noble gas targets to improve Monte Carlo modeling of detectors. An improved model of TPB will inform and improve detector design and data/Monte Carlo comparison.

Chapters 6 and 7 present the first ever direct measurement of the intrinsic quantum efficiency (QE) of TPB evaporated thin films, defined as the probability that a photon absorbed by a TPB molecule is reemitted, and its dependence on incident wavelength. Also presented are measurements of the absorption length of TPB in the VUV regime and a measurement of the average efficiency of the secondary reemssion process, referred to as SQE, in the region where the TPB absorption and reemission spectra overlap. As part of this work, room temperature measurements of the reemission spectrum of TPB as a function of incident wavelength are presented. The wavelength shifting efficinecy (WLSE) of film, as defined in [93], is also studied for the purpose of a direct comparison to this work. These results cover the spectral range studied by [93] with improved precision, while extending the measurements down to 50 nm.

Sec. 6.1 provides an review of previous studies of TPB relevant to this work. Sec. 6.2 provides an overview of the hardware components of the experimental apparatus. Sec. 6.3 describes the various apparatus configurations used to cover the full wavelength region of interest (ROI). Sec. 6.4 describes the sample fabrication. Sec. 6.5 describes the data acquisition methods. Sec. 7.1 contains descriptions of the analysis methods used to calculate the absolute WLSE, the detailed Monte Carlo model used to simulate the setup, and the tech-

niques to extract the VUV QE, VUV absorption lengths and SQE. Sec. 7.2 presents results. Sec. 7.3 provides a comparison of this work to previous studies and discusses the impact of various improvements to the measurements. Future work and conclusions are presented in Sec. 7.4 and Sec. 7.5 respectively.

6.1 Previous TPB Measurements

This section provides a review of previous TPB measurements relevant to this work.

The previous measurements provide motivation for this study as well as references to compare the measurements and model predictions made in this work to previous comparable measurements.

6.1.1 2010 Absolute Fluorescence Efficiency Measurement

A study of the absolute wavelength shifting efficiency (WLSE) of thin films of vacuum-deposited TPB on an acrylic substrate was performed by Gehman et al. in 2011 [93]. Shown in Fig. 6.1, this measurement was performed without reference to other materials in the range of 120–250 nm.

The WLSE as defined in [93] is a "black-box" definition of the efficiency that includes both the intrinsic QE of the TPB as well as certain optical properties of the TPB film and substrate. The resulting quantity is the efficiency that a photon absorbed by the sample is reemitted from the sample. This measurement is thus sample dependent, including effects of scattering and absorption, and cannot be universally applied to other apparatus as a property of TPB.

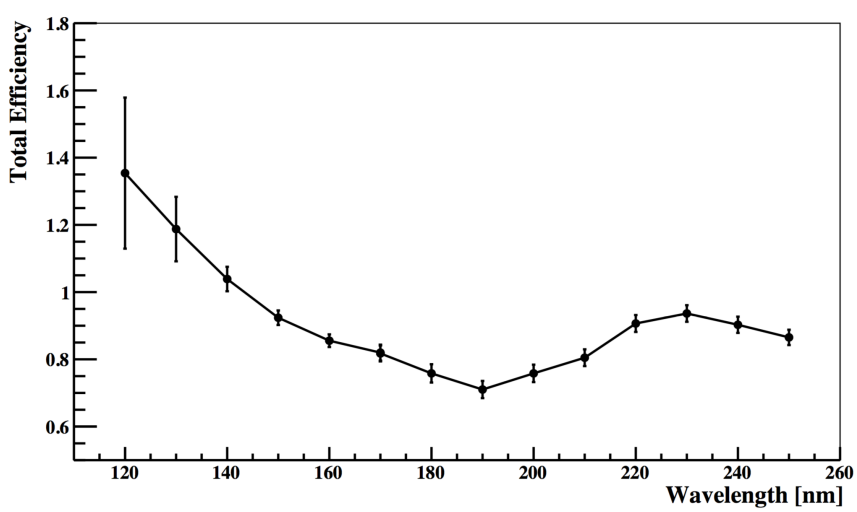

Figure 6.1: Integrated fluorescence efficiency as measured by Gehman et al. in [93] in 2011.

The 120 nm lower limit of the measurement in [93] was due to a limitation with the light source used in the measurement. The increasing interest in He and Ne targets, along with the observed upward tend observed at short wavelengths (Fig. 6.1), was the primary initial motivation of this work to extend the absolute WLSE measurements to lower wavelengths. Along with Gehman, much of the hardware elements used in [93] were used in this work.

6.1.2 Relative efficiency for various thicknesses

A study by McKinsey et al. in 1997 [153] measured the fluorescence efficiency of several wavelength shifters relative to a sodium salicylate as a function of deposition method and film thickness at 58.4- and 74.0-nm (Fig. 6.2). This study determined that evaporated TPB films yielded the highest relative efficiency with an optimal coating thickness of 0.2 mg cm^{-2}. The fluorescence efficiency of evaporated TPB films (at the optimal thickness) relative to the sodium salicylate reference was found to be 3.9 $\pm$ 0.1 at 58.4 nm and 3.7 $\pm$ 0.1 at 74.0 nm. This study demonstrated that TPB is a very efficient wavelength shifter in the XUV compared to sodium salicylate, that evaporated TPB thin films were the preferred deposition method to maximize the wavelength shifting efficiency, and the optimal thickness of evaporated TPB films is 0.2 mg cm^{-2} (2- to 3-μm film thickness equivalent).

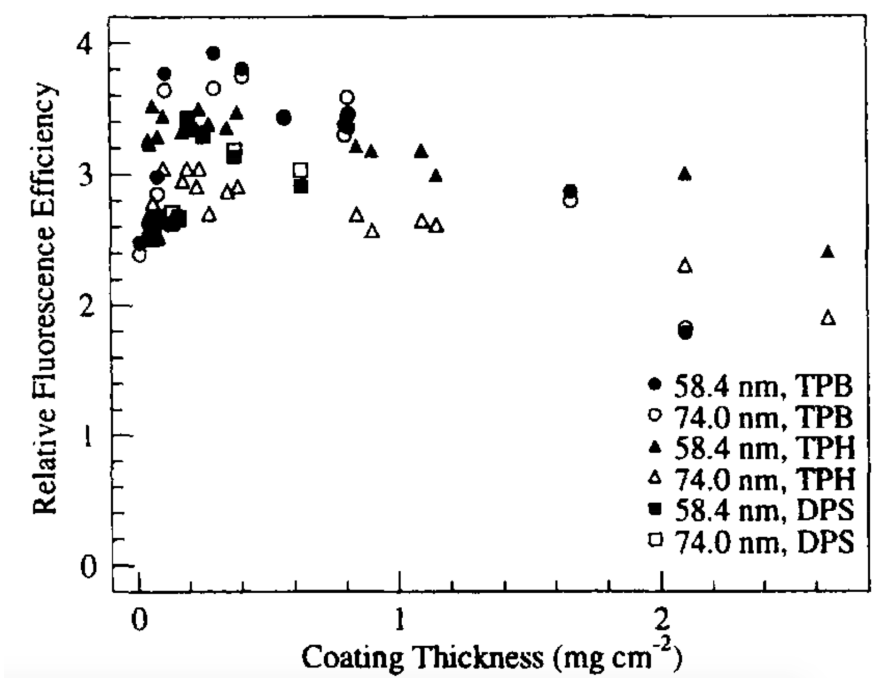

Figure 6.2: Fluorescence efficiency of TPB and other samples as a function of thickness relative to a sodium salycilate reference for 74 nm and 58 nm incident light [153].

The QE of sodium salicylate was measured by Brumer in 1969 [158] and was found to be 0.42 at 58.4 nm and 0.37 at 74.0 nm. Comparing this to the relative efficiency measurements

in [153] suggests that the QE of TPB at these XUV measurements is greater than unity, though McKinsey et al. explicitly state that "No attempts are made to directly measure absolute fluorescence efficiencies". In particular, if one takes the simple approach of multiplying the QE values from [158] with the relative efficiency measurements of [153], this suggests that the QE of TPB may be as high as 1.64 at 58.4 nm and 1.37 at 74.0 nm.

The scale and upward trend of the absolute WLSE observed in [93] (Fig. 6.1) combined with the inferred greater than unity QE by combining measurements from [158] and [153] further motivated this study to measure the WLSE of TPB at sub-100 nm wavelengths.

6.1.3 Temperature-dependent Optical Characterization

A 2013 study by R. Francini et al. [154] provided insight into TPB's emission intensity and reemission spectra as a function of temperature, shown in Fig. 6.3 and Fig. 6.4 respectively, for evaporated TPB films on a glass substrate.

As seen in Fig. 6.3, the relative integrated fluorescence intensity of evaporated TPB films increases with lower temperature.

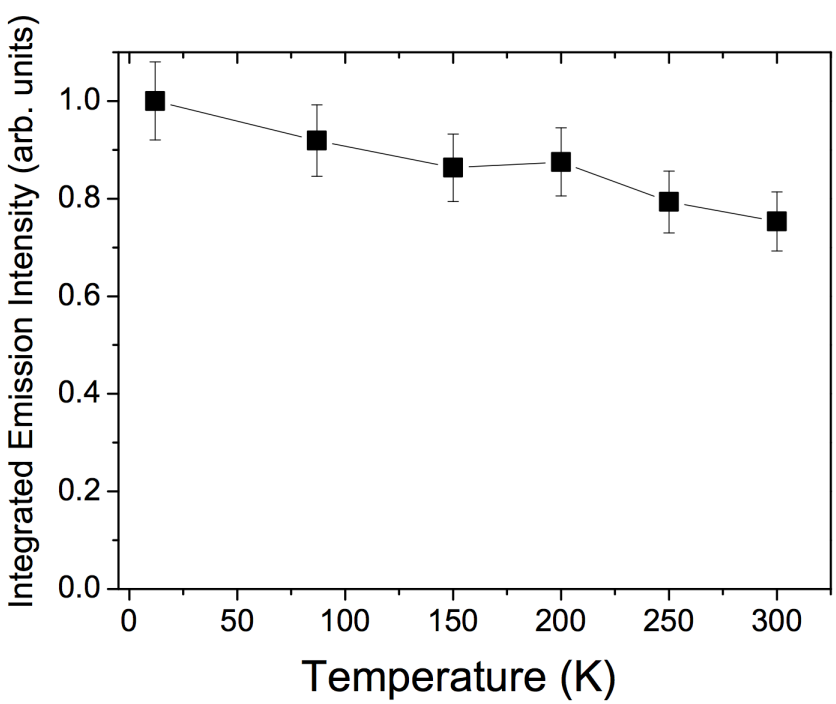

Figure 6.3: Relative integrated fluorescence intensity of an evaporated TPB film as a function of temperature for 128 nm excitation light [154]. The lowest temperature measurement is normalized to one.

Interesting structures appear when looking at the reemission spectra as a function of

temperature (Fig. 6.4). As the temperature of the TPB film is decreased, distinct peaks begin to appear. R. Francini et al. attribute the apperance of these peaks to unresolved vibronic structures at 300K becoming visible as the temperature is decreased [154]. The structure and spacing of peaks in the low temperature reemission spectra "closely corresponds to an effective vibrational mode associated to the stretching mode vibration of trans-butadiene" [154, 159, 160].

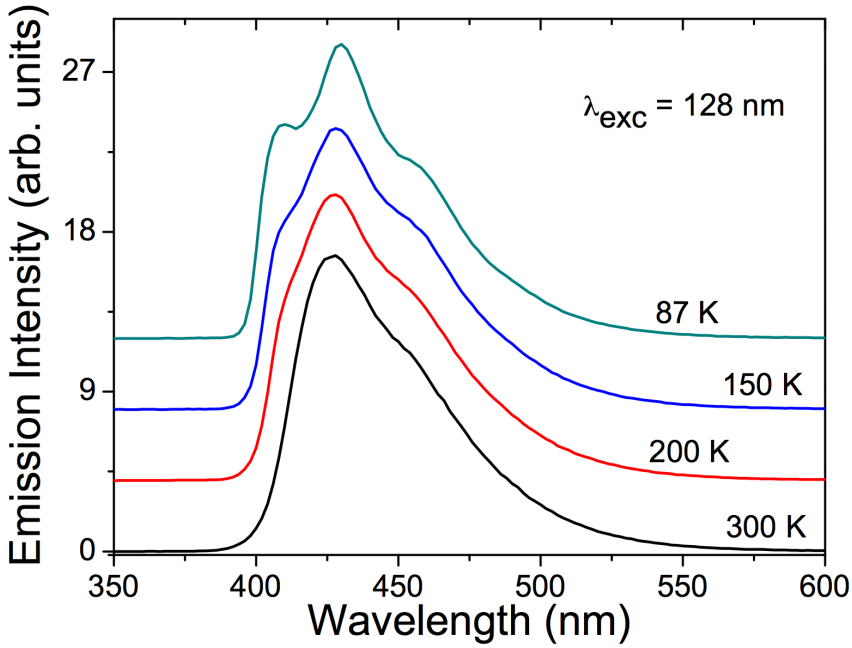

Figure 6.4: TPB reemission spectra as a function of temperature for 128 nm excitation light [154].

R. Francini et al. also observed a red-shifting of the reemission spectrum as a function of sample thickness at room temperature. This is shown in Fig. 6.5. The red-shifting is explained by reemitted photons being reabsorbed by the TPB in the blue tail where the absorption and reemission spectra overlap. As expected, the red-shifting increases with sample thickness.

6.2 Experimental apparatus

The primary objective of this work is to measure the intrinsic QE of TPB and the characteristic VUV photon absorption length in TPB, and its dependence on incident wavelength. Also measured are the room-temperature reemission spectrum and the black-box WLSE, with its dependence on sample thickness and incident wavelength. These measurements

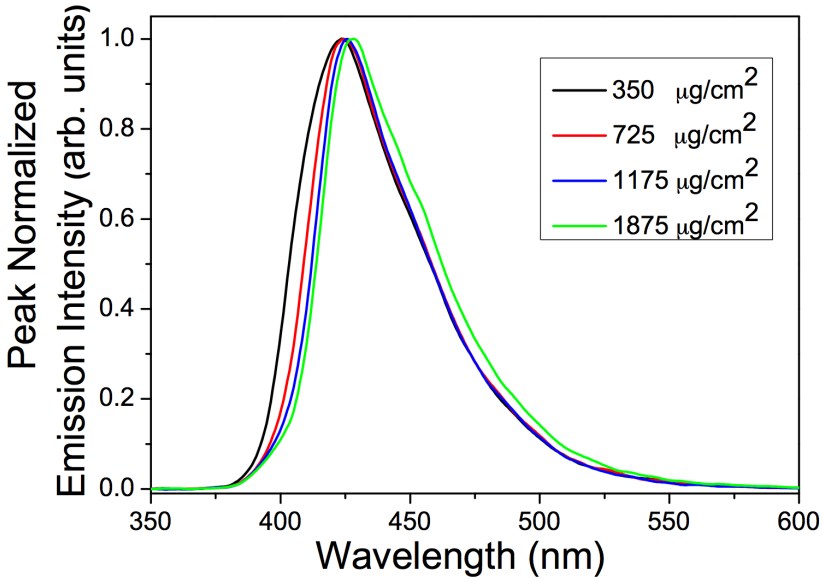

Figure 6.5: Peak normalized TPB reemission spectra as a function of sample thickness at room temperature [154].

are performed by exposing TPB thin film samples to UV light of a known wavelength and intensity and measuring the amount and spectrum of light reemitted from fluorescence.

A cartoon representation of the experimental apparatus is shown in Fig. 6.6. The setup consists of a broad spectrum UV light source, filters, optical elements, a monochromator, a sample mounting assembly and photon detectors. All of the apparatus components are installed within a windowless vacuum chamber and held at vacuum. The setup is designed to produce and project monochromatic UV light onto thin film WLS samples in a repeatable fashion. A photodiode is used to separately measure the flux of photons incident on and reemitted by the samples. A spectrometer is used to measure the reemission spectrum of the samples.

Individual elements used in the experimental apparatus are described in this section. Because this work covers a wide range of wavelengths (50 – 250 nm), several distinct hardware configurations are used. Each of these configurations are constructed from elements described in this section. The distinct apparatus configurations are described in Sec. 6.3.

6.2.1 UV light source

This work uses two distinct light sources. Each light source is specialized to a subset of the entire 50 – 250 nm wavelength ROI. Only one light source may be attached to the setup at a time.

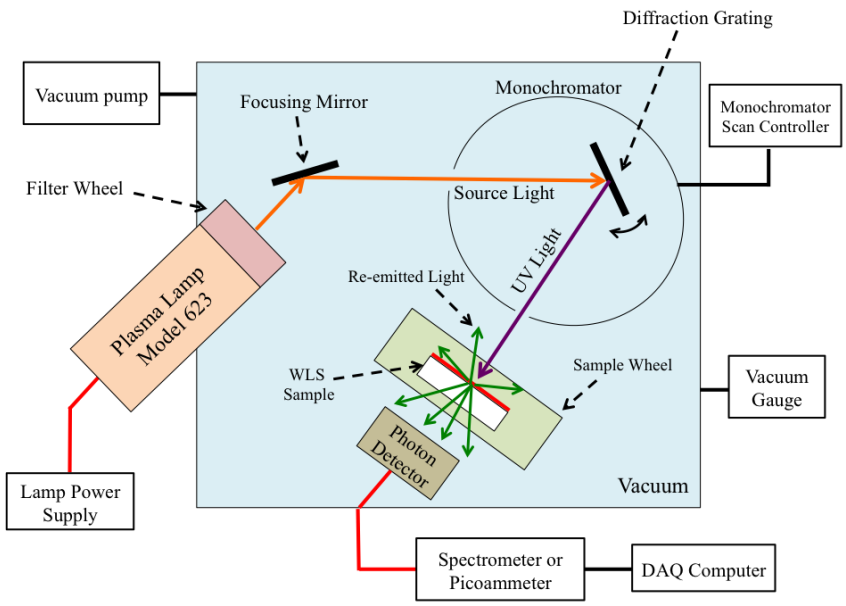

Figure 6.6: A cartoon schematic of the experimental setup for the Long Wavelength Configuration (Sec. 6.3.1).

6.2.1.1 Deuterium light source

The McPherson Model 623 light source, referred to as the Deuterium Light Source (DLS), produces light for measurements in the range of 125 – 250 nm. The DLS contains a sealed deuterium gas volume which is ionized to produce broad spectrum light with a bright UV component. The output light passes through a circular 1" diameter MgF_2 exit window. The MgF_2 window has a transmission cutoff wavelength of 115 nm which drives the lower limit of emission for this source [161]. The DLS is powered using a McPherson Model 732 power supply.

6.2.1.2 Windowless light source

The McPherson Model 629 Hollow Cathode Gas Discharge Source, referred to as the windowless light source, produces light for measurements in the range of 45 – 150 nm. Unlike the DLS, the windowless light source does not have a window at its output. A feed gas is supplied to the lamp at a constant pressure and is ionized using high voltage. The spectrum of light output by the lamp depends on the choice of the feed gas. Because there is no sealing window between the light source and the rest of the setup, a differential pumping port near the lamp output is used to reduce the gas load on the vacuum from the feed gas flowing out of the light source's output.

6.2.2 Optical chain

This section describes the elements that make up the optical chain. These are the filter wheel, focusing mirror and monochromator.

6.2.2.1 Filter wheel

An Action Research Corporation Model 52 filter wheel is coupled directly downstream of the light source. The filter wheel is used to apply optical filters to the broad spectrum light output from the light source for certain classes of measurements (Sec. 6.5). The filter wheel has four slots which can each hold a 1.90-cm diameter disk. Changing the selected filter slot is done using an exterior nob and is possible while the setup is under vacuum. When a slot is selected, the filter is placed concentrically in the light output from the light source. All light must pass through the selected filter wheel slot to continue along the optical chain.

Three of the four slots in the filter wheel are used. The first slot is empty, which allows for a no-filter condition. The second slot contains a 0.48-cm thick, uncoated fused quartz silica filter which has a 155 nm cutoff. The third slot holds a 0.48-cm thick, uncoated MgF_2 with a 115 nm cutoff. The fused quartz silica and MgF_2 filters are used as high-pass optical filters which allow measurements of background levels (Sec. 6.5.1.4).

6.2.2.2 Focusing mirror

A McPherson Model 615 focusing elbow sits between the filter wheel and monochromator entrance slit. The focusing elbow contains a curved Al+MgF_2 focusing mirror which focuses the light passing through the filter wheel onto the monochromator entrance slit. The focus of the mirror is adjusted using three set screws and is configured to maximize the light output at the monochromator's exit for wavelengths in the ROI.

6.2.2.3 Monochromator

A McPherson Model 234/302 Vacuum Ultraviolet Monochromator is used to output monochromatic light of a selected wavelength from a broad spectrum input. The light entering the monochromator passes through an entrance slit which is 1.78-mm wide and 4.88-mm high. The entrance slit projects incoming light onto a rotatable holographic diffraction grating positioned near the center of the monochromator. The angle between the diffraction grating and the incoming light determines the wavelength of light projected from the grating onto the monochromator's exit slit. The diffraction grating's angular position is adjusted and set using a servo motor which is controlled using the McPherson Model 789A-3 Scan Controller. The exit slit of the monochromator has the same dimensions as the entrance slit. Fig. 6.7 shows a comparison of monochromator wavelength setting and the measured spectrum of the output light. The peak of the output light spectrum is in good agreement with the monochromator setting.

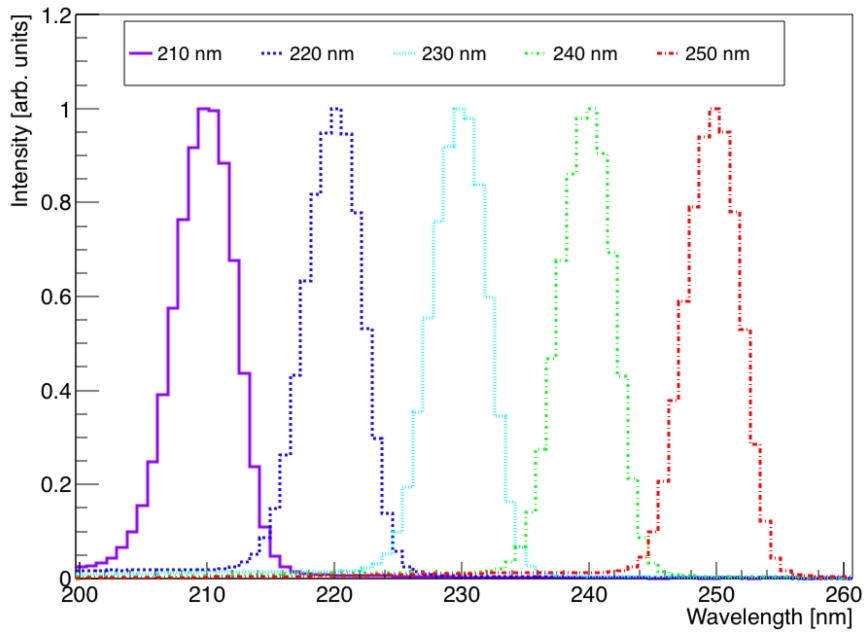

Figure 6.7: A set of light specta measured downstream of the monochromator's exit slit for several wavelength settings using an Al+MgF_2 diffraction grating. Each label indicates what the monochromator was set to when each spectrum was taken. There is good agreement between the monochromator setting and the output spectrum. All spectra peaks are normalized to one.

This work uses two types of diffraction gratings. The monochromator only holds one grating at a time. Similar to the light sources, each diffraction grating is specialized to a subset of wavelengths in the ROI. The two diffraction gratings are an Al+MgF_2 coated grating with 1200 gratings per mm, and a Platinum (Pt) coated grating with 2400 gratings per mm. As shown in Fig. 6.8, the Al+MgF_2 coated grating outperforms the Pt coated grating for wavelengths greater than 105 nm.

6.2.3 Sample holder

The monochromator's outlet attaches to a McPherson Model 648 Vacuum Filter Wheel, referred to as the sample wheel. The sample wheel contains five 2.54-cm diameter slots for sample disks. The sample disks are installed in the wheel and fixed in place using snap rings. The selected slot in the sample wheel is changed using an external knob and may be adjusted when the setup is under vacuum. The adjustment knob allows the cycling of multiple samples in and out of the UV beam during a data acquisition run. When a slot is selected, the sample slot is placed concentrically in the monochromatic UV beam exiting the monochromator. The sample slots are labeled 1 to 5. Slot 1 contains a thick aluminum disk, used to perform a dark current measurement. Slot 2 is left empty to allow for a measurement

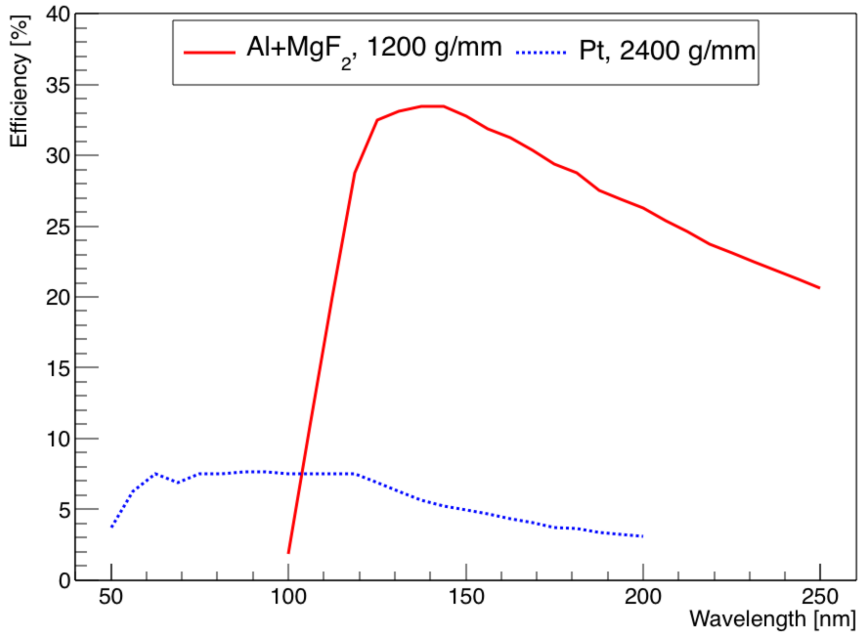

Figure 6.8: A comparison of the reflective efficiencies for an Al+MgF_2 coated grating and a Platium (Pt) coating grating. Plot data provided by McPherson Inc. [162].

of the total VUV flux incident on the samples from the monochromator's output. Slots 3 through 5 hold WLS samples to be studied.

6.2.4 Photon detection

This work uses two types of photon detectors: a photodiode and a spectrometer. The setup uses one of these detectors at a time. As shown in Fig. 6.6, photon detection occurs downstream of the sample wheel.

6.2.4.1 Photodiode

An Opto Diode AXUV100G photodiode [163, 164, 165, 166] is used to measure the flux of VUV light incident on samples as well as the flux of reemitted light from WLS samples in the sample wheel. The device is a passive, windowless photodiode cell with an active area of 1 cm by 1 cm. A vacuum electrical feedthrough and coaxial cable (outside of the vacuum space) electrically couple the photodiode to an external Keithley 485 picoammeter for photocurrent readout. A data acquisition computer connected to the picoammeter queries real-time current readings using a LabVIEW graphical user interface (GUI) and stores the values for offline analysis. The absolute response of the photodiode was calibrated by National Institute of Standards and Technology (NIST) in February of 2016 [166] in the range of 50 – 1100 nm. The absolute response as a function of wavelength is shown in Fig. 6.9.

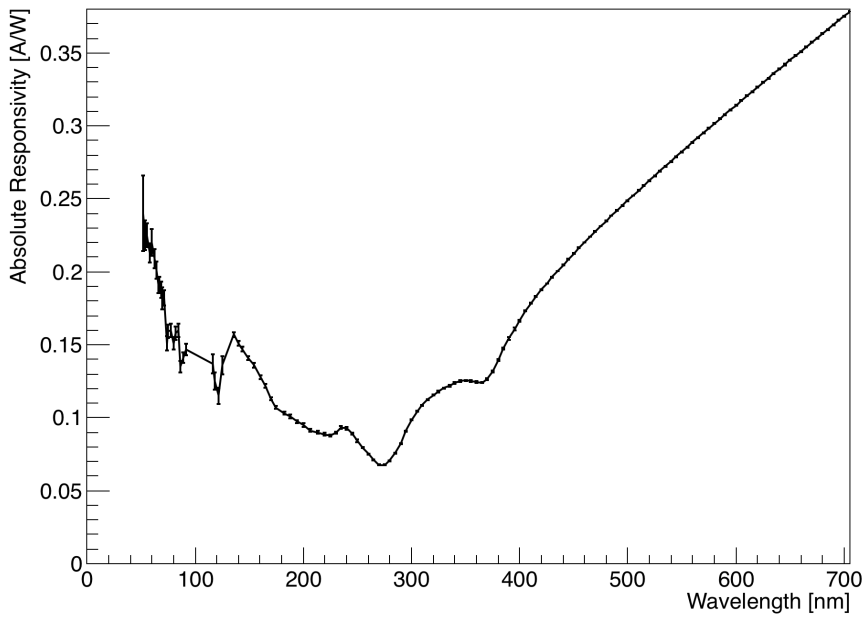

Figure 6.9: The AXUV100G photodiode [163] absolute responsivity calibration as a function of wavelength from NIST in the range of 50 – 700 nm. The photodiode was calibrated in February 2016 [166] for wavelengths 50 – 1100 nm.

6.2.4.2 Spectrometer

An Ocean Optics QE65000 spectrometer is used to measure the reemission spectrum of WLS samples. A vacuum feedthrough assembly consisting of a collimating lens and fiber optic allows light to be collected and routed out of the vacuum space for analysis. A 200-μm diameter quartz fiber couples the vacuum feedthrough assembly output to an input port on the spectrometer.

The spectrometer is sensitive to wavelengths in the range 200 – 1000 nm. The Ocean Optic's Spectra Suite software package installed on the data acquisition computer is used to configure and read out the spectrometer.

6.3 Apparatus configurations

Three apparatus configurations are used to cover the ROI (50 – 250 nm). These are the long wavelength, intermediate wavelength, and short wavelength configurations. Each configuration specializes to a subset of VUV wavelengths in the ROI and is composed of the hardware elements described in Sec. 6.2. The long wavelength and intermediate wavelength configurations overlap in the range of 130–150 nm which allows for cross checks of configuration–dependent systematic uncertainties.

The hardware composition of each configuration maximizes the intensity of VUV light exiting the monochromator within its particular wavelength range. Maximizing VUV intensity is done to produce the best signal to noise possible, since the amount of observed reemitted light from the samples should be proportional to the incidient light flux.

6.3.1 Long wavelength configuration

The Long Wavelength Configuration (LWC) is used to measure the WLSE and reemission spectra of samples for incident wavelengths in the range of 125 – 250 nm. As shown in Fig. 6.6, this configuration uses the DLS, filter wheel, focusing mirror, monochromator with the Al+MgF_2 diffraction grating and sample wheel.

6.3.2 Intermediate wavelength configuration

The Intermediate Wavelength Configuration (IWC) is used to measure the WLSE and reemission spectra of samples for incident wavelengths in the range of 100 – 150 nm. A cartoon representation of this configuration is shown in Fig. 6.10. This configuration uses the windowless light source, filter wheel, monochromator with the Al+MgF_2 grating and sample wheel. Unlike the LWC, this configuration uses the windowless light source and does not use the focusing mirror. A high purity N_2 or argon feed gas is used in the windowless light source in this configuration.

6.3.3 Short wavelength configuration

The Short Wavelength Configuration (SWC) is used to measure the WLSE and reemission spectra of samples for incident wavelengths in the range of 45 – 100 nm. This configuration is very similar to the IWC. The only differences are that a Pt diffraction grating is used instead of the Al+MgF_2 grating, and the feed gas used for the windowless light source is a 90% Neon, 10% Helium mixture.

6.4 Sample fabrication

Several TPB thin-film samples were fabricated using thermal evaporators at the Molecular Foundry at Lawrence Berkeley National Laboratory and in the Dr. Daniel McKinsey Laboratory at the University of California at Berkeley. A tabulation of samples used in this work are shown in Table 6.1. The films were deposited on stabilized ultraviolet-transmitting (SUVT) acrylic manufactured by Polymer Plastics Company, LC. A stock acrylic sheet was cut into circular disks with a 2.54-cm diameter and 0.318-cm thickness. The transmission of the SUVT acrylic, shown in Fig. 6.12, was measured and shown to be consistent with the manufacter's data sheet [167]. The acrylic's transmission is 90% for wavelengths longer than 300-nm and 0% for wavelengths below 250-nm, as shown in Fig. 6.12. This is important

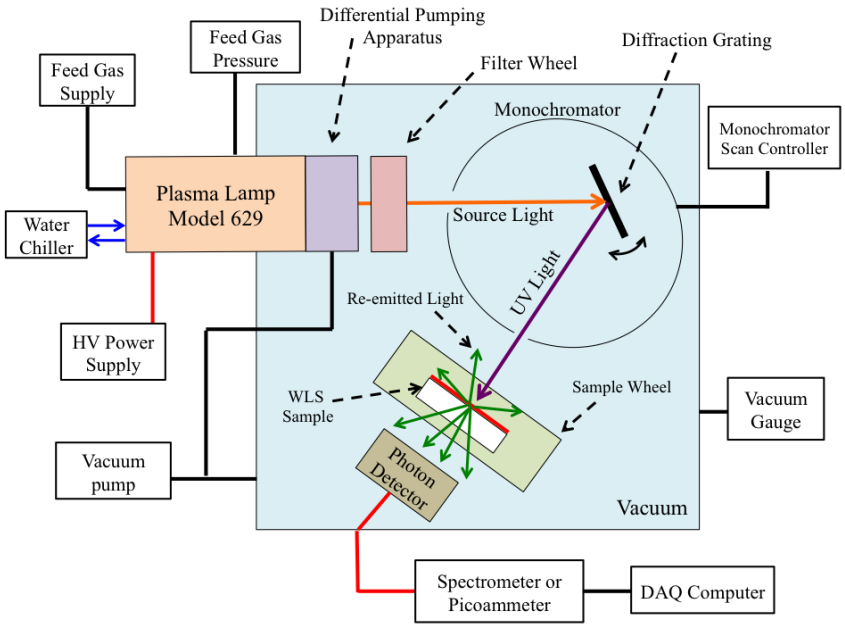

Figure 6.10: A cartoon schematic of the experimental setup for the IWC and SWC (Sec. 6.3.2 and Sec. 6.3.3).

because the acrylic substrate should behave as a high-pass filter, being transparent to the reemitted light from the TPB but opaque to the UV light incident on the sample.

Evaporative deposition was performed at a pressure less than 5E-6 torr. Film thicknesses between 0.5μm and 3.7μm were chosen so that our samples would be comparable in thickness to those used in [93] and in the MiniCLEAN and DEAP-3600 experiment.

The final thicknesses of the TPB thin films were measured using a Dektak Profilometer. Before evaporative deposition, two small pieces of Kapton tape were placed on opposite edges of the acrylic substrate. Following evaporation, the Kapton tape was removed to provide a location to measure film thickness. This was done by measuring the height of the step between the acrylic substrate (where the Kapton was attached) and the TPB film. Step measurements were performed at least three times at each location and averaged. Measurements at opposite locations of the sample were within the quoted uncertainty, indicating that thickness gradients across the sample were small. No attempts to directly measure the gradient profile across the full surface of the sample were performed due to a concern that the profilometer tip could damage the TPB surface. As conservative measure, the quoted uncertainty in TPB film thickness (Table 6.1) is larger than the any difference in film thickness observed at opposite ends of the samples.

Due to evidence that ambient ultraviolet light can degrade the WLS performance of TPB thin films [153, 122], after fabrication the samples were stored in a separate dark, clean vacuum chamber held at a pressure of less than 1E-1 torr using an oil-less diaphragm pump.

Sample	Thickness [μm]	Uncert. [μm]
A	0.5	0.1
B	0.7	0.1
C	0.9	0.1
D	1.8	0.2
E	2.2	0.2
F	2.55	0.2
G	3.1	0.2
H	3.7	0.2

Table 6.1: Summary of samples fabricated and studied in this work. The thickness column referes to the TPB film thickness as measured by a profilometer.

Each sample was measured within a month of its fabrication, and each sample was only measured up to three times in each configuration. Results from the repeated measurements were consistent with each other, suggesting no degradation for this level of exposure to within the uncertainty of the measurement.

6.5 Measurement procedure

This section describes the two classes of measurements performed in this work: photocurrent readout for WLSE measurements, and reemission spectra.

6.5.1 Photocurrent measurements

A measurement of the photocurrent output by the photodiode is required to determine the flux of VUV light incident on the samples as well as the flux of reemitted light captured by the photodiode. These photocurrent measurements are used as inputs in the WLSE calculations, described in Sec. 7.1. The four types of photocurrent measurements made are Dark, Light, Sample and Background. Each of these are described in this section, and are illustrated in Fig. 6.11.

6.5.1.1 Dark photocurrent

The dark photocurrent measurement provides a baseline measurement of the dark current for subtraction. This is shown in the top left of Fig. 6.11. It is performed by selecting slot 1 in the sample wheel, which contains a 2.54-cm diameter aluminum disk with 0.635-cm thickness. The aluminum disk blocks any light from reaching the photodiode, allowing for a proper baseline measurement.

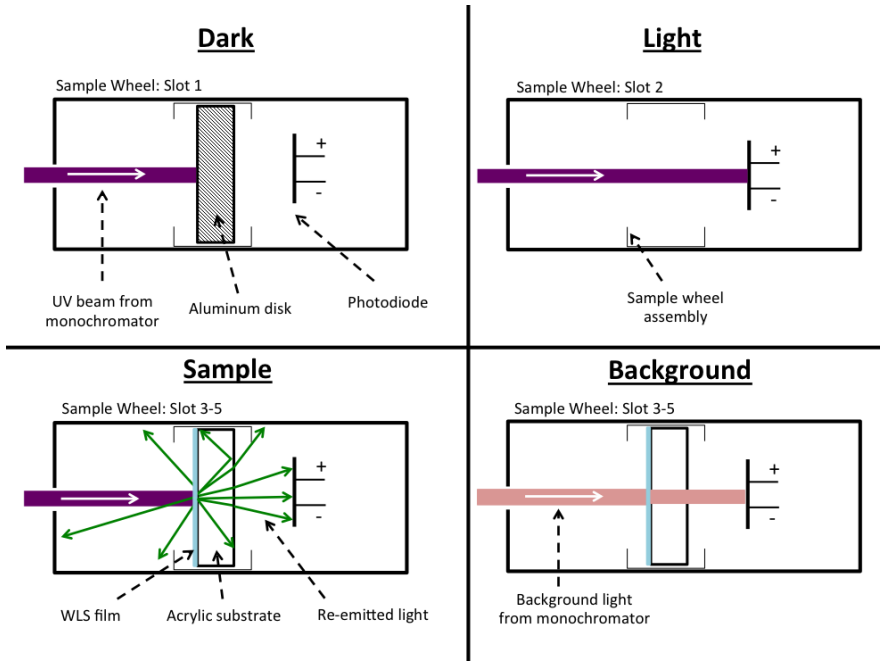

Figure 6.11: A cartoon representation of the four types of photocurrent measurements.

6.5.1.2 Light photocurrent

The light photocurrent measurement provides a measurement of the flux of VUV light incident on the samples. This is done by selecting slot 2 on the sample wheel, which is empty. A representation of this is shown in the top right portion of Fig. 6.11. The photodiode's active area fully captures all of the UV light that would be absorbed by a sample placed in the beam.

6.5.1.3 Sample photocurrent

The sample photocurrent measurement provides a measurement of the reemitted light flux at the photodiode's location. This measurement is performed on slots that contain WLS samples (slots 3 to 5). A representation of this measurement is shown in the bottom left of Fig 6.11. The UV beam from the exit slit of the monochromator is absorbed by the WLS thin film and the acrylic substrate. Photons are reemitted from the WLS film in the forward and backward direction according to a currently unknown angular distribution. A portion of the total number of reemitted photons are collected by the photodiode. The determination of the total amount of reemitted light from this measurement is described in Sec. 7.1.1.

The sample photocurrent measurements are performed less than one minute after the light photocurrent measurement. The lamp output intensity was confirmed to be stable on timescales much longer than one minute, thus providing confidence that the flux of incident

VUV light on the sample does not change between a light photocurrent measurement and a sample photocurrent measurement.

6.5.1.4 Background photocurrent

The background photocurrent measurement provides a measure of the stray light contamination in the UV beam and its contribution to the light and sample photocurrent measurements. This measurement is performed by applying a high-pass optical filter using the filter wheel located near the light source (Sec. 6.2.2.1). The filter absorbs the component of the light source's output below the cutoff wavelength of the filter. For monochromator wavelength settings below the cutoff wavelength of the selected filter, the UV light normally exiting the monochromator, which is used to drive the reemission from WLS samples, is eliminated. This leaves any background light above the filter's cutoff incident on the sample. A sample is left in the beam during the measurement to account for the transmission of the thin film. The possibility of fluorescence originating from the filter was crosschecked by measuring the light flux with no sample in the beam, and with a filter applied for an incident VUV wavelength below the cutoff of the filter. The light flux was found to be consistent with background for both filters at all incident VUV wavelengths of interest below the cutoff wavelength of the filters. This verifies that any fluorescence originating from the filters is negligible to within our sensitivity.

The possibility of fluorescence originating from VUV photons terminating in the acrylic substrate was crosschecked by performing a sample photocurrent measurement on a blank acrylic disk. This photocurrent measurement was found to be consistent with background which verifies that any fluorescence of the acrylic from VUV photons is below our sensitivity.

It should be noted that light and sample photocurrent measurements are often several orders of magnitude greater than the background photocurrent; background current corrections are negligible for wavelengths in the range 100–250 nm. The background corrections become important when the sample photocurrent is of the order of the background current. For wavelengths below 100 nm (the measurements performed at 50 and 73 nm) the correction is non-negligible; at its peak, the background can reach roughly one half of the sample photocurrent. In all cases, the uncertainty on the background is included in the final photocurrent measurement.

6.5.2 Spectrometer measurements

Reemission spectra are measured using the setup described in this section. These spectra are used as inputs for the efficiency calculations discussed in Sec. 7.1.

The spectrometer is configured to integrate for 10 seconds for each spectral measurement. Three spectral measurements are averaged online and the result is written to disk as a text file. This is repeated 20 times during the course of a data run resulting in 20 files written to disk. The files written to disk are used as inputs for an offline analysis.

Two classes of data runs are required to measure a WLS sample's reemission spectrum: Dark and Sample. In the same way as the dark photocurrent measurement, a dark spectrum is measured by selecting the aluminum disk in slot 1 of the sample wheel to block all light from reaching the spectrometer. This provides a baseline for subtraction in an offline analysis. The sample spectrum is measured by selecting the appropriate slot on the sample wheel (slots 3–5). This is exactly analogous to the sample photocurrent measurement shown in Fig. 6.11, because only the spectrum of reemitted light is measured in this configuration.

An offline analysis is performed using the ROOT data analysis package [111] to extract the corrected reemission spectrum. The measurements from the dark spectrum run are averaged and subtracted from the average of the WLS sample reemission spectrum run. The result is then corrected by the acrylic transmission (Fig. 6.12) and the relative transmittance of the collimating lens/fiber assembly and quartz fiber (Fig. 6.13).

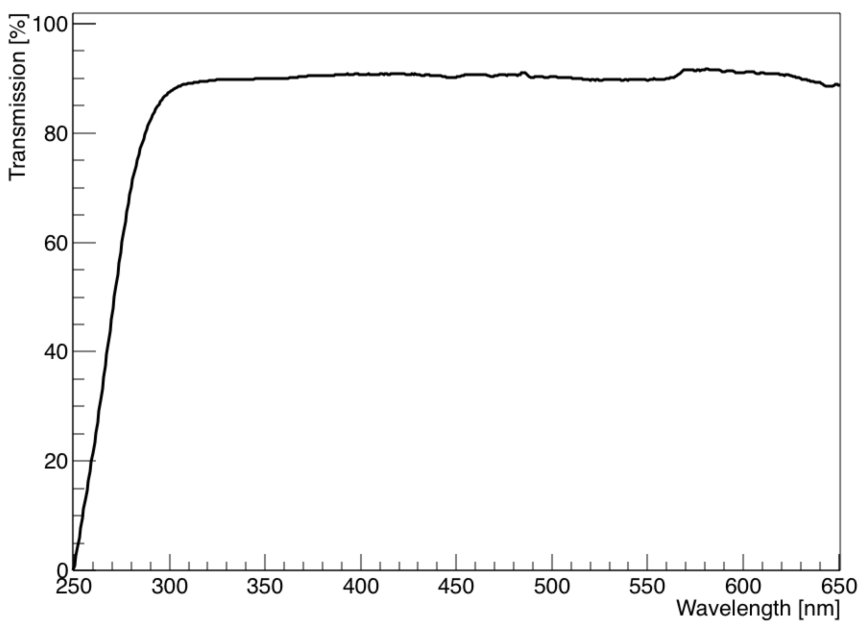

Figure 6.12: Transmission as a function of wavelength for 2.54-cm diameter and 0.32-cm thick SUVT acrylic disk. This was measured using the spectrometer and the LWC.

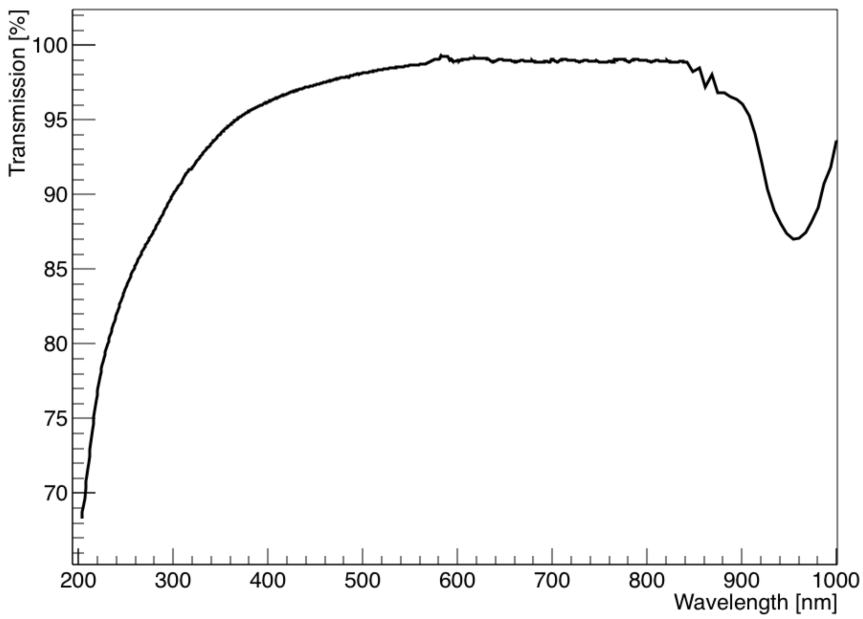

Figure 6.13: Relative transmittance of collimating lens/fiber vacuum feedthough and 200 μm fiber leading to the spectrometer.

Chapter 7

Wavelength Shifter R&D: Analysis, Results and Discussion

7.1 Analysis methods and model

The absolute "black-box" WLSE of a fluorescing thin film for incident light of wavelength λ is defined to be the ratio of the number of photons reemitted by the sample (film and substrate) to number of photons incident on the film. Equivalently, this can be interpreted as the probability that an incident photon of a certain wavelength will be absorbed and reemitted, at a wavelength according to the reemission spectrum, and escape the WLS sample.

As discussed in Sec. 6.1.1, the WLSE defined and measured in this way combines the true, microphysical QE of the material with optical effects of the film and the substrate, treating the sample as a "black box". It is the efficiency with which the black-box sample wavelength shifts incident photons, rather than the efficiency for a TPB molecule to do so. Because reemitted photons can be reabsorbed before they escape the film, the WLSE defined in this was has a dependence on film thickness and is a property of the specific sample, rather than a property of the material. Physically, the underlying QE is the more interesting result because it is an intrinsic property which should not depend on film thickness.

The VUV QE, VUV absorption length and SQE of TPB are determined by measuring the WLSE of several films of different thickness and unfolding the intrinsic microphysical parameters from the optical effects of the thin film by comparing to a detailed microphysical simulation. Sec. 7.1.1 describes the method of calculating the absolute WLSE of a sample from raw photocurrent data. Sec. 7.1.2 describes the details of the Monte Carlo model and Sec. 7.1.3 discusses the method to extract the microphysical parameters from measurements using the model.

7.1.1 Absolute wavelength shifting efficiency

Because the WLSE of a fluorescing thin film is defined as a ratio of photon fluxes, the total flux of photons incident on and reemitted by a wavelength-shifting sample must be determined.

The total flux of UV photons incident on a sample is determined from the light photocurrent measurements (Sec. 6.5.1.2). The geometry of the setup is arranged such that all of the UV light incident on the samples is captured by the photodiode, which allows for a direct measurement of the total flux of UV photons incident on the sample.

The flux of reemitted photons detected at the location of the photodiode is determined from the sample photocurrent measurement (Sec. 6.5.1.3). Because the photons reemitted by the TPB are emitted in the forward and backward directions and according to a currently unknown but usually assumed Lambertian angular distribution, only a fraction of the total reemitted photons are collected by the photodiode during a sample photocurrent measurement. The ratio of reemitted photons collected by the photodiode to the total number of reemitted photons leaving the sample is defined as the geometric acceptance fraction (GAF).

The GAF is interpreted as the probability that a reemitted photon that has escaped the sample (TPB film + acrylic disk) is observed by the photodiode. The GAF is independent of the choice of modeled QE because the GAF is simply a ratio of the number of visible photons detected to the number of visible photons escaping the TPB sample – it represents the geometric acceptance of the photodiode. Changing the VUV QE parameter changes the normalization (the average number of visible photons that are produced) but does not change the fraction of these that are detected. This expected behavior was verified with the Monte Carlo simulation. The GAF is dependent on specifics of the setup geometry, with a second-order dependence on the VUV absorption length and TPB thickness. The latter arises due to re-absorption and scattering of visible photons in the bulk TPB, which alters the angular distribution of photons emitted from the sample and, thus, the fraction observed by the photodiode.

The GAF is determined from a detailed microphysical Monte Carlo (Sec. 7.1.2) simulation of the setup and is used to determine the total reemitted photon flux from the measured reemitted photon flux.

The measured photocurrents are a convolution of the spectrum of light incident on the photodiode, multiplied by the photon energy, with the photodiode's calibrated response (Fig. 6.9), $R(\lambda)$. For light photocurrent measurements at wavelength λ, the incident light spectrum is given by the wavelength distribution at the monochromator's exit, $M(\lambda - \lambda')$, centered around λ. As shown in Fig. 6.7, $M(\lambda - \lambda')$ can be accurately modeled as a Gaussian with the width set by the type of diffraction grating used in the monochromator. For sample photocurrent measurements the TPB reemission spectrum, $P(\lambda)$, is used. The reemission spectrum of TPB was shown to be constant for illumination wavelengths from 128–250 nm in [93]. This has been verified in this work and has been extended down to 45 nm incident light (Sec. 7.2.1).

The light photocurrent, $I_{\text{light}}(\lambda)$, and sample photocurrent, $I_{\text{TPB}}(\lambda)$, measurements are

corrected for dark photocurrent (Sec. 6.5.1.1) and background photocurrent (Sec. 6.5.1.4). The dark photocurrent measurement provides a baseline correction while the background photocurrent corrects for stray light components in $M(\lambda - \lambda')$. The total photocurrent correction, $I_{\text{corr}}(\lambda)$, is the sum of the dark photocurrent and background contributions and is defined in Eq. 7.1.

$$I_{\text{corr}}(\lambda) = \begin{cases} I_{\text{dark}} + I_{\text{background}} & \text{if } \lambda \leq 150 \text{ nm} \\ I_{\text{dark}} & \text{if } \lambda > 150 \text{ nm} \end{cases} \tag{7.1}$$

The background photocurrent is included in $I_{\text{corr}}(\lambda)$ for wavelengths less than or equal to 150 nm instead of the full ROI due to the filter availability. As described in Sec. 6.5.1.4, background measurements can only be performed below the cutoff wavelength of the filter. The longest available cutoff wavelength is the fused quartz silica filter with a cutoff wavelength of 150 nm. It should be noted that only measurements using the LWC (Sec. 6.3.1) for wavelengths above 150 nm do not include background corrections. It was verified using the spectrometer and photocurrent measurements on uncoated acrylic disks that background levels in this range are consistent with dark current measurements i.e. below our sensitivity, thus eliminating the need for background measurements in this range.

As discussed in Sec. 7.1, the WLSE is computed by taking the ratio of the flux of reemitted light at the photodiode to the flux of incident light and dividing by the GAF, A_i. For convenience, the ratio of the measured photon fluxes, $\beta_{i,exp}(\lambda)$, and the WLSE , $\varepsilon_i(\lambda)$, are defined separately. These values are calculated for each sample where i denotes the sample index. The measured photon ratio is given in Eq. 7.2:

$$\beta_{i,exp}(\lambda) = \frac{I_{\text{TPB}}(\lambda) - I_{\text{corr}}(\lambda)}{I_{\text{light}}(\lambda) - I_{\text{corr}}(\lambda)} \times \frac{\int d\lambda' \frac{hc}{\lambda'} R(\lambda') M(\lambda - \lambda')}{\int d\lambda'' \frac{hc}{\lambda''} R(\lambda'') P(\lambda'')}. \tag{7.2}$$

The WLSE of the ith sample is given in Eq. 7.3:

$$\varepsilon_i(\lambda) = \beta_{i,exp}(\lambda) \times \frac{1}{A_i}. \tag{7.3}$$

A complete derivation of the WLSE and the GAF is provided in Sec. A.1.

7.1.2 Monte Carlo simulation

The purpose of the Monte Carlo simulation is two fold. First, it is used to determine the GAF for calculation of the absolute WLSE (Sec. 7.1.1), and second, to unfold several underlying microphysical parameters of TPB from the optical effects (Sec. 7.1.3).

The simulation is performed using the MiniCLEAN version of the Reactor Analysis Tool (RAT). MiniCLEAN RAT contains the functionality to simulate photon absorption and reemission of TPB thin films. Additional details of RAT are provided in Sec. 3.3.1.

7.1.2.1 Model

The dimensions of the experimental apparatus were carefully measured and a model was constructed in RAT. Each dimension was measured 5 times. The average of the 5 measurements was used while the RMS provided the uncertainty. A rendering of the geometry as modeled in RAT is shown in Fig. 7.1. Important dimensions are provided in Table 7.1.

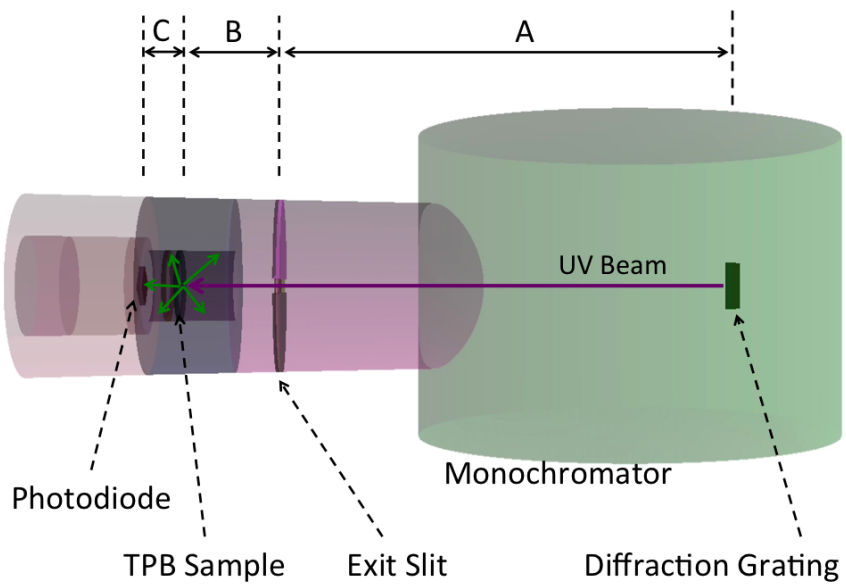

Figure 7.1: A rendering of the experimental setup as modeled in RAT. Several key elements and dimensions are labeled. Values and uncertainties for the dimensions are given in Table 7.1. Dimension A is the distance from the center of the diffraction grating face to the monochromator exit slit. Dimension B is the distance from the exit slit to the TPB surface. Dimension C is the distance from the TPB surface to the photodiode surface.

Dimension	Value [cm]	Uncert. (+/−) [cm]
A	18.33	0.07
B	4.003	0.025
C	1.328	0.025
Exit slit width	0.152	0.013
Exit slit height	0.488	0.005
Acrylic thickness	0.318	0.013

Table 7.1: Important apparatus dimensions and their uncertainties.

In the simulation, monochromatic photons are generated at the center of the diffraction grating surface. The photons are generated one at time and in the direction of the monochromator's exit slit. The angular distribution of the photons leaving the source vertex uniformly fills a cone with a 2 degree opening angle.

Many of the generated VUV photons terminate on the monochromator's exit slit. The fraction that pass through the slit propagate to the TPB surface boundary where they pass into bulk TPB or are reflected, according to Snell's law. The index of refraction for bulk TPB was estimated by a member of the MiniCLEAN collaboration [168] using the methods in [169] and compared to values of similar molecules in [170]. A value of 1.67 ± 0.05 is used in the simuation for all wavelengths. The TPB/vacuum interface is modeled as a rough surface using the GLISUR surface model [171] in GEANT4 with a polish value of $0.01 \pm^{0.09}_{0.01}$.

VUV photons that enter the bulk TPB are then absorbed according to wavelength–dependent absorption lengths. The absorption lengths of photons with wavelengths less than 250 nm in TPB were determined by fitting to the thickness dependence of the photon ratio for each incident wavelength in the ROI, as described in Sec 7.1.3. Photons are reemitted isotropically at the same vertex where the VUV photon was absorbed and according to the measured visible reemission distribution, which is consistent with [93]. The average number of photons reemitted when a VUV photon is absorbed is determined by a chosen value of the QE. The simulation assumes energy must be conserved, meaning the sum of reemitted photon energies is less than or equal to the absorbed VUV photon energy.

The absorption length for photons in TPB for wavelengths greater than 250 nm are taken from [152] and is shown in Fig. 7.2. The TPB reemission and absorption spectra overlap in the blue tail, thus it is possible for photons to be absorbed and reemitted several times. This secondary reemission leads to red-shifting of the TPB reemission spectra in thicker samples [154]. This effect is naturally included in the Monte Carlo model and is discussed in Sect. 7.1.2.2. The efficiency of this secondary reemission process, referred to as secondary QE (SQE), is evaluated from our data. The SQE is interpreted as the average intrinsic QE of TPB in the wavelength region where the absorption and reemission spectra overlap. Determination of the SQE is discussed in Sec 7.1.3.

As shown in by the black dashed-dotted line in Fig. 7.2, fitting an exponential to the long wavelength tail of the absorption spectrum yields a good fit to the data. The simulation uses the results from this exponential fit as an input rather than a linear extrapolation between neighboring data points. This yields a smoother absorption behavior in the blue tail of the reemission spectrum and exhibits a behavior close to that seen in data (Sec. 7.2.1.1).

Diffuse scattering of visible light occurs in TPB. To account for this, the Rayleigh scattering of visible reemitted photons is modeled. A mean scattering length of $2.75 \pm^{0.15}_{0.85}$ μm is used for reemitted photons [155]. Reemitted photons are produced isotropically at the time of creation, as shown in Fig. 7.3.

Scattering within the TPB layer and diffuse reflections at the rough TPB/vacuum interface is observed to produce the expected behavior of an approximate Lambertian angular distribution (i.e. linear in $\cos(\Theta)$) in the forward/backward directions for photons exiting the TPB sample. Fig. 7.4 shows the predicted angular distribution from Monte Carlo of

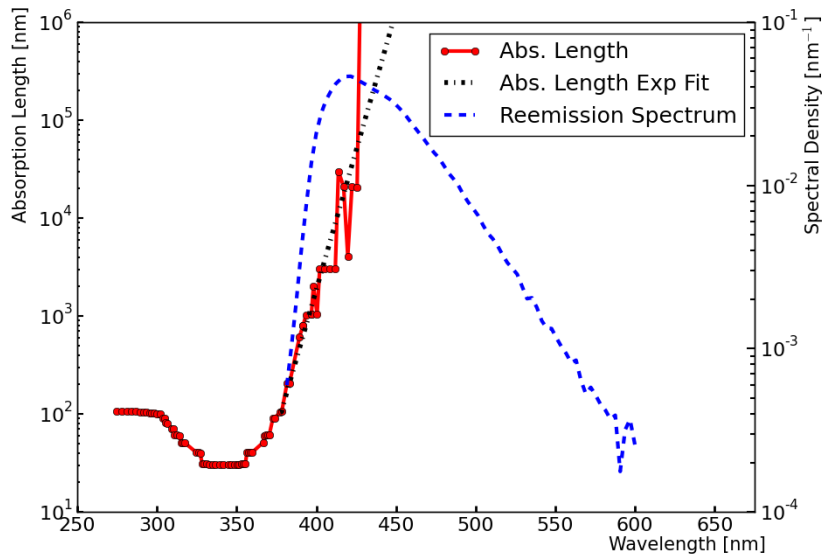

Figure 7.2: Absorption length of photons in TPB in nanometers plotted with the area normalized reemission spectrum of TPB. The absorption was taken from [152] while the reemission spectrum was measured in this work.

photons leaving the sample in the forward direction (i.e. toward the photodiode) for samples of various thickness. A $\cos(\Theta)$ equal to one corresponds photons leaving the sample parallel to the surface normal (in the direction of the photodiode), while $\cos(\Theta)$ close to zero corresponds to photons leaving the sample nearly parallel to the acrylic's surface.

As seen in Fig. 7.4, the thickest sample is the closest approximation to a Lambertian angular distribution. This is because thicker samples allow for more internal scattering of reemitted photons on average. Thinner samples are also approximately Lambertian but with an isotropic perturbation at angles near the normal. This is consistent with the idea that internal scattering of reemitted photons in thinner samples, especially near the normal and when the sample thickness is less than the mean scattering length in TPB of 2.75 μm.

The reemitted visible photons produced in the TPB are propagated until they are reabsorbed by the TPB or absorbed on walls, the surface of the photodiode, or by the acrylic. All photons which terminate on the photodiode surface are assumed to be detected. Optical effects, such as refraction and reflections, are included in the simulation. The measured SUVT acrylic transmission (Fig. 6.12) and manufacturer supplied index of refraction are used in the simulation of the acrylic. The tracks of all photons are stored in a ROOT file for post simulation analysis.

C++ and python analysis script loops over the stored photon tracks and calculates values of interest. For comparison to data, the photon ratio, $\beta_{i,sim}$, is evaluated by taking the ratio of the number reemitted photons which terminate on the photodiode surface, N_{pd}, to the

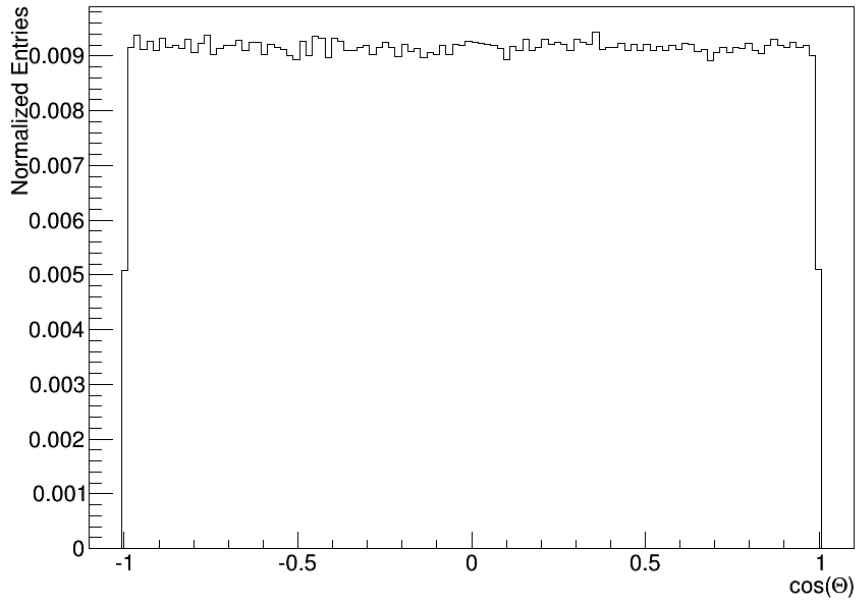

Figure 7.3: Local angular distribution in cos(Θ) of reemitted photons at the time of creation in Monte Carlo simulation. The flat distribution in cos(Θ) demonstrates that photons are modeled as being reemitted isotropic at time of creation.

number of VUV photons which were incident on the TPB surface, N_{inc}, in the simulation. As expected, $\beta_{i,sim}$ depends on the choice of the QE, the sample thickness, and the optical properties of TPB and other materials which are constrained by measurements and values from the literature. $\beta_{i,sim}$ is defined in Eq. 7.4 as:

$$\beta_{i,sim}\,(QE) = \frac{N_{pd}}{N_{inc}}. \tag{7.4}$$

7.1.2.2 Red-shifting of reemission spectrum

As discussed in Sect. 7.1.2.1 and seen in Fig. 7.2, the reemission and absorption spectra overlap in the blue tail of TPB's reemission spectrum. This naturally leads to red-shifting in the observed reemission spectra for thicker TPB films and was shown in [154] for the case of TPB evaporated on glass substrates. This is because photons reemitted inside of the TPB film may be reabsorbed and reemitted before escaping (i.e. secondary reemission). In principle reemitted photons may be reabsorbed and reemitted several times before escaping or being totally absorbed (which is possible for a SQE less than 1).

The secondary reemission quantum efficiency (SQE) is defined as the average number of photons reemitted when a visible photon is absorbed in the region where the absorption and reemission spectra overlap. This is interpreted as the average intrinsic QE of TPB averaged over this overlap region (approx. 375–420 nm) weighted by the strength of the absorption length at each wavelength. The measurement of this value is discussed in Sect. 7.1.3.

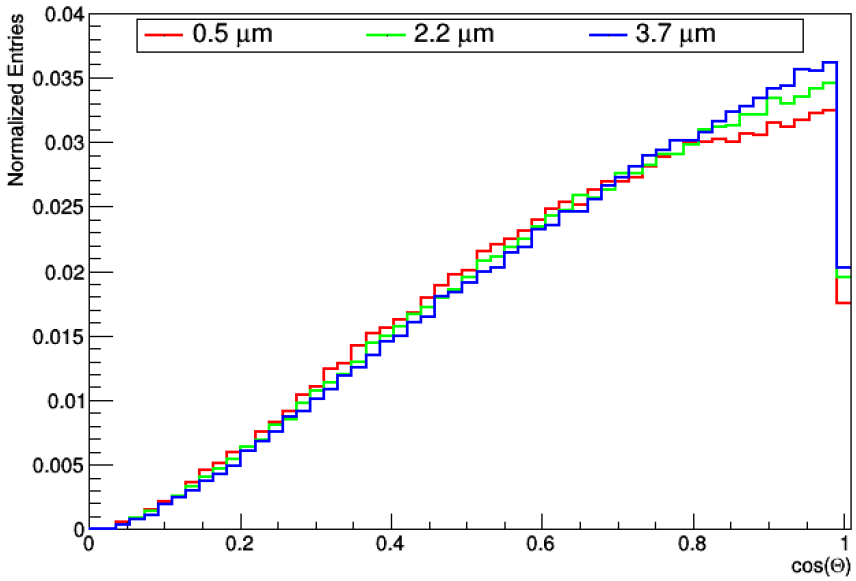

Figure 7.4: Resulting angular distribution in simulation of photons leaving the sample in the forward direction as a function of cos(Θ) from the normal for various film thicknesses. All samples exhibit an approximately Lambertian angular distribution with an isotropic perturbation for angles close to the normal for thinner samples. The thinnest sample has the largest isotropic perturbation due to less scattering near the normal on average.

The model assumes that the secondary reemission spectrum is the same as the inputted/measured reemission spectrum for TPB (shown in Fig. 7.2). The TPB reemission spectrum inputted into the simulation is the measured reemission spectrum for a 0.5 μm-thick TPB film. The reemission spectrum from the 0.5 μm thick TPB film sample was chosen because it was the thinnest film studied and should be closest to TPB's intrinsic reemission spectrum (i.e. containing as little as possible thickness dependent red-shifting).

When reemitted photons are being created in the TPB, the wavelength of the photon to be created is determined by sampling the reemission spectrum PDF. Additionally, an energy constraint is imposed where the energy of the reemitted photon must be less than or equal to the energy of the photon which was absorbed. This creates no constraints for photons with wavelengths shorter than the lower bound of the reemission spectrum (i.e. UV photons being absorbed in the TPB), but does constrain photons undergoing secondary reemission. For example, if a blue reemitted photon is the reabsorbed by the TPB and secondary reemission is to take place (according to the rate specified by the SQE), the resulting reemitted photon will not have a wavelength shorter than the original blue photon which was absorbed.

Fig. 7.5 shows the reemission spectra predicted by the Monte Carlo model for TPB films of various thickness as viewed at the location of the photodiode (i.e. downstream of the sample). These predictions are compared to measurements in Sec. 7.2.1.1.

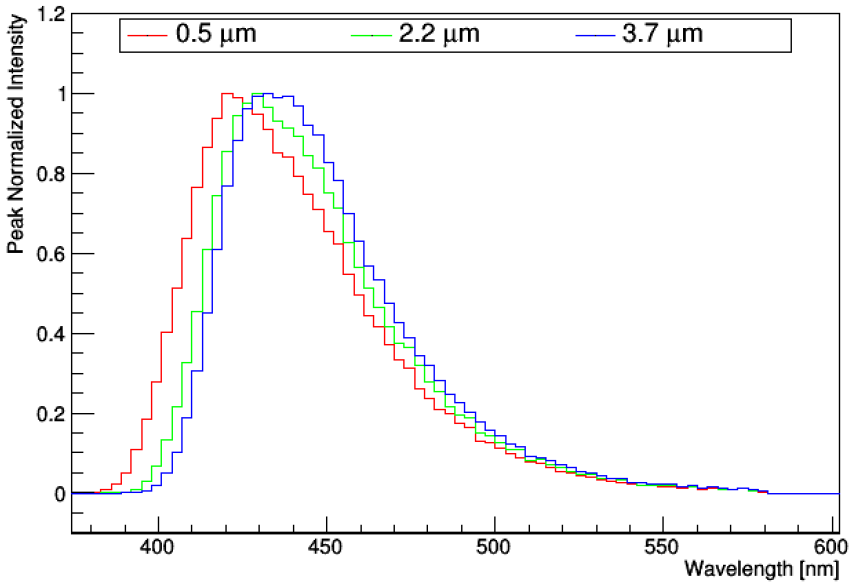

Figure 7.5: Predicted reemission spectra of TPB films of various thicknesses from the Monte Carlo simulation. The simulation predicts a red-shifting of the peak and blue tail which depends on the thickness of the TPB film.

7.1.3 Microphysical Parameter Extraction

As discussed at the beginning of Sec. 7.1, the VUV QE, VUV absorption length, and SQE of TPB for a given wavelength of incident VUV light is determined by comparing the thickness-dependent response of samples to a detailed microphysical Monte Carlo simulation. By comparing the photon ratio measurements to simulation, it is possible to unfold the intrinsic microphysical properties from the optical effects of the sample and experimental setup.

More specifically, the measured photon ratio, $\beta_{i,exp}$, is compared to the photon ratio from simulation, $\beta_{i,sim}$, for samples of different thickness. For a given set of model value inputs for the TPB VUV QE, VUV absorption length, and SQE, the χ^2 difference between data and simulation is evaluated. The χ^2 is defined in Eq. 7.5 as:

$$\chi^2 = \sum_{i=1}^{n} \left(\frac{\beta_{i,exp} - \beta_{i,sim}}{\sigma_{i,exp}} \right)^2 . \tag{7.5}$$

The preferred value for each of these microphysical parameters is found by minimizing the χ^2. Fig 7.6 shows the measured photon ratio along with several simulated photon ratios using different values of VUV QE and VUV absorption length. The solid line represents VUV QE and VUV absorption length choices that minimize the χ^2 for the case of 130-nm incident light, while the dotted and dashed lines show the effect of sub-optimal choices for these parameters. As seen by the dotted line, changing the VUV QE affects the overall amount of light produced, which scales the photon ratio up and down. The dashed line illustrates that

adjusting the VUV absorption length affects the shape of the thin-sample tail while leaving thicker samples unchanged. This behavior is expected because when the VUV absorption length is on the order of the sample thickness a non-negligible fraction of VUV photons will pass through the TPB and be "lost" in the acrylic substrate. As the simulated VUV absorption length is decreased the effect is thus more significant for thinner samples: more VUV photons start to be absorbed in these samples thus increasing the extracted response, or simulated photon ratio. The effect on thicker samples is small because close to 100% of the VUV photons penetrating the film are absorbed in either case.

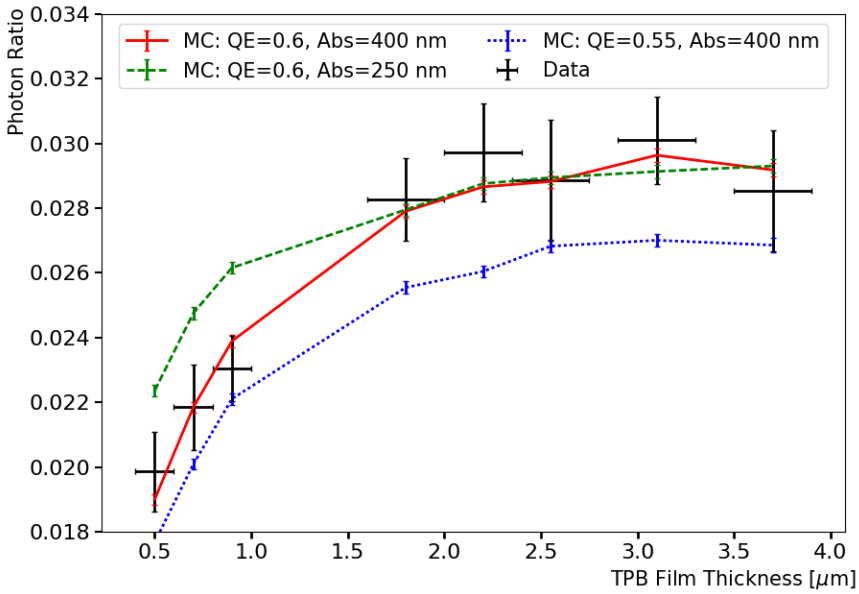

Figure 7.6: The measured, $\beta_{i,exp}$, and simulated, $\beta_{i,sim}$, photon ratios plotted as a function of sample thickness for data and Monte Carlo for several choices of VUV QE and VUV absorption length for 130-nm incident light. The SQE is held fixed at 0.9.

Fig. 7.7 shows a heat map of χ^2 values for many choices of VUV QE and absorption length for 130 nm incident light. A minimum χ^2 can be seen clearly at values of 0.6 and 400 nm for the VUV QE and absorption length respectively. This 2-D parameter sweep, as shown in Fig. 7.7, is performed for each incident wavelength studied in the ROI to identify the preferred VUV QE and absorption length values for a fixed value of the SQE.

As discussed in Sect. 7.1.2.1 and seen in Fig. 7.2, the TPB absorption spectrum overlaps with the blue tail of the TPB reemission spectrum. This allows for secondary reemission, where blue reemitted photons may be reabsorbed and reemitted by the TPB film. The efficiency of this process is referred to as the secondary reemission QE (SQE).

To evaluate the preferred value of the SQE, a 3-D scan of the χ^2 space is performed. Because the secondary reemission process affects the visible reemitted photons, it has a correlated impact on data sets for all incident wavelengths. At each value of the SQE, a

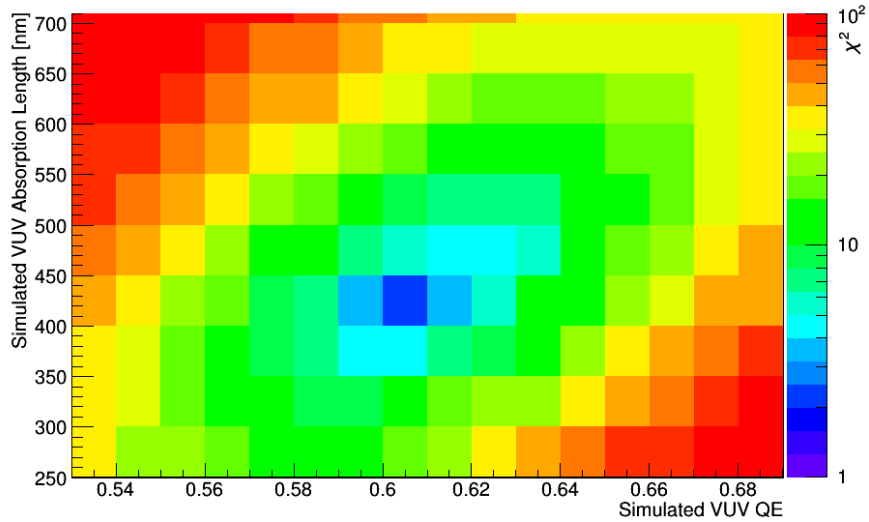

Figure 7.7: A heat map of the χ^2 for a 2-D sweep of VUV QE and absorption lengths for 130 nm incident light. The SQE is held fixed at 0.9. The pair of VUV QE and absorption length values that minimizes the χ^2 is 0.6 and 400 nm. The χ^2 value at the minimum is equal to 2.0

2-D sweep of VUV QE and absorption length is performed at each wavelength in the ROI. The minimum χ^2 values for each wavelength are summed to determine the global χ^2 value, $\chi^2_{global}(SQE)$, for that choice of SQE. This is shown in Eq. 7.6 as:

$$\chi^2_{global}(SQE) = \sum_{i=1}^{N} \chi^2_{min,i}. \tag{7.6}$$

where N is the number of incident wavelengths considered in the ROI, and $\chi^2_{min,i}$ is the minimum value of the χ^2 found from a 2-D sweep of VUV QE and absorption length for the ith incident wavelength. This process is repeated for several different choices of SQE. The SQE value that minimizes $\chi^2_{global}(SQE)$ is taken to be the preferred value. Fig. 7.14 shows the χ^2_{global} plotted as a function of SQE.

7.2 Results

The results are presented in this section. Sec. 7.2.1 presents the measured reemission spectrum for several incident wavelengths. Sec. 7.2.2 presents the measured absolute WLSE of TPB films of different thicknesses as a function of incident wavelength. Sec. 7.2.3 presents the extracted VUV QE and VUV absorption length of TPB as a function of incident wavelength. Also presented is a value for the SQE.

7.2.1 Reemission spectrum

The visible reemission spectrum was measured for each of several incident wavelengths: 45, 128, 160, 175 and 250 nm. The 45-nm measurement was taken using the SWC and is the brightest peak produced using a HeNe gas mixture. The 128-nm peak measurement was performed using the IWC while the 160-, 175- and 250-nm spectra were taken using the LWC. The 128 and 175 nm wavelengths correspond to the argon and xenon scintillation wavelengths. The area-normalized reemission spectrum for each of these incident wavelengths is presented in Fig. 7.8.

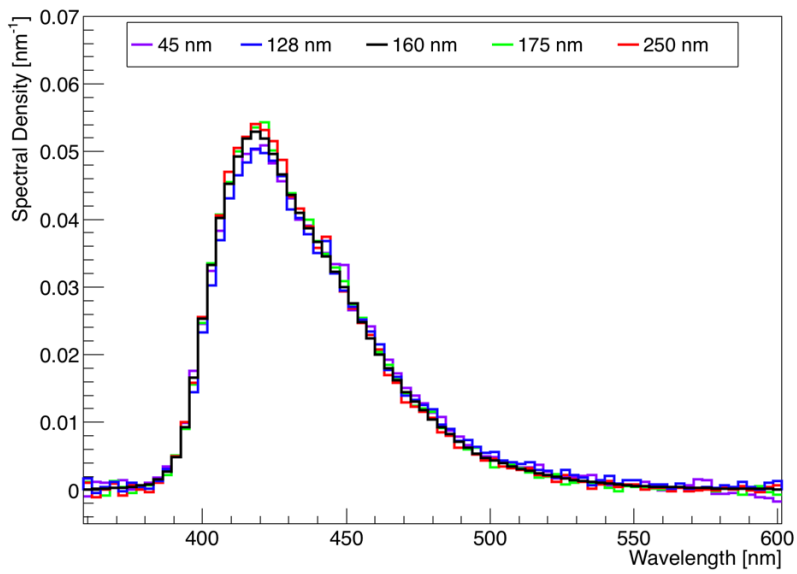

Figure 7.8: The measured reemission spectra of a 1.8 μm TPB film for several incident wavelengths. No dependence of the reemission spectrum of TPB on incident wavelength was observed.

No dependence of reemission spectrum on incident wavelength was observed. All spectra have a peak near 420 nm and cut off below 400 nm.

In this work, the measured binned spectrum is used in the Monte Carlo model. For the purposes of non-Monte Carlo based modeling, an analytic model is provided here for this spectrum. The reemission spectrum for 160-nm incident light was fit to a weighted sum of a Gaussian and exponentially modified Gaussian:

$$f\left(\lambda \mid A, \alpha, \sigma_1, \mu_1, \sigma_2, \mu_2\right) = A\frac{\alpha}{2}e^{\frac{\alpha}{2}(2\mu_1+\alpha\sigma_1^2-2\lambda)}\times \\ \operatorname{erfc}\left(\frac{\mu_1+\alpha\sigma_1^2-\lambda}{\sqrt{2}\sigma_1}\right) + (1-A)\times\frac{1}{\sqrt{2\sigma_2^2\pi}}\times e^{\frac{-(\lambda-\mu_2)^2}{2\sigma_2^2}}. \tag{7.7}$$

The fit is shown in Fig. 7.9. The fit was performed using the RooFit package in ROOT [147]. The 160 nm wavelength was chosen because it is the brightest peak of any configuration, which provides the best signal to noise. Because no significant dependence of the reemission spectrum on incident wavelength was observed (Fig. 7.8), a model built from this fit can be reasonably applied to other incident wavelengths. The fit has a chi-squared value of 0.626. The fit parameters and the associated uncertainties are given in Table 7.2.

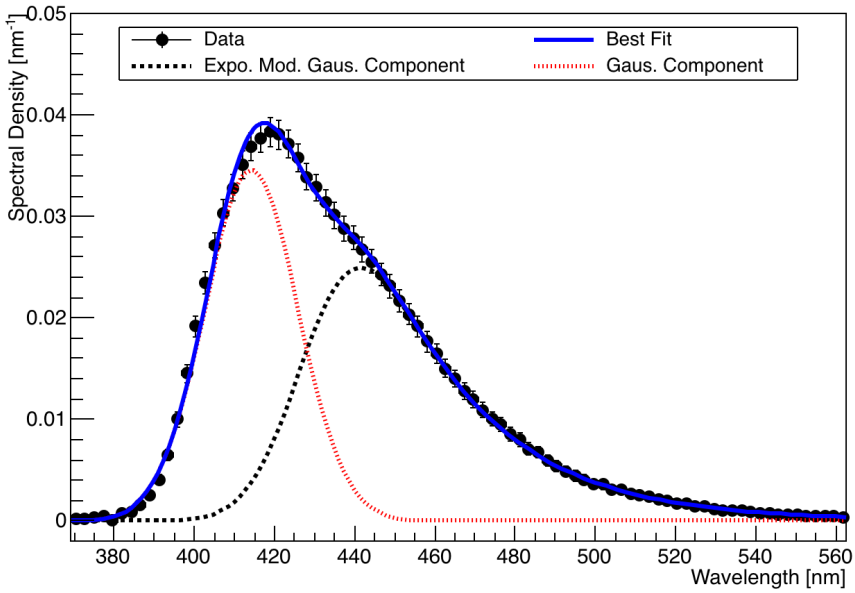

Figure 7.9: The best fit to the TPB reemission spectrum for 160 nm incident light. The reemission spectrum fits well to the weighted sum of a Gaussian (red) and an exponentially modified Gaussian (black). The total fit is given in blue.

Parameter	Value	Uncert. (+/-)
A	0.782	2.3E-2
α	3.7E-2	5.9E-4
σ_1	15.43 nm	0.42 nm
μ_1	418.1 nm	1.1 nm
σ_2	9.72 nm	0.43 nm
μ_2	411.2 nm	0.6 nm

Table 7.2: A table of parameters returned by the best fit to the TPB reemission spectrum is Fig. 7.9

7.2.1.1 Red-shifting of TPB's reemission spectrum

This section shows the measured red-shifting of reemission spectra for samples of various thickness. The measured reemission spectra are also compared to predictions made by the Monte Carlo in Sec. 7.1.2.2.

As seen in Fig. 7.10, the measured reemission spectrum viewed downstream of the sample is red-shifted for thicker TPB films. In particular, the blue tail is red-shifted without a large change elsewhere in the reemission distribution.

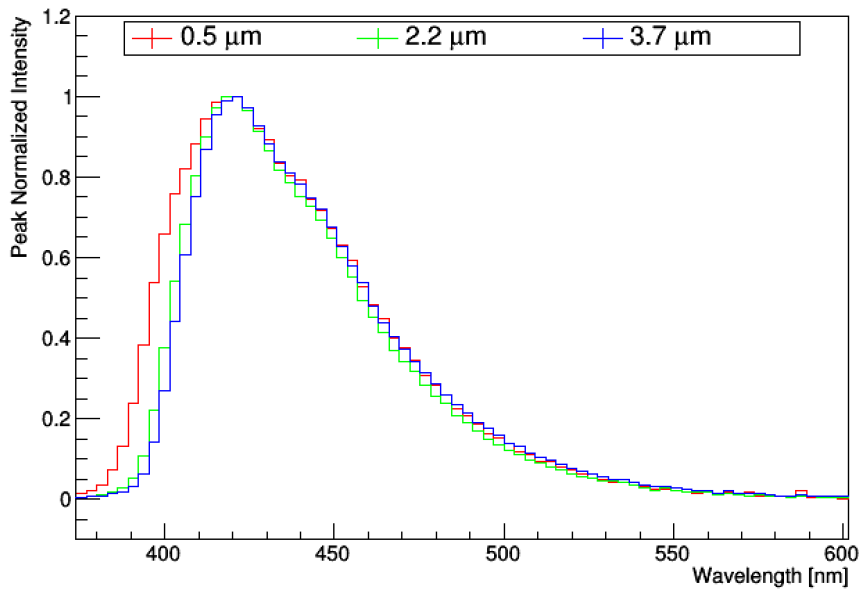

Figure 7.10: Measured reemission spectra for samples of various thicknesses. A the blue tail of the reemission spectra are red-shifted for thicker samples.

When comparing Fig. 7.5 and Fig. 7.10, differences in the predicted and measured reemission spectra are apparent near the peak. The simulation does a good job predicting the red-shifting of the blue tail with increasing thickness, but over-estimates the red-shifting near the peak. The peak position vs. sample thickness for simulation and data are plotted in Fig. 7.11.

The author suspect that the difference between the simulation and measured red-shift could be from the assumption that the secondary reemission process's reemission spectrum is identical to the measured reemission spectrum for incident VUV light, which may not be the case. The difference in red-shifting between the simulation and data is not expected to affect the QE results because the photodiode response does not change significantly over the range of the observed difference. Further, as shown in Fig. 7.6, the simulation does a good job predicting the thickness dependence of the photon ratio. This suggests that the differences arising from red-shifting to the QE is a second order effect.

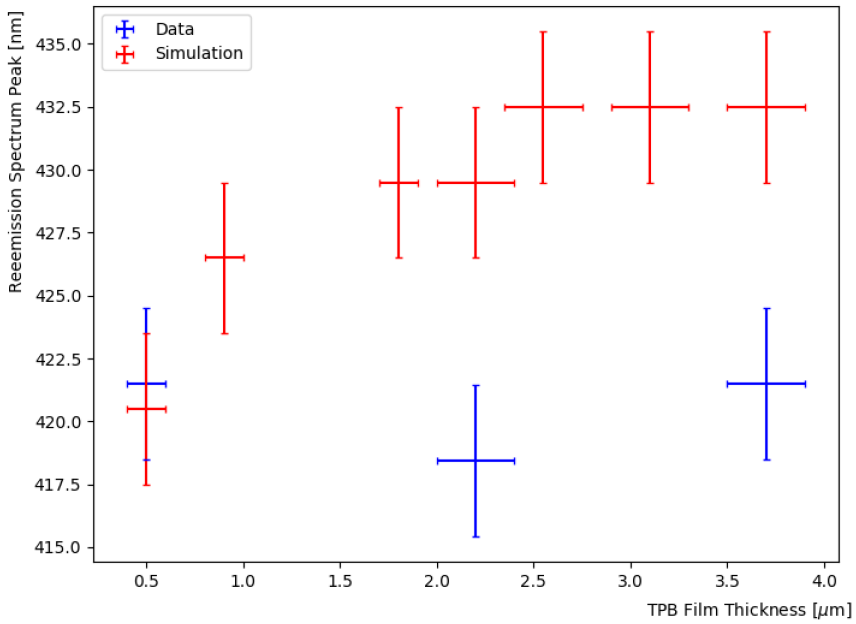

Figure 7.11: A comparison of the predicted (Fig. 7.5) and measured (Fig. 7.10) reemission spectrum peak wavelength as a function of TPB film thickness.

7.2.2 Sample-dependent wavelength shifting efficiency

For comparison to the literature, the measure of sample-dependent WLSE is provided here in the form presented in [93]. The WLSE measured for samples of different thickness are presented in this section.

As discussed in Sec. 7.1.1, the GAF is determined from simulation and used to convert the observed photon ratio of a sample to the absolute WLSE (Eq. 7.3). The GAF was found to take an average value of 0.059 with a slight dependence on sample thickness.

Fig. 7.12 presents the measured absolute WLSE efficiency for a representative set of samples: B, C, D, E, and H (as defined in Table 6.1). In general, thinner samples have a smaller WLSE, up to approximately 2 μm. Samples between 2- and 3-μm thick exhibited the largest absolute WLSE. A slight decrease in the WLSE is observed for thickest sample.

It should be emphasized that the WLSE results are dependent on both environmental factors and the exact setup. In this work, the TPB samples were measured at room temperature and in vacuum. For typical LNG applications, the TPB surfaces are often submerged in a cryogenic liquid target. Liquid noble targets have an index of refraction closer to that of acrylic and TPB, so one could expect slightly higher WLSE since there will be fewer reflections at the LNG/TPB and LNG/acrylic interfaces for VUV and reemitted photons. Additionally, one may also see increases in TPB's response when the TPB is at cryogenic temperatures compared to room temperature, as shown in [154].

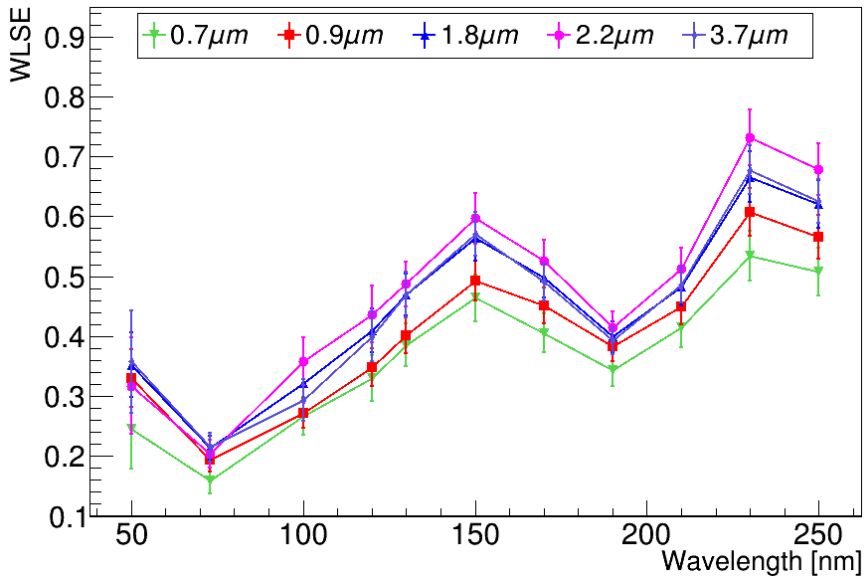

Figure 7.12: Absolute WLSE efficiency for several samples of various thickness.

7.2.2.1 Uncertainties

Several sources of uncertainty were considered. The total uncertainty and its components are plotted as a function of incident wavelength in Fig. 7.13. Each of the components were added in quadrature to evaluate the total uncertainty, which is provided in Fig. 7.12.

Photocurrent RMS The photocurrent uncertainty is the RMS in the light, dark, and sample photocurrents propagated through Eq. 7.2 during the course of a measurement. The lamp intensity was determined to be very stable. In particular, the ratio of the RMS to measured photocurrent during light measurements was observed to be 10^{-5} for the most intense peaks in the region of interest (160 nm with LWC), and 10^{-4} for the least intense spectral lines (73 nm with SWC).

VUV and Visible Photon Flux The "UV Photons" component is the uncertainty in the number of UV photons when folding in the uncertainty in incident light spectrum and photodiode response at the incident wavelengths. The uncertainty in the light spectrum exiting the monochromator was assumed to be the $\pm$ 1σ bounds of a Gaussian fit to the measured spectra shown in Fig. 6.7 integrated over the response of the photodiode.

Similarly, the "Vis Photons" is the uncertainty in the reemission spectrum of TPB and the corresponding uncertainty of the photodiode's response at the reemission wavelengths. The uncertainty in TPB's reemission spectrum is taken from the total uncertainty in the fit shown in Fig. 7.9.

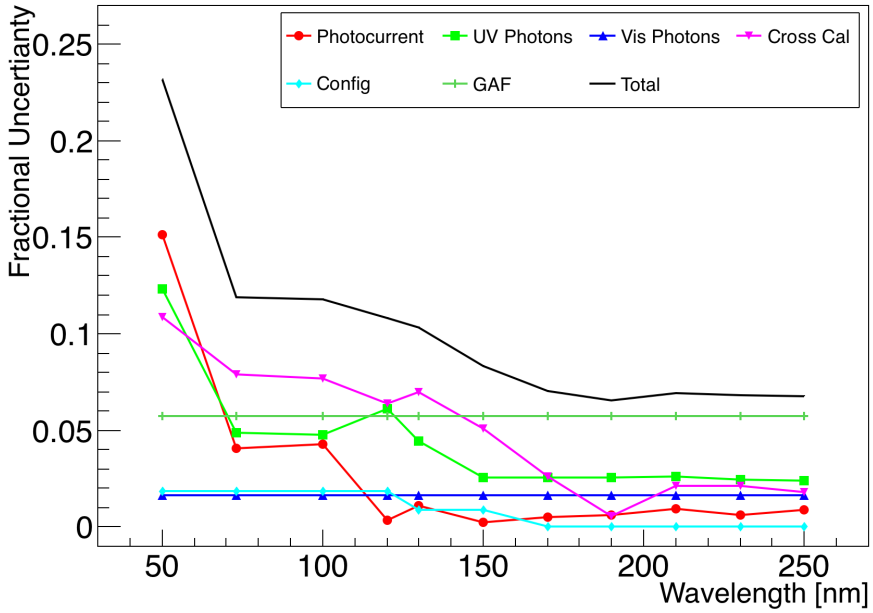

Figure 7.13: Average values for various classes of uncertainties displayed as a function of incident wavelength. The total fractional uncertainty is determined by adding each of the uncertainties in quadrature.

Configuration Offset When comparing data taken using the LWC and MWC in the region of overlapping measurements (130–150 nm), an offset of 9.8% ± 2% was found. This offset was found to be independent of incident wavelength and sample thickness and was corrected for on all data sets taken using the windowless lamp (MWC and SWC). The procedure used to evaluate the configuration offset factor and its uncertainty is described in Appendix B, Sec. B.1.

The configuration dependent offset is likely due to the different illumination profiles on the diffraction grating for the LWC and MWC/SWC. The illumination profile of light incident on the diffraction grating was studied and optimized for the LWC by adjusting the focusing mirror and is thought to be well represented in the Monte Carlo model. This provides reasonable justification to correct the constant offset seen in the MWC/SWC to the LWC.

Photodiode Cross Calibration One photodiode (PD-1) was used for the majority of the measurements. A second photodiode (PD 2) was calibrated relative to a NIST standard and used as a reference to cross-check the calibration of PD-1 at the time of final measurements. The "cross cal" component is the uncertainty in the re-calibration of PD-1 to the PD-2 standard. Additional details of the cross-calibration procedure are provided in Appendix B, Sec. B.1.

Geometric Acceptance Fraction The uncertainty in the GAF contains two components. The first is the statistical uncertainty of its evaluation in the simulation and is approximately 0.3%. The second and dominant component is the systematic uncertainties of the inputs used in the Monte Carlo model. The systematic uncertainty in dimensions of the setup, as defined in Table 7.1, was found to be 3.7% which is independent of incident wavelength. To evaluate this systematic, each critical dimension of the setup in turn was changed by $\pm 1\sigma$ to evaluate the resulting change in the GAF. The uncertainties from each test were assumed to be uncorrelated and were added in quadrature. Other contributions to the systematic uncertainty of the GAF were the surface roughness of the TPB (1.5%), index of refraction of the TPB (3.2%), and scattering length of visible photons in the TPB (2.5%). These uncertainties were obtained by varying these inputs by $\pm 1\sigma$ from their default values, provided in Sec. 7.1.2.1, and determining the resulting change in the GAF.

Total Uncertainty The statistical and systematic uncertainties were assumed to be uncorrelated and added in quadrature to yield a total GAF uncertainty of approximately 5.7% which is independent of incident wavelength.

7.2.3 VUV QE, Absorption Length, and SQE

The extracted intrinsic VUV QE and absorption length of TPB as a function of incident wavelength and the preferred value of the SQE are presented in this section.

Using the process described in Sec. 7.1.3 and shown in Fig. 7.14, the SQE was found to have a preferred value of 0.9 ± 0.1. The uncertainty in SQE is given by $\pm\ 1\ \Delta\chi^2_{global}$. The VUV QE and absorption length results presented in this section were determined using SQE equal to 0.9.

The VUV QE values are shown in Fig. 7.15. The QE extraction was performed using the process described in Sec. 7.1.3. The VUV QE follows the shape of the WLSE efficiency curves. The QE has local maxima near 230 nm and 150 nm incident light. There is a general trend toward lower QE for shorter wavelengths.

Recalling the definitions of the VUV QE and WLSE, it is to be expected that the VUV QE is larger than the WLSE. This is because the WLSE efficiency is the intrinsic QE of TPB folded in with the optics of the film, sample and setup. For the scenario where the SQE is less than or equal to 1, the intrinsic QE represents the upper limit for the WLSE which is reduced by the absorption of reemitted photons by the TPB and acrylic.

The extracted VUV absorption lengths are shown in Fig 7.16.

7.2.3.1 Uncertainties

Several sources of uncertainty were considered in evaluating the VUV QE and absorption lengths.

Correlated uncertainties in the VUV QE and absorption lengths are exacted from the 2-D scans at the preferred SQE value (Fig. 7.7). The uncertainties are evaluated by finding

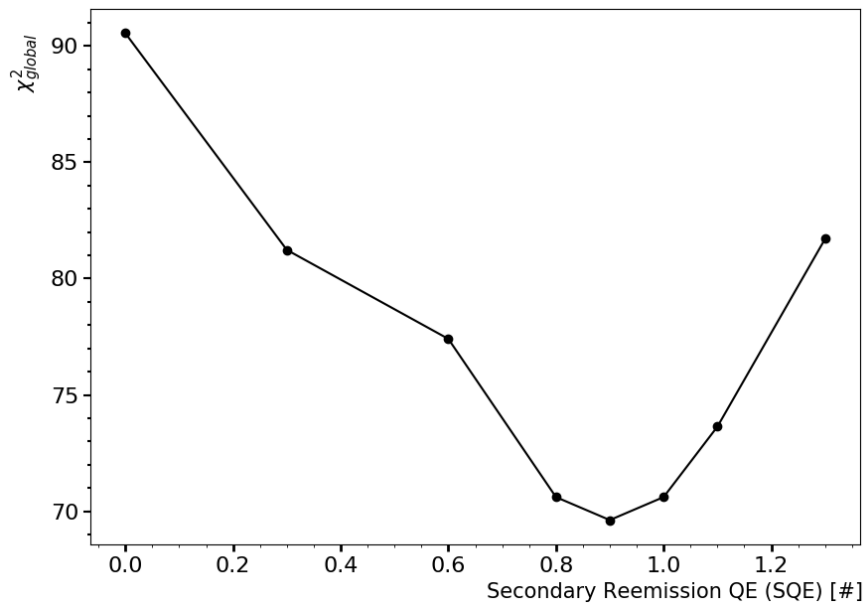

Figure 7.14: The results of χ^2_{global} plotted as a function of SQE. The minimum at 0.9 is taken to be the preferred value of the SQE. An uncertainty of 0.1 is given by $\pm$ 1 $\Delta\chi^2_{global}$ from the minimum.

the contour at $+1\Delta\chi^2$ from the minimum and projecting onto the x and y axes [172]. This yields an average uncertainty of 1.8% in VUV QE and 12% in VUV absorption length.

The uncertainty in these quantities due to the SQE was determined by evaluating the change in preferred values of VUV QE and absorption using SQE values $\pm$ $1\Delta\chi^2_{global}$ from the minimum at 0.9 (Fig. 7.14). This yields an average uncertainty of 4.4% in VUV QE and 12% in VUV absorption length.

In addition, each model input was varied independently within uncertainties, as described in Sec. 7.1.2.1, to determine the impact on the VUV QE and absorption length result. The systematic uncertainty from the geometry's dimensions was 4% for the QE. The uncertainty from TPB's index of refraction was 1.8% for the VUV QE and 12% for the absorption length. The uncertainty from the visible scattering length was 3.3% for the VUV QE. No impact on the absorption length results was observed when changing the geometry's dimensions, TPB index of refraction, or visible scattering length.

Adding these uncertainties in quadrature yields an average uncertainty of approximately 8% in VUV QE and 26% in VUV absorption length. The uncertainties shown in Figs. 7.15 and 7.16 include all contributions.

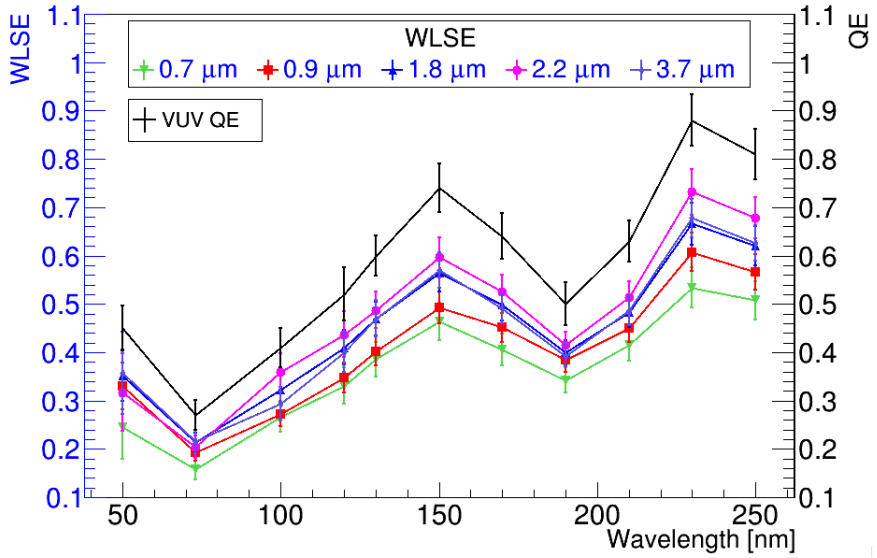

Figure 7.15: The extracted QE of TPB as a function of incident wavelength (right axis). This is plotted alongside WLSE results shown in Fig. 7.12. These quantities are plotted on different axes because of their fundamentally different definitions.

7.3 Discussion

The key results of this work are centered around extracting important microphysical parameters critical to modeling TPB thin films in detector simulations. In particular, measurements of the intrinsic QE and absorption lengths of room temperature TPB thin films are presented as a function of incident wavelength in the VUV regime. Also presented is a measurement of the SQE - the average efficiency of secondary reemission of visible photons in the regime where the TPB absorption and reemission spectra overlap.

In an effort to directly compare with results presented in [93], the sample-dependent WLSE of several samples of different thickness and reemission spectra are also presented as a function of incident wavelength. These results cover the spectral range studied by [93] with improved precision, while extending the measurements down to 50 nm.

To the best of our knowledge, the extraction of the SQE and intrinsic VUV QE and absorption lengths as a function of incident wavelength for evaporated TPB thin films, without reference to other materials, is a new result. These intrinsic properties are more broadly applicable than the blackbox WLSE, because they depend on the properties of the material rather than specifics of the sample. For the purposes of modeling TPB, the intrinsic VUV QE, absorption length, and SQE are critical inputs to current and future liquid noble gas experiments and are now well constrained.

The WLSE result presented in this work is in tension with those presented in [93]. The authors believe the differences can be attributed to unaccounted for systematic uncertainties related to photodiode calibration and the setup optics in [93], and to differences in the

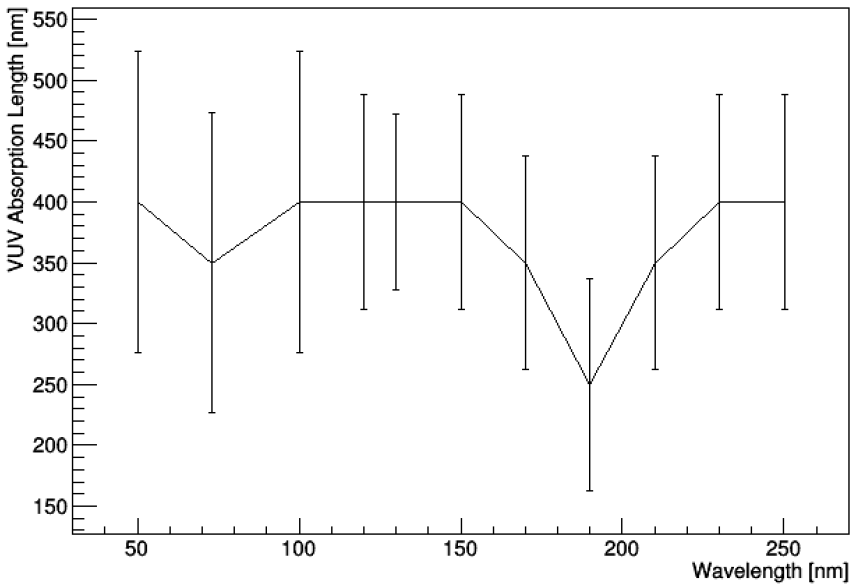

Figure 7.16: The extracted VUV absorption lengths of evaporated thin films of TPB as a function of incident wavelength.

Monte Carlo model used to evaluate the GAF. The details of the differences are discussed in Sec. 7.3.1.

Previous measurements of the WLSE of TPB were performed relative to Sodium Salicylate [153]. Combining the Sodium Salicylate reference [158] with the relative measurements suggests the QE of TPB should be larger than that determined in this work. The authors believe that this difference is being driven by the optical model of the TPB, which may not be effectively represented in the Sodium Salicylate reference. Also presented in [153] is the relative response of samples as a function of thickness. Data and Monte Carlo predictions from this work are compared in a relative fashion to the data in [153] as an independent check. This is discussed in section 7.3.2.

The reemission spectrum result is consistent with the literature and has confirmed that the reemission spectrum of room temperature TPB thin films remains constant for incident wavelengths as low as 45 nm.

7.3.1 Comparison with previous 2011 measurement

This work builds on much of the original work in [93], and several items of equipment were shared between the two efforts. The authors of this article worked closely with the authors of [93], one of whom is an author of this work.

Differences exist between the TPB efficiency measurements presented here and what is presented in [93], as shown in Fig. 7.18. Several factors can account for the differences in

the measurements. These are described in Secs. 7.3.1.1– 7.3.1.4. Following many detailed systematic checks, as described, there is confidence that the differences are understood.

7.3.1.1 Photodiode calibration

The authors believe the largest differences between this work and what is presented in [93] arise from issues with photodiode calibrations. The photodiode used in [93] was calibrated in 2008 by NIST and had the response given by the solid curve in Fig. 7.17 [173]. Before the start of this work, the same photodiode was recalibrated at NIST and followed the response curve given by the dotted curve [174]. A large change in the photodiode's response occurred between 2008 and 2014, especially in the range of 120–150 nm. The previous work was published in 2011 [93].

The photodiode's response degradation was likely due to UV damage from prolonged exposure and the build up of an oxidation layer on the bare face of the silicon photodiode surface [174, 175]. A build up of an oxidation layer can drastically reduce the response of the photodiode for wavelengths below 150 nm. Interestingly, an oxide layer may also increase the response at longer wavelengths because the layer creates an anti-reflective layer (interactions inside of the oxide film). An oxide layer effectively leaves the response at the visible wavelengths unchanged. This explanation is consistent with what is seen in Fig. 7.17.

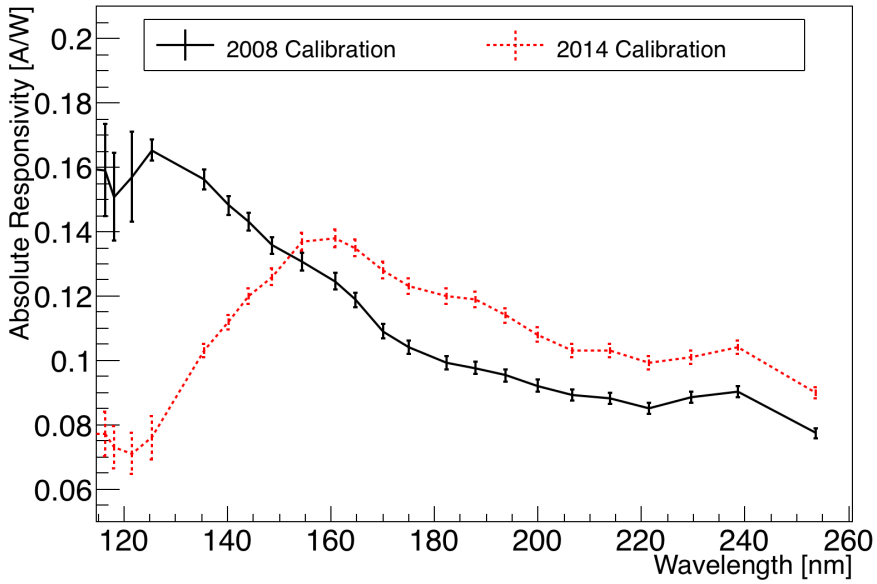

Figure 7.17: A comparison comparison of the NIST calibrations of the photodiode used in [93] in 2008 (solid) and in 2014 (dotted). The 2008 curve was used as the photodiode response function in [93]. There is a substantial difference between the 2008 and 2014 response functions, suggesting that significant degradation in the photodiode's response occurred between 2008 and 2014.

Because the response of the photodiode used in the 2011 publication changed by a large amount, two new photodiodes were purchased in 2016 after the start of this work. NIST calibrated one of these photodiodes (PD 1) (Fig. 6.9) in February of 2016. The second photodiode (PD 2) was calibrated relative to the NIST supplied calibration of PD 1 by the author. PD 1 was used for the bulk of our measurements in this work while PD 2 was used to track the relative response of PD 1 over time.

With access to the raw data from the 2011 publication, another analysis was performed using the 2014 calibration of the photodiode used in [93]. Fig. 7.18 shows the results of this reanalysis as a dotted line, along with the published 2011 result from [93] as a solid line. For short wavelengths (120 – 150 nm), an unaccounted degradation in the photodiode's response would lead to an underestimation of the number of UV photons incident on the sample, thus increasing the photon ratio and WLSE at those wavelengths. The opposite is true for the longer wavelengths where an increase in the photodiode's response was observed (150 – 250 nm).

Interestingly, the shape of the reanalyzed raw data from the 2011 result using the 2014 calibration curve agrees fairly well with the results presented in this work, though there is a normalization offset which will be explained in Sec. 7.3.1.2. This suggests that the bulk of the Gehman et al. photodiode's response degradation occurred between the 2008 calibration and the 2011 publication and that the published result does not account for changes in the photodiode's response.

7.3.1.2 GAF determination

The GAF, described in Sec. 7.1.1, determines a scale factor to evaluate a sample's WLSE from the photon ratio (otherwise known as the forward efficiency in [93]). A derivation of the WLSE and GAF is provided in Sec. A.1.

After looking closely at the evaluation of the GAF and its relation to the definition of the WLSE in [93], a logical error was found by the author of this work in the evaluation of the GAF used in [93]. This error is derived and explained in Sec. A.2. In summary, it was determined that the equality relating Eq. 1 and 3 in [93] leads to an implicit assumption, not realize in [93], which in general is not true (Eq. A.22 in Sec. A.2). As a consequence, this led to an under-estimation of the GAF evaluated and used in [93] thereby leading to an overestimation in the reported WLSE (since the GAF sets the scaling of the WLSE).

Additionally, the GAF is observed to have a strong dependence on the distance of the photodiode from the sample. This suggests careful measurements of the apparatus dimensions are required and careful treatment of these uncertainties is critical. This systematic uncertainty has been included in our result and is the dominant uncertainty contribution for several wavelengths. The work presented in [93] also used a Monte Carlo simulation to determine the GAF. The model was less detailed (a python ray-tracing model only accounting for refraction at interfaces and the transmission of the acrylic) than that used in this work and the systematic uncertainty on the GAF was assumed to be zero. Additionally, the TPB model in [93] was treated as an infinitesimally thin film which did not account for

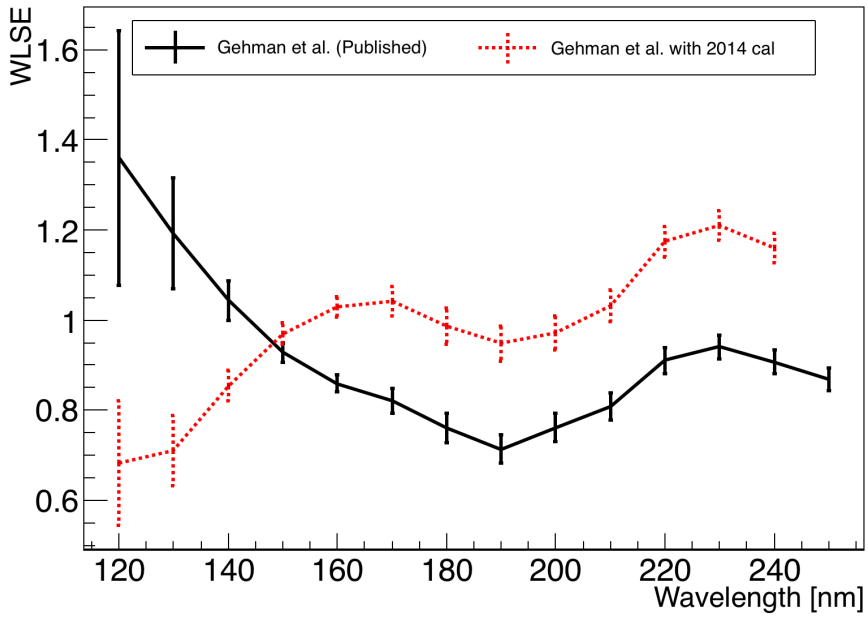

Figure 7.18: A comparison of the published results in [93] (solid line) to a reanalysis of the raw data from [93] using the 2014 calibration (dotted line). When the 2014 calibration is applied, the result from [93] has a similar shape as the results from this work. The scale offset is explained in Sec. 7.3.1.2.

important TPB optical effects, such as the scattering length, thickness dependent effects, and secondary reemission of visible light. The authors believe the simplified Monte Carlo model in [93], in combination with the previously mentioned logical error, underestimated the value of the GAF which led to systematically higher WLSE results.

As a crosscheck, the setup and sample used in [93] was modeled using the Monte Carlo described in this work, to determine the impact on the WLSE of using the more sophisticated model to evaluate the GAF. Differences between the setup used in [93] and this work include a thicker acrylic substrate and the distance between the TPB surface and photodiode. Both of these differences were accounted for in the evaluation of a GAF for the apparatus used in [93]. Applying this newly-evaluated GAF to the results in Fig. 7.18 yields Fig. 7.19. The shaded region spanning the dashed and dotted lines illustrates the uncertainty in the photodiode calibration used in [93] at the time of the 2011 measurement. For comparison, the WLSE from this work for a sample of comparable thickness is plotted as a solid line. This result is consistent with the GAF-corrected results from [93] to within the limits driven by the uncertainty in that work's photodiode calibration.

These differences in evaluating the GAF and its uncertainty contribute to differences in scale between the WLSE measurements presented in this work and those presented in [93].

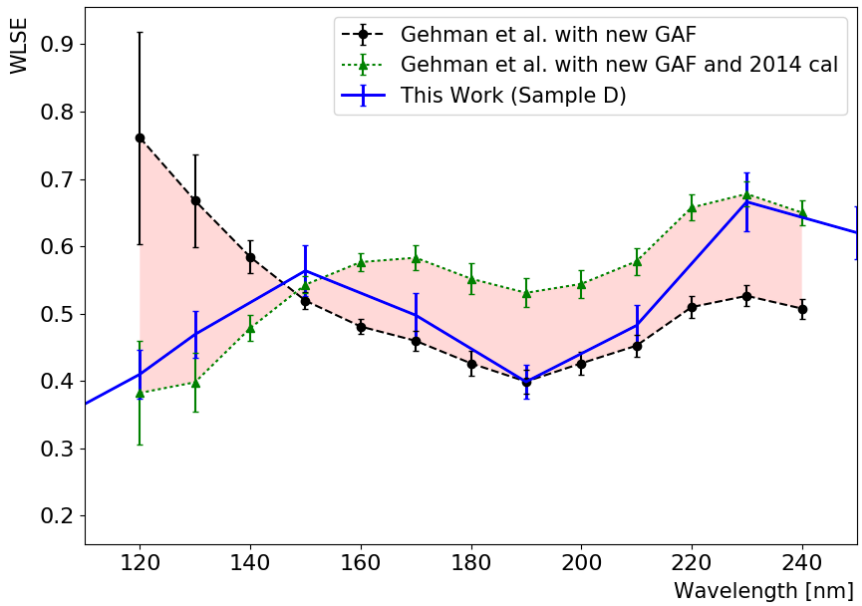

Figure 7.19: Impact of re-analyzing data from [93] using the Monte Carlo model described in this work. The solid line shows the WLSE of a sample of comparable thickness to that studied in [93]. The shaded region spanning the dashed and dotted lines illustrate the uncertainty in the photodiode calibration used in [93] at the time of the 2011 measurement.

7.3.1.3 Background subtraction and beam intensity

This work used much of the same hardware as was used in [93]. It was determined that the original focusing mirror and Al+MgF_2 diffraction grating required replacement because of discoloration on the optical surfaces likely resulting from years of use. The damaged elements are shown in Fig. 7.20. It was observed that the level of background light was elevated, shown in Fig. 7.21, and the intensity of light at short wavelengths was attenuated when using the discolored optical elements. When the damaged optical elements were replaced at the start of this work, the amount of background light visible by the spectrometer was substantially reduced and the VUV light output at wavelengths between 120 – 250 nm was improved by between 20 – 50% across the wavelength range of interest.

A brighter light source leads to smaller statistical errors in the ratio of measured dark and background subtracted photocurrents given in (7.3). This is a dominant reason why the statistical error in the WLSE measurements of this work are smaller at most wavelengths than in [93]. Higher statistics resulting from a more intense incident UV beam also result in the cleaner, more stable measured reemission spectra presented in this work (Fig. 7.8).

It is also important to note that in this work, a background subtraction is performed in addition to a dark current subtraction for wavelengths below 150 nm (7.1). Because any measurement of reemitted light from a TPB sample is actually a sum of reemitted light plus

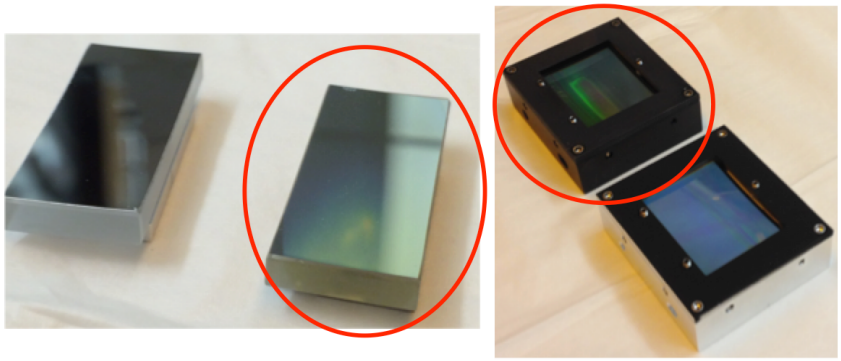

Figure 7.20: A comparison of damaged optical elements inherited from the setup used in [93] to replacements purchased at the start of this work. Damaged elements from [93] are are circled in red. The left image shows the focusing mirror while the right image show the Al+MgF_2 coated diffraction grating.

any background light, a separate measurement is required to determine the magnitude of the background light, as described in Sec. 6.5.1. This correction was not included in [93] – only a dark current subtraction was performed. Background levels at short wavelengths (below 135 nm) were observed to be on the order of the reemitted signal when using the discolored optics inherited from the setup used in [93]. The spectrum of the elevated backgrounds when using the discolored optics from[93] is seen in Fig. 7.21. The background levels were observed to increase in intensity for shorter wavelength monochromator output settings. It is likely that elevated background levels may have been unaccounted for in their TPB signal measurements biasing their WLSE result toward larger values.

7.3.1.4 Overlapping measurements

This work was able to leverage two distinct light sources to make multiple measurements of the total wavelength shifting efficiency in the range of 130 – 150 nm. Referred to as the overlap region, the ability to measure the WLSE in this region using multiple configurations and light sources provides a nice crosscheck of configuration dependent systematic uncertainties. All measurements from the various configurations in this overlap region agree well, providing confidence that there is reasonable control of configuration-dependent systematic uncertainties.

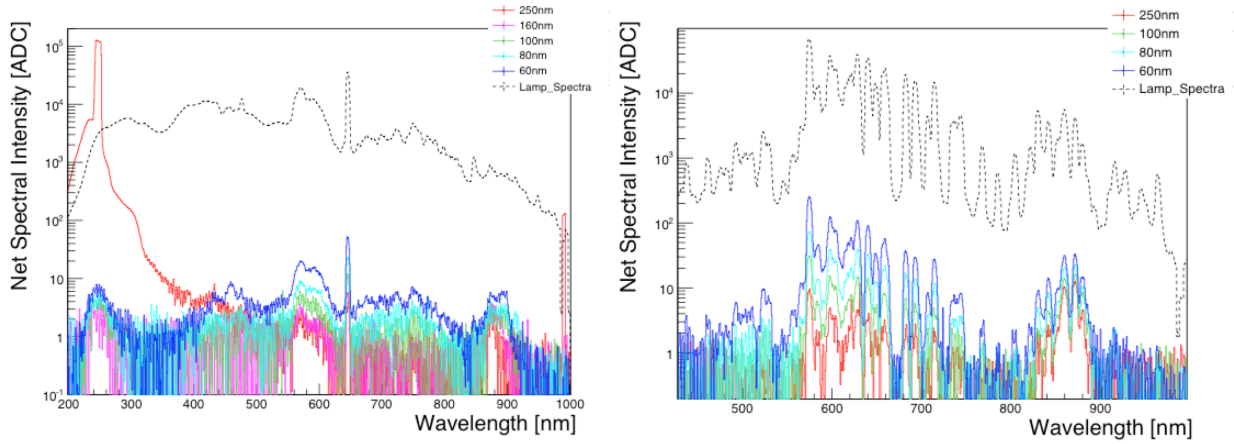

Figure 7.21: Elevated backgrounds backgrounds observed when using discolored optics inherrited from the setup in [93] as a function of monochromator output setting. The elevated background levels mirror the broad-band spectra entering the monochromator (black dotted line) where the left plot is for the deuterium lamp spectra and the right is for the He-Ne gas mixture. The background levels increase with shorter wavelength settings on the monochromator. It is likely that the damaged surface on the diffraction grating (right-side image in Fig. 7.20) diffusely reflected the inputted spectrum which elevated background levels that were not accounted for in [93].

7.3.2 Comparison to McKinsey et al. 1997 Measurement

7.3.2.1 Relative Efficiency vs. Sample Thickness

As discussed in Sec. 6.1.2 and seen in Fig. 6.2, McKinsey determined the optimal thickness for TPB evaporated films by studying the relative efficiency as a function of thickness. As an additional check of the thickness dependence of our data and model, results were compared to the relative response of samples of various thickness in [153].

Fig. 7.22 shows the relative response of samples as a function of TPB film thickness where the sample with the largest response is normalized to 1 for 74 nm incident light. The data reported in [153] is a function of coating thickness (mg/cm^2) and was converted to film thickness in micrometers using the inferred evaporated film density of 1.46 g/cm^3 from [93] and the assumption that the evaporated films in [153] were uniform.

As seen in Fig. 7.22, the peak-normalized data from [153], data from this work, and the Monte Carlo model used in this work are in fairly good agreement. This comparison provides a crosscheck of the thickness-dependent behavior predicted by the micro-physically motivated Monte Carlo model developed in this work, demonstrating that this model is consistent with independent data sets, and can be used to extrapolate to film thicknesses greater than those used in this work.

It should be emphasized that all of the values used in the Monte Carlo simulation in

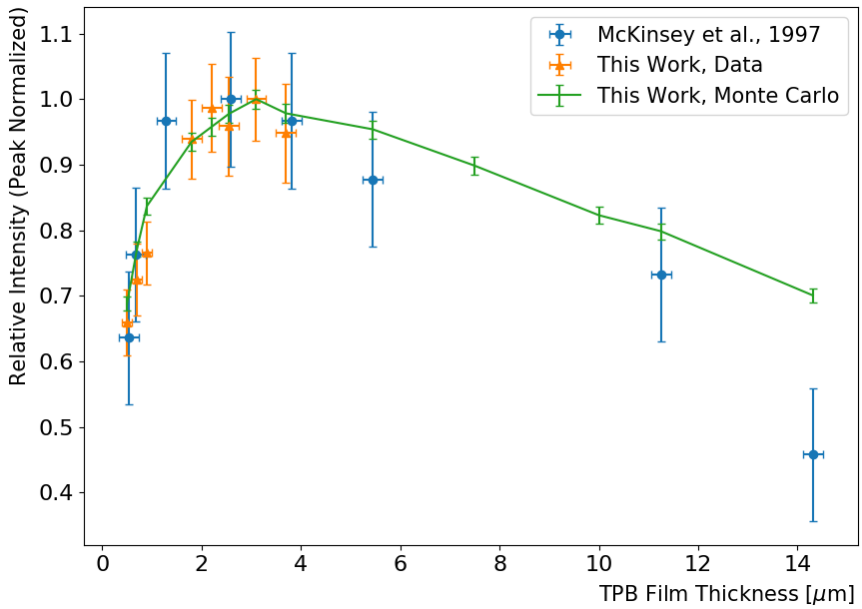

Figure 7.22: A comparison of the relative response of samples as a function of TPB film thickness for evaporated TPB thin film data in [153], data from this work, and Monte Carlo model predictions with the model used in this work.

this work, except for the VUV QE, absorption length and SQE, were set by measurement (remission spectrum) or values in the literature. Given the highly constrained nature of this model, the fact that the model accurately predicts the dependence of photon ratio on sample thickness (Fig. 7.6, Fig. 7.22) suggests that the Monte Carlo model used in this work is a good representation of the optical properties of TPB.

7.3.2.2 Scale of the QE Comparison

As discussed in Sec. 6.1.2, if one takes the simple approach of multiplying the QE values from [158] with the relative efficiency measurements of [153], this suggests that the QE of TPB may be as high as 1.64 at 58.4 nm and 1.37 at 74.0 nm. The absolute scale of this result disagrees with the results shown in Sec. 7.2 even though the relative thickness dependence is consistent (Fig 7.22). The author suspects that the difference arises from the absolute QE values of the sodium salicylate reference from [158] as that work used a simplified analytic optical model for sodium salicylate and is not consistent with the highly-constrained Monte Carlo model developed in this work. This hypothesis to explain the difference in the QE scale has not been proven and remains unresolved.

It is also important to note that there is some tension between the relatively lower TPB QE results presented in this work with the published light yield of existing experiments, such as DarkSide, that use TPB in their optics chain. When considering the known scintillation

yield of argon and the various efficiencies of elements in the optics chain, a low TPB efficiency would make it difficult to arrive at the measured 9 PE/keV$_{ee}$ seen in DarkSide [60]. However, there are other demonstrator liquid argon experiments in development (including MiniCLEAN) which seem to not be able to achieve the light yield predicited by simulations which use the larger numbers published by Gehman et al. in [93], but seem to agree substantially better when using the efficiency numbers from this work. At the time of this writing, this point of tension is not yet fully understood and is being investigated by the author and others.

Ultimately, the author believes the discrepancies uncovered in [93] and the development of a detailed microphysical model of TPB in this work are a step in the "right direction". At a minimum, the author hopes that this work will lead the field to conclude that the previous numbers provided in [93], which are used by many experiments, are questionable and that additional studies to validate the measurements made in this work should be considered.

7.4 Future Work

This section covers projects that have planned and may be completed in the near future.

7.4.1 Nanoparticles

Thin films containing high densities of nanoparticles show promise as an alternative wavelength shifting medium to TPB. Nanoparticles can be made form several different material species and can be engineered to have relatively narrow and specific reemission spectra. The ability to customize the reemission spectrum can be useful for optimizing the outputted spectrum to the peak efficiency of light detectors (e.g. PMTs) and/or minimal absorption of the propagating medium. Further, the QE of many nanoparticles are relatively flat with incident wavelength which would be a useful property of wavelength shifters used in detectors.

The wavelength shifting efficiency and reemission spectra of several commonly used nanoparticles species are not well known for the incident VUV wavelength in region of interest studied in this work. Several nanoparticle samples of various species were fabricated by the Paul Alivisatos group in the UC Berkeley Physical Chemistry department. The reemission spectra of these samples were measured for 160 nm incident light and is shown in Fig. 7.23.

There are plans to measure the WLSE of several nanoparticle species relative to TPB at VUV wavelengths. Preliminary measurements suggest that the WLSE of the samples shown in Fig. 7.23 are a fraction (less an 30%) of that of TPB samples studied in this work. Additional work needs to be done to be performed to determine optimal coating techniques for these nanoparticle thin films to ensure surface uniformity and film homogeneity.

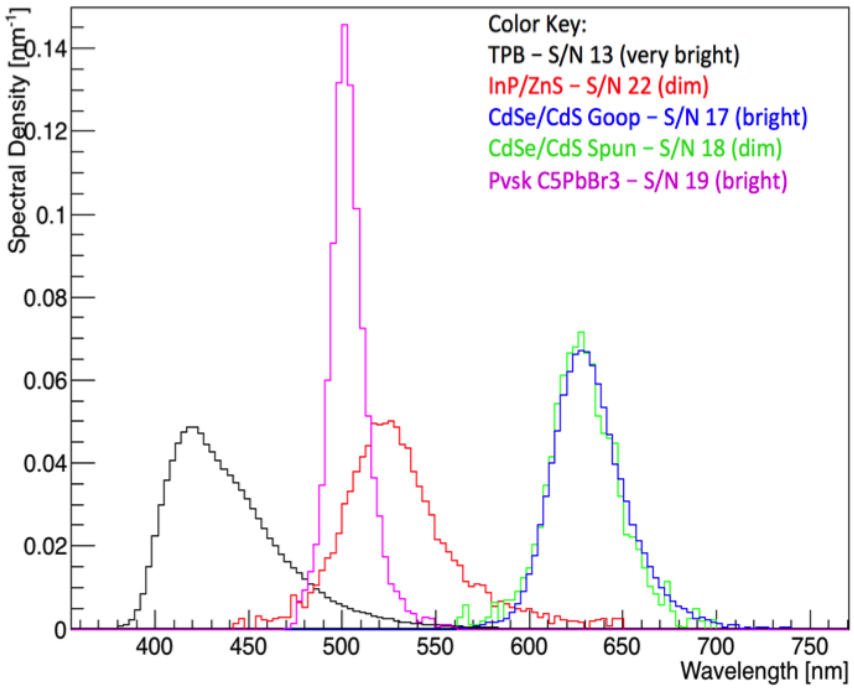

Figure 7.23: Area normalized reemission spectra of various nanoparticle species fabricated by the Alivisatos group (UC Berkeley, Physical Chemistry)

7.4.2 Reemission Angular Distribution Measurements

The angular distribution of the reemitted photons exiting a TPB thin film has not yet been measured and is usually assumed to be Lambertian in the forward and backwards direction [93].

As discussed in Sec. 7.1.2, the detailed Monte Carlo simulation developed in this work naturally predicts an approximately Lambertian angular distribution for photons leaving the TPB sample in the forward and backwards direction (Fig. 7.4). An approximately Lambertian distribution naturally falls out of the simulation even though the reemitted photons are reemitted isotropically at the point of creation (Fig. 7.3). The Lambertian angular distribution is due to internal scattering inside of the TPB and diffuse reflections at the TPB/vacuum interface.

As seen in Fig. 7.4, the Monte Carlo predicts a thickness dependence to the shape of the angular distribution. In particular, thinner samples are more isotropic for angles close to the normal.

Independently measuring the angular distribution of reemitted photons would provide provide a nice cross check of the predictions made by the model developed in this work. Additionally, measuring this distribution would provide feedback on the microphysical inputs mostly responsible for the shape of the angular distribution (i.e. scattering length and TPB

surface roughness model).

Early progress has been made on designing a setup to check the reemission angular distribution of TPB. The setup consists a TPB sample illuminated by a pulsed UV LED in a dark box. The TPB sample and UV LED are suspended above a PMT (or array of PMTs). The angular distribution of light leaving the TPB sample is measured by moving the TPB around, mapping the angular intensity and comparing to simulation. This work is still in the design phase could leverage the existing expertise and equipment from the CheSS experiment [176] in the Orebi Gann group.

7.5 Conclusion

This chapter presents the first measurement of certain microphysical parameters of TPB wavelength-shifting films. This leads to development of a complete model of the optical properties of vacuum-deposited TPB thin films at room temperature, independent of optical effects in the setup and the samples themselves, which is thus broadly applicable to other detectors. Results include the first measurement of the intrinsic QE and absorption lengths in the VUV regime as a function of wavelength. Also presented is a measurement of the SQE - the average efficiency of secondary reemission of visible photons in the regime where the TPB absorption and reemission spectra overlap.

These results enable high-precision modeling of VUV light detection in liquid noble gas experiments, such as those probing cutting-edge neutrino and dark matter physics.

Chapter 8

Summary and Conclusion

As discussed in Chap. 1, there are many compelling examples of indirect evidence pointing to the existence of dark matter. While many theoretical models have been developed in an attempt to explain the origin and properties of dark matter, experiments have only been able to set limits and to rule out certain candidate models due to a lack of direct evidence. The WIMP is a well-motivated dark matter candidate that is currently being investigated by several experiments. A variety of detector technologies are utilized, including liquid noble detectors, to look for WIMP scattering as a direct signature of dark matter.

The CLEAN experiment is a proposed single-phase, monolithic, large-scale liquid argon experiment designed to look for high-mass WIMPs. A liquid neon target could be exchanged with the argon target to study solar neutrinos and to test the A^2 dependence of a possible dark matter signal. Before scaling up to the multi-tonne scale of the full CLEAN detector, the design philosophy and background rejection capabilities are to be tested using the MiniCLEAN prototype. As of mid-2018, MiniCLEAN has been constructed at SNOLAB and is currently being filled with natural liquid argon for a dark matter run. Following a short dark matter run, MiniCLEAN will be spiked with elevated levels of ^{39}Ar to test the scaling limits of PSD. These results will inform the DEAP-3600 experiment and future liquid argon experiments. The author was heavily involved in the construction and commissioning of the MiniCLEAN experiment with contributions that were described in Chap. 4.

As discussed in Chaps. 2 and 5, the time structure and yield of scintillation light in noble gas targets depends strongly on the purity of the target. Nitrogen and/or oxygen contamination on the order of ppm can reduce the amount of light produced (via non-radiative deexcitation) and shorten the observed triplet decay time constant, which reduces energy resolution and the background rejection power of PSD. Chap. 5 presented measurements of the triplet time constant and relative light yield of scintillation light produced in cold gaseous argon as a function of impurity level. This result reported the longest triplet time constant found in the literature (3484 $\pm$ 65 ns) and a reaction rate between triplet excimers and impurities consistent with previous measurements. It was also determined that late light from the triplet state contributes approximately 6.37 times more light than the prompt and intermediate components at a triplet time constant of 3484 ns. This result is consistent with

previous measurements, but with improved precision and quantified over a larger range of impurity levels. These findings are expected to the improve modeling of scintillation light in gaseous argon. They could also be used to help determine impurity levels in gaseous argon experiments from measurements of the triplet time constant when direct measurement of impurity levels is impractical.

As mentioned in Chap. 2, tetraphenyl butadiene (TPB) thin films are used in many experimental efforts, including MiniCLEAN, as an intermediate step in the optics chain to down-convert the energetic VUV scinillation light to visible wavelengths for detection using PMTs. A good understanding of the underlying microphysical properties of these thin films is important as they are critical inputs into detector models. Chap. 6 and 7 describe measurements of several parameters critical to constructing a microphysically-motivated model of TPB thin films. These include the incident wavelength dependence of the intrinsic quantum efficiency and absorption length, and the average quantum efficiency of secondary reemission. Differences between the results of this work and those presented in [93] are explained and discussed in Sec. 7.3. Aside from improving and expanding the measurement of these parameters over previous works, the detailed microphysical model of TPB developed in this work reproduces expected behaviors of TPB films, such as the thickness dependence of film performance, Lambertian angular distribution of reemitted photons, and the general red-shifting of the reemission spectrum for thicker films. These measurements and the development of an improved microphysical model of TPB are expected to improve the modeling of TPB in current and future detectors including the international DUNE long-baseline neutrino experiment, and the LEGEND neutrinoless double beta decay search, as well as next-generation dark matter searches.

Bibliography

[1] F. Zwicky, Astrophys. J. **86** 217 (1937).

[2] V. C. Rubin, *et al.*, Astrophys. J. **238** 471-487 (1980).

[3] NASA/CXC/CfA/M.Markevitch *et al.*; Optical: NASA/STScI; Magellan/U.Arizona/D.Clowe *et al.*; Lensing Map: NASA/STScI; ESO WFI; Magellan/U.Arizona/D.Clowe *et al.*.

[4] K. Freese, EAS Pub. Ser. **36** 113-126 (2009).

[5] A. Refregier, Ann. Rev. Astron. Astrophys. **41** 645-668 (2003).

[6] S. Alam, *et al.*, Astrophys. J. Supp. Ser. **219** 1 (2015).

[7] C. L. Bennett, *et al.*, The Astro- physical Journal Supplement Series, **208**(2):20, 2013.

[8] https://map.gsfc.nasa.gov/resources/imagetopics.html

[9] G. Jungman, *et al.*, Phys. Rep. **267**, 195 (1996).

[10] E. W. Kolb and M. S. Turner, The Early Universe, Addison-Wesley (1989).

[11] http://pdg.lbl.gov/2018/reviews/rpp2018-rev-dark-matter.pdf

[12] J. Buckley, *et al.*, arXiv:1310.7040 [astro-ph] (2013).

[13] V. A. Mitsou. J. of Physics: Conf. Series **651** 012023 (2015).

[14] R. Peccei and H. R. Quinn, Phys. Rev. Lett. **38**, 1440-1443 (1977).

[15] M. Dine, *et al.*, Phys. Lett. B **104**, 14-16 (1981).

[16] M. A. Shifman, *et al.*, Phys. Lett. B **104**, 493 (1980).

[17] G. Rybka, Phys. Dark. Univ. **4**, 14-16 (2014).

[18] N. Du, *et al.* (ADMX Collaboration) Phys. Rev. Lett. **120**, 151301 (2018).

[19] B. M. Brubaker, *et al.* Phys. Rev. D 96, 123008 (2017).

[20] L. Baudis, arXiv:1509.00869 [astro-ph] (2015).

[21] K. Olive, *et al.*, Chin. Phys. C **38** 090001 (2014).

[22] K. N. Abazajian, *et al.*, arXiv:1204.5379 [hep-ph] (2012).

[23] L. Wyrzykowski, *et al.*, MNRAS **413** 493-508 (2011).

[24] Particle Data Group, Dark matter review. http://pdg.lbl.gov/2018/reviews/rpp2018-rev-dark-matter.pdf. Accessed May 2018.

[25] M. Milgrom, Can. J. Phys. **93**, 107 (2015).

[26] L. Bernard and L. Blanchet, Phys. Rev. D **91**, 103536 (2015).

[27] J. Aasi, *et al.* (LIGO Collaboration) Classical and Quantum Gravity **32**, 074001 (2015).

[28] J. M. Ezquiaga, and M. Zumalacarregui, https://arxiv.org/pdf/1710.05901.pdf (2017).

[29] T. Caldwel. Ph.D. Thesis, University of Pennsylvania, (2015).

[30] M. W. Goodman and E. Witten, Phys. Rev. D **31**, 3059 (1986).

[31] M. Drees and M. Nojiri, Phys. Rev. D **48**, 3483 (1993).

[32] V. A. Bendyakov, *et al.*, Phys. Rev. D **50**, 7128 (1994).

[33] J. D. Lewin and P. F. Smith, Astropart. Phys. **6**, 87-112 (1996).

[34] R. H. Helm, Phys. Rev. **104**, 1466 (1956).

[35] M. Reid, *et al.*, Astrophys. J. **700** 137-148 (2009).

[36] S. Gillessen, *et al.*, Astrophys. J. **692**, 1075-1109 (2009).

[37] S. Yellin, Phys. Rev. D **66**, 032005 (2002).

[38] S. Henderson, *et al.*, Phys. Rev. D **78**, 015020 (2008).

[39] J. Conrad, Astropart. Phys. **62**, 165-177 (2015).

[40] S. Biller and S. Oser, Nucl. Inst. and Methods A, **774** 103-119 (2015).

[41] E. Aprile *et al.* (XENON Collaboration) Phys. Rev. Lett. **119**, 181301 (2017).

[42] T. Saab, arXiv:1203.2566 [ins-det] (2012).

[43] R. Bernabei, *et al.*, The European Physical Journal C **56**, 333 (2008).

[44] DM-Ice Collaboration, arXiv:1509.02486 [ins-det] (2015).

[45] J. Amare, *et al.*, Journal of Physics: Conference Series **203**, 012044 (2010).

[46] G. Alner, *et al.*, Science **616**, 17 (2005).

[47] S. Yoshida, *et al.*, Nuclear Physics A **721**, 2003.

[48] V. Chepel and H. Araujo. JINST **8**, R04001 (2013)

[49] K. Rielage *et al.*, (MiniCLEAN Collaboration), Phys. Proced **61**, 144 (2015).

[50] A. Hime (MiniCLEAN Collaboration), arXiv:1110.1005 (2011).

[51] M. G. Boulay (DEAP Collaboration), J. Phys.: Conf. Ser. **375**, (2012).

[52] K. Abe *et al.* (XMASS Collaboration), Nucl. Instrum. Meth. A **716**, 78–85 (2013).

[53] P.-A. Amaudruz *et al.* (DEAP-3600 Collaboration), arXiv:1707.08042 [astro-ph.CO], (2017).

[54] http://www-sk.icrr.u-tokyo.ac.jp/xmass/about/status/index-e.html, Accessed May 2018.

[55] Xiangyi Cui *et al.* (PandaX-II Collaboration) Phys. Rev. Lett. **119**, 181302 (2017).

[56] D. S. Akerib, *et al.* (LUX Collaboration), Nucl. Instrum. Meth. A **704**, 111–126 (2013).

[57] D.S. Akerib, *et al.* (LUX Collaboration), PRL, **118**, 021303 (2017).

[58] D. Y. Akimov, *et al.* (ZEPLIN Collaboration), Phys. Let. B, **709**, 0370-2693 (2012).

[59] D. S. Akerib, *et al.* (LUX-ZEPLIN Collaboration), arXiv:1802.06039 (2018).

[60] P. Agnes, *et al.* (DarkSide Collaboration), Phys. Lett. B **743**, 456–466 (2015).

[61] J. Calvo, *et al.* (ArDM Collaboration), Journal of Cosmology and Astroparticle Physics, **2017**, 021 (2017).

[62] C. E. Aalseth, *et al.* (CoGeNT Collaboration) Phys. Rev. D, **88**, 012002 (2013).

[63] C. E. Aalseth, *et al.*, arXiv:1401.3295 [astro-ph] (2014).

[64] C. Cuesta, *et al.*, arXiv:1507.07612 [ins-det] (2015).

[65] G. Benato, for the GERDA Collaboration, arXiv:1509.07792 [nucl-ex] (2015).

[66] G. K. Giovanetti, *et al.*, J. Phys. Conf. Ser. **375**, 012014 (2012).

[67] N. Abgrall, *et al.* (Majorana Collaboration), Phys. Rev. Lett. **118**, 161801 (2017).

[68] G. Angloher, *et al.* (CRESST-II Collaboration), Astroparticle Physics **31** 270–276 (2009).

[69] C. Alduino, *et al.*, Phys. Rev. Lett. **120**, 132501 (2018).

[70] F. Alessandria, *et al.*, JCAP05, 007, (2013).

[71] R. Agnese, *et al.* (SuperCDMS Collaboration) Rhys. Rev. D., **95**, 082002 (2017).

[72] F. Aubin, *et al.*, New J. of Phys. **10**, 103017 (2008).

[73] E. Behnke, *et al.*, Phys. Rev. Lett. **106**, 021303 (2011).

[74] E. Behnke, *et al.*, (PICASSO Collaboration) Astroparticle Physics **90**, 8592 (2017).

[75] W. J. Bolte, *et al.*, (COUPP Collaboration) Journal of Physics: Conference Series **39**, 126 (2006).

[76] C. Amole, *et al.*, (PICO Collaboration) Phys. Rev. Lett. **118**, 251301 (2017).

[77] S. Amerio, *et al.* (ICARUS Collaboration), Nucl. Instrum. Meth. A **527**, 329–410 (2004).

[78] R. Brunetti, *et al.* (WARP Collaboration), New Astron. Rev **49**, 265 (2005).

[79] C.Amsler, *et al.* (ArDM Collaboration), Acta Phys. Polon. B **41**, 1441-1446 (2010).

[80] R. Acciarri, *et al.* (MicroBooNE Collaboration), JINST **12**, P02017 (2017).

[81] R. Acciarri, *et al.* (DUNE Collaboration), arXiv:1512.06148 (2016).

[82] D. Y. Akimov, *et al.* (ZEPLIN Collaboration), Astroparticle Phys. **27**, 46–60 (2007).

[83] E. Aprile, *et al.* (XENON Collaboration), Astroparticle Phys. **35**, 573–590 (2012).

[84] J. Aalbers *et al.* (DARWIN Collaboration), JCAP **1611**, 17 (2016).

[85] J. Lindhard, *et al.*, Matt. Fys. Medd. Dan. Vid. Selsk **33**, 10 (1963).

[86] P. Sorenson and C. E. Dahl, Phys. Rev. D **83**, 063501 (2011).

[87] E. Dahl., Ph.D. Thesis, Princeton University, (2009).

[88] J. Thomas and D. A. Imel, Phys. Rev. A **36**, 614 (1987).

[89] H. Cao, *et al.*, Phys. Rev. D **91**, 092007 (2015).

[90] D.-M. Mei, et al., Astropart. Phys. **30**, 12–17 (2008).

[91] tudrtTheted

[92] W.H. Lippincott, *et al.*, Phys. Rev. C **78** 035801 (2008).

[93] V. M. Gehman, *et al.*, Nucl. Instrum. Meth. A **654**, 116–121 (2011).

[94] S. Jaditz, Ph.D. Thesis, Massachussettes Institute of Technology, (2015).

[95] J. Wang. Ph.D. Thesis, University of New Mexico, (2017).

[96] M.C. Chen, Nucl. Phys. Proc. Suppl. **145**, 65–68 (2005).

[97] S. Andringa, *et al.* (SNO+ Collaboration), Adv. High Energy Phys. **2016**, 6194250 (2016).

[98] G. Bellini, *et al.*, Phys. Rev. D **89**, 112007 (2014).

[99] S. Abe, *et al.* Phys. Rev. C **84**, 035804 (2011).

[100] A. Suzuki, Eur. Phys. J. C, **74**, 3094 (2014).

[101] W. H. Lippincott, *et al.*, Phys. Rev. C **86**, 015807 (2012).

[102] M. G. Boulay, *et al.*, arXiv:0904.2930 [ins-det] (2009).

[103] J.J. Van Deemeter, *et al.*, Chem. Eng. Science Vol. **5**, 271-289 (1956).

[104] M.K. Harrison, *et al.*, Nucl. Inst. and Methods A **570**, 556-560 (2007).

[105] Bodmer, M, *et al.* Nucl. Instrum. Meth. A. **697**, 99106 (2013).

[106] D.-M. Mei and A. Hime, Phys. Rev. D. **73**, 053004 (2006).

[107] B. Aharmin, *et al.*, Phys. Rev. D **80**, 012001 (2009).

[108] M. Aoki, Y. Iwashita, M. Kuze, and T. Bolton, Nucl. Phys. B (Proc. Suppl.) **149**, 166 (2005).

[109] J. Allison, *et al.*, IEEE Trans. Nucl. Sci. **53** 270-278 (2006).

[110] S. Agostinelli, *et al.*, Nucl. Inst. Meth. A **506** 250-303 (2003).

[111] R. Brun and F. Rademakers, Nucl. Instrum. Meth. A, **389**, 81–86 (1997).

[112] MiniCLEAN internal RAT documentation, https://deapclean.org/rat/trac/wiki/UserGuide/Overvie (2015).

[113] M. Akashi-Ronquest, *et al.*, Astroparticle Physics, **65**, 40-54, (2015).

[114] https://web.archive.org/web/20070509023017/. Accessed April 2018.

[115] http://www.geoberg.de/text/geology/07011601.php. Accessed April 2018.

[116] P. Benetti, *et al.* Nucl. Instrum. Meth. A **574**, 83-88 (2007).

[117] B. Wang, MiniCLEAN internal document cl1107034, (2011).

[118] SNOLAB Gamma Assays, https://www.snolab.ca/users/services/gamma- assay/links.html.

[119] D.-M. Mei, *et al.*, Nucl. Instrum. Meth. A **606**, 651-660 (2009).

[120] S. Liu, M. Sci. Thesis, Massachusettes Institute of Technology (2011).

[121] K. Palladino, MiniCLEAN internal document cl1404008, (2014).

[122] B. Jones, *et al.*, JINST **18** P01013 (2013).

[123] http://www.saespuregas.com/Products/Gas-Purifier/PS4-MT315.html. Accessed Aug. 2015.

[124] https://webbook.nist.gov/. Accessed Sept. 2016

[125] MiniCLEAN Gas Analysis paper draft (2018).

[126] B. M. Smirnov, Soviet Physics Uspekhi **26**, 31 (1983).

[127] P. Moutard, *et al.*, The Journal of Chemical Physics **87**, 4576 (1987).

[128] A. Hitachi, *et al.*, Phys. Rev. B **27**, 5279 (1983).

[129] N. Thonnard and G. S. Hurst, Phys. Rev. A **5**, 1110 (1972).

[130] L. Goubert, *et al.*, Chemical Physics Letters **219**, 360 (1994).

[131] E. Velazco, *et al.*, The Journal of Chemical Physics **69**, 4357 (1978).

[132] W. Krotz, *et al.*, Phys. Rev. A **43**, 6089 (1991).

[133] A. K. Amirov, *et al.*, Journal of Physics B: Atomic, Molecular and Optical Physics **27**, 1753 (1994).

[134] P. Grimm, *et al.*, Nucl. Instrum. Meth. A **262**, 394 (1987).

[135] J. Wieser, *et al.*, Optics Communications **173**, 233 (2000).

[136] T. Moeller, and G. Zimmerer. Physica Scripta T17 **177** (1987).

[137] R. Sauerbrey, *et al.*, J. Phys. B: At. Mol. Phys. **17**, 2057 (1984).

[138] C. Amsler, *et al.*, Journal of Instrumentation **3**, P02001 (2008).

[139] R. E. Gleason, *et al.*, Journal of Chemical Physics **66**, 1589 (1977).

[140] P. Millet, *et al.*, Journal of Physics B: Atomic and Molecular Physics **15**, 2935 (1982).

[141] M. Carvalho and G. Klein, Journal of Luminescence **18**, 487 (1979).

[142] T. Suemoto, *et al.*, Physics Letters A **61**, 131 (1977).

[143] J. W. Keto, *et al.*, Phys. Rev. Lett. **33**, 1365 (1974).

[144] T. Oka, *et al.*, The Journal of Chemical Physics **70**, 3384 (1979).

[145] F. Marchal, *et al.*, Journal of Physics B **42**, 015201 (2009).

[146] E. Segreto, Phys. Rev. C **91**, 035503 (2015).

[147] W. Verkerke, *et al.*, eConf C0303241 MOLT007 (2003).

[148] D. W. Loeb, *et al.*, The Journal of Chemical Physics **74**, 3270 (1981).

[149] C. Benson, *et al.* Eur. Phys. J. C **78**, 329 (2018).

[150] J. A. R. Samson, John Wiley & Sons, Inc. (1967).

[151] W. M. Burton *et al.*, Applied Optics, **12**, 87 (1973).

[152] S. E. Wallace-Williams, *et al.*, J. Phys. Chem., **98**, 60–67 (1994).

[153] D. McKinsey *et al.*, Nucl. Instrum. Meth. B **132**, 351–358 (1997).

[154] R. Francini, *et al.* JINST **8** P09006 (2013).

[155] D. Stolp, *et al.* JINST **11** C03025 (2016).

[156] S. P. Regan, *et al.*, Applied Optics, **33**, 3595 (1994).

[157] R. Allison *et al.*, Opt. Soc. Amer., **54**, 747–750 (1964).

[158] E. C. Bruner Jr., Opt. Soc. Amer. A, **59**, 204 (1969).

[159] J. Cornil, *et al.*, Chem. Phys. Lett. **247**, 425 (1995).

[160] M. Ashraf El-Bayoumi, J. Chem. Phys. **80**, 2259 (1976).

[161] http://mcphersoninc.com/pdf/634.pdf

[162] http://www.mcphersoninc.com/pdf/234302.pdf

[163] http://optodiode.com/pdf/AXUV100G.pdf

[164] L. R. Canfield *et al.*, Metrologia, **35**, 329 (1998).

[165] E. M. Gullikson *et al.*, Journal of Electron Spectroscopy and Related Phenomena, **80**, 313 (1996).

[166] R. Vest, NIST Photodiode Calibration Report, (2016).

[167] Polymer Plastics Company, LC. UVT Acrylic Ultraviolet Transmitting Sheet. *http* : *//www.polymerplastics.com/transparents*$_u$*vta*$_s$*heet.shtml*

[168] M. Kuzniak. Personal Communication, (2009).

[169] D. Bower, An Introduction to Polymer Physics, Cambridge University Press, New York, (2002).

[170] H. Huber, *et al.*, Canadian J. of Chem., **42**, 2065 (1964).

[171] http://geant4.slac.stanford.edu/UsersWorkshop/PDF/Peter/OpticalPhoton.pdf

[172] W. H. Press *et al.*, Numerical recipes in C: The Art of Scientific Computing,Cambridge University Press New York (1992),

[173] R. Vest, NIST Photodiode Calibration Report, (2008).

[174] R. Vest, NIST Photodiode Calibration Report, (2014).

[175] C. S. Tarrio, *et al.*, Proceedings of SPIE, **7271**, (2009).

[176] J. Caravaca, *et al.*, Phys. Rev. C **95**, 055801, (2017).

Appendix A

Derivation of Absolute WLSE and GAF

The purpose of this appendix is two-fold: 1) To derive the absolute WLSE presented in Eq. 7.3 (Sec. A.1) and 2) show a logical error in calculating the WLSE in [93] (Sec. A.2).

A.1 WLSE Derivation

This section derives the absolute WLSE equation using a toy model approach. The framework constructed in this section will be used to prove a logical error in the WLSE defined in [93] in Sec. A.2.

As seen in Fig. A.1, when a WLS sample is placed in the VUV beam, the VUV photons exiting the monochromator are incident on the TPB surface. The number of VUV photons exiting the monochromator that are incident on the TPB surface after time Δt, α_{UV}, is defined in Eq. A.1 as:

$$\alpha_{UV} = (N_{UV,slit})(f_{slit/TPB}) \tag{A.1}$$

where $N_{UV,slit}$ is the number of VUV photons exiting the monochromator and $f_{slit/TPB}$ is the fraction of VUV photons that hit the TPB surface after exiting the monochromator. $f_{slit/TPB}$ is equal to 1 for the setup used in this work.

Fig. A.2 shows the case of light photocurrent measurement (Sec. 6.5) where the empty slot is selected in the sample wheel allowing the VUV photons to pass directly to the photodiode.

The number of VUV photons detected by the photodiode in the light photocurrent measurement, ϕ_{UV}, is defined in Eq. A.2 as:

$$\phi_{UV} = (N_{UV,slit})(f_{slit/PD})(\gamma_{UV}) \tag{A.2}$$

where $f_{slit/PD}$ is the fraction of VUV photons that hit the PD surface after exiting the monochromator and γ_{UV} represents the probability that that a VUV photon incident on the

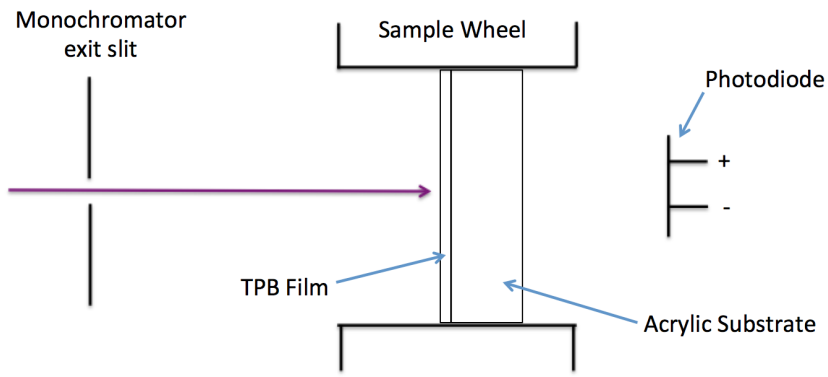

Figure A.1: A cartoon and annotated representation of UV photons exiting the monochromator incident on the TPB thin film in the setup described in Sect. 6.5. The photodiode is located behind the acrylic substrate.

photodiode is detected. For the setup used in this work, $f_{slit/PD}$ was determined to equal 1 and γ_{UV} is assumed to equal 1.

As seen in Eq. A.1 and Eq. A.2, a convention is used where α_i represents the total number photons incdient on or leaveing the TPB sample, while ϕ_i represents the number of photons that are detected at the location of the photodiode.

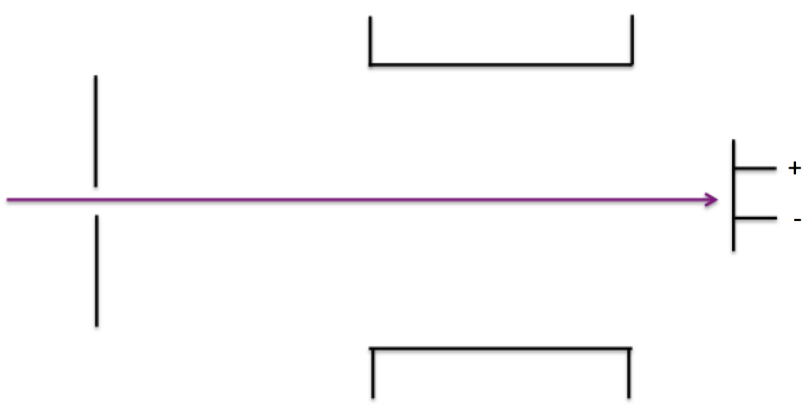

Figure A.2: A cartoon representation of UV photons exiting the monochromator incident on the photodiode for a light photocurrent measurement.

Fig. A.3 shows the case of a sample photocurrent measurement where a TPB sample is selected in the sample wheel and placed in the VUV beam. VUV photons are absorbed by the TPB film and visible photons are reemitted according to the TPB reemission spectrum.

The number of visible photons which are created, $N_{tot,vis}$, and which escape the sample (TPB and acrylic), α_{vis}, are defined in Eq. A.3 and Eq. A.4 as:

$$N_{tot,vis} = (\alpha_{UV})(T_{UV,tpb})(f_{UV,abs})(\epsilon_{QE}) \tag{A.3}$$

$$\alpha_{vis} = (N_{tot,vis})(f_{vis_esc}) = N_{vis,f} + N_{vis,b} + N_{vis,s} \tag{A.4}$$

where $T_{UV,tpb}$ is the fraction of UV photons that are incident on the TPB that pass into the TPB (UV transmission), $f_{UV,abs}$ is the fraction of UV photons that pass into the TPB that are absorbed by the TPB, ϵ_{QE} is the intrinsic quantum efficiency of the TPB at the wavelength of the incident photon (average number of photons reemitted per VUV photon absorbed), f_{vis_esc} is the fraction of photons created in the TPB that escape the sample (TPB + acrylic disk), $N_{vis,f}$ is the number of reemitted photons which escape in the forward direction (toward the photodiode), $N_{vis,b}$ is the number of reemitted photons which escape in the backwards direction, and $N_{vis,s}$ is the number of reemitted photons which escape out of the side of the sample.

The VUV transmission fraction, $T_{UV,tpb}$, is a value less than one due to reflections at the TPB/vacuum boundary (modeled as a rough surface in this work's model). $f_{UV,abs}$ is a value typically less than one and depends on the VUV absorption length in TPB and the thickness of the TPB sample. f_{vis_esc} is a value less than one which depends on the visible absorption spectrum in TPB, sample thickness, secondary reemission efficiency, visible absorption length in acrylic and the index of refraction in acrylic and TPB.

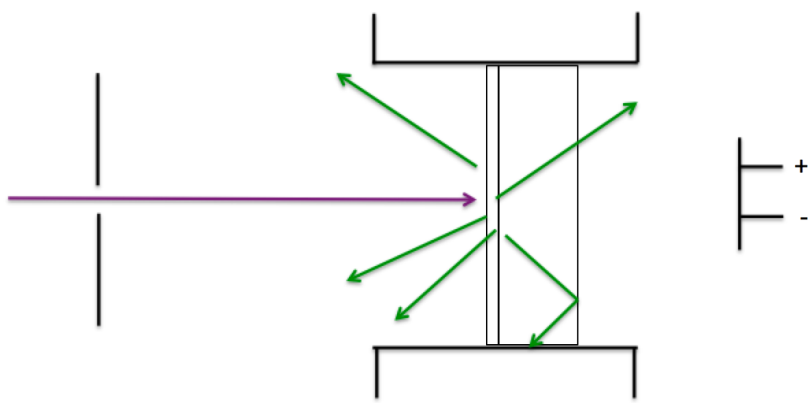

Figure A.3: A cartoon representation of reemitted photons being produced and propagating in and out of the sample.

Fig. A.4 shows the subset of reemitted photons that have escaped the sample and are detected by the photodiode. The number of reemitted photons which are detected by the

photodiode, ϕ_{vis}, is defined in Eq. A.5 as:

$$\phi_{vis} = (\alpha_{vis})(f_{vis,PD})(\gamma_{vis}) \tag{A.5}$$

where $f_{vis,PD}$ is the fraction of reemitted photons that have escaped the sample that terminate on the photodiode's active area and γ_{vis} is the probability that a photon terminating on the photodiode's surface is detected. $f_{vis,PD}$ is the geometric acceptance fraction of the photodiode, as defined in Sec. 7.1.1, which depends on the specifics of the setup and the angular distribution of photons exiting the sample.

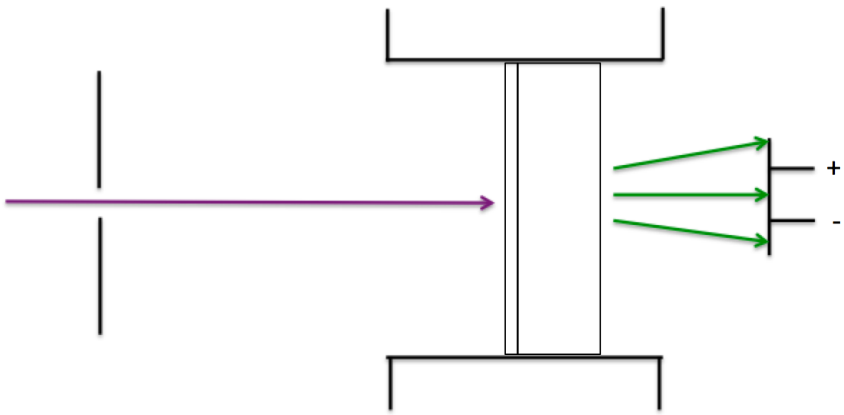

Figure A.4: A cartoon representation of the subset of reemitted photons to be captured by the photodiode.

We define the absolute wavelength shifting efficiency, ϵ', also known as the "black-box" WLSE, as the number of reemitted photons escaping the sample to the number of VUV photons incident on the sample. This is defined in Eq. A.6 as:

$$\epsilon' = \frac{\alpha_{vis}}{\alpha_{UV}} = \frac{(\alpha_{UV})(T_{UV,tpb})(f_{UV,abs})(\epsilon_{QE})(f_{vis_esc})}{\alpha_{UV}} \tag{A.6}$$

which simplifies to Eq. A.7:.

$$\epsilon' = (T_{UV,tpb})(f_{UV,abs})(\epsilon_{QE})(f_{vis_esc}) \tag{A.7}$$

Eq. A.7 therefore shows a simple form of how to compute the "black-box" WLSE for a given sample at a particular wavelength of incident VUV light.

It is useful to define the ϵ' in terms of the our observables measured in the apparatus, i.e. ϕ_{vis} and ϕ_{UV}. Solving for α_{UV} and α_{vis} in Eq. A.2 and Eq. A.5 yields in Eq. A.8:

$$\alpha_{UV} = \frac{(\phi_{UV})(f_{slit,tpb})}{(f_{slit,PD})(\gamma_{UV})}; \alpha_{vis} = \frac{\phi_{vis}}{(f_{vis,PD})(\gamma_{vis})} \tag{A.8}$$

Plugging Eq. A.8 into the definition of ϵ' in Eq A.6 yeilds Eq. A.9:

$$\epsilon' = \frac{\alpha_{vis}}{\alpha_{UV}} = \frac{\phi_{vis}}{\phi_{UV}} \frac{1}{(f_{vis,PD})(\gamma_{vis})} \frac{(f_{slit,PD})(\gamma_{UV})}{f_{slit,tpb}}. \tag{A.9}$$

Recalling from Sec. 7.1.1, VUV photon flux from a light measurement is given in Eq. A.10 as :

$$\phi_{UV} = \frac{I_{light} - I_{corr}}{\int d\lambda' \frac{hc}{\lambda'} R(\lambda') M(\lambda - \lambda')} \tag{A.10}$$

where $I_{light} - I_{corr}$ is the dark/background corrected light photocurrent measurement, $R(\lambda)$ is the absolute responsivity of the photodiode at wavelength λ, and $M(\lambda - \lambda')$ is the spectrum of light of VUV exiting the monochromator (well approximated as a Gaussian, Fig. 6.7). In similar fashion, the measured reemitted photon flux is given in Eq. A.11 as:

$$\phi_{vis} = \frac{I_{tpb} - I_{corr}}{\int d\lambda'' \frac{hc}{\lambda''} R(\lambda'') P(\lambda'')} \tag{A.11}$$

where $I_{tpb} - I_{corr}$ is the dark/background corrected sample photocurrent measurement, and $P(\lambda)$ is the reemission spectrum of TPB.

Looking back to Eq. A.9, the middle term on the RHS (i.e. $(f_{vis,PD})(\gamma_{vis})$) is interpreted as the inverse of the reemitted photon geometric acceptance fraction multiplied by the photodiode collection efficiency. The last term (i.e. $\frac{(f_{slit,PD})(\gamma_{UV})}{f_{slit,tpb}}$) is interpreted as an equivalent VUV geometric acceptance fraction for the setup used in this work multiplied by the photodiode collection efficiency. Plugging Eq. A.10 and Eq. A.11 into Eq. A.9 yields Eq. A.12:

$$\epsilon' = \frac{(I_{tpb} - I_{corr})}{(I_{light} - I_{corr})} \frac{\int d\lambda' \frac{hc}{\lambda'} R(\lambda') M(\lambda - \lambda')}{\int d\lambda'' \frac{hc}{\lambda''} R(\lambda'') P(\lambda'')} \frac{1}{(f_{vis,PD})(\gamma_{vis})} \frac{(f_{slit,PD})(\gamma_{UV})}{f_{slit,tpb}}. \tag{A.12}$$

Simplifications for the setup used in this work are defined in Eq. A.13 as:

$$f_{slit,PD} = 1; f_{slit,TPB} = 1; \gamma_{UV} = 1; \gamma_{vis} = 1 \tag{A.13}$$

and applied to Eq. A.12 in Eq. A.14:

$$\epsilon' = \frac{(I_{tpb} - I_{corr})}{(I_{light} - I_{corr})} \frac{\int d\lambda' \frac{hc}{\lambda'} R(\lambda') M(\lambda - \lambda')}{\int d\lambda'' \frac{hc}{\lambda''} R(\lambda'') P(\lambda'')} \frac{1}{f_{vis,PD}} \tag{A.14}$$

which is the equivalent to Eq. 7.3. Note that A_i in Eq. 7.3 is equivalent to $f_{vis,PD}$.

This completes the derivation of the absolute WLSE. The relationships constructed in this section will be used to demonstrate a logical issue found in [93] in Sec A.2.

A.2 Logical Error

This section heavily references equations and text in [93].

Shortly after the definition of Eq. 1 in [93], Gehman et. al defines their geometric efficiency, g, as "the ratio of the number of UV photons reaching the photodiode when the filter wheel is in the open position to the number of visible photons observed by the photodiode when a TPB sample is in position, assuming unit fluorescence efficiency". In terms of the model constructed in Sec. A.1, this is defined in Eq. A.15 as:

$$g = \frac{\phi_{UV}}{\phi vis} = \frac{\phi_{UV}}{(\alpha_{UV})(T_{UV,tpb})(f_{UV,abs})(\epsilon_{QE})(f_{vis,esc})(f_{vis,PD})(\gamma_{vis})}. \tag{A.15}$$

Using the relationship in Eq. A.16:

$$\phi_{UV} = \frac{(\alpha_{UV})(f_{slit,PD})(\gamma_{UV})}{f_{slit,tpb}} \tag{A.16}$$

in Eq. A.15 and simplifying yields Eq. A.17:

$$g = \frac{\phi_{UV}}{\phi vis} = \frac{(f_{slit,PD})(\gamma_{UV})}{(f_{slit,tpb})(T_{UV,tpb})(f_{UV,abs})(\epsilon_{QE})(f_{vis,esc})(f_{vis,PD})(\gamma_{vis})}. \tag{A.17}$$

Eq. A.17 can be further simplified for the setups used in [93] and this work using Eq. A.18:

$$f_{slit,PD} = 1; f_{slit,tpb} = 1; \gamma_{UV} = 1; \gamma_{vis} = 1 \tag{A.18}$$

which yields Eq. A.19:

$$g = \frac{1}{(T_{UV,tpb})(f_{UV,abs})(\epsilon_{QE})(f_{vis,esc})(f_{vis,PD})}. \tag{A.19}$$

Eq. A.19 suggests that the definition of g in [93] contains dependencies on the VUV QE and optics of the TPB.

In [93], Eq. 1 is set equal to Eq. 3, which requires using the equality defined by Eq. A.20:

$$g = \frac{1}{A}. \tag{A.20}$$

Using the notation from Sec. A.1 and Eq. A.19, the equality in Eq. A.20 then becomes Eq. A.21:

$$g = \frac{1}{(T_{UV,tpb})(f_{UV,abs})(\epsilon_{QE})(f_{vis,esc})(f_{vis,PD})} = \frac{1}{f_{vis,PD}}. \tag{A.21}$$

Simplifying Eq. A.21 yields the equality shown in Eq. A.22:

$$(T_{UV,tpb})(f_{UV,abs})(\epsilon_{QE})(f_{vis,esc}) = 1 \tag{A.22}$$

which, in general, is not true.

It was determined that g, as defined in Eq. A.15, was evaluated in [93] using a Monte Carlo simulation. The equality defined in Eq. A.20 was then used to convert the forward efficiency (Eq. 2 in [93]) to the WLSE (Eq. 3 in [93]). Therefore the equality in Eq. A.22 was an implicit assumption that was made which in general is not true.

From the detailed Monte Carlo simulation used in this work, the following values were typical for samples of comperable thickness to that studied in [93]: $T_{UV,tpb} \approx 0.94$, $f_{UV,abs} \approx 0.99$, $\epsilon_{QE} \approx 0.6$ (at 130 nm), $f_{vis,esc} \approx 0.85$. The product of the values is far from unity and depends on sample thickness and the optical properties of TPB and the acrylic substrate. This logical error in the computation and application of the "geometric efficiency" therefore contributed to an over-estimation of the WLSE reported in [93]

Appendix B

Supplementary Information: WLSE Uncertainty

B.1 Configuration Offset

An configuration dependent offset in the observed photon ratio was observed for wavelengths in the overlap region (130–150 nm). This offset was found to be a constant, independent of incident wavelength and TPB film thickness (to within our uncertainties), only depending on the particular light source is used.

The offset is likely due to different illumination profiles on the diffraction grating. As mentioned in Sec. 6.3, the LWC uses the DLS and focusing mirror while the IWC and SWC only use the windowless lamp (no focusing mirror). The focusing mirror was adjusted and optimized to uniformly project light onto the face of the diffraction grating inside of the monochromator when using the LWC. Because the IWC and SWC do not use the focusing mirror (because the Al+MgF_2 coating absorbs very short wavelengths), the illumination profile of the diffraction grating can not be adjusted and is different than the LWC. In simulation, the photons are modeled as leaving the surface of the diffraction grating with uniform illumination, consistent with the LWC. This motivates uniformly correcting the IWC and SWC photon ratios by the observed offset to account for this effect.

Fig. B.1 shows the photon ratio as a function of sample thickness for the LWC and IWC for 150 nm incident light. An offset can be seen between the data sets from each configuration. The same offset is observed for 130- and 140-nm incident light (not shown).

Because the offset is constant as a function of incident wavelength and sample thickness, the optimal scalar to scale the IWC to the LWC photon ratios may be determined by choosing a value which minimizes the χ^2 difference between two photon ratios. All sample thicknesses for each of the overlapping wavelengths (130-, 140-, and 150- nm) are used in the evaluation

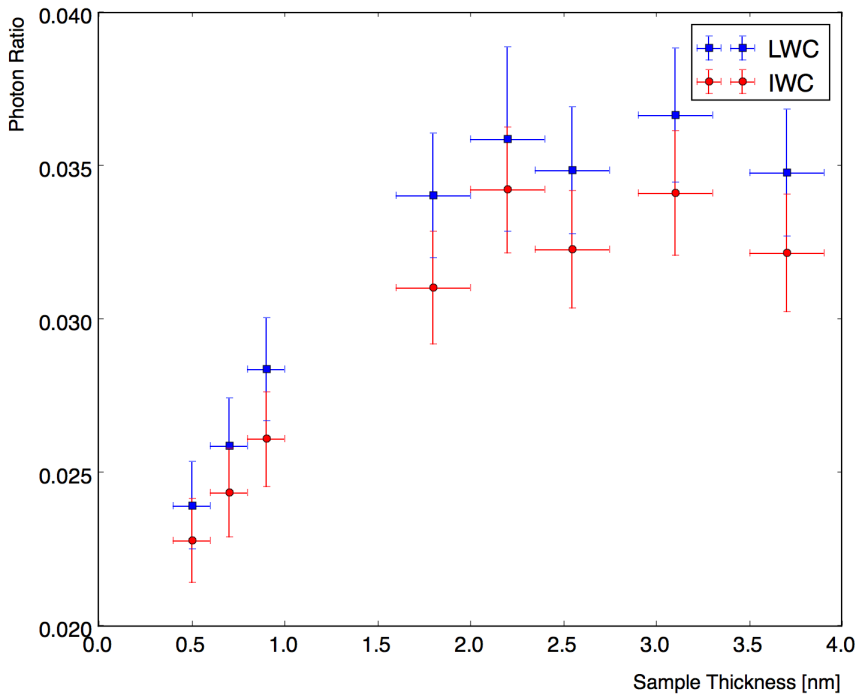

Figure B.1: Measured photon ratios as a function of TPB film thickness for configuration using two different at 150 nm incident wavelength. A relative offset, independent of sample thickness, can be observed between the two configurations.

of the χ^2. This is defined in Eq. B.1 as:

$$\chi^2 = \sum_{j=1}^{3} \sum_{i=1}^{N} \left(\frac{\beta_{i,j,LWC} - (A)(\beta_{i,j,IWC})}{\sqrt{\sigma^2_{i,j,LWC} + \sigma^2_{i,j,IWC}}} \right)^2 \tag{B.1}$$

where j is the summation index over the three wavelengths in the overlap region, N is the number of samples of different thickness, $\beta_{i,j,LWC}$ is the photon ratio of the ith sample at the jth wavelength using the LWC, $\beta_{i,j,IWC}$ is the photon ratio of the ith sample at the jth wavelength using the IWC, $\sigma_{i,j,LWC}$ is the uncertainty in the photon ratio of the ith sample at the jth wavelength using the LWC, $\sigma_{i,j,IWC}$ is the uncertainty in the photon ratio of the ith sample at the jth wavelength using the IWC, and A is the factor used to scale $\beta_{i,j,IWC}$ to $\beta_{i,j,LWC}$. The χ^2 is plotted as a function of A in Fig. B.2 with a minimum present at A equal to 1.098 $\pm$ 0.02. The uncertainty is evaluated from the $+1\Delta\chi^2$ from the minimum.

Fig. B.3 shows the effect on the IWC photon ratios after applying the scale factor for the case of 150 nm light. This illustrates that the data sets are in good agreement after the scale factor is applied. The associated uncertainty is propagated though the evaluation of the photon ratio uncertainty for IWC and SWC data sets, as described in Sec. 7.2.2.1.

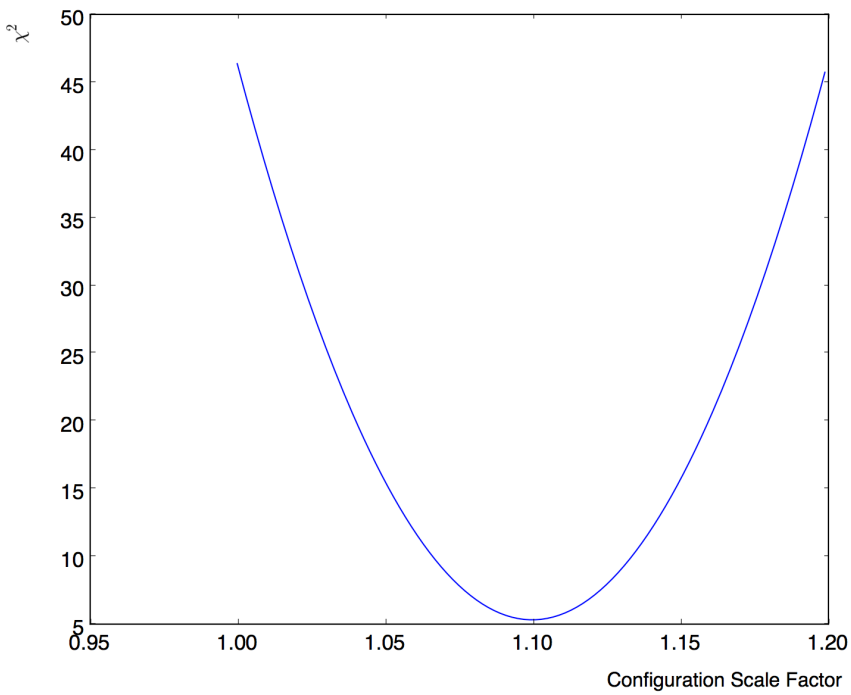

Figure B.2: χ^2 from Eq. B.1 plotted as a function of scale factor A. A minimum is present at A equal to 1.098. A 0.02 uncertainty is evaluated from the $+1\Delta\chi^2$ from the minimum

B.2 Photodiode Cross-Calibration

Two photodiodes, referred to as PD-1 and PD-2, were purchased at the start of this work following the discovery that the reponse of the photodiode used in [93] had changed significantly since its first calibration in 2008. PD-1 was calibrated by NIST at the beginning of 2016. The response of PD-2 was mapped relative to PD-1 immediately before and after PD-1's NIST calibration at the start of 2016 across the full region on interest. The response of PD-1 and PD-2 were found to be have identical responses within the errors the cross-calibration measurement. This cross-calibration procedure was done to allow PD-2 to be used as a calibration reference in the future. PD-2 was the placed in long term storage while PD-1 was solely used for systematic-cross checks and preliminary measurements.

Once the setup and samples were ready for final data acquisition, PD-2 was removed from storage and used to cross-check the response of PD-1 immediately after the final data acquisition period. PD-2 was only exposed to 2 data runs per configuration to minimize time in UV beam. Two runs per configuration were required to verify the stability between calibration measurements. During both cross-calibrations, the response of PD-2 (by looking at both the VUV and visible spectrum response for a reference TPB sample thickness and the ratio of sample/light photocurrents) was found to be the same as when it was initially calibrated.

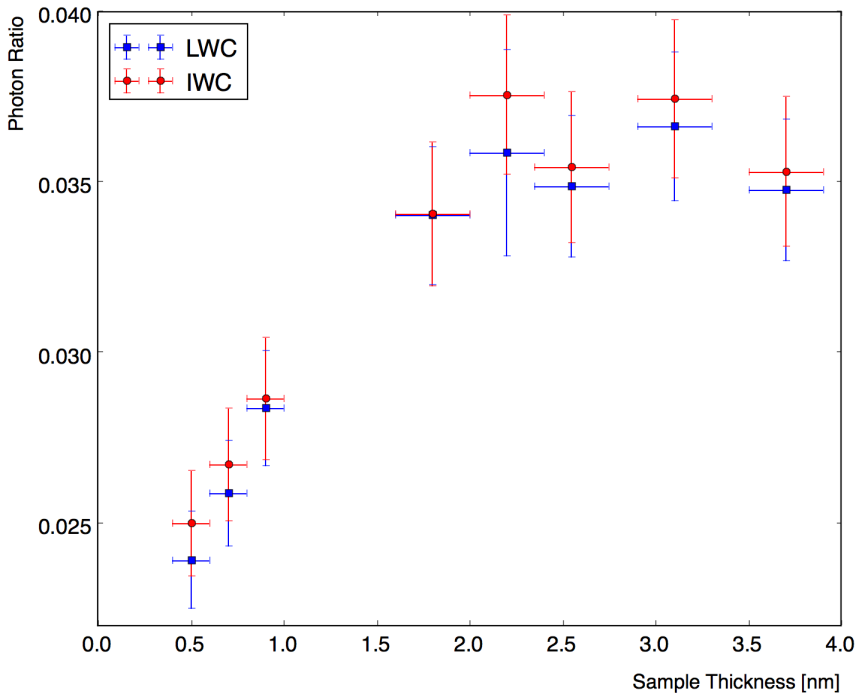

Figure B.3: Measured photon ratios from Fig. B.1 after applying the configuration dependent correction. After the correction, photon ratios for all samples at all wavelengths (130- and 140- nm) not shown agree to within their uncertainties.

By comparing the response of PD-1 to the PD-2 calibration reference, it was determined that the response of PD-1 (the photodiode used for cross-checks and data acquisition) had changed from its original calibrated state given by the 2016 NIST calibration (Fig. 6.9). This change is shown in Fig. B.4. The change is similar to changes seen in photodiode used in [93] (Fig. 7.17) providing further evidence that an unaccounted for change in the photodiode calibration is plausible explaination for differences. However, because a carefully maintained calibration reference was made available, this change has be quantified and corrected for in this work where it was not in [93].

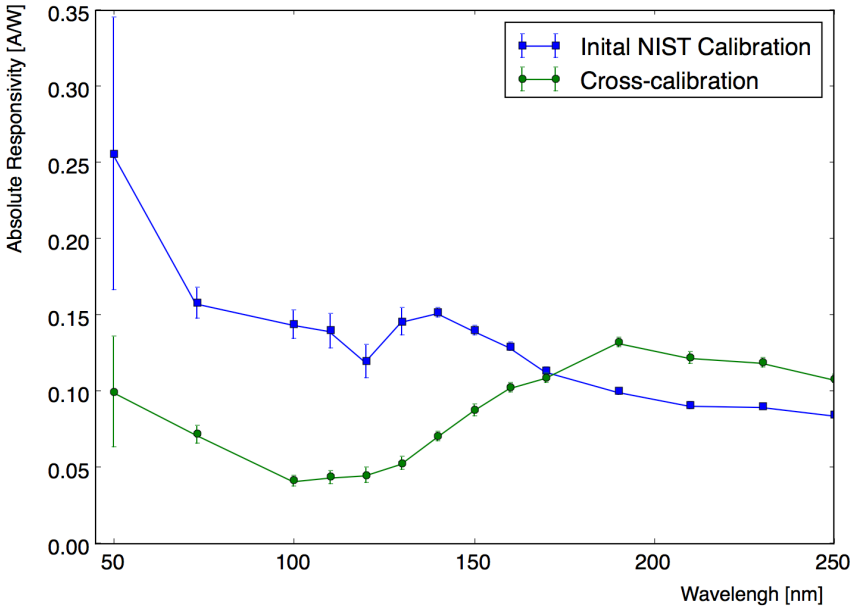

Figure B.4: The calibration of PD-1 used in this work at various points in time. The initial calibration was performed by NIST in early 2016. The cross-calibration was performed immediately after final data acquisition was complete.